ORIGIN OF DOLOMITES AND ASSOCIATED POROSITIES IN LOWER ORDOVICIAN BOAT HARBOUR FORMATION CARBONATES, WESTERN NEWFOUNDLAND, CANADA

by

Babatunde John Olanipekun (MSc)

A thesis submitted to the School of Graduate Studies in partial fulfillment of the requirements for the degree of

Doctor of Philosophy

Department of Earth Sciences/Faculty of Science

Memorial University of Newfoundland

March, 2016

St. John's, Newfoundland and Labrador

ABSTRACT

The Boat Harbour Formation constitutes the upper part of the Lower Ordovician St. George Group on the Northern Peninsula, western Newfoundland. It varies in thickness from 140 m at Main Brook to 96 m at Daniel's Harbour (about 200km). Dolomitization of the carbonate sequence is more pervasive in the lower 30–40 m at Main Brook, whereas at Daniel's Harbour the section is entirely dolomitized.

Petrography suggests that the formation has been affected by three phases of dolomitization: earliest (near-surface/syn-sedimentary) phase is D1 dolomicrite, mid–burial phase D2 dolomite, and late stage D3 dolomite. The earliest (near-surface/syn-sedimentary) phase is D1 dolomicrite. The geochemical composition suggests that D1 was developed from fluids of a mixture of meteoric and marine waters at near-surface conditions.

The mid–burial phase D2 dolomite consists of coarse planar sub–euhedral crystals that precipitated from hot fluids that circulated through crustal rocks with progressive burial. The late stage D3 dolomite has large and coarse non–planar crystals that exhibit sweeping extinction. In addition to its micro-thermometric data these factors suggest that it likely precipitated during deeper burial in pulses and from hot fluids.

For porosity the data suggest that it is mainly associated with the mid–burial D2 dolomite. Intercrystalline porosity is the dominant type and it varies in the formation from <1 to 8 % at Main Brook and from 7 to 12 % at Daniel's Harbour.

Recrystallization to more stoichiometric dolomite is usually accompanied by characteristic textural and geochemical signatures. These signatures are primarily studied using multiple populations of crystals, comparison of modern and ancient dolomites, or from results of high temperature dolomite formation experiments. This approach is inadequate.

Therefore study was done using multi proxy high resolution approaches to carry out imaging and ion microprobe elemental analyses of individual dolomite (burial) crystals viz: Scanning Electron Microscopy (SEM), SEM based cathodoluminescence (SEM-CL), Secondary Ion Mass Spectrometer (SIMS). This is to better understand geochemical variations across the crystal traverses and to constrain possible conditions of crystal growth.

The study reveals multiple mechanisms of dolomite crystal growth within constrained diagenetic settings and also shows that recrystallization and episodes of dolomitization evidenced by multi-crystal population, are also apparent within dolomite crystals. Further to this, photo-luminescence (PhL) features of the dolomite crystals were obtained using epifluorescence microscope. Combined with SEM-CL, SIMS measured Mn, Fe and REE-Y content of zoned and unzoned dolomite crystal facies are correlated with their luminescence characters (Chapter Four).

The study affirms that, at low concentrations (<200 ppm), the correlation of activators (Mn and REE) and quenchers (Fe) with occurrence and intensity of luminescence remains speculative. Broadly speaking, REE-Y content was too low to control luminescence and

Fe could not be conclusively demonstrated to have caused quenching, using the employed methods.

Morphology and genesis of nanopores and micro-inclusions hosted in intracrystalline areas of dolomites and their association/s with dolomite formation was investigated (Chapter Five). Burial dolomite samples of the Boat Harbour Formation were subjected to Broad Ion Beam (BIB) argon milling. Thereafter, Scanning Electron Microscope (SEM) was used to examine, at high resolution, micrometer to nanometer scale pores hosted in the crystals of the dolomites. Intracrystalline nanopores are abundant within the burial dolomite crystals. They are shown to have developed as a result of imperfection associated with the alignment process of crystallites' agglomeration. This occurred during the formation of the dolomite's major crystal face. Furthermore, the origin of mineral inclusions, 'which are accidentals' in intracrystalline nanopores is related to the mechanism of dolomitization that involves dissolution of precursor carbonate mineral (calcite or early dolomite) and precipitation of dolomite.

ACKNOWLEDGEMENTS

" Except the Lord build the house, they labor in vain that build it…" Ps. 127:1

First of all it is but the Lord who has brought me to this level of academic achievement and ALL of the glory belong to Him as He has made it to come to pass in His appointed time.

I would like to express the deepest appreciation to my committee chair Prof. Karem Azmy, who has continually and persuasively pointed me in the right direction in regard to research and scholarship. Without his supervision and constant help this dissertation would not have been possible. I would also like to thank Prof. Uwe Brand who is never fed up of reviewing my draft copies. He gave me constructive criticisms throughout the entire period of my program, most especially on the section on ion microprobe study of dolomite crystals. The support and regular critique of Prof. Elliot Burden is appreciated.

Dr. Folashade Olanipekun, my beautiful wife. Thank you very much for the love, support (in various forms), patience and endurance during my Phd program. Of course, you were able to achieve these through the support that you, in turn, got from your family (the most wonderful family I have ever seen!). You believed in me and I did not fail you. My mother (Mrs. Caroline Olanipekun) thank you very much for your unwavering love, care and support during my PhD program. The same goes to my sisters Funmi Akinjagunla and Yemi Famoroti. Daddy (Mr Oluwole Olanipekun) your unwavering belief in me, even when I nearly gave up is simply awe inspiring. I thank God for blessing me with such a wonderful dad.

Michael Oyeleke (MBA), my best friend. I do not know where to begin, but there is so much I would have left undone without the support (financial and moral) that you heartily gave me during the program. God bless and enrich you sir!

Engr. Oluseyi Lanipekun, my dear friend and cousin, you push me onto good things and this is one of them. It has yielded good success. Thank you.

Home in St. John`s: The support I got from my friends is significantly instrumental to my research strategy/approach: Drs James Conliffe (Newfoundland Geological Survey), Dario Harazim (Chevron, USA), Florian Bulle and Lina M Stolze (Norway). I will also like to Glenn Piercey who supported with SIMS analyses for almost 2 years. I will also like to thank the colleagues (Ebube Azomani, Amir Kabir and Alexander Charest) in my research group. Also I will like to thank my office mate (A.K.M Fayazul Kabir).

My friends: Julia I Aghanenu, Gift Madojemu and Paida Chawainetera. Thank you very much for being there for me. Same goes to Charlotte Chitaimani, Yemi Yusuf and many many others that time do not permit me to add but that will forever remain green in my memory.

Lastly but very importantly, I thank the Provincial Government of Newfoundland and Labrador for providing the funds for the research through the Petroleum Exploration Enhancement Program (PEEP).

LIST OF FIGURES

Chapter 1

Chapter 2

Chapter 5

Figure 5.5. Frequency distribution chart showing the aspect (length/breadth) ratios of the studied nanopores.

LIST OF TABLES

Chapter 2

Chapter 3

Chapter 4

1 CHAPTER 1

INTRODUCTION AND OVERVIEW

Background information and comprehensive literature review is contained in each of the subsequent chapter of the thesis. Therefore this section discusses the broad aspects of the dolomite as well as the rationale and objective of this research project.

Dolomite formation (Eqns. 1.1 and 1.2) may occur in different episodes, during the diagenetic history of a carbonates rock, depending on the evolution of pore-fluid chemistry, temperature and other kinetic factors. It involves the through put of fluids rich in Mg^{2+} and under a condition of minimal kinetic restraint (Warren, 2000). The kinetic factors involved in precipitation of dolomite in a sedimentary environment are ambiguous and sometimes complex, however, geochemical (commonly major-Mg, Ca, trace element-Sr, Mn, Fe, Na and stable isotopes-O and C) study in tandem with petrography (plane polarized light, scanning electron microscope, luminescence and fluid inclusion), is usually the best approach for understanding their origins (Machel, 2004).

$Ca^{2+}_{(aq)} + Mg^{2+}_{(aq)} + CO_3^{2-}{}_{(aq)} = CaMg(CO_3)_{2\,(S)}$ ……..….1.1

$1.74CaCO_{3\,(calcite)} + Mg^{2+} + 0.26CO_3^{2-} = CaMg\,(CO_3)_{2(dolomite)} + 0.74Ca^{2+}$ (dolomitization) (Merino and Canals,

2011)……...1.2

Equation 1.1 leads to sedimentary dolomite formation while equation 1.2 leads to dolomite replacement of limestone-dolomitization proper.

Dolomite may be formed at the surface to early burial condition and also at intermediate to deep burial conditions. This indicates that it may form from hot or cold aqueous solutions in a sedimentary system. Dolomite mineral is more abundant in ancient (Phanerozoic) carbonates that have undergone intermediate to deep burial diagenesis than in recent to sub-recent (Pleistocene to Holocene) formations.

Significant hydrocarbon reservoirs in Appalachian carbonates are associated with dolomitization (e.g., Selleck, 2004; Lavoie and Chi, 2008). More so, many hydrocarbon plays are hosted in the Permian basin's dolomitized Lower Ordovician Ellenburger Group carbonates (Broadhead et al., 2004), an equivalent of the St George Group carbonates. In addition dolomites are commonly found associated with base metals in Mississippi Valley deposits type (e.g., Lane, 1990; Gregg, 2004).These underscore the importance of characterizing the dolomites of the St George Group (e.g., Azmy et al., 2008, 2009; Conliffe et al., 2009; Azmy and Conliffe, 2010; Conliffe et al., 2012).

The pertinent literature review for this research project is embedded in each of the subsequent chapter as appropriate. This is to ensure that each chapter is independent as much as possible and for the reader to view the theoretical underpinnings relevant to that chapter.

However other background information that forms the rationale for this research project is presented in this chapter. The factors in this regard are the 'dolomite problem' and porosity associated with dolomitization.

1.1. The 'Dolomite Problem'

Attempts have been made by numerous authors to precipitate dolomite (in accordance with Eqn. 1.1) at conditions reminiscent of earth surface, but with little success. Arvidson and Mackenzie (1997; 1999) concluded, after well controlled attempts, that dolomite precipitation rate is much too slow to be replicated in the laboratory. Land (1998) also agreed with the latter authors, when he concluded that achieving the required cation order will take geologic time. In fact, Lippmann (1973) stated that dolomite 'does not precipitate or crystallize directly from seawater or related brines' but could form from fluids that were derived from seawater and that have deposited calcium carbonate. The latter author further commented that dolomite reaction rates are slow up to over 200^{o}C, which is not obtained in a normal sedimentary environment.

The only successful experiments known till now (2015) on low temperature dolomite formation are those carried out using sulphate reducing microbes (e.g., Vasconcelos et al., 1999; Warthmann et al., 2000; van Lith, et al., 2003). Some breakthrough was also recorded by Deelman, (2003; his Figure 3) with low temperature dolomite precipitation by addition of urea to the reactants, however only one superstructure reflection was detected and it is not conspicuous. In view of this, the bulk of the knowledge of dolomite properties has come from the high temperature precipitation of synthetic dolomite at

temperatures in excess of 200^{o}C (e.g., Nordeng and Sibley, 1994), which are extrapolated to low temperature conditions as the case may be.

In modern sedimentary environments, dolomite has only been found in supratidal to shallow sub-tidal, marginal, hydrologically restricted, hypersaline settings such as Coorong lakes of Australia and sabkhas of the Persian Gulf and in Florida (Avon Park). What is common to these locations are: increased alkalinity, high Mg/Ca ratios, high CO_3^{2-} , and variable salinities. The dolomites formed are commonly non-stoichiometric and disordered dolomites (Fig. 1.1) with weak superstructure intensity, and therefore have been termed neo/proto-dolomite to distinguish them from ideal dolomite minerals. The crystal sizes of the proto dolomite crystals as documented in these locations are mainly a few microns, in contrast to their ancient contemporaries which are largely well ordered and more stoichiometric with abundant coarser grains.

Variations in seawater chemistry have implication on the abundance of sedimentary dolomite. On the basis of Mg/Ca ratio, modern seawater is regarded to be supersaturated with respect to dolomite, but other factors exist that determine their formation and abundance. This can be explained using the history of seawater chemistry which shows that even though the present ocean (the last 100mya) contains elevated Mg/Ca, it also contains high SO_4/Ca ratios (Arvidson et al., 2008), and depressed CO_2 and carbonate saturation states (Lippmann, 1973). This state is therefore broadly accompanied with relative inhibition of organic matter accumulation and also minimal rate of dolomite precipitation. Conversely, the oceans during the early Paleozoic (especially Ordovician) were relatively lower in Mg/Ca and SO_4/Ca ratios, but higher CO_2 and carbonate

saturation state. This favoured high abundance of organic matter and sulphate reduction rates and ultimately sedimentary dolomite accumulation from the seawater to the extent that it was considered an Mg sink, hence controlling the chemistry of the seawater (Arvidson et al., 2008; Arvidson et al., 2011).

Natural dolomite currently forming in low temperature environments responds strongly to increases in carbonate alkalinity supplied by either aragonite dissolution or bicarbonate production during sulphate reduction and slight increase in temperature (Arvidson and Mackenzie, 1997; 1999). This was supported by laboratory experiment on dolomite nucleation on seeded aggregates (Arvidson and Mackenzie, 1999).

The stronger Mg^{2+}-H_2O bond in an aqueous system bond must have contributed to the failure of dolomite to precipitate from seawater because of the problem of dehydrating the Mg^{2+} (Lippmann, 1973; Tucker and Wright, 1990). However, it should be noted that, laboratory synthesis of anhydrous $MgCO_3$ by Deelman (2003) is inconsistent with former concept.

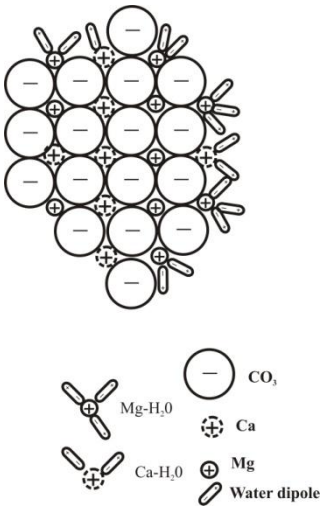

Figure 1.1.Sketch of a non-ideal lattice structure of dolomite showing between water dipoles and cations during slow dolomite nucleation. (After Lippmann, 1973).

1.2. Origin of porosity in dolomites

Despite insufficient knowledge on the nature of dolomite formation at surface conditions, it is known that dolomitization of limestone affects porosity. The conversion of limestone (calcite) and hydrous magnesium carbonates to dolomite results in increased porosity. Dolomitization of limestone according to Equation 1.3 leads to molar volume decrease from about 200 grams to about 184.4 grams accompanied by porosity increase of about 13%.

$$2CaCO_{3\,(calcite)} + Mg^{2+}_{(aq)} = CaMg\,(CO_3)_{2(dolomite)} + Ca^{2+} \quad \text{.....1.3}$$

This value may be reduced when calcite is precipitated as a precursor to the dolomitization process. However, if the dolomitization proceeds according to Equation 1.4, dolomite formation will proceed in the form of cement occluding pore spaces (Lucia, 2004).

$$CaCO_{3\,(calcite)} + Mg^{2+}_{(aq)} + 2CO_3^{2-}{}_{(aq)} = CaMg\,(CO_3)_{2(dolomite)} \quad \text{.....1.4}$$

This may happen if the system is open to an external supply of magnesium and carbonate (Lucia and Major, 1994; Lucia, 2004) subsequent to complete dolomitization of the limestone. An analogy for the dependence of porosity on the degree of openness of the system can be found in the experiment demonstrating the replacement process of KBr by KCl (Putnis, 2009). KBr was inserted into a solution supersaturated with respect to KCl resulting in disequilibrium with the KBr crystal. During the dissolution of the KBr crystal, a porous and permeable rim of K(Br,Cl) started to develop (Fig. 1.2). With

continuous residence of KBr in the solution and increasing volumetric supply of KCl, the reaction continued and the pores were eventually occluded.

The evolution of porosity during dolomitization of limestone sequences depends on the mode of replacement operating during dolomitization as well as the scale under consideration. At the crystal scale, dolomite replacement proceeds via a volumetric mode, whereby a crystal of dolomite replaces the same volume of precursor calcite and also occludes any precursor void spaces therein (Dockal, 1988; Maliva and Siever, 1988a; Maliva et al., 2011; Merino and Canals, 2011). Alternatively, at the bed scale, decrease in molar volume may lead to enhancement of porosity if mole-for-mole replacement mode controls the dolomitization process, whereby increase in the amount of dolomite in the limestone may yield increase in porosity. However, if the system is open to external supply of magnesium and carbonate, then there would be dolomite cementation which would reduce the porosity (Lucia and Major, 1994; Lucia, 2004) subsequent to complete dolomitization of the limestone.

The 'coupled' dissolution-precipitation as described above does not create void spaces. However, when dolomitization is near completion *and* dissolution of calcite still proceeds, then void spaces will be created away from the dolomite crystals (Maliva and Canals, 2011). Furthermore, porosity increase in dolomite may occur when limestone dolomitization proceeds through the intermediate phase of hydromagnesite [$(Mg_5(CO_3)_4(OH)_2.4H_2O$] and/or nesquehonite [$Mg(HCO_3)(OH).2(H_2O)$] formation before the final phase of dolomite formation. This phenomenon may yield up to 40% porosity (Lippmann, 1973).

Cautiously, porosity change explained by the molar volume difference model alone suffers a setback in that there are other mineral replacement reactions in the geologic system that are not accompanied by porosity differences. One of these is the serpentinization of olivine (Mg_2SiO_4; molar volume of ~50cm^3mol^{-1}) through orthopyroxene ($MgSiO_3$; molar volume of ~25cm^3mol^{-1}) to serpentine {$Mg_3[Si_2O_5](OH)_4$, molar volume of 100cm^3mol^{-1}}. This is supposed to lead to a volume expansion rather is often accompanied by pseudomorphic (constant volume) replacement (Putnis, 2009).

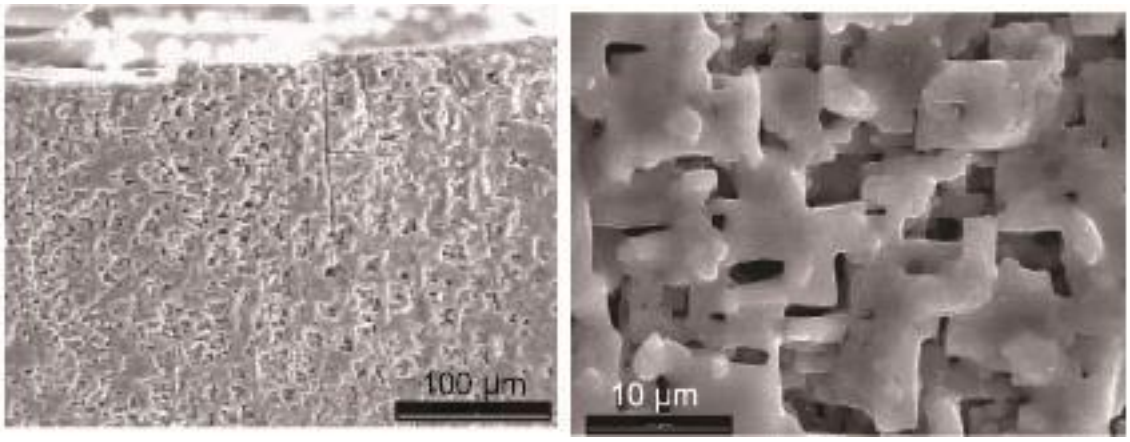

Figure 1.2. SEM image showing the pore spaces developed on the rim of a crystal of KBr immersed in KCl solution. (Putnis, 2009).

1.3. Rationale and Objectives

This section contains the overall rationale and objectives of the entire project. The global significance of dolomites in exploration/production of hydrocarbons (conventional and unconventional) and base metal (e.g., sphalerite and galena) deposits (Mississippi Valley Type sulphide mineralization) is undeniable. Yet this mineral, which may occur from multiple episodes, remains enigmatic.

Unravelling the origin of dolomites, requires multi-scale (field, multiple crystal populations, individual crystals) study, carried out by using as many tools (e.g., field relationships, logging tools, petrography, fluid inclusion and geochemistry) as appropriate and as available. Field study, which has led to the proposed models of dolomitization (e.g., sabkha style, Coorong style, brine reflux style, organogenic/methanogenic style, hydrothermal style) and multiple populations of dolomite crystal groups have been numerously documented (e.g., Amthor and Friedman, 1991; Amthor et al., 1992; Montanez, 1994; Saller, 2004; Lavoie, 2008; Conliffe et al., 2012). Indeed, it was from field studies that geologists realized that the massive quantity of burial dolomites is much more than can be accounted for by mass-balance. This is because the source of Mg that could form such volume of dolomite in a burial environment could not be unambiguously explained (e.g., Machel, 2004; Merino and Canals, 2011). This is in addition to the 'dolomite problem' explained in Sub-section 1.1.

In the quest to understand dolomite origin, numerous field studies have been carried out (e.g., Amthor and Friedman, 1991; Montanez, 1994; Saller, 2004; Lavoie, 2008). Field study, in addition to that of multiple population of dolomite crystals, is needed to

establish region wide diagenetic setting for dolomite formation. However, this approach, used in Chapter 2 to study the origin of dolomites in Boat Harbour Formation, is inadequate. To properly constrain the origin of dolomite, high resolution investigation of individual crystals using robust suite of elemental composition is necessary (Chapter 3). Yet this is very rare in the literature, especially in ancient carbonates. Such studies will shed light on the mechanism of dolomite crystal growth because a single crystal may be formed as a result of multiple dolomitization episodes.

Carbonates are very reactive minerals compared to silicates, hence geochemical proxies (e.g., major elements-Mg, Ca; trace elements-Fe, Mn, Sr, Na, Rare Earth Elements, Y; and stable isotopes-O and C) (e.g., Budd, 1997; Land 1998; Machel, 2004) are essential in their study. In tandem with textural features, these geochemical proxies enable researchers to trace the origin of respective dolomitization episodes. It should be mentioned that REEs are not uncommonly employed due to their susceptibility to contamination by minerals that are unrelated to dolomite. The ion microprobe approach employed in this study (Chapters 3 and 4) is a way to minimize such contamination during analyses within regions of interest that are less than about 40 μm Therefore, in combination with textural characteristics, compositional zonation and/or lack of it can be used to explain mechanism of dolomite formation.

Researchers, in quest to establish chemostratigraphy of sequences, have attempted to correlate luminescence zones in carbonates across km-wide regions (e.g., Montanez, 1994). This is to better understand the paragenesis of the dolomites they study. The current study seeks to investigate the local reaction site of dolomite formation to show if

the controls on zoning within dolomite crystals are a local phenomenon or wider in extent. In addition, controls on luminescence characters of carbonates are examined by correlating Mn, Fe and REE contents with luminescence features of Boat Harbour Formation burial dolomites (Chapter 4).

Porosity associated with the process of dolomite formation has been questioned (e.g., Lucia et al., 1994; Lucia, 2004). Many researchers believe that these pores are products of dissolution and fracturing (e.g., Gregg et al., 1993; Merino and Canals, 2011). Some pore types such as vugs and fractures, understandably result from dissolution and fracturing, respectively. However, such phenomena may not unambiguously account for intercrystalline and intracrystalline porosity of dolomites. Of the pore types in carbonate, intracrystalline pores have remained little studied. Perhaps this due to the fact that the usual mechanical grinding and polishing impose artifacts such as modification of pore morphologies on the samples. Using Broad Ion Beam milling, a novel approach, to process dolomite samples, these pores, as well as mineral micro-inclusions, can be examined *in situ* within the dolomite crystals (Chapter 5). The examination of such features sheds light on their relationship to the condition of dolomite formation. It should be noted that the study of dolomite using this style of micro-milling has not been found (by the author) to be the focus of other published work on dolomite.

1.4. Secondary Ion Mass Spectrometry (SIMS): Principles and Applications.

SIMS is a powerful microprobe technique used for surface analysis of composition and layer structure of solids. It is based on the detection of emitted secondary atomic and molecular charged particles when a material is irradiated by energetic particles (Francisco, 2012). The ion microprobe has a focused primary ion beam, which permits *in situ* microanalysis of mineral phases in geological samples prepared as polished sections (Hinton, 1995, p. 235).

Among the published reviews on microprobe techniques {e.g., Francisco, 2012; de Offman and Stroobant, 2007; Shimizu and Hart 1982; Evans Analytical Group, Materials Characterization, SIMS description section, n.d[1].; SIMS description, University of Edinburgh, n.d.}, the report from Hinton (1995, p. 235) was found to provide the most comprehensive review of the SIMS equipment and application tailored for use in the geological sciences. Therefore, a significant part of SIMS description contained in this section is drawn from his review. In the current research project, the most important advantage of SIMS, especially over the electron microprobe technique, is its high sensitivity (at the ppb level) for the detection of most elements of the periodic table including the lightest. Though other factors (e.g., cost and time) did not allow greater utilization, SIMS also has the ability to distinguish isotopes. These features make SIMS an attractive analytical method, well suited for analyzing crystal scale mineral phases in geological samples.

[1] n.d. means No Date.

Regardless of these advantages, SIMS has its own attendant limitations. Quantification poses a challenge because SIMS only detects the ionized fraction of the species being measured, which is difficult to evaluate in general (Francisco, 2012). Furthermore, uncertainties exist in the analytical results due to the dependence of secondary ion formation on mineral chemistry (i.e. matrix effects), as well as interferences resulting from the complexity of the secondary ion mass spectra generated by the sputtering of multi-element geological material (Hinton, 1995, p. 235).

1.4.1. Fundamentals (Instrumentation and Principles)

The fundamental components of a SIMS instrument are: *the primary ion source*; an *extraction* system which transfers the secondary ions from the surface of the sample to the entrance slit of the mass analyzer; the *mass analyzer* and *detector*.

Primary ion Source

SIMS uses a focused energetic primary ion beam to bombard (sputter) a solid sample surface. Modern SIMS instruments are equipped with a duoplasmatron (O^-, O_2^-, O_2^+), liquid metal Cs (Cs^+) or a Ga source. The primary beam most commonly used for analysing most geological materials is either O^- or Cs^+ ions with energies that range from 4 keV to 20 keV (e.g., Hinton, 1995, p. 239). The minimum Cs^+ spot size that can be achieved is about 0.1-0.2 µm, compared to about 0.5 µm for O_2^+ and 5 µm for O^- (Hinton, 1995, p. 239). For trace elements analyses, beam currents of 1 to 10 nA are typical used.

At these currents, a beam diameter of 1-10 μm is possible for Cs^+ but only 10-25μm for O^- (Hinton, 1995, p. 240).

The sputtering process involves an implantation of the primary ions into the sample. The impact of these highly energetic ions displaces atoms in the sample by setting up a 'collision cascade'. This causes surface atoms that receive energy higher than their binding energy to be sputtered (Fig. 1.3). This results in the emission of various secondary particles, consisting of electrons, neutral species atoms or molecules, and atomic and cluster ions. Among these secondary particles, positive or negative elemental and molecular ionized species are extracted and subsequently accelerated by an electrostatic field for mass spectrometric analysis.

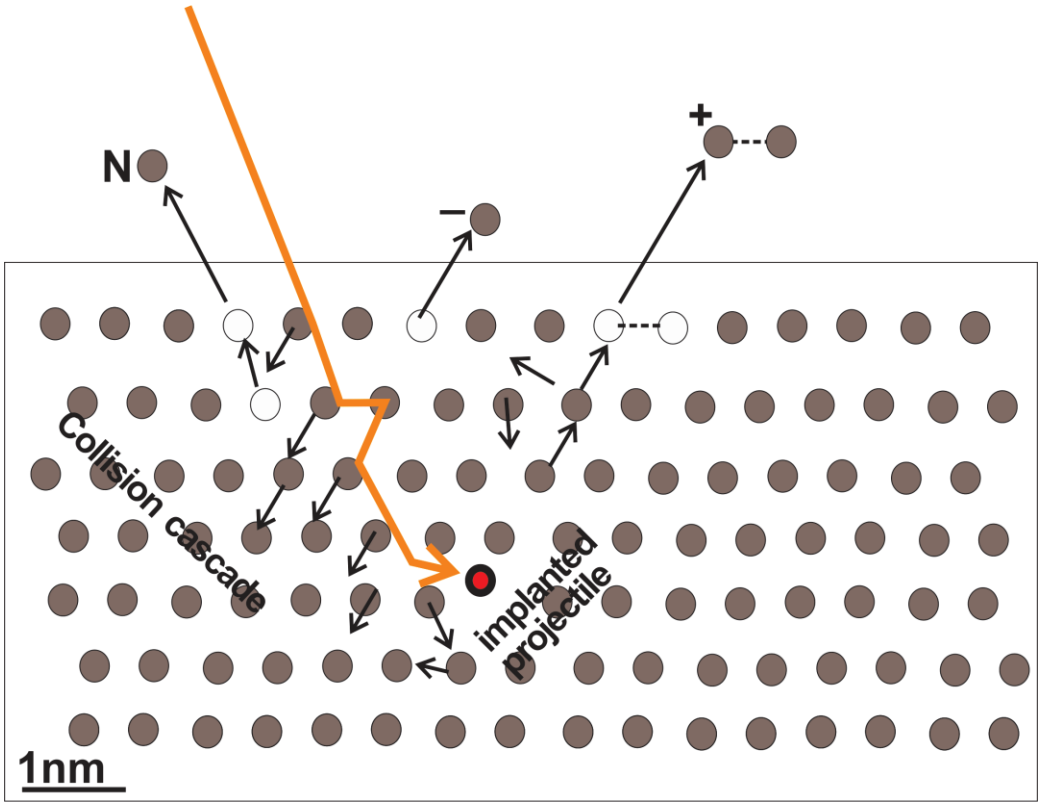

Figure 1.3. Schematic of the primary ion bombardment and its impact on solid sample surface. Open circles are surface locations where atoms were ejected from. N = neutral secondary ion species. Orange arrow is the primary ion beam and black arrows depict the motion of atoms caused by impact in impinging primary ion.

The number of ions formed per atom sputtered, known as the sputter yield *Y*, is highly variable between different elements and matrices (Hinton, 1995, p. 236). The sputter yield *Y* is related to the energy transmitted by an incident ion on the target surface, or energy loss per unit length in the direction normal to the surface (Francisco, 2012). For average-mass ions and 1 keV energy, *Y* takes values between 0.5 and 20. According to Hinton

(1995, p. 236) the ionization efficiency is typically lower than 1% for many elements (for either positive or negative secondary ions). The ion yield for a given element might vary by orders of magnitude depending on the chosen primary ion beam and the nature of matrix.

To enhance ionization efficiency, the user can choose an optimal primary beam species based on whether cations or anions are required for analyses. It follows that sputtering the sample surface with Cs^+ ion beam increases the number of negative secondary ions formed by elements with high electron affinity (e.g., halogens, C, N, O, S) by decreasing the surface work function (Hinton, 1995, p. 237). In contrast, an oxygen ion (e.g., O^-) primary beam correlates directly with ionization potential, thus increases the number of positive secondary ions (Hinton, 1995, p. 237). This is because when metal-oxygen bonds break in the ion emission process, the oxygen becomes negatively charged and inhibits positive charging due to its high electron affinity and high ionization potential. Thus the metal is left with positive charge (Evans Analytical Group, Materials Characterization, SIMS description section, n.d.). Therefore an oxygen ion beam is best suited for analyzing elemental compositions of carbonates, because cations such as Mg^{2+}, Ca^{2+}, Sr^{2+}, Mn^{2+},Fe^{2+}, Na^+, Zn^{2+}, REE^{3+} are the best understood proxies for deciphering the nature of carbonate minerals.

Lastly, it is important to note that, among the oxygen species produced in the duoplasmatron (O^-, O_2^-, O_2^+), O^- has the advantage of preventing static charge build up on the insulating sample surfaces (SIMS description, University of Edinburgh, n.d.).

Secondary ion extraction system

According to Hinton (1995, p. 240), secondary ions are sputtered from the surface of the sample with a variety of kinetic energies, in various directions and from different positions within the area sputtered (which in some cases may be up to 500 µm across). Most of the ejected ions leave the sample surface with relatively low kinetic energy (less than 20 eV) compared with the keV energy of the primary species (Shimizu and Hart, 1982). Although these sputtered species exhibit spatial, energy and angular variations, the mass spectrometer must have the capacity to resolve small differences in mass in order to overcome isobaric interferences from molecular ions. Secondary ion extraction systems are therefore designed such that maximum possible number of sputtered secondary ions is transmitted through the entrance slit of the mass spectrometer (Hinton, 1995). Importantly, the sample is held at high voltage (1-10 kV), thereby transferring added kinetic energy to the ions, which are then accelerated towards an extraction electrode held at ground potential. Note that, in some instruments the initial extraction voltage may be less than 200 V, but the ions are subsequently accelerated to high energy (several kV) (Hinton, 1995).

Analyzers

The CAMECA IMS 3f SIMS used in this project is equipped with the Nier-Johnson geometry of double-focusing spectrometers which consists of an Electrostatic Sector Analyzer (ESA) that is placed before and in series with the Magnetic Sector Analyzer (MSA) (e.g., Shimizu, 1997). This method achieves high mass resolution as secondary

ions are dispersed according to their velocity in the ESA and then focused according to their momentum by the MSA (Hinton, 1995, p. 243).

Electrostatic Sector Analyzer

Electrostatic Sector Analyzer (ESA) is often referred to as energy analyzer because it separates ions according to their kinetic energies (de Offman and Stroobant, 2007). The secondary ions generated during the collision cascade have a large kinetic energy spread. Subsequent to extraction of secondary ions from the sample surface, a second 'transfer lens' (or lenses) in the electrostatic energy analyser sector provides direction focusing of the ion beam into the magnetic sector through mechanical slits (Hinton, 1995; de Offman and Stroobant, 2007). The ESA contains the inner and outer spherical metallic electrode surfaces of the energy analyser and they have voltages of opposite polarity. As the secondary ions are accelerated into the electrostatic energy analyser, ions with lower kinetic energy are more strongly deflected than those with high kinetic energy. A movable mechanical energy slit located after the energy analyser can therefore select a small portion of the dispersed secondary ions and allow them to pass into the MSA for mass analyses (SIMS description, University of Edinburgh, n.d.).

Magnetic Sector Analyzer

The MSA carries out the high resolution mass analyses once it receives the ions transmitted by the ESA. As in the Inductively Coupled Plasma Mass Spectrometer (ICP-MS) and Thermal Ionization Mass Spectrometer (TIMS), MSA uses the concept that the motion of ions in a uniform magnetic field is governed by their charge, energy and mass. The energy (E = eV) of a given ion is the sum of that provided by the extraction potential (1-10kV) and any energy imparted by the sputtering process (0 to > 150eV).

The accelerating ion is subjected to a magnetic field force acting at right angles to both the direction of motion of the ion and to the direction of the magnetic field. This ion moves in a circular trajectory with a radius of curvature *r* so that the centrifugal force equilibrates the magnetic force F_{mag}:

$$F_{Mag} = qvB \quad \text{.....1.5}$$

and:

$$qvB = \frac{mv^2}{r} \quad \text{.....1.6}$$

or $$mv = qBr \quad \text{.....1.7}$$

(Hinton, 1995, p. 243; de Offman and Stroobant, 2007).

Therefore for every value of *B,* the ions with the same charge (*q*) and momentum (*mv*) have a characteristic *r* value. This implies that the magnetic analyzer separates ions according to their momentum.

It follows that considering kinetic energy of the ion at the source outlet and re arranging the equations results in:

$$mv^2 = 2qU \quad \text{.....1.8}$$

Such that:

$$m/q = r^2B^2/2U \quad \text{.....1.9}$$

where U (V) is the ion accelerating voltage and B (Wb/m^2) is the strength of the magnetic field, r is the radius of curvature of the magnetic field (m).

If q=1 for all ions, the magnetic analyzer selects the ions according to their mass, provided that they all have the same kinetic energy. This is achieved by electrostatic energy focusing in ESA. It therefore follows that ions with the same kinetic energy but different m/q have trajectories with different r values. These ions emerge from the magnetic field at different positions. Therefore ions with identical charge and mass are dispersed by a magnetic field according to their kinetic energy (de Offman and Stroobant, 2007). Furthermore, in a mass spectrometer with a single collector, r is fixed, therefore the mass of the ion which passes through the exit slit is dependent on B (for a given accelerating voltage) (Hinton, 1995, p. 243).

Detectors

Mass spectrometers are equipped with one or more detectors which are used to detect secondary ions that pass through their exit slit. Typical detectors are: Faraday cup collector, an electron multiplier, an image plate and a resistive anode encoder. The detectors convert the impact of each secondary ion into a charge pulse, which can be recorded individually by the data acquisition system.

Faraday cup collectors are suited for detecting secondary ions that have very high intensities ($>10^6$ counts sec^{-1}) and the current can be measured directly. This type of detector does not discriminate between the types of ions or their energies (SIMS description, University of Edinburgh, n.d.). On the other hand, electron multipliers (EM) are used for ion intensities that are lower than 10^6 counts sec^{-1}. This is used in CAMECA IMS 3f and is best suited for trace elements and rare earth elements, which are often in the ppb level in pure carbonates. In the electron multiplier, the incident secondary ions are converted into electrons upon hitting a string of dynodes with the electron numbers multiplying at each stage to produce a current. The output pulses are amplified and then passed to the counting system (Hinton, 1995, p. 240; de Offman and Stroobant, 2007).

As noted by Hinton (1995, p. 240), it is important to point out that the detection of very low concentrations is ultimately dependent on the detector background. The background count rate for an electron multiplier is normally less than 0.1 counts sec^{-1} and is often less than 0.01 counts sec^{-1}. If the observed count rate on a peak is close to that of the background, i.e. the analytical signal is approaching the detection-limit level, it is

necessary to measure the background at the same time as the peak. This involves the measurement of a dummy mass within the measurement cycle, at a position where no secondary ion peaks are expected.

Conversion of signals to concentration

The basic SIMS equation that relates the measured signals to concentrations of the respective elements of interest in the analyzed geological sample is given as:

Secondary ion current $I(A^q)$ of species A detected (cps):

$$I(A^q) = I_P * Y * \alpha(A^q) * c(A) * T \quad \text{.....1.10}$$

q = charged state (e.g. + or -)

I_p = Primary ion current density (ions/sec)

Y = Total sputtered yield

$\alpha(A^q)$ = Ionization probability to charge state q

c(A) = Fractional concentration of A in the surface layer

T = mass spectrometer transmission function.

As pointed out earlier, the number of secondary ions formed per atom (Eqn. 1.10) sputtered is highly variable between different elements and matrices. Furthermore, the physical models of the secondary ion-forming process are inadequate to predict ion yields. Therefore, conversion of measured secondary ion counts rates to either absolute concentrations or relative isotopic abundances are done by comparison with well characterized standards.(Shimizu and Hart, 1982; Hinton, 1995, p. 237; Chapter 4. SIMS. Dissertation. Freie Universitat, Berlin. n.d.). To minimize the gross matrix effects and variations caused by changes in primary beam current and secondary ion transmission,

secondary ion intensities are usually normalized to a major element in the matrix (e.g. Si for silicates and Ca for carbonates).

1.4.2. Molecular interference

High mass resolution is very critical for handling isobaric molecular interference issues caused by the fact that several ejected secondary ions can have the same nominal masses. Thus, mass resolution setting forms an essential aspect of the mass spectrometer. The mass resolving power of the mass spectrometer is defined by $M/\Delta M$, where ΔM is the difference in mass between two species of mass number M. The difference between the absolute mass of an isotope, given in atomic mass units (1 amu = 1/12 of the mass of Carbon-12) and the nominal mass or mass number M (the total number of protons and neutrons) is known as the 'mass defect' and usually given in milli-mass units, or mmu ($=10^{-3}$). In perspective, a spectrum recorded at mass 56 in garnet will show two major peaks that consist of Fe^+ and CaO^+, which have mass defects of -65.09 mmu (mass 55.93491) and -42.05 mmu (mass 55.95795) respectively (Hinton, 1995, p. 240, their Figure 6.8). The difference in mass ΔM is 23.04 mmu and a mass resolution of 2430 (56/0.02304) is thus required to resolve these peaks, if the two peaks are of equal heights (unlikely in carbonates). Most spectrometers used in SIMS for geological applications are capable of high mass resolution of at least 10,000 and up to 100,000 (Shimizu, 1997) made possible by the double-focusing mass spectrometer geometry.

Energy filtering method

In order to resolve molecular interferences, an alternative option to the mass resolution setting is the *energy filtering* method or by analyzing an alternative isotope of the target element that is less prone to molecular interferences in the respective sample (e.g., ^{54}Fe instead of ^{57}Fe with $^{40}Ca^{16}OH^{+}$ as interference molecule).

Energy filtering method involves voltage offset (usually of about -25 eV to -80 eV) (Macrae et al., 1993; Hinton, 1995, p. 253) technique which uses the energy analyzer to reduce acceleration voltage of secondary ions. In tandem the energy window, a very narrow mechanical slit located after the electrostatic analyzer is adjusted so that only higher energy ions are transmitted into the MSA. Most ions leave the sample surface with an energy of 0-20 eV; however, some have energies of > 100 eV (Hinton, 1990). It follows that there is rapid decrease in count rate with increase in energy, such that molecular ions decrease much more rapidly than elemental ions. The ESA thus deflects lower energy ions by a larger angle, essentially discriminating against molecular interferences relative to the mass analyzer. However this also reduces the intensity of monoatomic species but analytical demand can guide the analyst to optimally achieve a tolerable signal (Evans Analytical Group, Materials Characterization, SIMS description section, n.d.).

Energy filtering method is generally the most favourable option for resolving molecular interferences that affect elements of mass 70 and above as it does not result in intensity loss as much as the mass resolution technique does (Shimizu and Hart, 1982).

1.4.3. Applications

The interpretation of data from 'bulk' analyses of mineral separates or fragments is often influenced, not by growth zoning or heterogeneity within a given mineral, but by the presence of other mineral phases. As an *in situ* technique, SIMS has enabled determinations of trace element abundances in rock-forming minerals and glasses. This has advanced the knowledge of trace element behaviour in geochemical processes and re-established their usefulness as geochemical tracing (Shimizu, 1997, p. 241) proxies for constraining origin of mineral phases.

The earliest results (known to the author of the current work) of SIMS application to the study of carbonates was published in Veizer et al. (1987). The result affirms the importance of the utility of SIMS to analyze for major and trace elements in calcites and dolomites. It used these elements, which are sometimes present at <30 ppm (their Table 3), to constrain the diagenetic processes of carbonates at the micrometer scale. Likewise, Savard et al. (1995) employed SIMS technique to measure major and trace elements in natural calcites. It correlated SIMS measured Mn and Fe contents with optical cathodoluminescence images in order to determine the control of these trace elements in luminescence of natural calcites. The study served to provide cautions on the complexity in correlating trace element compositions with luminescence features of carbonates.

In other geological materials, SIMS was used to demonstrate oscillatory zoning of trace elements in augite (Shimizu, 1990) with very large changes in concentration over small (micrometer scale) distances. Lately (as of 2015), King et al. (2014) used SIMS to constrain the origin of sulfur isotopes in the solid bitumen. The reported SIMS measure

results showed that $\delta^{34}S$ was zoned across <150 μm traverse of the solid bitumen sampled.

The above cited examples of published SIMS application to geological materials are by no means exhaustive as there must be other equally important work in the literature that are not listed.

1.5. Ion Beam cross-section polishing

Essential information about the crystal structure, morphology and abundance of voids among others often revealed under a Scanning Electron Microscope (SEM) have enabled geologists to resolve very important geological questions. However, many of rock features are altered when samples are prepared using the mechanical grinding and polishing technique. In contrast, argon ion beam cross section polishing technique provides an appropriate surface devoid of such artifacts.

1.5.1. Fundamental principles and instrumentation

A fundamental cross section polisher contains a specimen chamber with a vacuum system, an optical microscope for specimen positioning and a stationary ion gun for cutting and etching. The stage in the specimen chamber consists of a specimen holder and a masking plate. The region of interest to be cross sectioned is selected under the optical microscope following which a masking plate is placed across the region. After evacuating the specimen chamber, the region is irradiated with a broad argon ion beam (e.g., Stevie et al., 2005). Accelerating voltage range of the argon ion beam is set to 2 to 6 kV. During ion beam milling, the specimen stage can be rotated 30^{o}. For one, sputtering yield is enhanced by increasing the angle of incidence of the ion (Giannuzi et al., 2005, p. 38). However, more important advantage of this to milling geological samples is that inclining the samples prevents beam striations and ensures uniform etching for samples composed of materials with different hardness (Giannuzi et al., 2005; Erdman et. al., 2006).

Ions impinging into a solid can cause different ion-solid interaction effects because of nuclear and electronic energy losses of the striking ions. Similar to the SIMS description offered in the previous section, typical secondary effects of these interactions, are:

- Generation of secondary electrons, ions, photons, and phonons;
- Implantation of impinging ions;
- Removal of target atoms by sputtering.

Ion bombardment-induced sputtering involves removal of atoms from solid surfaces, combined with a modification of surface topography. The associated displacement of target atoms by ion sputtering allows controlled ion beam preparation of materials, which can be used for surface cleaning, surface etching and target thinning and cutting for layer's cross sections. Ion sputtering, similar in principle to the sputtering process of SIMS, can be defined as the target erosion by ion bombardment. In this process, surface atoms are removed by physical knock-on processes caused by collisions between incident primary ions and secondary recoiled target atoms with near-surface atoms of a target. The basic quantity is the sputtering yield which typically depends on: ion species (mass), ion energy, ion beam direction and target matrix composition (e.g., Giannuzi et al., 2005; Behrisch and Eckstein, 2007; Schmidt and Wetzig, 2013, p. 254).

The particles that are emitted from the ion bombarded target predominantly consist of neutral atoms in the ground state with broad energy and angular distributions.

For multi-component materials, there exists the so-called preferential sputtering in polycrystalline and/or heterogeneous materials. Furthermore, the sputtering yield of

crystalline solids is influenced by *channeling effect* (Giannuzi et al., 2005, p. 43; Schmidt and Wetzig, 2013, p. 254).

1.5.2. Ion Beam Cutting

Ion beam cross-sectional cutting of samples generates representative cross sections through heterogeneous materials. This method can be applied to most targets, especially to materials with very different components as metal-matrix composites, brittle insulators, porous materials and organic samples. Ion beam cutting can be carried out *in situ* under electron microscopic control in an SEM. This has two distinct advantages. The cutting process can be immediately studied and the virgin cross section can be investigated without any air exposure or transport problems. Furthermore, ion beam cutting is an advantageous preparation method to get cross sections for micro-analytical methods as SIMS, AES, XPS, and also analytical TEM. The ion beam cutting technique is possible as an ion beam slope cutting, using a broad ion beam (BIB) or a focused ion beam (FIB) in the scanning mode. However, FIB commonly uses heavy gallium ions (Ga^{+}) which can cause some damage to the sample surface (Erdman et. al., 2006) but argon ion typically used in BIB milling operate at low voltage, which mills away individual atoms of the material without significant disruptions to its neighbours.

1.5.3. Advantages of the technique

The major deformation artifacts imparted on samples by mechanical grinding and polishing technique include:

- In composite materials, softer components are cut faster than harder components, generating uneven surfaces;
- In samples with macro and nanometer scale pores, the morphology of the voids can be significantly altered by stretching or even completely shut;
- Water-soluble minerals are difficult to preserve. For example NaCl daughter minerals in breached fluid inclusion cavities (Erdman et. al., 2006).

The main advantages of the cross section polishing technique are:

- High quality cross sections of composites of soft and hard materials;
- Minimum strain and distortion of the polished surface, enabling observation of grain contrast (channeling contrast) clearly and easily;
- Large cross section areas relative to FIB
- No particle embedding in the polished surface as compared to mechanical polishing
- Ease of operation (Erdman et. al., 2006).

Among other advantages, a broad argon ion beam polishing technique can mill an area that is 10^4 times than possible with focused ion beam (FIB) technique (Hauffe et. al, 2002).

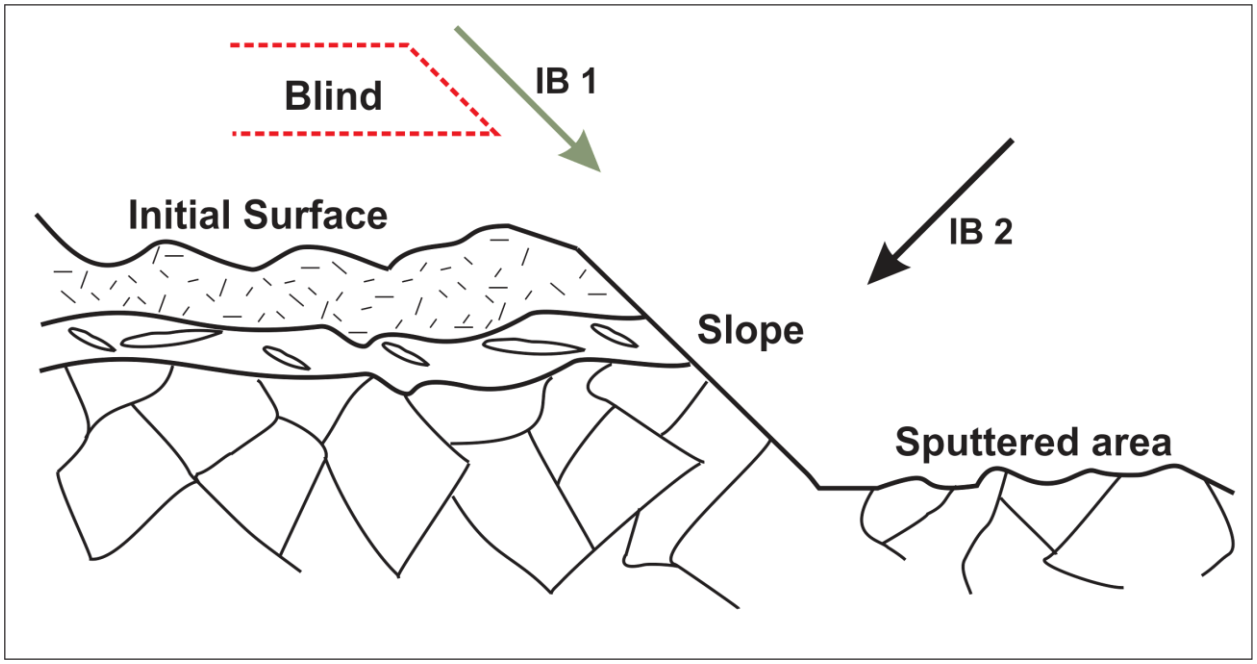

Figure 1.4. Principle of the ion beam slope cutting technique (adapted from Hauffe, 2007, his Figure 1).

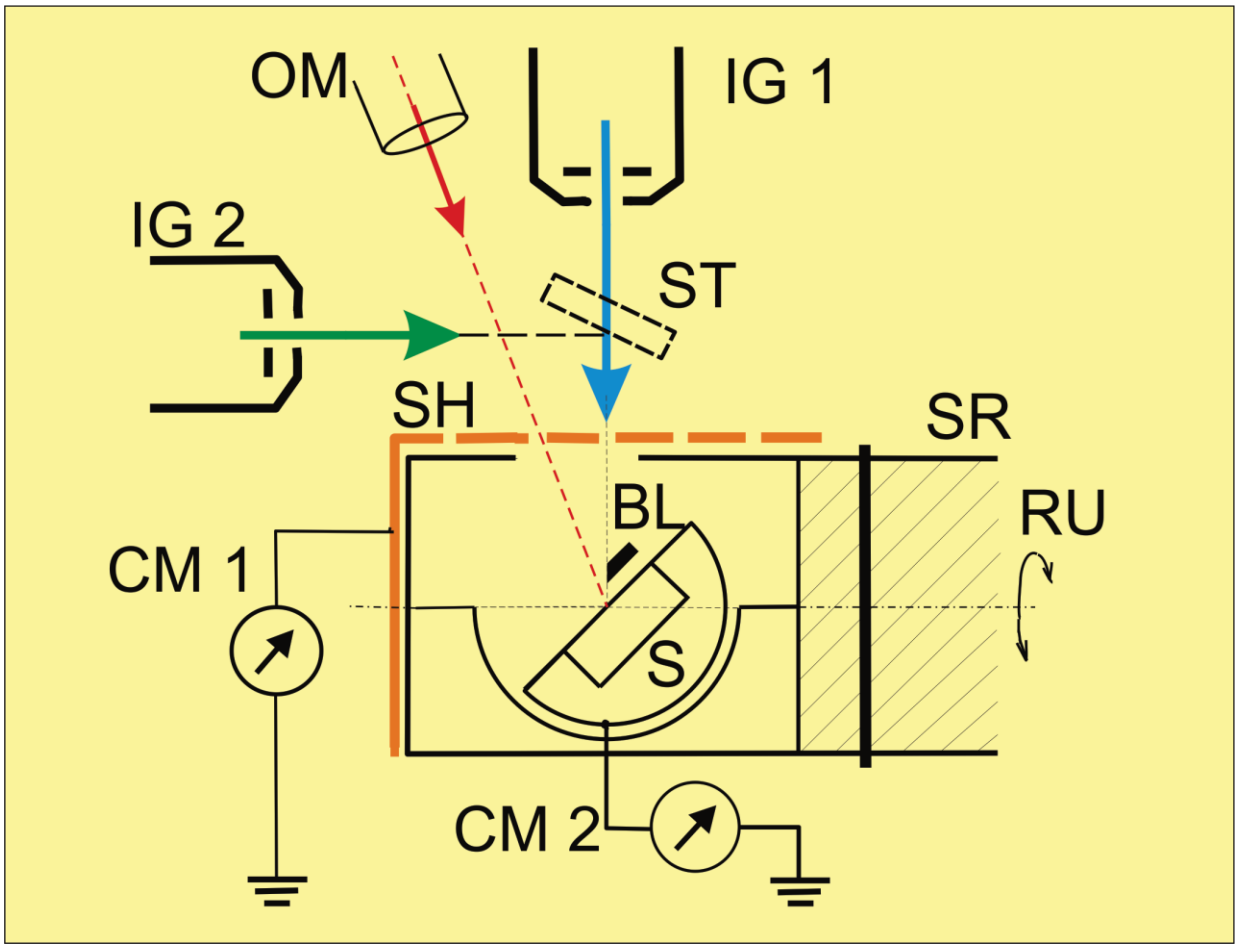

Figure 1.5. Schematic of ion beam equipment and its components:

IG 1 ion gun for smooth removal, etching and cutting; IG 2 ion gun for coating; S sample; BL blind; SR sample rod; RU rocking/rotation unit; ST sputter target; SH shutter; OM optical microscope; CM 1 shutter ion beam current measurement; CM 2 sample ion beam current measurement. (Hauffe, 2007, his Figure 1).

1.6. Thesis Overview

This thesis is written in manuscript style and its constituent chapters are either published, under review in or ready to be submitted to a scholarly journal. Accordingly, the reference style for each chapter is prepared to conform to the guidelines of its respective journal. The origin of Boat Harbour Formation dolomites is explored in Chapters 2 to 4. Intercrystalline porosity in those dolomite is addressed in Chapter 2 while intracrystalline micro- and nanoporosity and its relationship to the process of dolomite formation, supported by paragenesis of intracrystalline mineral micro-inclusions is the focus of Chapter 5.

Geological setting pertinent to each chapter was adequately described in the respective sections to provide quick reference to the background information needed to understand the respective chapter.

Chapter Two

This chapter investigated the origin of lower Ordovician Boat Harbour Formation dolomites at the bed scale and its implication for porosity evolution. The study was carried out on drill cores from Main Brook and Daniel's Harbour localities, about 200 km apart.

Petrography suggests that the formation has been affected by three phases of dolomitization: earliest (near-surface/syn-sedimentary) phase is D1 dolomicrite, mid–burial phase D2 dolomite, and late stage D3 dolomite.

The earliest (near-surface/syn-sedimentary) phase is D1 dolomicrite. The geochemical composition suggests that D1 was developed from fluids of a mixture of meteoric and marine waters at near-surface conditions.

The mid–burial phase D2 dolomite consists of coarse planar sub–euhedral crystals that precipitated from hot fluids that circulated through crustal rocks with progressive burial.

The late stage D3 dolomite has large and coarse non–planar crystals that exhibit sweeping extinction. In addition to its micro-thermometric data these factors suggest that it likely precipitated during deeper burial in pulses and from hot fluids.

The data obtained in the chapter suggests that porosity in the Boat Harbour Formation is mainly associated with the mid–burial D2 dolomite. Intercrystalline porosity is the dominant type and it varies in the formation from <1 to 8 % at Main Brook and from 7 to 12 % at Daniel's Harbour. Vugs are less common but are associated with D3 dolomite. The porous zones are sometimes associated with disconformity.

Chapter Three

The rationale for undertaking the research presented in this chapter is borne out of the popular notion that recrystallization to more stoichiometric dolomite is usually accompanied by characteristic textural and geochemical signatures. These signatures are primarily studied using multiple populations of crystals by comparison of modern and ancient dolomites or from results of high temperature dolomite formation experiments.

However in Chapter 3, the investigation used multi proxy high resolution approaches to carry out imaging and ion microprobe elemental analyses of individual dolomite crystals viz: Scanning Electron Microscopy (SEM), SEM based cathodoluminescence (SEM-CL) Secondary Ion Mass Spectrometer (SIMS). This is to better understand geochemical variations across the crystal traverses and also to constrain their condition/s of crystal growth.

Chapter Four

Chapter four uses the same SIMS measured geochemical data and SEM-CL images used in Chapter three.

The study correlates measured Mn, Fe and REE-Y content of zoned and unzoned dolomite crystal facies with their luminescence characters. Luminescence was obtained using SEM-CL (Cathodoluminescence) and epifluorescence microscope (photoluminescence, PhL).

The study affirms that, at low concentrations (<200 ppm), the correlation of activators (Mn and REE) and quenchers (Fe) with occurrence and intensity of luminescence remains speculative. Broadly speaking, REE-Y content was too low to control luminescence and Fe could not be conclusively demonstrated, using the employed methods, to have caused quenching.

Chapter Five

Chapter five discussed the morphology and genesis of nanopores and micro-inclusions hosted in intracrystalline areas of dolomites and their association/s with dolomite formation. The major rationale for undertaking this research is the economic importance of dolomite porosity as well as the fact that the origin of porosity associated with dolomitization remains, to some extent, a matter of debate. More so, study of porosity in dolomites is commonly focused on micrometer (greater than tens of micrometer) scale intercrystalline pores that are visible in thin sections and at times in hand specimens. Meanwhile, comprehensive evaluation of formation process should incorporate the properties of pores at the nanometer scale too.

The samples were subjected to Broad Ion Beam (BIB) argon milling. Thereafter, Scanning Electron Microscope (SEM) was used to examine, at high resolution, micrometer to nanometer scale pores hosted in the crystals of the dolomites. Notably, the ion milling is a novel approach, which provides flat surfaces that lack topography due to differential hardness and also reduces the probability of creating artifact induced pores that may be caused by plucking during manual sample polishing.

Intracrystalline nanopores are abundant within the burial dolomite crystals. They are shown to have developed as a result of imperfection that are associated with the alignment process of crystallites' agglomeration. This occurred during the formation of the dolomite's major crystal face. Furthermore, the origin of mineral inclusions, 'which are accidentals' in intracrystalline nanopores is related to the mechanism of

dolomitization that involves dissolution of precursor carbonate mineral (calcite or early dolomite) and precipitation of dolomite.

A major implication for this study is that the abundant nanopores can be converted to useful flow channels for increased hydrocarbon production if the reservoir is acidized or fractured.

1.7. Statement of Originality

This dissertation comprises materials that are the result of a research project under the supervision of Prof. Karem Azmy. Chapter 2 of this thesis was published in the American Association of Petroleum Geologists Bulletin. Chapter 3 has benefited from sound critique by reviewers of Chemical Geology and subsequent to taking care of all their concerns, the article has now been re-submitted to Chemical Geology. Chapter 4 is sequel to Chapter 3 and is currently being prepared for submission to Sedimentary Geology. Chapter 5 has been submitted to Marine and Petroleum Geology journal and is currently under review.

Babatunde John Olanipekun is the primary author and researcher for all manuscripts/chapters including formulating specific research questions, experimental design, data collection, synthesis and interpretation of data and manuscript preparation.

Prof. Karem Azmy is a co-author on all manuscripts (Chapters 2 - 5) included in this dissertation. Dr. Azmy provided insight and direction during the conceptual design stage of each project (article/chapter).

He was involved in discussing issues involving both data collection and interpretation. He also played a significant role in reviewing and editing each manuscript.

Prof. Uwe Brand is a co-author in manuscripts presented in Chapters 2 and 3. As a seasoned researcher who is a former editor in Chemical Geology, he reviewed and edited these manuscripts.

REFERENCES

Amthor, J. E. and Friedman, G.M. (1991). In Friedman G. M. (Ed.), *Dolomite-rock textures and secondary porosity development in Ellenburger Group carbonates (lower Ordovician), west Texas and southeastern New Mexico*. International: Blackwell: Oxford-Boston, International.

Amthor, J. E., & Friedman, G. M. (1992). Early- to late-diagenetic dolomitization of platform carbonates; lower Ordovician Ellenburger Group, Permian Basin, west Texas. *Journal of Sedimentary Petrology, 62*(1; 1), 131-144. doi:10.1306/D42678AC-2B26-11D7-8648000102C1865D.

Arvidson, R. S., Guidry, M. W., & Mackenzie, F. T. (2011). Dolomite controls on Phanerozoic seawater chemistry. *Aquatic Geochemistry, 17*(4-5; 4-5), 735-747. doi:10.1007/s10498-011-9130-7.

Arvidson, R. S., Guidry, M., & Mackenzie, F. T. (2008). Chemostatic modes of the Phanerozoic; calcite-dolomite versus aragonite seas and their control by weathering, carbonate precipitation, and basalt-seawater reactions. *Abstracts with Programs - Geological Society of America, 40*(6; 6), 268-268.

Arvidson, R. S., & Mackenzie, F. T. (1997). Tentative kinetic model for dolomite precipitation rate and its application to dolomite distribution. *Aquatic Geochemistry, 2*(3; 3), 273-298.

Arvidson, R. S., & Mackenzie, F. T. (1999). The dolomite problem; control of precipitation kinetics by temperature and saturation state. *American Journal of Science, 299*(4; 4), 257-288.

Azmy, K., Lavoie, D., Knight, I., & Chi, G. (2008). Dolomitization of the lower Ordovician Aguathuna Formation carbonates, Port Au Port Peninsula, western Newfoundland, Canada: implications for a hydrocarbon reservoir. *Canadian Journal of Earth Sciences, 45*, 795-813. doi:doi:10.1139/E08-020.

Azmy, K., & Conliffe, J. (2010). Dolomitization of the lower St. George Group on the Northern Peninsula in western Newfoundland; implications for lateral distribution of porosity. *Bulletin of Canadian Petroleum Geology, 58*(4; 4), 361-374. doi:10.2113/gscpgbull.58.4.361.

Behrisch, R., and Eckstein, W. (2007). Introduction and overview. In R. Behrisch, & W. Eckstein (Eds.), *Sputtering by particle bombardment* (pp. 1-19). New York, USA: Springer-Verlag Berlin Heidelberg.

Broadhead, R. F., Raatz, W. D., Dutton, S. P., & Kim, E. M. (2004). Play analysis and digital portfolio of major oil reservoirs in the Permian Basin; New Mexico. *Annual Meeting Expanded Abstracts - American Association of Petroleum Geologists, 13*, 17-17.

Budd, D. A. (1997). *Cenozoic dolomites of carbonate islands; their attributes and origin*. Elsevier: Amsterdam, Netherlands.

Conliffe, J., Azmy, K., & Greene, M. (2012). Dolomitization of the Lower Ordovician Catoche Formation: implications for hydrocarbon exploration in western Newfoundland. *Marine and Petroleum Geology, 30*(1), 161-173. doi:10.1016/j.marpetgeo.2011.10.007.

Conliffe, J., Azmy, K., Knight, I., & Lavoie, D. (2009). Dolomitization of the lower Ordovician Watts Bight Formation of the St. George Group, western Newfoundland; evidence of hydrothermal fluid alteration. *Canadian Journal of Earth Sciences = Revue Canadienne Des Sciences De La Terre, 46*(4; 4), 247-261. doi:10.1139/E09-019.

Deelman, J. C. (2003). *Low-temperature formation of dolomite and magnesite*. Compact Disc Publications: Eindhoven, Netherlands.

de Hoffmann, E., & Stroobant, V. (2007). *Mass spectrometry: Principles and applications* [Spectrométrie de masse.] (3rd ed.). Chichester, England ; Hoboken, NJ: J. Wiley.

Dockal, J. A. (1988). *Thermodynamic and kinetic description of dolomitization of calcite and calcitization of dolomite (dedolomitization)*. Northeastern Science Foundation, Inc., Rensselaer Center of Applied Geology : Troy, NY, United States.

Erdman, N., Campbell, R., and Asahina, S. (2006). Argon beam cross sectioning. *Advanced Materials and Processes (ASM International), 164*(6).

Francisco, L. (2012). *Secondary ion mass spectrometry (SIMS): Principles and applications* (Handbook of instrumental techniques from CCiTUB. Barcelona. Spain: Unitat SIMS, Centres Cientifics I Tecnologics (CCiTUB), Universitat de Barcelona. Marti i Franques.

Giannuzzi, L. A., Prenitzer, B. I., and Kempshall, B. W. (2005). Ion - solid interactions. In L. A. Giannuzzi, & F. A. Stevie (Eds.), *Introduction to focused ion beams: Instrumentation, theory, techniques and practice* (pp. 13-52). New York, USA: Springer.

Gregg, J M. (2004). Basin fluid, base-metal sulphide mineralization and the development of dolomite petroleum reservoirs. In Braithwaite, C.J.R, Rizzi, G and Darke, G (Ed.), *In: The geometry and petrogenesis of dolomite hydrocarbon reservoirs.* (pp. 157-175). London: Geological Society, London, Special Publications, 235.

Gregg, J.M., Shelton, K.L.,Woody, R.E., & Laudon, P.R. (1993). Porosity evolution of the Cambrian Bonneterre dolomite, southeastern Missouri. *Sedimentology, 40*(6), 1153-1169.

Hauffe, W. (2007). Broad ion beam (BIB) slope cutting through sn-coated copper wires for 3D scanning electron microscopy and microanalysis. *Microscopy and Microanalysis, 13*(Supplement S02), 1526-1527. doi:10.1017/S1431927607073308.

Hauffe, W., Gloess, D., and Mitro, R. J. (2002). 3D microscopy and microanalysis of heterogeneous SEM samples by broad ion beam processing: Cutting - etching - coating. *Microscopy and Microanalysis, 8*(Supplement S02), 552-553.

Hinton, R. (1995). Ion microprobe analysis in geology. In P. Potts, J. W. Bowles, S. B. Reed & M. Cave (Eds.), (pp. 235-289) Springer US. doi:10.1007/978-1-4615-2053-5_6.

King, H. E., Walters, C. C., Horn, W. C., Zimmer, M., Heines, M. M., Lamberti, W. A., et al. (2014). Sulfur isotope analysis of bitumen and pyrite associated with thermal sulfate reduction in reservoir carbonates at the big piney-la barge production complex. *Geochimica Et Cosmochimica Acta, 134*, 210-220. doi:10.1016/j.gca.2013.11.005.

Land, L. S. (1998). Failure to precipitate dolomite at 25 °C from dilute solution despite 1000-fold oversaturation after 32 years. *Aquatic Geochemistry, Earth and Environmental Science, 4*, 361-368.

Lane, T. E. (1990). *Dolomitization, brecciation and zinc mineralization and their paragenetic, stratigraphic and str.....* Unpublished PhD, Memorial University of Newfoundland, Canada.

Lavoie, D., & Chi, G. (2008). Paleozoic hydrothermal dolomites in eastern Canada; multiple new targets for oil and gas exploration. *Abstracts: Annual Meeting - American Association of Petroleum Geologists, 2008.*

Lippmann, F. (1973). *Sedimentary carbonate minerals*. Berlin, New York: Springer-Verlag.

Lucia, F. J. (2004). Origin and petrophysics of dolostone pore space. *In:* Braithwaite, C.J.R., Rizzi, G., Darke, G. (Eds.), *The geometry and petrogenesis of dolomite hydrocarbon reservoirs.* (pp. 141-155) Geological Society, London, Special Publications.

Lucia, F. J., & Major, R. P. (1994). In Major, R. P. (Ed.), *Porosity evolution through hypersaline reflux dolomitization*. International: Blackwell: Oxford, International.

Machel, H.G., (2004). Concepts and models of dolomitization: a critical reappraisal. In: Braithwaite, C.J.R., Rizzi, G., Darke, G. (Eds.), *The Geometry and Petrogenesis of Dolomite Hydrocarbon Reservoirs.* (pp. 7-63) Geological Society of London, special publications, London, UK.

MacRae, N. D., Bottazzi, P., Ottolini, L., & Vannucci, R. (1993). Quantitative REE analysis of silicates by SIMS; conventional energy filtering vs. specimen isolation mode. *Chemical Geology, 103*(1-4; 1-4), 45-54.

Maliva, R. G., Budd, D. A., Clayton, E. A., Missimer, T. M., & Dickson, J. A. D. (2011). Insights into the dolomitization process and porosity modification in sucrosic dolostones, Avon Park Formation (Middle Eocene), east-central Florida, U.S.A. *Journal of Sedimentary Research, 81*(3; 3), 218-232.

Maliva, R. G., & Siever, R. (1988). Diagenetic replacement controlled by force of crystallization. *Geology (Boulder) (August 1988), 16*(8), 688-692.

Merino, E., & Canals, A. (2011). Self-accelerating dolomite-for-calcite replacement; self-organized dynamics of burial dolomitization and associated mineralization. *American Journal of Science, 311*(7), 573-607.

Montanez, I.P. (1994). Late diagenetic dolomitization of lower Ordovician, Upper Knox carbonates: A record of the hydrodynamic evolution of the southern Appalachian basin. *American Association of Petroleum Geologists, 78*(8), 1210-1239.

Nordeng, S. H., and Sibley, D. F. (1994). Dolomite stoichiometry and Ostwald's step rule. *Geochimica Et Cosmochimica Acta, 58*(1; 1), 191-196. doi:10.1016/0016-7037(94)90456-1

Putnis, A. (2009). Mineral replacement reactions. *Reviews in Mineralogy and Geochemistry, 70*, 87-124.

Savard, M. M., Veizer, J., & Hinton, R. (1995). Cathodoluminescene at low fe and mn concentrations; a SIMS study of zones in natural calcites. *Journal of Sedimentary Research, Section A: Sedimentary Petrology and Processes, 65*(1; 1), 208-213.

Schmidt, B., and Wetzig, K. (2013). *Ion beams in materials processing and analysis*. Vienna: Springer Vienna: Imprint: Springer.

Selleck, B. W. (2004). Exposing the roots of hydrothermal dolomite hydrocarbon reservoirs in the Adirondack Lowlands; fluid alteration and fault systems. *Abstracts with Programs - Geological Society of America, 36*(2; 2), 119-119.

Shimizu, N. (1997). Principles of SIMS and modern ion microprobes. In R. Gill (Ed.), *Modern analytical geochemistry, an introduction to quantitative chemical analysis techniques for earth, environmental and material scientists* (pp. 235-242). Essex, U. K: Addison Wesley Longman.

Shimizu, N. (1990). The oscillatory trace element zoning of augite phenocrysts. *Earth-Science Reviews*, *29*(1), 27-37. doi:http://dx.doi.org/10.1016/0012-8252(0)90025-Q.

Shimizu, N., & Hart, S. R. (1982). Applications of the ion microprobe to geochemistry and cosmochemistry. *Annual Review of Earth and Planetary Sciences*, *10*, 483-526.

Stevie, F. A., Giannuzzi, L. A., and Prenitzer, B. I. (2005). The focused ion beam instrument. In L. A. Giannuzzi, and F. A. Stevie (Eds.), *Introduction to focused ion beams: instrumentation, theory, techniques and practice* (pp. 1-12). New York. USA: Springer.

Tucker, M.E. & Wright, V.P. (1990). *Carbonate sedimentology.* Boston: Blackwell Scientific Publications.

van Lith, Y., Warthmann, R., Vasconcelos, C., & McKenzie, J. A. (2003). Sulphate-reducing bacteria induce low-temperature Ca-dolomite and high Mg-calcite formation. *Geobiology, 1*(1; 1), 71-79.

Vasconcelos, C., van Lith, Y., Warthmann, R., & McKenzie, J. A. (1999). Experimental microbial mediated anaerobic carbonate precipitation; implications for Precambrian carbonate sedimentation. *Abstracts with Programs - Geological Society of America, 31*(7; 7), 322-322.

Veizer, J., Hinton, R. W., Clayton, R. N., & Lerman, A. (1987). Chemical diagenesis of carbonates in thin-sections; ion microprobe as a trace element tool. *Chemical Geology, 64*(3-4; 3-4), 225-237.

Warren, J. (2000). Dolomite: Occurrence, evolution and economically important associations. *Earth-Science Reviews, 52*(1–3), 1-81. doi:10.1016/S0012-8252(00)00022-2.

Warthmann, R., van Lith, Y., Vasconcelos, C., McKenzie, J. A., & Karpoff, A. (2000). Bacterially induced dolomite precipitation in anoxic culture experiments. *Geology[Boulder], 28*(12; 12), 1091-1094. doi:10.1130/0091-7613(2000)028<1091:BIDPIA>2.3.CO;2.

Web References:

Chapter 4. SIMS. Dissertation. Freie Universitat, Berlin. No date (n.d.). http://www.diss.fu-berlin.de/diss/servlets/MCRFileNodeServlet/FUDISS_derivate_000000001802/04_Chapter4.pdf?hosts=. Viewed on April 30, 2015.

Evans Analytical Group, Materials Characterization, SIMS description section. No date (n.d.). http://www.eag.com/mc/sims-secondary-ion-yields-primary-beam.html#next;. Viewed on April 01, 2015.

Secondary Ion Mass Spectrometry (SIMS) description, University of Edinburgh. No date (n.d.). http://www.geos.ed.ac.uk/facilities/ionprobe/SIMS4.pdf. Viewed on March 20, 2015.

2 CHAPTER 2.

DOLOMITES OF THE BOAT HARBOUR FORMATION IN THE NORTHERN PENINSULA, WESTERN NEWFOUNDLAND, CANADA: IMPLICATIONS FOR DOLOMITIZATION HISTORY AND POROSITY CONTROL.

BABATUNDE JOHN OLANIPEKUN [a*]***; KAREM AZMY*** [a]***; UWE BRAND*** [b]

[a] Department of Earth Sciences, Memorial University of Newfoundland. St. John's, NL, Canada A1B 3X5.

[b] Department of Earth Sciences, Brock University. St. Catharines, ON, Canada L2S 3A1.

[*] Corresponding author.

Published in: American Association of Petroleum Geologists (AAPG) Bulletin: doi:10.1306/08281312141. (*v. 98 no. 4* ***p. 765-7910).***

ABSTRACT

The Boat Harbour Formation constitutes the upper part of the Lower Ordovician St. George Group on the Northern Peninsula, western Newfoundland. It varies in thickness from 140 m at Main Brook to 96 m at Daniel's Harbour. Dolomitization of the carbonate sequence is more pervasive in the lower 30–40 m of the formation at Main Brook, whereas at Daniel's Harbour the section is entirely dolomitized.

Petrography suggests that the Boat Harbour Formation has been affected by three phases of dolomitization. The earliest (near-surface/syn-sedimentary) phase is D1 dolomicrite (4–55 μm), which exhibits dull to no luminescence. It commonly occurs as laminae 'capping' cycles and as breccias in the younger dolomite phases. It has low Sr (228 ±30 ppm) and average $\delta^{18}O$ value of –6.0 ± 0.8 ‰ (VPDB) in the Main Brook section but more depleted signatures for $\delta^{18}O$ of –8.8 ±1‰ (VPDB) and lower Sr contents (45 ±8 ppm) in the Daniel's Harbour section. The geochemical composition suggests that D1 was developed from fluids of a mixture of meteoric and marine waters.

The mid–burial phase D2 dolomite consists of coarse planar sub–euhedral crystals (30–400 μm) that show concentric cathodoluminescence (CL) zoning, and are also cross-cut by microstylolites. Its $\delta^{18}O$ values vary between –6.6 ±1.3 ‰ (VPDB) at Main Brook and –9.0 ±0.5 ‰ (VPDB) at Daniel's Harbour. This dolomite likely precipitated from fluids that circulated through crustal rocks with progressive burial (T_h value of 114±11°C and salinity value of 23±1.8 Eq. wt. %NaCl).

The late stage D3 dolomite has large and coarse non–planar crystals (125 μm – 7 mm) that exhibit sweeping extinction under crossed polars, which is characteristic of saddle dolomite, and also sometimes shows thin, brightly luminescent rims. It was likely precipitated during deeper burial in pulses and from hot fluids (T_h values of 148±19^{o}C and 115±19.6^{o}C, and mean salinities of 24±2 and 22±2 eq. wt% NaCl at Main Brook and Daniel's Harbour, respectively). This is also supported by their relatively more depleted $\delta^{18}O$ (–11.1±1.2 and –12.3±1.4 ‰ VPDB, respectively), and low Sr contents (88±36 and 38±5.9 ppm, respectively).

Porosity in the Boat Harbour Formation is mainly associated with the mid–burial D2 dolomite. Intercrystalline porosity is the dominant type and it varies in the formation from <1 to 8 % at Main Brook and from 7 to 12 % at Daniel's Harbour. Vugs are less common but are associated with D3 dolomite. The porous zone in the formation at Main Brook starts about 10–15 m below the Lower Boat Harbour Disconformity and extends down to the lower formational boundary, whereas porous zones in the formation at Daniel's Harbour are indiscriminately distributed throughout the section.

2.1. INTRODUCTION

Significant hydrocarbon reservoirs in the Appalachian carbonates are associated with dolomitization (e.g., Selleck, 2004; Lavoie and Chi, 2008). More so, many hydrocarbon plays are hosted in the Permian basin's dolomitized Lower Ordovician Ellenburger Group carbonates (Broadhead et al., 2004), an equivalent of the St George Group carbonates. These underscore the importance of characterizing the dolomites of the St George Group (e.g., Azmy et al., 2008, 2009; Conliffe et al., 2009; Azmy and Conliffe, 2010; Conliffe et al., 2012).

Azmy et al., (2009) studied the dolomitization of the Boat Harbour Formation of the St George Group carbonates using an outcrop located in Isthmus Bay (south of western Newfoundland). However, the hydrology of the dolomitizing fluids could have been modified by the Paleozoic orogenic processes and associated sea-level fluctuations, resulting in varying intensity of dolomitization across western Newfoundland region region (Lane, 1990; Knight et al., 2008). Therefore it is necessary to investigate the dolomitization across the region to better understand the overall diagenetic history and patterns of dolomite distribution within the formation.

Dolomitization processes may occur at near–surface conditions but effectively starts at a temperature range of 80^{o} to 90^{o}C and pore fluid Ca/Mg ratio of about 1.5 to 2.3(cf. Usdowski, 1994). However, the process ultimately depends on original porosity and permeability of the host unit. Reconstruction of the dolomitization history of carbonates requires an understanding of the fluid chemistry, source and flow path, mineralogical and

textural characteristics of the limestone precursor, and rate and duration of the dolomitization process (e.g., Lucia and Major, 1994; Warren, 2000; Machel, 2004).

Several dolomitization events have influenced the petrophysical properties of Paleozoic Appalachian carbonates, which have received attention from researchers (e.g., Montanez, 1994; 1997; Lavoie et al., 2005; Smosna et al., 2005; Lavoie and Chi, 2010; Anderson, 2010). Therefore, origin of dolomite is a cornerstone in understanding its relationship to porosity development in carbonate hydrocarbon reservoirs (e.g., Montanez 1994; Saller, 2004; Azmy et al., 2008, 2009; Conliffe et al.,, 2012), particular because there are many dolomite phases that are not associated with porosity increase (Maliva et al., 2011).

The main objectives of the current study are:

1. To investigate the petrography of the Boat Harbour Formation dolomites from two cores in the Northern Peninsula, western Newfoundland (at Main Brook and Daniel's Harbour, about 130 km apart);
2. To investigate the nature of dolomitization and its control on the associated porosity in the formation, and;
3. To evaluate the dolomitization and patterns of porosity distribution across western Newfoundland in the formation.

2.2. GEOLOGIC SETTING AND STRATIGRAPHIC FRAMEWORK

The Lower Ordovician St. George Group in western Newfoundland (Fig. 2.1) consists entirely of carbonates, which were deposited in a shallow shelf environment on a passive margin that evolved during development of the Lower Paleozoic St. Lawrence platform. It formed as a mega–sequence subsequent to the rifting of the Iapetus Ocean and it signifies the transgression that ended the deposition of siliciclastic materials found at the base of the group (Knight and James, 1987; James et al., 1989; Cooper et al., 2001). These carbonates exhibit the characteristically regular repetition of peritidal carbonates and they were buried up to 2 to 3 km during the Late Ordovician to Late Silurian (Lane, 1990). The carbonate sequence was affected by major tectonic activities during the Paleozoic, particularly the Taconic Orogeny, and by the Siluro–Devonian Acadian Orogeny which led to the inversion of some extensional faults (Cooper et al., 2001; Lane, 1990).

From the base upwards, the St. George Group (Fig. 2.2) consists of the Watts Bight, Boat Harbour, Catoche, and Aguathuna Formations (Knight et al., 2007, 2008). The stratotype section for the Boat Harbour Formation is exposed in Boat Harbour and consists of three members: the Lower member, Middle member and upper Barbace Cove member (Knight and James, 1987; Knight et al., 2008). Falls in relative sea level interrupted deposition resulting in the upper Boat Harbour Disconformity (BHD) and a lower disconformity. The parasequences of the Boat Harbour Formation commonly have laminated dolomitic lime mudstones that are characterized by planar lamination, mud cracks and laminar fenestrae caps (Knight et al., 2007; 2008). The lithostratigraphy of the Boat Harbour

Formation has been studied in detail and refined by several authors (e.g., Lane, 1990; Knight et al., 2008 and references therein) and will be briefly summarized below.

On the Northern Peninsula location (Fig. 2.1), the Boat Harbour Formation comprises a basal section (the Lower member; 39-45 m thick), with sparry hydrothermal dolomites having replaced limestones and dolomicrites (Knight et al., 2008). The limestone facies comprises dark–grey and burrowed carbonates with abundant gastropods and common collapse breccias. The Middle member (85 m thick) is rich in stromatolitic and thrombolitic boundstone mounds that are associated with thin beds of dolomitic limestone and sparry dolomite. The upper part of the section is less burrowed suggesting slightly hypersaline conditions (Knight et al., 2008; Flügel, 2010). The uppermost member, Barbace Cove Member, is a tidal flat parasequence bounded at its base by the Upper Boat Harbour Disconformity and overlain by beds of thrombolitic boundstone and grainstone facies (Knight et al., 2007). The member varies in thickness from 10m to 15 m across the Northern Peninsula (Knight, 2007).

At the Isthmus Bay location (Fig. 2.1), Knight et al. (2008) documented abundant grainstones rich in brachiopods and capped by dololaminites in the Lower member (46 m thick), which are overlain by oblate to domal stromatolite mounds of the Middle member (83 m thick). The top of the Middle member is characterized by emergence features such as truncation surfaces and localized mud cracks. The Barbace Cove member (50 m thick) has a scour base and consists mainly of microbial mounds, (thrombolites and stromatolites) with abundant grainstones and rudstones facies rich in skeletal and intraclastic materials (Knight et al., 2007).

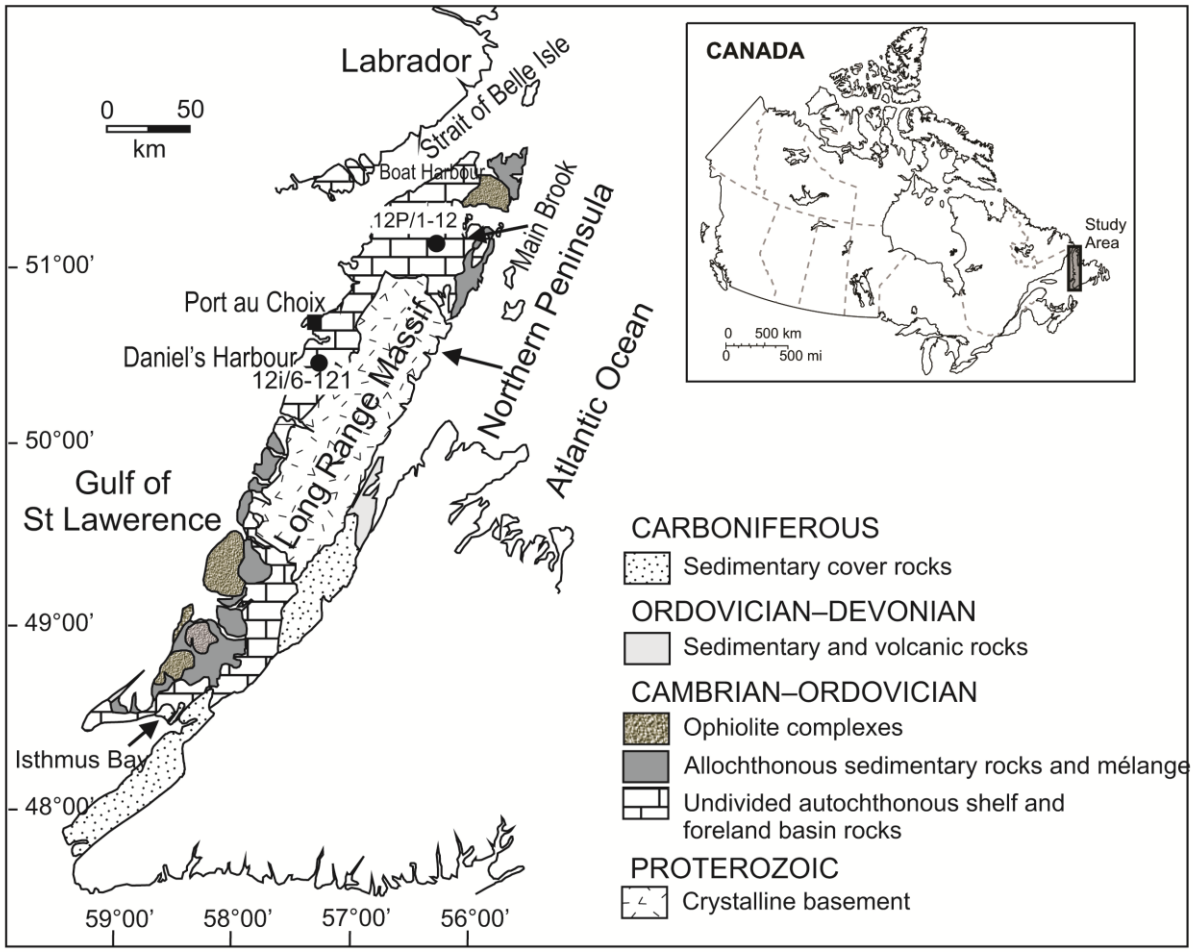

Figure 2.1. Location map of western Newfoundland showing the study area and the investigated drillhole locations (12P/1-12; 51º 08' 23" N; 56º 10' 54‘’W at Main Brook and 12i/6 121; 51º17' 46" N; 57º27' 22" W at Daniel’s Harbour) on the Northern Peninsula (modified from Zhang and Barnes, 2004).

2.3. METHODOLOGY

Two drill cores, each covering the thickness of the Boat Harbour Formation, were investigated from the Northern Peninsula of western Newfoundland. Drillhole 12P/1 12 (51^{o} 08' 23" N; 56^{o} 10' 54‘’W, Fig. 2.1) is located at Main Brook, and Drillhole 12i/6 121 (51^{o}17' 46" N; 57^{o}27' 22" W) is located at Daniel’s Harbour and samples were collected at intervals of approximately 2 m or less. Thin sections and fluid-inclusion wafers were prepared and the remaining mirror–image slabs were polished and cleaned using Ultrasonic cleanser and de–ionized water prior to sampling for geochemical analyses with a microdrill under a binocular microscope.

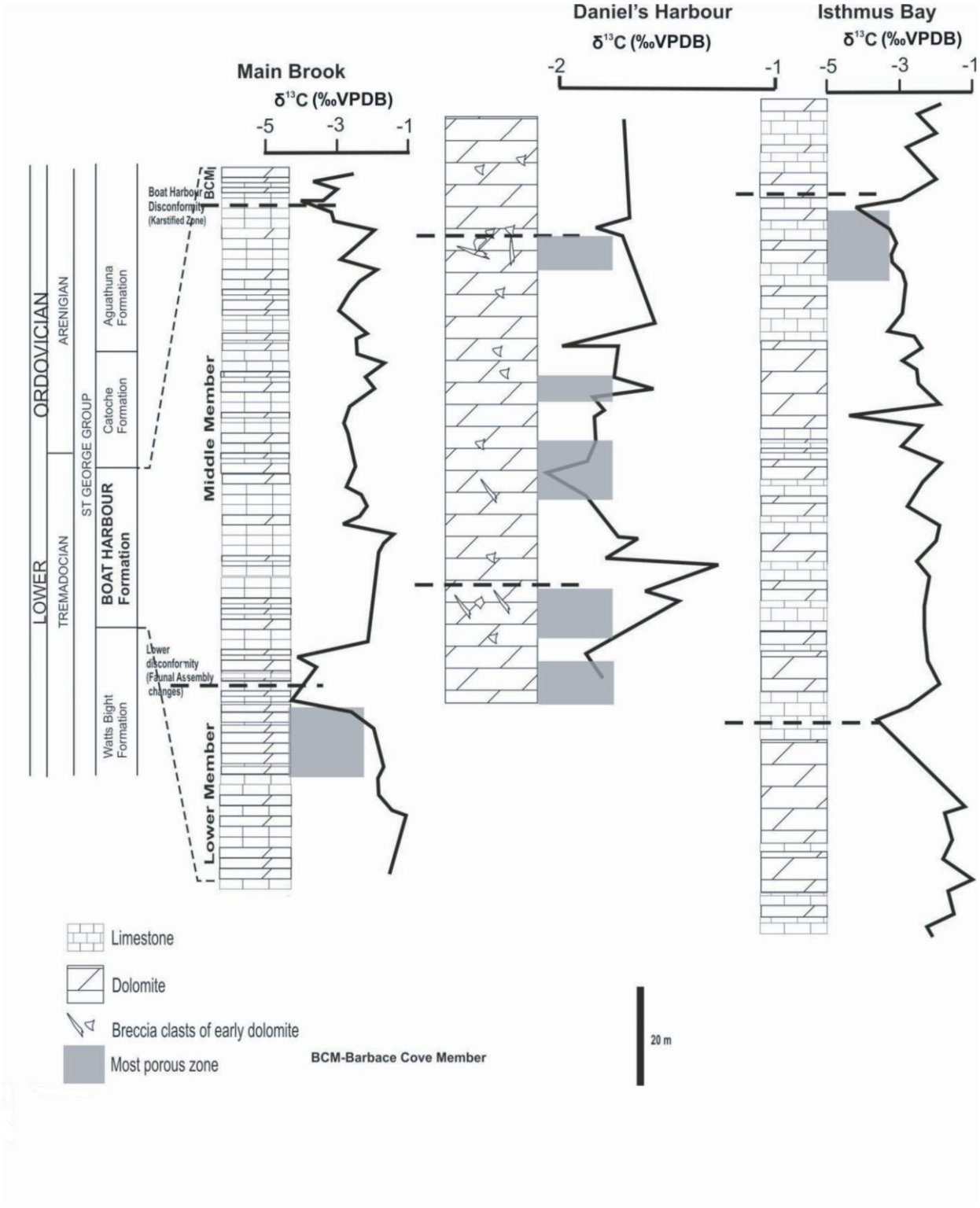
Main Brook
δ13C (‰VPDB)
-5
-3
-1
Daniel's Harbour
δ13C (‰VPDB)
-2
-1
Isthmus Bay
δ13C (‰VPDB)
-5
-3
-1
LOWER ORDOVICIAN
TREMADOCIAN
ARENIGIAN
ST GEORGE GROUP
Aguathuna Formation
Catoche Formation
BOAT HARBOUR Formation
Watts Bight Formation
BCM
Boat Harbour Disconformity (Karstified Zone)
Middle Member
Lower disconformity (Faunal Assembly changes)
Lower Member
Limestone
Dolomite
Breccia clasts of early dolomite
Most porous zone
BCM-Barbace Cove Member
20 m

Figure 2.2. Stratigraphic framework of the St. George Group and Boat Harbour Formation (see Knights et al., 2008 for detail). The figure also illustrates the $\delta^{13}C$ profiles of the equivalent sections in the Northern Peninsula (Cores 12P/1–12 and 12i/6 121) and Isthmus Bay. The grey bars mark the porous horizons. The $\delta^{13}C$ profile for the Isthmus Bay section was reproduced Azmy et al., (2009).

2.3.1. Petrography

Thin sections were stained using a mixture of potassium ferricyanide and Alizarin Red–S solution (Dickson, 1966) in order to distinguish between the different carbonate phases (calcite vs dolomite). The thin sections were examined under transmitted light microscope, cold cathodoluminescence (CL), and UV luminescence (UV). The CL examination was carried out with a Technosyn cold cathodoluminoscope operated with 12kV accelerating voltage and ~ 0.7mA gun current, and UV–luminescence with a CRAIC–QDI 202 UV unit mounted on a Zeiss imager D1m microscope. Due to the small diameter (~2.5 cm) of the studied borehole, no permeability measurements could be performed on the samples.

Microthermometric measurements were performed according to the procedure outlined in Goldstein and Reynolds (1994) using a Linkam THMSG600 heating–freezing stage, which is calibrated with synthetic H_2O and CO_2 fluid inclusion standards (syn flinc, USA) at temperatures between –56.6° and 374.1°C. Precision is ±0.2°C at –56.6°C and ±1°C at 300°C. Homogenization temperatures (T_h), initial melting temperatures (T_i) and final ice melting (Tmi) of the primary fluid inclusion assemblage were measured and estimates of salinities were calculated with the (T_{mi}) data following the protocol of Bodnar (1992).

2.3.2. Geochemistry

The carbonate phases were micro–sampled from the clean polished slabs under a binocular microscope. About 10 mg of powder sample was extracted using a low–speed microdrill. The O– and C– isotope analyses were carried out by the reaction of ~200 μg of powdered sample in an inert atmosphere with 100% orthophosphoric acid at 70^{o}C in a Thermo–Finnigan Gasbench II. The CO_2 produced from the reaction was automatically flushed through a chromatographic column and then delivered to the source of a Thermo–Finnigan DELTA V plus isotope ratio mass spectrometer in a stream of helium, where the gas was ionized and measured for ratios of the isotopes. Uncertainties of better than 0.1‰ (2σ) for the analyses were determined by repeated measurements of NBS–19 ($\delta^{18}O$ = –2.2 ‰ and $\delta^{13}C$ = +2.0‰ vs. VPDB) and L–SVECS ($\delta^{18}O$= –26.6 ‰ and $\delta^{13}C$ = –46.5 ‰ VPDB) as well as internal standards during each run.

For major and trace element analyses (Ca, Mg, Sr, Mn and Fe), a subset of sample powder (each 7 mg) was digested in 2.5 % (volume-volume) pure HNO_3 acid for 70–80 min (Coleman et al., 1989) using a PerkinElmer Sciex's ELAN DRCII inductively coupled mass spectrometer (ICP–MS). The relative uncertainties are better than 5%. Results of major and trace element concentrations are based on an insoluble residue–free basis (100% soluble dolomite or calcite).

2.4. RESULTS

The trends exhibited by petrographical and geochemical data of the Boat Harbour Formation dolomites in Main Brook, Daniel's Harbour and Isthmus Bay (Azmy et al., 2009) sections are illustrated in Figure 2.3. It is a panoramic view that allows a broad comparison of the dolomites' attributes across western Newfoundland, with the data detail given below.

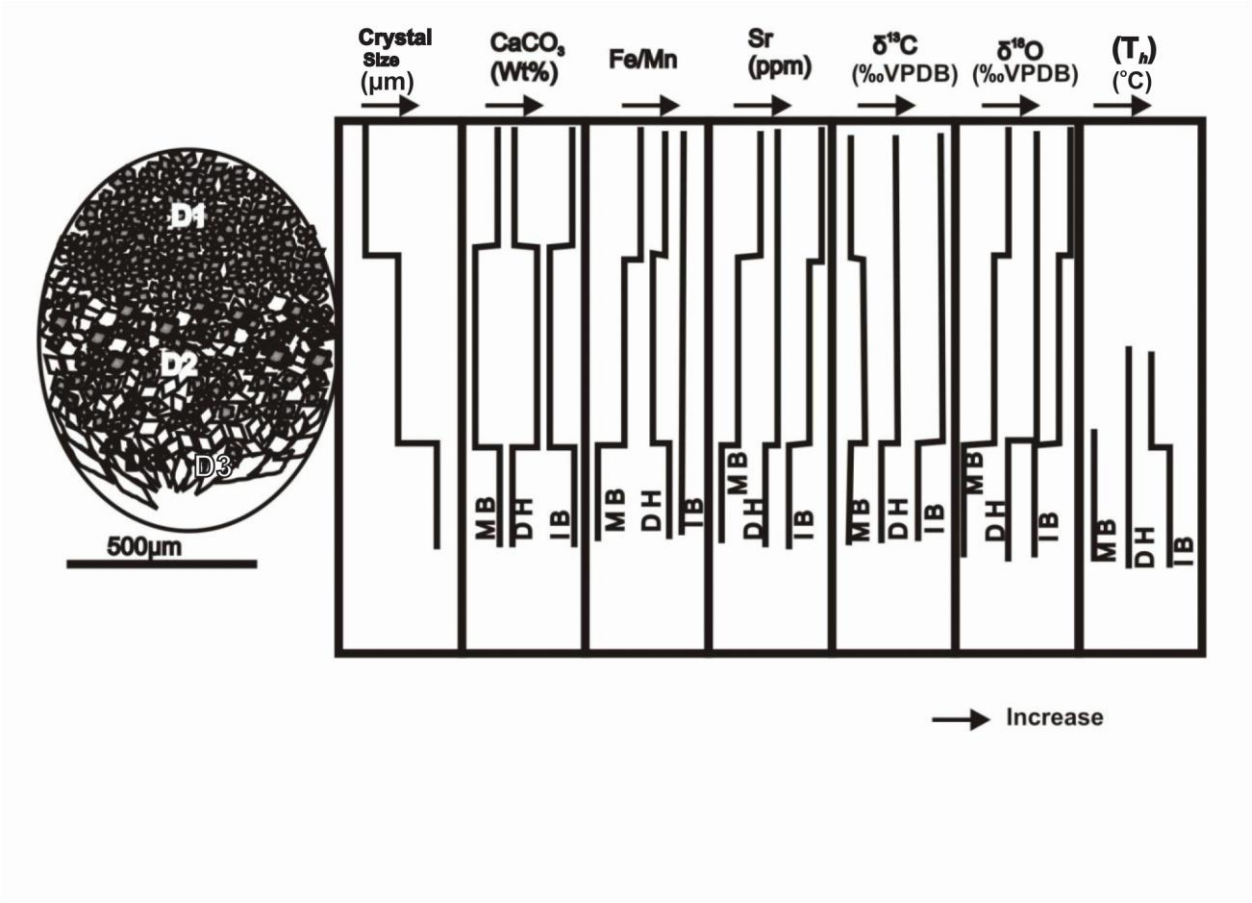

Figure 2.3. Schematic diagram of petrographical and geochemical trends of the investigated dolomites of Main Brook (M.B), Daniel's Harbour (D.H) and Isthmus Bay (I.B) in western Newfoundland.

2.4.1. Petrography

Figure 2.4 summarizes the paragenetic sequence of the Boat Harbour carbonates. At Main Brook, the section is generally less dolomitized (approximately 40% by volume of dolomite) compared with that at Daniel's Harbour where it is completely dolomitized (Tables 2.A1 and A2). Microfacies investigation reveals that the Boat Harbour Formation at Main Brook has low skeletal grain contents relative to its equivalent at Isthmus Bay (Azmy et al., 2009). The limestone facies (C1: Fig 2.5a) at Main Brook are sparsely to moderately bioturbated lime mudstones to wackestones, sometimes intercalated with peloidal laminae packstones and peloidal aggregates with grain sizes of 0.3 to 0.5mm. The lime mudstones may have microbial laminations and few skeletal fragments that are locally present in the form of ghost structures.

Textural and fabric properties of the investigated carbonates suggest three main distinct generations of dolomites. These properties were also used to estimate the volume (percentage) of the respective dolomite phases present in the Boat Harbour Formation (Tables 2.A1 and 2.A2).

D1 Dolomite (approximately 22 % at Main Brook and approximately 20% at Daniel's Harbour)

This dolomite phase is micritic to finely crystalline with crystal sizes varying from 4 to 55 μm (Fig. 2.5c, d, g). The coarse end–member crystals (30–55 μm) of D1 dolomite, which occur mainly in the Daniel's Harbour section (Fig 2.5g), vary from planar–s to planar–e types (Fig. 2.5d; according to the classification of Gregg, 2004). This phase appears

generally dull under CL and with inconspicuous mottling in the D1 of the Daniel's Harbour location.

In the Main Brook section, D1 dolomite is more common within the top and middle part of the formation compared with the lower part (Table 2.A1) where it sometimes mimics the precursor lime mudstone fabric. In the Daniel's Harbour section, D1 dolomite is patchy and occurs as a matrix of brecciated facies, and as laminae capping cycles.

D2 Dolomite (approximately 8% at Main Brook and 70% at Daniel's Harbour)

This phase has coarser crystals than those of D1 dolomite, and the crystals range from 30 to 400 μm (Fig. 2.5e, i, j and k). They have inclusion–rich cores but thin clear rims under plane polarized light. D2 Dolomite crosscuts, or is crosscut by microstylolites and sometimes their crystals are transected by microfaults (Fig. 2.5l). The D2 dolomite is mainly replacive and consists of planar–e and rare planar–s crystals. It exhibits concentric zoning under CL but sometimes the core of the crystals exhibits 'mottled' luminescence (Fig. 2.5l). This generation occurs mainly in the lower part of the Main Brook section, concentrated around the lower disconformity (Fig. 2.2; Table 2.A1).

At Daniel's Harbour, based on textures, the D2 dolomite can be divided into two subtypes: dolomites D2a and D2b (Fig. 2.5i and j). The D2a dolomite is a sub– to anhedral interlocking mosaic of dolomite rhombs without obvious crystal boundaries and it is locally cross–cut by microstylolites (Fig. 2.5i), while dolomite D2b has euhedral to subhedral crystals with planar boundaries and cross–cuts microstylolites (Fig. 2.5g). Both dolomites, at this location, are associated with intercrystalline porosity, but D2b dolomite

is relatively more porous (7–12 % in D2b vs 2-5% in D2a), and most of those pores are now occluded by bitumen (Fig. 2.5j and k).

In general, intercrystalline porosity is the dominant pore type in the Boat Harbour Formation dolomites (up to 8 % at Main Brook and up to 12% at Daniel's Harbour).

D3 Dolomite (app. 8 % at Main Brook and 10% at Daniel's Harbour)

It represents the latest phase of dolomitization and it is more dominant throughout the lower part of the Main Brook core section (Table 2.A1). It mainly fills fractures and cements breccias within the Daniel's Harbour section, rarely replacing the matrix. The dolomite crystals are non–planar, coarse anhedral to subhedral ranging from 125 μm to 7 mm (Fig. 2.5f) and have a milky white appearance in polished slabs (e.g., Radke and Mathis, 1980; Lonee and Machel, 2006; Azmy et al., 2009). They have curved crystal boundaries and exhibit sweeping extinction under crossed polars and dull to no luminescence under CL, with some crystals exhibiting luminescent rims. A volumetrically insignificant phase of coarse crystalline (200 μm to 4 mm) calcite spar (C3) with blocky texture postdates the D3 dolomite. The calcite C3 (Fig. 2.5f) occurs as replacive or vug/fracture–filling, exhibiting distinct twinning and dull CL.

In addition to field evidences for the upper Boat Harbour Disconformity (BHD) and the lower disconformity (Section 2), petrographic examination of the horizons shows a suite of emergence features at the Main Brook, Daniel's Harbour and Isthmus Bay. These features include μm- to mm-sized nodular fabrics and reworked clasts of peloidal

aggregates in micritic matrix (Fig. 2.5b) and fine grain matrix at the Main Brook and Isthmus Bay section.

Many of the nodules and clasts in these horizons are poorly sorted and contain circumgranular and wrinkled micro-cracks that are spar in-filled. These nodules are also sometimes corroded by dark brown insoluble substances (pressure solution?). D2 dolomite is pervasive within 15m below the disconformities. In the Daniel's Harbour section, the disconformity zones contain brecciated clasts of laminated D1 dolomite, which are cemented by D3 dolomite and non-carbonate substances. Supportively, these carbonate horizons exhibit depleted $\delta^{13}C$ values in both Main Brook and Isthmus Bay sections, while they have been significantly obscured by multiple episodes of dolomitization in the Daniel's Harbour section (Fig. 2.2). Some sphalerite in the sections replaces D3 dolomite.

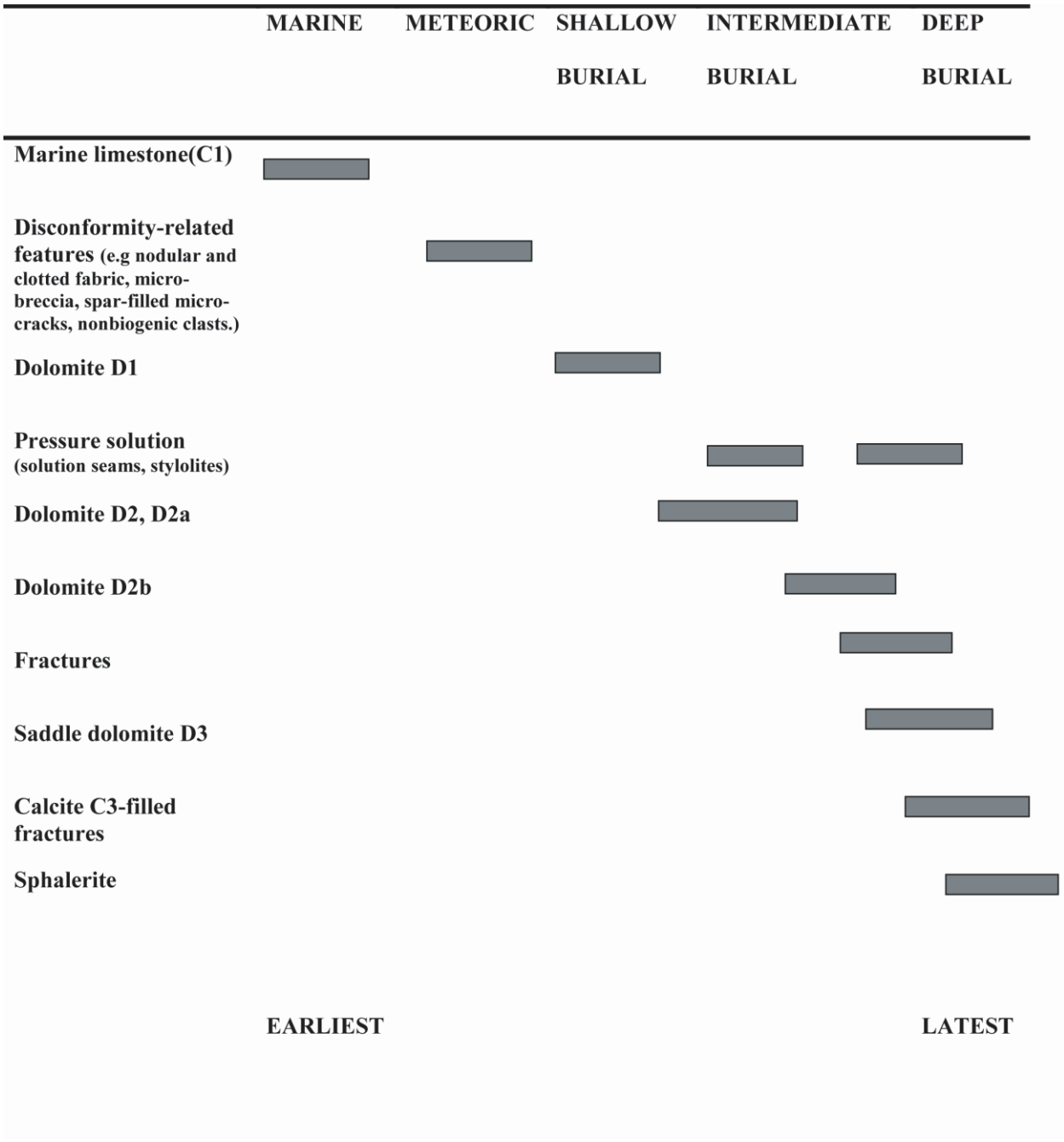

Figure 2.4. Paragenetic sequence derived for the Boat Harbour Formation at Northern Peninsula, inferred from cross-cut relationships.

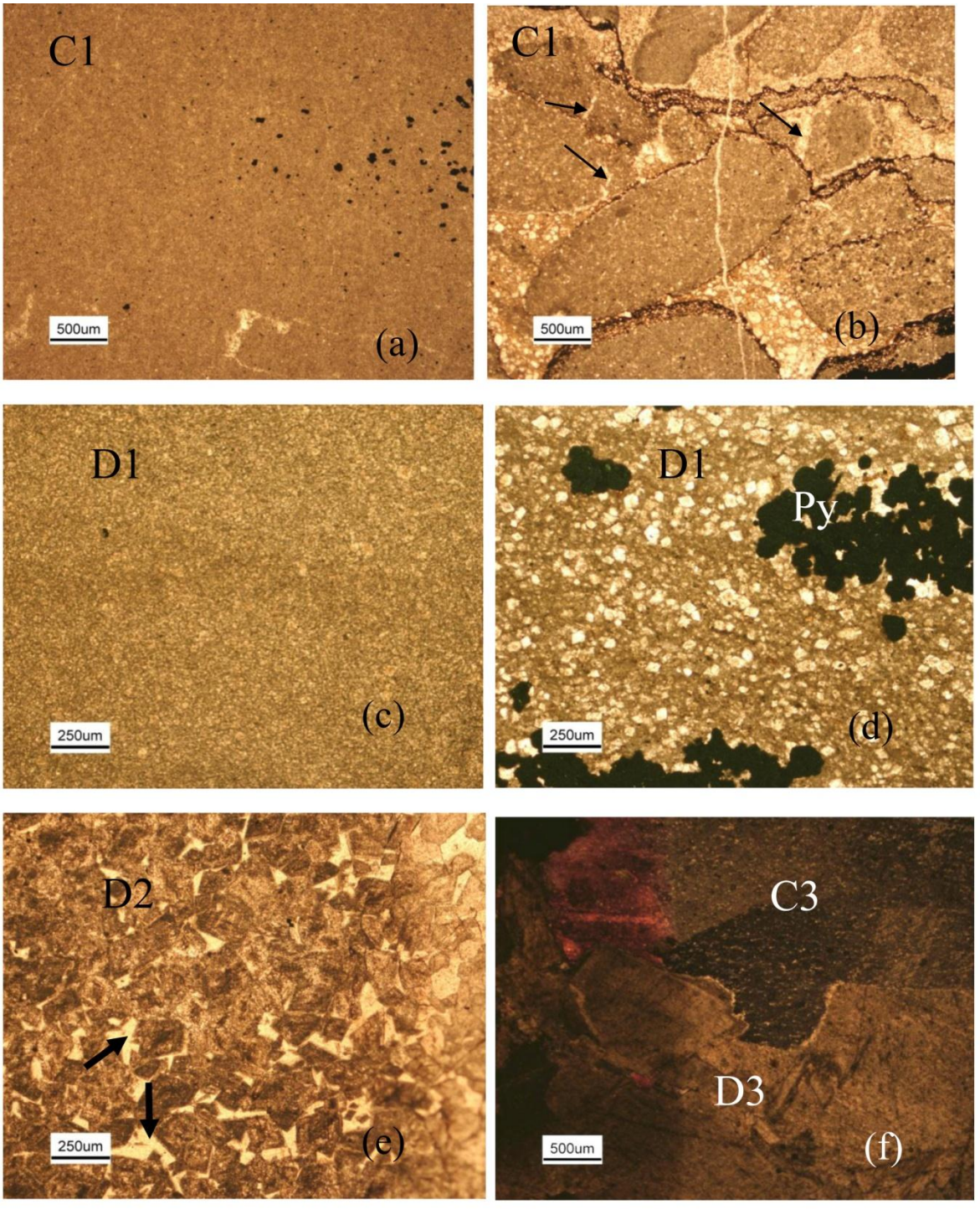
C1
500um
(a)
C1
500um
(b)
D1
250um
(c)
D1
Py
250um
(d)
D2
250um
(e)
C3
D3
500um
(f)

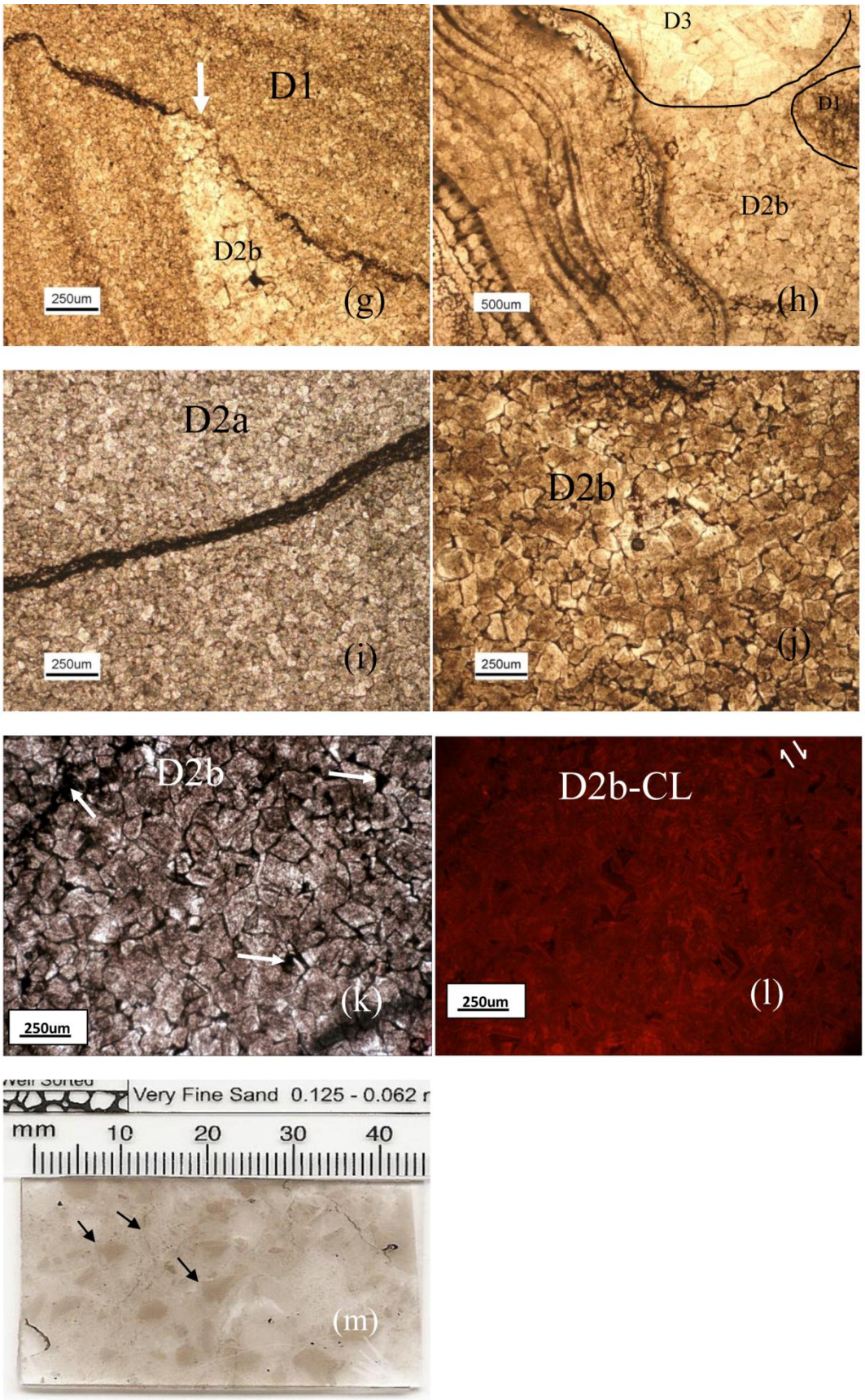
D1
D2b
250um
(g)
D3
D1
D2b
500um
(h)
D2a
250um
(i)
D2b
250um
(j)
D2b
250um
(k)
D2b-CL
250um
(l)
Very Fine Sand 0.125 - 0.062 r
mm
10
20
30
40
(m)

Figures 2.5a-m. Photomicrographs of selected diagenetic features of Boat Harbour Formation, in Main Brook (2.5a-f) and Daniel's Harbour (2.5g-m) under plane-polarized light (PL), crossed-polarized light, (XPL) and cathodoluminescence (CL) showing:

a. PL image of marine lime-mudstone with disseminated pyrite crystals (C1: Sample P-50; 50m depth);
b. PL image of poorly sorted micrite nodules with spar-filled micro-cracks (black arrows) in lower Boat Harbour disconformity zone. Some of the cracks are truncated by the corroding brown substance (pressure solution?) indicating that the cracks may be emergence rather than deep burial features (Sample P-148; 148m depth);
c. PL image of early dolomite (D1) in a partially dolomitized lime-mudstone (Sample P-56; 56m depth; darker section is the precursor lime-mudstone);
d. PL image of dolomitized lime-mud matrix with pyrite (Py) filled burrow (sample id: P-62; 62m depth);
e. PL image of D2 showing intercrystalline porosity (black arrows) in D2 (sample id: P-154; 154m depth);
f. XPL image of saddle Dolomite D3 and latest coarse crystalline calcite (C3) staining pink and exhibiting unit extinction (Sample Id:P183.3; 184m depth);
g. PL image with D2 replacing D1. White arrow points at D2b which cross cuts solution seams (Sample Id:6-136; 129m depth);

h. PL image of D2b and D3 whereby the morphology of the precursor skeletal grain is preserved; (Sample Id: 6-216; 210m depth). Note the remnant of D1 on the North East section of the image;
i. PL image of a typical D2a being cross-cut by pressure solution indicating formation prior to deep burial.The vertical line on the left hand side is a thin-section artifact (Sample Id: 6-176; 170m depth;
j. PL image of a typical D2b.Note the cloudy core and clear rim in many of the crystals (Sample Id:6-172; 166m depth);
k. The PL image of intercrystalline porosity (white arrows) associated with D2b and occluded by bitumen (Sample Id:6-172; 166m depth);
l. CL view of (k) with distinct concentric and mottled (crystal core) zoning in D2, crystal fracturing and displacement (arrows);
m. Polished slab of showing D1 (arrows) dolomite breccias in D2a matrix (Sample Id: 6-138; 131m depth).

2.4.1.1. Fluid Inclusion Analyses

Microthermometric measurements of the primary two–phase (liquid and vapour) inclusions in the coarse crystals of dolomite D2, D3, calcite C3 and sphalerite (Goldstein and Reynolds, 1994) are summarized in Table 2.1 and Figures 2.6 and 2.7. These were obtained from 5 wafers studied from the Daniel's Harbour section and 3 wafers studied from the Main Brook section. Homogenization temperatures (T_h, minimum estimate of entrapment temperature) and melting points (T_{mi}; used to calculate salinity estimates) were measured in inclusions hosted in crystals covering the entire crystal size spectrum.

In the Main Brook section, no measurements were obtained from inclusions in dolomites D1 and D2 crystals because they were too small to yield reliable results. The D3 dolomite inclusions have T_h values ranging from 118° to 179°C, and salinity ranging from 20 to 26 % equivalent weight NaCl. The C3 calcite inclusions yielded higher T_h values ranging from 139° to 204°C (Table 2.1), but lower salinity values ranging between 9 and 13 % eq.wt NaCl. Primary fluid inclusions in sphalerite crystals provided T_h values ranging from 114 to 126°C and salinity with a narrow range of 24 to 25% eq.wt NaCl. The ranges of T_h and salinity estimates of the sphalerite are comparable with those of the D3 dolomite (Table 2.1).

In the Daniel's Harbour section, microthermometric data obtained from D2b has T_h values that range from 91°C to 140°C (114±11°C; Fig. 2.6) with a bimodal distribution and salinity estimates between 18 and 27 wt% NaCl (23±1.8 wt% NaCl, Table 2.1). The T_h values of D3 also exhibit bimodal distribution with two populations of 77 to 109°C

(93±11°C) and 110 to 140°C (128±10°C) but salinity estimates has one population, with a range from 18 to 24 wt% NaCl (21.5±2 wt% NaCl; Fig. 2.6, 2.7 and Table 2.1).

	Main Brook			Daniel's Harbour			
Phase		**T_h°C**	**Eq. wt(%) NaCl**	**Phase**		**T_h°C**	**Eq. wt(%) NaCl**
	n	38	24		***n***	50	16
	Average	148	23		**Average**	115	22
D3	**STDev**	18.9	1.9	**D3**	**Stdev**	19.6	2.0
	Max	179	26		**Max**	139	24
	Min	118	20		**Min**	77	19
					n	47	20
	n	8	7		**Average**	114	23
	Average	176	10	**D2b**	**Stdev**	11.0	1.8
C3	**STDev**	30.0	2.0		**Max**	140	27
	Max	204	13		**Min**	91	18
	Min	139	9				
	n	8	4				
	Average	120	25				
Sphalerite	**STDev**	4.3	0.6				

Max	126	25	
Min	114	24	

Table 2.1. Summary of microthermometric data from fluid inclusions in D2b, D3, C3 and Sphalerite in the Boat Harbour Formation from Main Brook and Daniel's Harbour locations on Northern Peninsula.

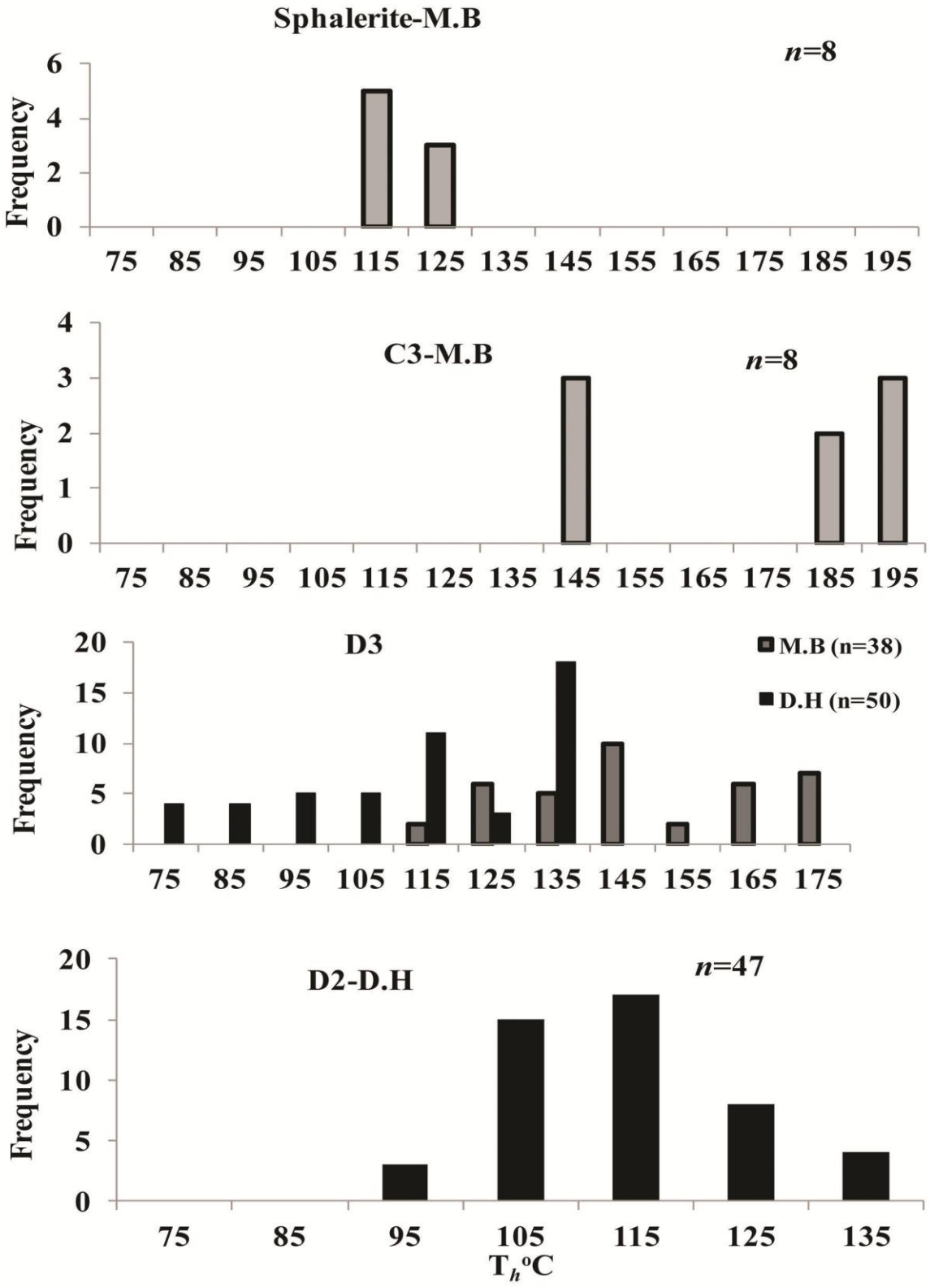
Sphalerite-M.B
n=8
Frequency
6
4
2
0
75 85 95 105 115 125 135 145 155 165 175 185 195
C3-M.B
n=8
Frequency
4
3
2
1
0
75 85 95 105 115 125 135 145 155 165 175 185 195
D3
M.B (n=38)
D.H (n=50)
Frequency
20
15
10
5
0
75 85 95 105 115 125 135 145 155 165 175
D2-D.H
n=47
Frequency
20
15
10
5
0
75 85 95 105 115 125 135
T_h°C

Figure 2.6. Histogram of homogenization temperatures (T_h ^oC) of fluid inclusions in: sphalerite (Sph); latest calcite (C3), latest dolomite (D3) and D2 in Boat Harbour Formation on the Northern Peninsula. M.B-Main Brook; D.H-Daniel's Harbour.

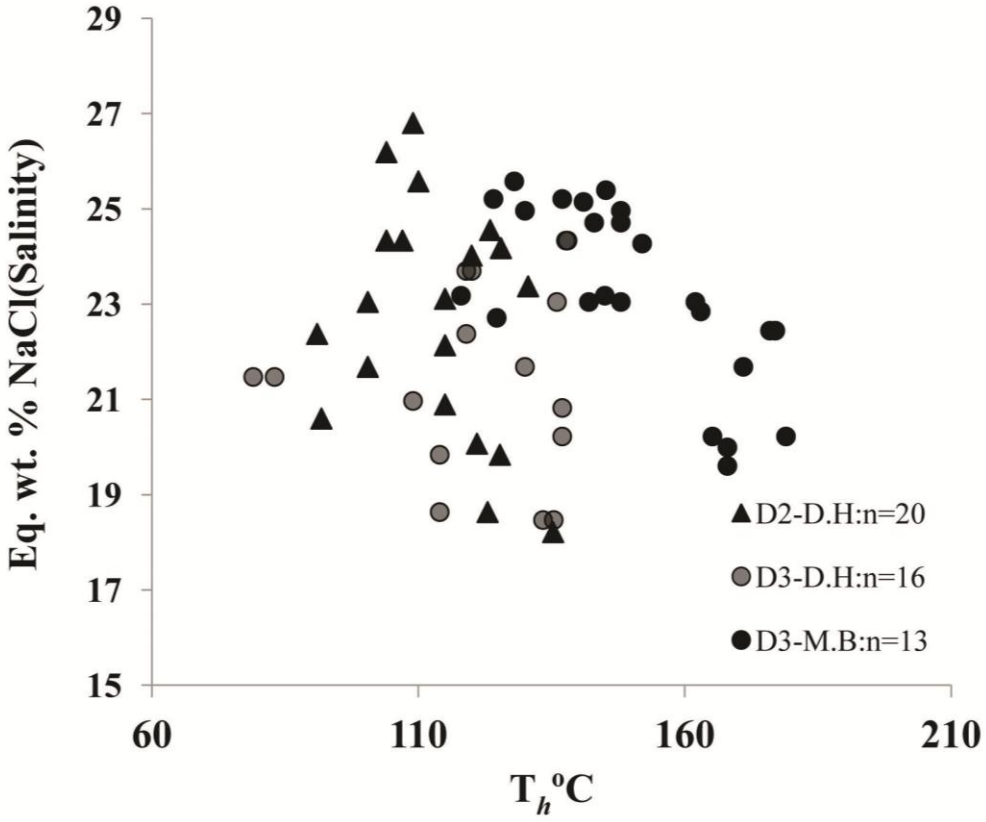

Figure 2.7. Plot of Salinity (eq.wt % NaCl) versus homogenization temperatures (T ^{o}C) of dolomite D2 and D3 in both Main Brook (M.B) and Daniel's Harbour (D.H). Detail in text.

2.4.2. Major and Trace Elements

Calcite (C1, ~ 98±2 wt% $CaCO_3$, and C3 ~95±6wt% $CaCO_3$) was observed in the Main Brook section only (Table 2.2), whereas dolomite occurs in both sections.

The dolomites of Main Brook section increase in stoichiometry (i.e. reducing mean $CaCO_3$ composition) from the fine-grained D1 dolomite (65 ±2 wt%) to the coarser D2 dolomite (61±6 wt%), and to the D3 dolomite (64±6 wt%). In the Daniel's Harbour section, dolomites D1 (55±1 wt%), D2a (56±1wt%) and D2b (56±1 wt%) are similar in $CaCO_3$ compositions, but D3 dolomite has a lower (53±1wt%). In general, dolomites at Main Brook have higher $CaCO_3$ compositions than those at Daniel's Harbour (Table 2.2).

Trace element concentrations (e.g., Fe, Mn and Sr) of diagenetic carbonates depend on bulk composition of the diagenetic fluid, precursor carbonates and distribution coefficient values of the respective elements (e.g., Brand and Veizer, 1980; Land 1980; Veizer, 1983). At Main Brook, mean Mn concentrations decrease from 104±32 ppm in D1 dolomite to 86±28 ppm in D2 dolomite; whereas it is highest (158±64 ppm) in D3 dolomite (Table 2.2). The concentrations of Fe show a decreasing pattern from D1 dolomite with 5323±2397ppm, to D2 dolomite with 3234±1135ppm, to D3 dolomite with 1437±476ppm (Table 2.2). Furthermore, data from the Main Brook section also indicate that the mean Sr concentrations of the carbonates show a progressive depletion from 228±30 ppm in dolomite D1 to 88±36 ppm in D3 (Table 2.2).

The Daniel's Harbour carbonates have a mean Mn concentration of 131±47ppm in D1 dolomite, 133±39 ppm and 180±32 ppm in dolomites D2a and D2b respectively, but

relatively higher contents in dolomite D3 with 274±133 ppm. The mean Mn concentrations of dolomites D2 and D3 at Main Brook appear to be lower than those of their Daniel's Harbour counterparts. As for mean Fe compositions, dolomite D1 contains 2234±769 ppm, D2 contains 1878±664 ppm, and 1696±604 in D2a and D2b respectively, and D3 shows more enrichment (3338±1690 ppm). Although mean Fe concentration values are more enriched in dolomites D1 and D2 but depleted in D3 at Main Brook, caution is advised, because micro-rhombs of bacterial pyrite and later hydrothermal pyrites may overprint the Fe concentrations in the individual dolomite phases. Strontium concentrations are generally more depleted in the Daniel's Harbour dolomites of the formation (D1, 45±8 ppm; D2a, 59±19 ppm; D2b, 45±8 ppm; D3, 38±6 ppm) compared with those from Main Brook (D1, 228±30 ppm; D2, 169±90 ppm; D3, 88±36 ppm).

2.4.3. Carbon and Oxygen Isotopes

The C– and O–isotope compositions of the investigated carbonates are summarized in Table 2.2 and their trends are shown in Figure 2.8a and 2.8b. The $\delta^{13}C$ of all dolomites in both sections show no significant variations. In contrast, $\delta^{18}O$ values of the dolomites at Daniel's Harbour (D1, –8.8±1 ‰ VPDB; D2a, –8.7±0.7 ‰VPDB; D2b, –9.0±0.5 ‰VPDB; D3, –12.3±1.4 ‰VPDB) are more depleted compared with their Main Brook (D1, –6.0±0.8 ‰ VPDB; D2, –6.6±1.3 ‰ VPDB; D3, –11.0±1.2 ‰ VPDB) counterparts. Within each individual section, the mean $\delta^{18}O$ values of dolomites D1 and D2 only show subtle changes (Table 2.2) whereas those of dolomite D3 are the most negative. The progressive depletion of $\delta^{18}O$ in the dolomites follows a similar trend documented for their Isthmus Bay counterparts (Table 2.2; Azmy et al., 2009).

		$CaCO_3$ (%)	$MgCO_3$ (%)	Mn (ppm)	Fe (ppm)	Sr (ppm)	$\delta^{13}C$ ‰(VPDB)	$\delta^{18}O$ ‰(VPDB)
Boat Harbour Formation (Main Brook)								
C1	***n***	12	12	12	12	12	42	42
	Average	**98**	**2**	**47**	**2091**	**374**	**-2.5**	**-8.0**
	Stdev	2	2	22	1392	100	0.7	0.7
	Max	99	7	82	5238	598	-1.0	-5.7
	Min	93	1	21	1266	262	-4	-10
C3	***n***	7	7	7	7	7	5	5
	Average	**95**	**5**	**138**	**2381**	**566**	**-3**	**-9**
	Stdev	6	6	98	2607	592	1.3	1.7
	Max	99	14	250	8271	1661	-1	-7
	Min	86	1	51	1222	118	-5	-11
D1	***n***	7	7	7	7	7	22	22
	Average	**65**	**35**	**104**	**5323**	**228**	**-2.4**	**-6.0**
	Stdev	2	2	32	2397	30	0.8	0.8
	Max	66	38	145	9553	261	-1.1	-5.3
	Min	62	34	61	1874	187	-4.1	-8.6

D2	***n***	7	7	7	7	7	5	5
	Average	**61**	**39**	**86**	**3234**	**169**	**-1.9**	**-6.6**
	Stdev	6	2	28	1135	90	0.3	1.3
	Max	76	44	143	4877	335	-1.5	-5.6
	Min	56	37	57	1714	54	-2.1	-8.7
D3	***n***	5	5	5	5	5	5	5
	Average	**64**	**36**	**158**	**1437**	**88**	**-2**	**-11.1**
	Stdev	6	6	64	476	36	1	1.2
	Max	70	42	264	2161	151	-1.3	-9.5
	Min	58	30	117	838	61	-3.1	-12.7

		$CaCO_3$ (%)	**$MgCO_3$ (%)**	**Mn (ppm)**	**Fe (ppm)**	**Sr (ppm)**	**$\delta^{13}C$ ‰(VPDB)**	**$\delta^{18}O$ ‰(VPDB)**
Boat Harbour Formation (Daniel's Harbour)								
	n	14	14	14	14	14	10	10
D1	**Average**	**55**	**45**	**131**	**2234**	**45**	**-1.7**	**-8.8**
	StDev	1.4	1.4	47	769	8	0.2	1.0
	Max	57	47	212	3561	56	-1.4	-7.2
	Min	53	43	72	1141	31	-2.1	-10.3

D2a	***n***	13	13	13	13	13	20	20
	Average	**56**	**44**	**133**	**1878**	**59**	**-1.7**	**-8.7**
	StDev	1.4	1.4	39	664	19	0.2	0.7
	Max	59	46	200	3260	96	-1.2	-7.5
	Min	54	41	94	1057	40	-2.0	-10.1
D2b	***n***	7	7	7	7	7	5	5
	Average	**56**	**44**	**180**	**1696**	**45**	**-1.8**	**-9.0**
	StDev	0.5	0.5	32	604	8	0.1	0.5
	Max	57	44	213	2519	55	-1.7	-8.5
	Min	56	43	130	735	34	-1.9	-9.8
D3	***n***	13	13	13	13	13	17	17
	Average	**53**	**47**	**274.4**	**3338**	**38**	**-1.8**	**-12.3**
	StDev	1.34	1.34	134	1690	5.9	0.3	1.4
	Max	56	48	651	8634	48	-1.4	-8.6
	Min	52	44	194	1982	28	-2.3	-14.2

Table 2.2. Summary of geochemical composition ($CaCO_3$, $MgCO_3$, Mn, Fe, Sr, $\delta^{13}C$ and $\delta^{18}O$) of Boat Harbour Formation carbonates from the Main Brook and Daniel's Harbour locations on the Northern Peninsula.

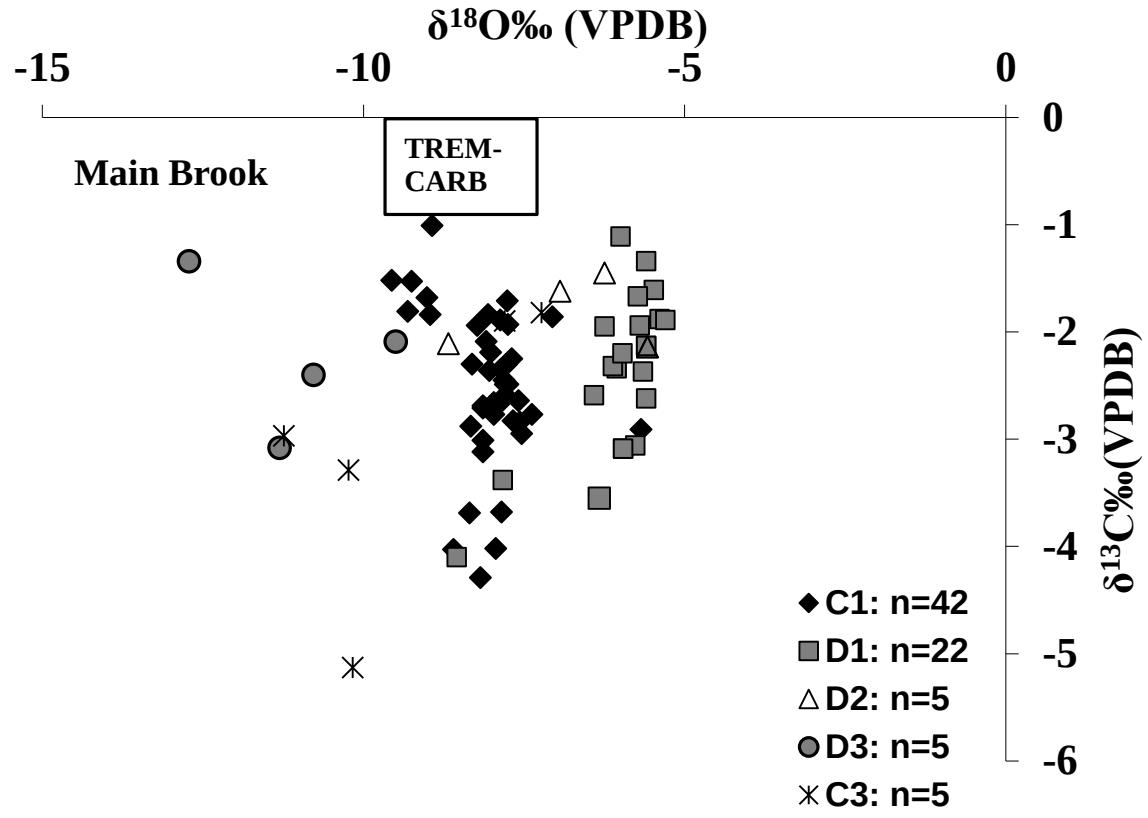

Figure 2.8A. A scatter diagram of $\delta^{18}O$ versus $\delta^{13}C$ in Boat Harbour Formation carbonates in (a) Main Brook on the Northern Peninsula. The box marks the range of well preserved low magnesium calcite from Tremadocian (Lower Ordovician; TREM-CARB inside box) sea water (cf. Prokoph et al., 2008).

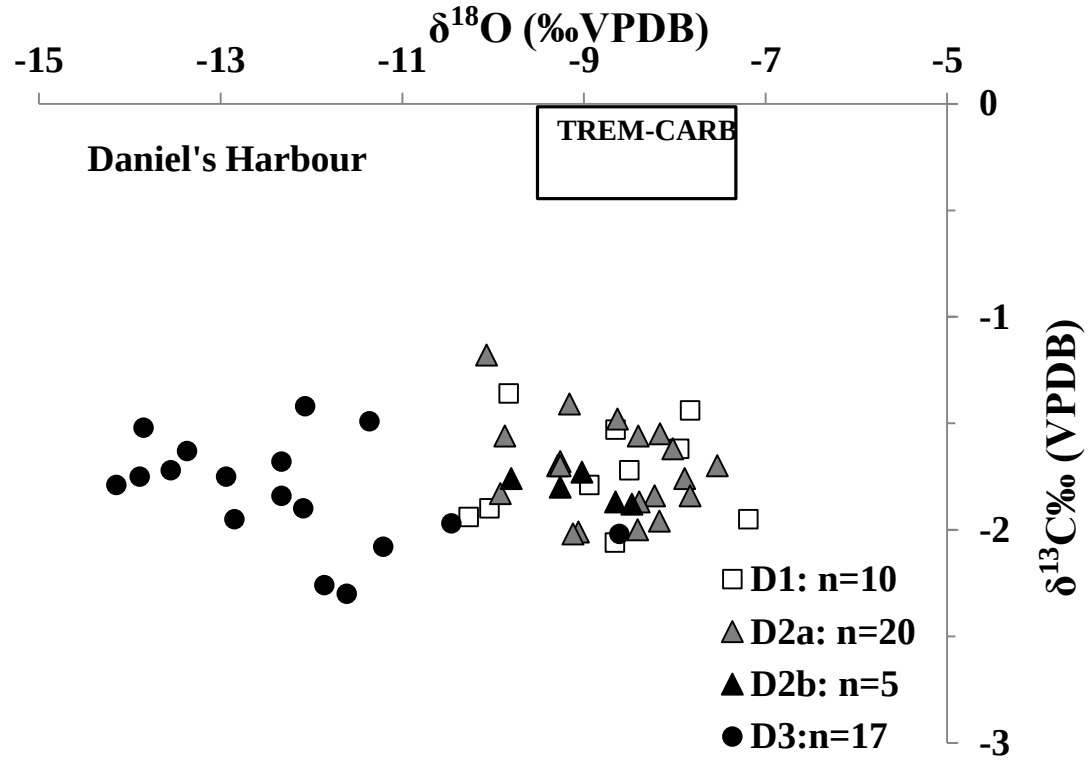

Figure 2.8B. A scatter diagram of $\delta^{18}O$ versus $\delta^{13}C$ in Boat Harbour Formation carbonates in Daniel's Harbour on the Northern Peninsula. The box marks the range of well preserved low magnesium calcite from Tremadocian (Lower Ordovician; TREM-CARB inside box) sea water (cf. Prokoph et al., 2008).

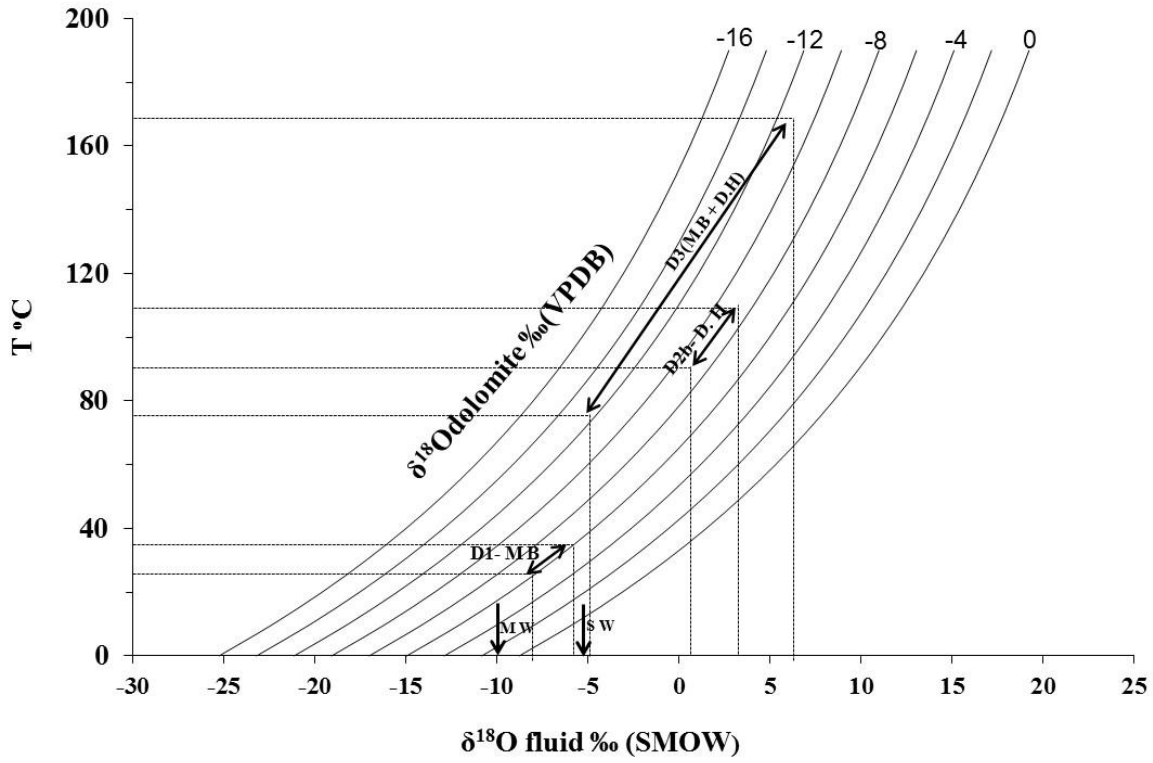

Figure 2.9. Temperature vs $\delta^{18}O_{(diagenetic\ fluid)}$ for various $\delta^{18}O_{(dolomite)}$ values using equation $10^3 ln\alpha = 3.2*10^6 T^{-2} - 3.3$(Land, 1983). Black arrows point at calculated range of $\delta^{18}O$ ‰SMOW for Tremadocian meteoric (MW) and seawaters (S.W).

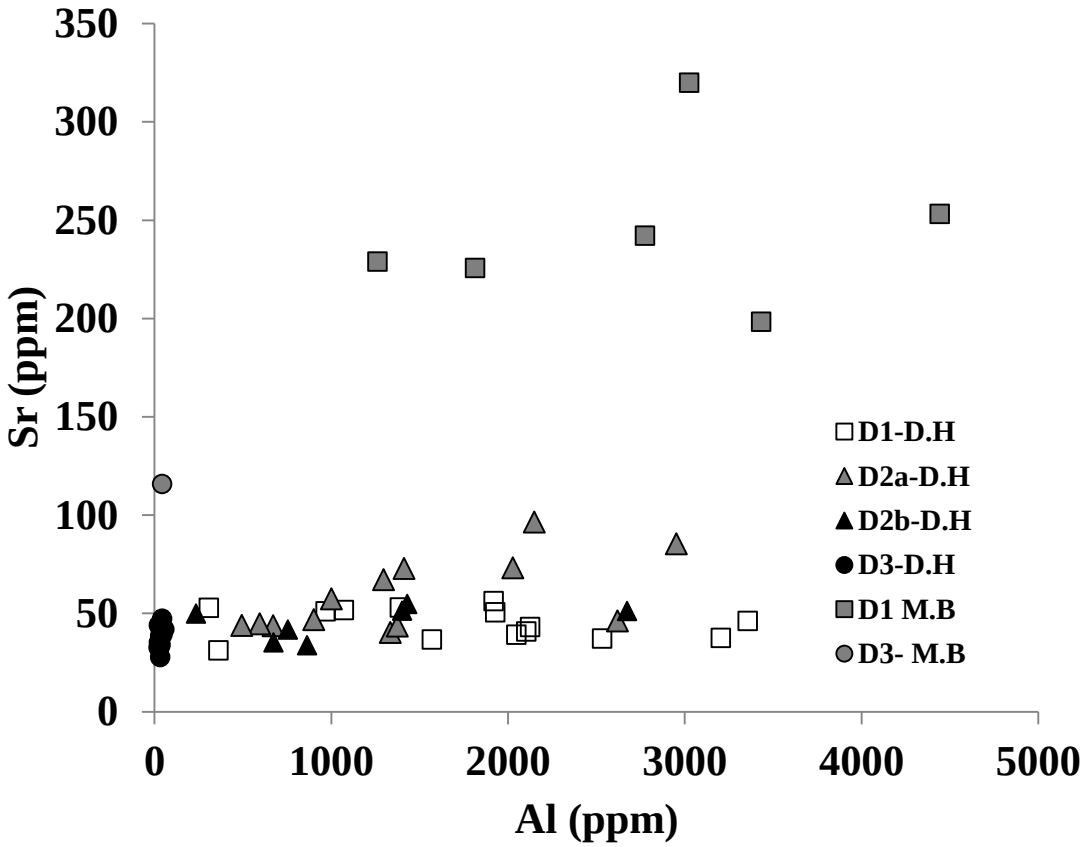

Figure 2.10A. A scatter diagram of Sr vs Al (ppm; Main Brook-M.B; Daniel's Harbour-D.H).

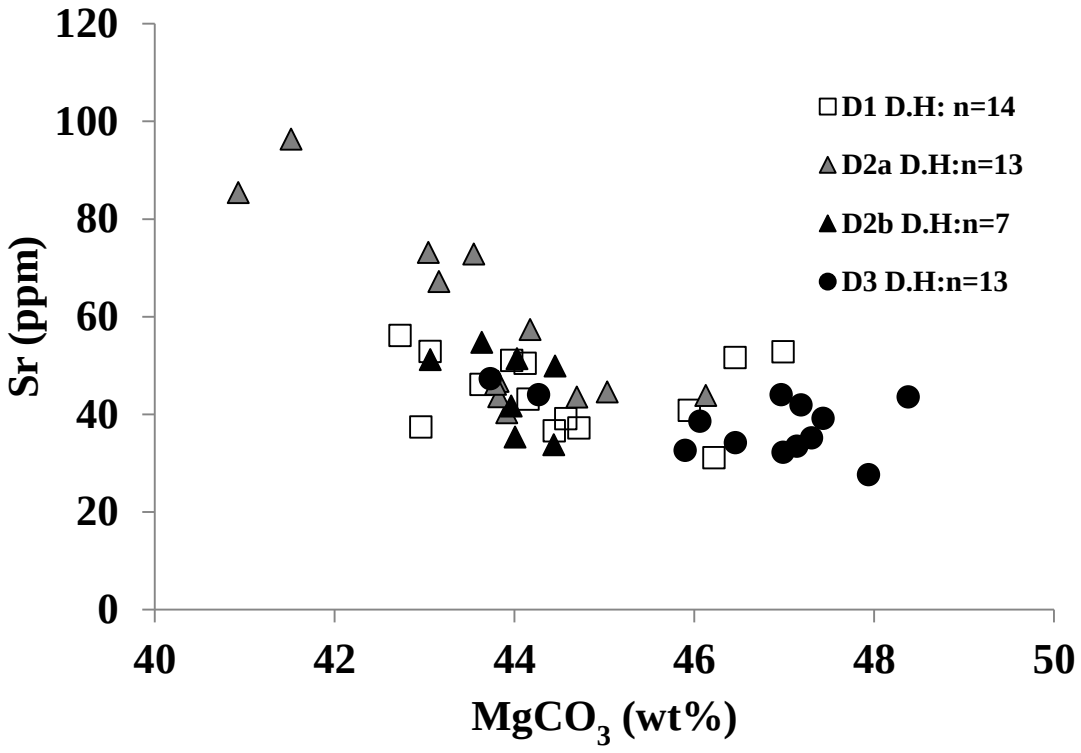

Figure 2.10B. A scatter diagram of Sr vs $MgCO_3$ at the Daniel's Harbour.

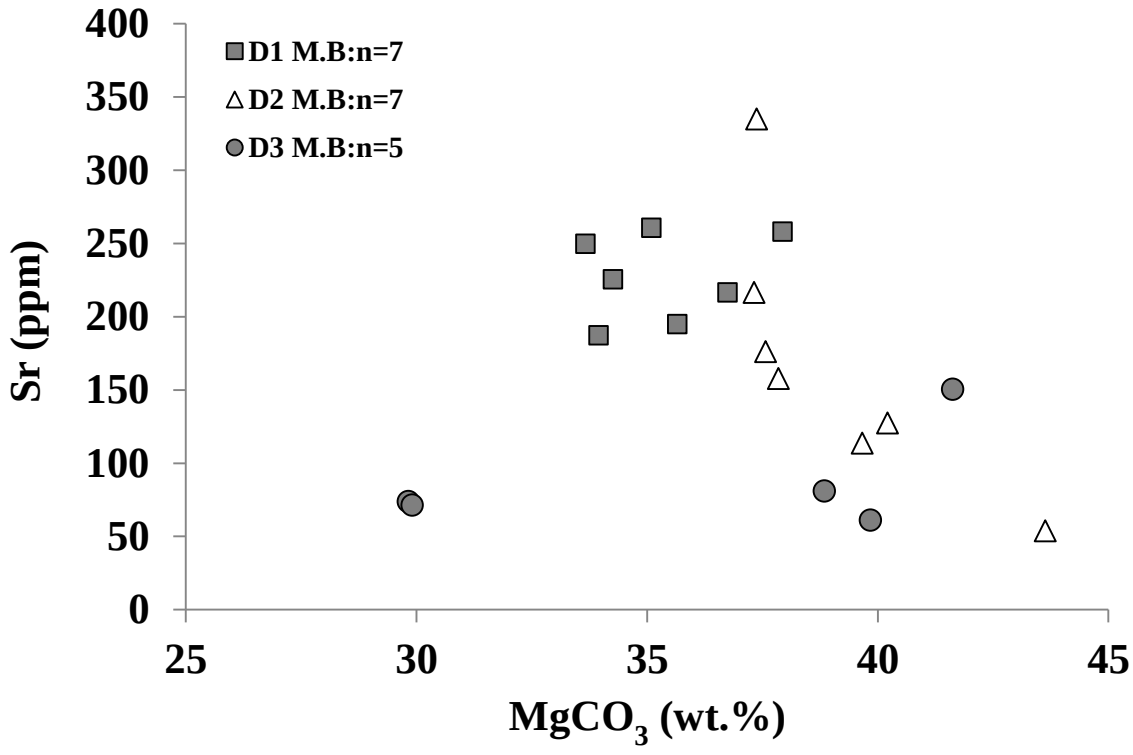

Figure 2.10C. A scatter diagram of Sr vs $MgCO_3$ at the Main Brook location.

2.5. DISCUSSION

2.5.1. Early dolomitization

The D1 dolomicrites at Main Brook are more fabric retentive, less stoichiometric and have higher Sr concentrations compared with their Daniel's Harbour counterparts and hence considered more representative of the early dolomitization episode that affected the Boat Harbour Formation. On the other hand, D1 dolomicrites at Daniel's Harbour are coarser than (compare Figs 2.5c and g) and geochemically similar to the later dolomite phases in the sequence, thus suggesting a possible recrystallization and reset of geochemical signatures.

The near–micritic to finely crystalline texture and relative fabric retention in D1 dolomite is consistent with early near–surface dolomitization (Fig. 2.5c). This is supported by other syn–sedimentary features such as lamination and stratigraphic 'capping' of the sequences (e.g., Knight et al., 2008; Azmy et al., 2009), and occurrence as breccia in the matrix of later dolomite phases (D2; Fig. 2.5m), and also in paleocavities of the disconformity zones. The occasional dissemination of framboidal pyrite (Fig. 2.5d) might further suggest that bacterial sulphate reduction might have played a role in the dolomitization of the lime mud (e.g., Montanez, 1992; Warren, 2000) but the carbon isotopic composition of D1 dolomite is not sufficiently low to support bacterial fractionation (Lippmann, 1973). In addition, the D1 early dolomite is calcitic (e.g., mean of 65wt% $CaCO_3$ at Main Brook; Table 2.2) and its $\delta^{13}C$ is similar to that of the precursor limestone (–2.4±0.7 ‰ in D1 and –2.5±0.7 ‰ VPDB in C1) suggesting that it has not undergone subsequent repeated recrystallization (cf. less ripening process; Sibley et al., 1987; Sibley, 1990). On

the other hand, the D1 dolomite at Daniel's Harbour (55 wt % $CaCO_3$) is more stoichiometric than its counterparts at Main Brook (65 wt% $CaCO_3$) and Isthmus Bay (74 wt% $CaCO_3$; Azmy et al., 2009) supporting relative possible recrystallization and alteration of its pristine signature. At Main Brook, similar to Isthmus Bay (Azmy et al., 2009), this is probably due to partial dolomitization with dolomite rhombs preserving precursor calcite in their cores.

The low Sr contents of Boat Harbour Formation dolomites at Main Brook (Table 2.2) suggest a marine source with diagenetic modifications (cf. Budd, 1997). The Sr values decrease from the early dolomite (dolomicrite, D1) to the latest dolomite (D3; Table 2.2), which may be due to recrystallization and/or precipitation during progressive burial (e.g., Land, 1980; 1983; Veizer, 1983; Warren, 2000; Al–Aasm et al., 2002; Conliffe et al., 2009). Also, the Sr trend is consistent with increasing stoichiometry and crystal sizes of the dolomites. However, this trend is not noticeable in the entirely dolomitized Daniel's Harbour section where the dolomites have comparable Sr values and are significantly depleted in Sr compared with their counterparts at Main Brook (Table 2.2). This implies that, even though the crystal sizes are similar, the D1 early dolomite at Daniel's Harbour has been altered/recrystallized during burial (cf. Machel, 1997). Furthermore, the relatively low Sr contents of the D1 dolomite (228 ±30 ppm) at Main Brook compared with that of a typical primary marine sabkha dolomite (≥470 ppm; Veizer, 1983, their Table 3.3) suggest that the dolomitizing fluids were not developed from heavily evaporated seawater but rather seawater diluted with other fluids of low Sr concentration such as meteoric water.

Accordingly, Sr/Ca molar ratio of carbonates can, at times, provide clues to the nature of their corresponding diagenetic fluids, given that the estimates of the Sr distribution coefficient between the fluid and the precipitated carbonates has already been established. Therefore, Sr/Ca molar ratio of the dolomitizing fluids can be calculated from equation 1:

$$\left({}^{m}Sr/_{m}Ca\right)_{\text{dolomite}} = D_{dol}^{sr}\left({}^{m}Sr/_{m}Ca\right)_{\text{fluid}} \quad \text{.....1}$$

where D_{dol}^{sr} is the distribution coefficient which varies between 0.05 to 0.06 for calcitic dolomites (cf. Banner, 1995), while ${}^{m}Sr$ and ${}^{m}Ca$ is the molar concentration of the respective Sr and Ca values. Thus, the calculated molar Sr/Ca ratios of the Boat Harbour Formation dolomitizing fluids, that precipitated the early dolomite D1 (dolomicrite) in the Main Brook area, range between 0.0097 and 0.0081, while it ranges between 0.0022 and 0.0018 in the Daniel's Harbour area (for D_{dol}^{sr} of 0.05 and 0.06 respectively). Therefore, relative to a value of 0.0086 for modern seawater (Drever, 1988) the low end member value of the molar (Sr/Ca)fluid, in the Main Brook area, suggests normal marine waters with some dilution with non–marine, likely meteoric waters, while the high end member value suggests a possible contribution from slightly evaporated seawater. Correspondingly, D1 dolomite likely originated from a mixture of seawater or slightly evaporated seawater and meteoric water. This interpretation is consistent with an earlier crush–leach analyses study on the same rocks from other locations in the area (Conliffe et al., 2010).

As noted in the previous paragraph, the range of $\delta^{13}C$ values of the C1 lime mudstone (–2.5 ±0.7 ‰) and D1 dolomite (–2.4 ±0.7‰) are very similar and fall within the range

recorded for pristine marine carbonates of Early Ordovician age (Veizer et al., 1999; Prokoph et al., 2008). This suggests that the D1 dolomite at Main Brook preserves a near–primary $\delta^{13}C$ signature of its precursor marine calcite. Unfortunately, lime mudstones were not found in the Daniel's Harbour section and therefore it is difficult to correlate the $\delta^{13}C$ value of the D1 dolomite (–1.73±0.24‰) with that of a potential precursor. However, the $\delta^{13}C$ value of the D1 dolomite at Daniel's Harbour is still more enriched than those of C1 calcite and D1 dolomite from Main Brook. This argues for preservation of near-primary $\delta^{13}C$ value and can also be attributed to a possible local geographic barrier that caused some slight restriction in shelf water circulation, and increased slightly the primary productivity in the shallow shelf settings. Therefore, it is suggested that D1 dolomite at Boat Harbour Formation was likely formed during early diagenesis by dolomitization of C1 lime mud at near–surface temperatures (25°–35°C) and from dolomitizing fluids with $\delta^{18}O$ values between –8.1 and –5.8 ‰ (VSMOW; Fig. 2.9, Land 1983).

The best preserved $\delta^{18}O$ value of Lower Ordovician tropical carbonates (–9‰VPDB; Veizer et al., 1999; Shields et al., 2003; Prokoph et al., 2008) suggests a seawater with a $\delta^{18}O$ value of –6 to – 5‰ VSMOW (Friedman et al., 1977). The $\delta^{18}O$ of meteoric water is usually ~4 ‰ lower than seawater (Clark and Fritz, 1997), which provides an estimate of Lower Ordovician meteoric water of –9 to –10 ‰ VSMOW. The estimates of $\delta^{18}O$ values of Lower Ordovician meteoric and seawater bracket the $\delta^{18}O$ end-member values suggested for the parent diagenetic fluids of D1 dolomite (Fig. 2.9), and support the implication that that D1 was likely precipitated from a mixture of seawater (source of

Mg) and meteoric water. However, occasional insignificant evaporation of the seawater might have occurred, possibly due to a local geographic barrier, as indicated by the Sr/Ca molar ratio. It should be noted that no major sedimentary evidence (Knight et al., 2008) has been found on the Northern Peninsula or Isthmus Bay (Azmy et al., 2009) to support an evaporative (sabkha) brine origin. The most enriched δ18O value of D1 dolomite at Main Brook is –5.3‰ (VPDB). Taking into consideration the enrichment of the $\delta^{18}O$ signature of carbonate caused by dolomitization ($D_{calcite–dolomite}$ = 4‰; Land, 1983), the estimated $\delta^{18}O$ of precursor calcite is –9.3‰ (VPDB), which is within the range of the documented best preserved Lower Ordovician marine carbonate signature (Veizer et al., 1999), and hence does not support a sabkha origin for these dolomites.

A near–surface seawater origin for the supply Mg^{2+} and CO_3^{2-} is consistent with the notion that seawater in the Early Ordovician was higher in CO_3^{2-} and lower in SO_4^{2-} saturation relative to the geologically recent seawater, and hence favourable to precipitation of dolomite from seawater (Arvidson et al., 2008; 2011). The presence of bioturbation and bioclasts such as brachiopods in the Boat Harbour Formation (Knight et al., 2008) also agrees with normal salinity for the seawater (Brand et al., 2003).

2.5.2. Burial dolomitization

2.5.2.1. Mid–Stage burial dolomitization

Burial and late–stage dolomitization is more pervasive in the Daniel's Harbour section (completely dolomitized) compared with its Main Brook counterpart. Unlike dolomite D1, D2 was precipitated in intermediate burial (600-1000 m, sensu Machel, 2005) settings and it is the most abundant dolomite phase in the Daniel's Harbour section. In this section, dolomites D2a and D2b are texturally different (Fig 2.5i and j) but have similar geochemical properties (Table 2.2) suggesting they formed from the same or similar dolomitizing fluids. They are subhedral to euhedral with a crystal size of 45 to 300 μm (Fig 2.5h–k), high homogenization temperatures (Fig. 2.6 and salinity (Fig. 2.7), and crystal fracturing (revealed by CL, Fig. 2.5l). In addition, they are cross–cut by and cross–cut micro stylolites, contain abundant micro–breccia and breccia clasts of D1 dolomite in their matrix as found in the Daniel's Harbour section (Fig. 2.5m). All these features suggest that the formation of D2 dolomite started during shallow burial and continued with deeper burial of the formation. Furthermore, their associated matrix intercrystalline pores are occluded by bitumen (Fig. 2.5j and k), thus further implying that D2 dolomite was precipitated in intermediate burial settings, prior to the emplacement of hydrocarbon (cf. Machel, 2005) and precipitation of the late–stage D3 saddle dolomite. Stylolites oblique to the bedding plane cross–cut some D2 dolomite suggesting that it formed prior to major compression (tectonic shortening) during the Silurian–Devonian Acadian Orogeny.

The parent fluid of D2 dolomite was progressively heated in the formation (mean T_h = 114°C), becoming more saline (mean salinity =22.7 wt% NaCl). This is in agreement with enriched $\delta^{18}O$ value (+0.5 to +3‰, SMOW, Fig. 2.9) derived for this fluid. The majority of the sub- to euhedral crystals of D2 dolomite exhibit characteristic concentric CL zoning (Fig 2.5l) indicating that they likely developed from multiple pulses of fluids under variable redox conditions but within the same dolomitization episode. The small-sized fluid inclusions in D2 dolomite crystals at Main Brook did not yield reliable microthermometric measurements however, their crystal shapes (euhedral to subhedral) and sizes are consistent with those at Daniel's Harbour and Isthmus Bay (cf. Azmy et al., 2009), which supports precipitation in an intermediate burial setting.

The zoning observed in transmitted light microscopy and CL, 'mottled' luminescence, combined with its spatial distribution in polished sections, suggests that D2 dolomite was developed by replacement of precursor limestones (C1) and/or recrystallization of D1 dolomite. The descending trend of mean Sr contents from dolomites D1 (228±30ppm) to D2 (169±90ppm) observed in the carbonates at Main Brook (Table 2.2) favours recrystallization, which is also supported by the slightly more stoichiometric composition of the D2 dolomite (61±6wt.% $CaCO_3$) relative to that of the D1 dolomite (65±2 wt.% $CaCO_3$). However, at Daniel's Harbour, D2 dolomites (D2a and D2b) and D1 have similar stoichiometry (~56 and ~55 wt% $CaCO_3$) but the cores of the D2 dolomite crystals exhibit 'mottled' luminescence (Fig. 2.5l), which might be remnants of a limestone precursor. This kind of replacement mechanism under semi– to closed system conditions could generate good reservoir porosity due to volumetric differences between

limestone and dolostone, and the intercrystalline pores in dolomite D2 at Daniel's Harbour are filled with bitumen. It is noteworthy that the overlap in Sr and Al (Fig. 2.10a) as well as $MgCO_3$ (Fig. 2.10b and 2.10c) contents in dolomites D1 and D2a may indicate similar diagenetic fluid with evolving composition during progressive burial. This also implies that the dolomitizing environment as a semi–closed setting that was conducive to porosity generation during the replacement process. On the other hand, the development of D2 dolomite by recrystallization of D1 dolomicrite should not result in porosity development since the net molar volume change would be minimal.

The association of burial D2 dolomite with stylolites allows for constraining the timing of its formation:

- D2 dolomites at Main Brook and D2a at Daniel's Harbour are crosscut by stylolites suggesting formation prior to the Middle Ordovician;
- D2b dolomites at Daniel's Harbour crosscut burial stylolites and are cross–cut by oblique–to–bedding stylolites suggesting formation between the Middle Ordovician and Late Silurian, since the oblique–to–bedding stylolites were formed by tectonic shortening during initiation of the Siluro–Devonian Acadian Orogeny (Cooper et al., 2001).

This is consistent with the suggested 2 to 3 km maximum burial depth for the St. George Group in the Northern Peninsula region, based on a conodont alteration index of 2 to 2.5 (Willams et al., 1998), which culminated between the Late Ordovician and Late Silurian (Lane, 1990). Furthermore, pressure solution seams form at minimum burial depths of

800 to 1000 m (Wierzbicki et al., 2006), and thus aid in determining minimum burial depths for the formation.

It is speculated that sulphide mineralizing fluid (Mississippi Valley Type) intensified D2 dolomitization in the Boat Harbour Formation. This is because the Daniel's Harbour location, where the formation is completely dolomitized and with the highest D2 volume, also has significant occurrences of economic MVT sulphide mineral deposits. Other western Newfoundland locations, such as Main Brook and Isthmus Bay that do not have economic MVT sulphide mineral deposits, also have less dolomite volume. If the sulphide mineralizing fluid enhanced burial dolomitization, then it was likely a fluid that was Mg–rich, mildly acidic and undersaturated with respect to dolomite (Merino and Canals, 2011). The Mg and $CO_3^{2-}$of this fluid could have been sourced during burial from trapped seawater in the formation, with contribution from dissolution of earlier-formed dolomite during water/rock interaction (Kupecz and Land, 1991). This fluid may have dissolved the precursor limestone (Equations 2 and 3, see below) and earlier dolomite becoming supersaturated with dolomite (Equation 4, see below) such that dolomite replacement proceeds in a coupled dissolution–precipitation process at constant volume (Equation 4, see below; Merino and Canals, 2011). Dolomitization through this mechanism often leads to very fine preservation of the initial morphology of the precursor texture at the micrometer scale (Fig. 2.5h; Merino and Canals, 2011).

$CaCO_{3(s)} + H^{+}_{(aq)} = Ca^{2+}_{(aq)} + HCO^{-}_{3\,aq)}$……..…….2

$CaCO_{3\,(calc)} = Ca^{2+} + CO_3^{2-}$ ……..…….……3

$1.74\ CaCO_{3\,(calc)} + Mg^{2+} + 0.2\ 6CO_3^{2-} = CaMg\ (CO_3)_{2(dolo)} + 0.74\ Ca^{2+}$…….……4

2.5.2.2. Late–burial dolomitization

The latest stage of dolomitization produced dolomite D3 and is associated with MVT mineralization, which is found in economic abundance in Newfoundland Zinc mines at Daniel's Harbour on the Northern Peninsula. Otherwise, MVT mineralization is in trace quantities across the remainder of the western Newfoundland region.

The very coarse D3 dolomite with sub– to anhedral crystals and curved planes (Fig. 2.5f) occurs as fracture–filling cement. This dolomite is calcitic, Fe rich (Table 2.2) with crystals that exhibit sweeping extinction under crossed polars, and hence it is interpreted as saddle dolomite. Typically, it is precipitated from hot saline brines at temperatures above 60^{o}C (Radke and Mathis, 1980; Gregg and Sibley, 1984; Al–Aasm et al., 2002) in deep–burial settings or as a hydrothermal mineral in shallower settings under reducing fluid conditions. Microthermometric measurements of D3 dolomite reveal high T_h values (148±18.9^{o}C at Main Brook and 115±19.6^{o}C at Daniel's Harbour) and significantly saline fluids (approximately 24.4 and 21.5 wt% NaCl at Main Brook and Daniel's Harbour, respectively). These observations are consistent with the most negative $\delta^{18}O$ values of –11.1±1 and –12.3±1.4 ‰ (VPDB) at Main Brook and Daniel's Harbour, respectively, for the D3 dolomite.

Petrographic and geochemical characteristics suggest that the dolomitizing fluid of D3 dolomite is different from that of D2 dolomite (e.g Figs. 2.10a, 2.10b and 2.10c). Tectonic control contributed to the development of fractures that acted as conduits for the latest D3 fluids (Cooper et al., 2001). This is further supported by the disconformity–related dissolution porosity, which is evident from D3 cement in breccia clasts of the disconformity zones. The latest calcite cement C3 and the metal sulphides were then precipitated subsequent to the formation of D3 (cf. Lane, 1990). Trace element compositions of the dolomite types are also in agreement with the notion of a distinctive origin and formational process for the D3 (Table 2.2) compared to D1 and D2.

The T_h data indicate that the temperature of precipitation of the latest stage D3 dolomites on the Northern Peninsula increases from south at Isthmus Bay (120±15 ^oC; Azmy et al., 2009) to north at Main Brook and Daniel's Harbour. This trend is also reflected in the Acritarch Alteration Index (AAI: 2.3 = 85^oC in Isthmus Bay vs. 3.4 = 140^oC on the Northern Peninsula; Williams et.al., 1998), which when compared with the T_h data of the late dolomites indicates the temperature of precipitation and ambient/rock temperature increases to the southwest of the Northern Peninsula region. This thermal anomaly has been suggested to be the effect of orogenic processes (possibly Acadian Orogeny) on the St George Group, during the Paleozoic era (Williams et.al., 1998; Nowlan and Barnes, 1987). The nearly bimodal distribution (Fig. 2.6) of the microthermometric data in the Daniel's Harbour section is consistent with the suggested precipitation of D3 dolomite from different pulses of the fluid. Lastly, the similar T_h and salinity measurements in

dolomite D3 and sphalerite as well as their close spatial association are also consistent with precipitation from the same fluid at Daniel's Harbour (cf. Merino and Canals, 2011).

2.6. REGIONAL IMPLICATIONS AND POROSITY DEVELOPMENT

The data presented here on the Boat Harbour Formation and the previously studied sequence at Isthmus Bay (Azmy et al., 2009) suggest that there are factors that can improve the flow of dolomitizing fluid: (1) occurrences of grainstone and boundstone facies as increase in grain size is at times associated with coarser dolomite crystals sizes; (2) enhanced disconformity–related dissolution effects and (3) proximity to post–depositional faulting. Whether acting independently and individually or in conjunction, these factors make burial dolomitization effective enough to enhance and/or generate porosity.

Intercrystalline porosity is the dominant type in Boat Harbour Formation dolomites and it is always associated with intermediate burial D2 dolomites. Stratigraphically speaking, this dolomite (D2) is usually associated with the locally dominantly subtidal middle member of the formation. On the other hand the lower and upper members are peritidal (Knight et. al., 2008) and D1 dolomites are more apparently associated with these facies.

Regionally, within the three sections (Main Brook, Daniel's Harbour and Isthmus Bay), the Middle member at Daniel's Harbour and Isthmus Bay consists of the most porous D2 dolomite. In the case of the Daniel's Harbour area, however, inverted basement–involved faults enabled migration of the fluid that intensified burial dolomitization thereby enhancing D2 dolomite formation (e.g., Cooper et al., 2001). In contrast, D2 dolomite abundance in the Isthmus Bay area is associated with the regionally developed disconformity which facilitated the movement of dissolution fluids through grainy rather

than muddy facies. The resulting secondary porosity aided circulation of the dolomitizing fluid.

Comparison of the investigated sections (cf. Knight and James, 1987; Knight et al., 2008) suggests that Isthmus Bay (outer shelf region) is more grainstone rich with an abundance of skeletal grains such as brachiopods, and boundstones made up of thrombolites and stromatolites facies; than other sequences on the Northern Peninsula (Main Brook and Daniel's Harbour); hence its greater capacity to trap pore water. This capacity might have been enhanced later by the Boat Harbour Disconformity, which then facilitated storage of pore fluids for burial dolomitization leading to more abundant D2 dolomite in this location compared to that at Main Brook (cf. Azmy et al., 2009). Furthermore, it is noteworthy that among the three studied sections in western Newfoundland, the influence of depositional factors is clearly observable at Main Brook and Isthmus Bay, whereas at Daniel's Harbour, dolomitization has largely obliterated the depositional features.

Most D3 saddle dolomite of the formation is associated with inter– crystalline and vuggy porosity, which occurred largely as a result of dissolution. However the vugs are rarely associated with bitumen infilling. Late C3 calcite was precipitated into these void spaces after the Mg content of the dolomitizing fluid had been exhausted (e.g., Merino and Canals, 2011). On the other hand, the D2 dolomite is coated with hydrocarbons, which may indicate that the timing of this porosity development during burial dolomitization coincides with hydrocarbon migration into St. George Group carbonates.

2.7. CONCLUSIONS

The Boat Harbour Formation at the Main Brook location is sparsely dolomitized (~40% in volume) compared with its counterpart at Daniel's Harbour which is completely dolomitized. Near–pristine features indicative of the early dolomitization process are more preserved at Main Brook while more extensive dolomitization altered the geochemical signature of these early phases at Daniel's Harbour.

Boat Harbour Formation carbonates on the Northern Peninsula at Main Brook and Daniel's Harbour, similar to its Isthmus Bay counterpart, were subjected to three major phases of dolomitization. The earliest was D1 dolomicrite, followed by D2 intermediate burial setting dolomite, and then late–stage deep burial D3 dolomite. The D1 dolomicrites (4–55μm) were likely formed from a mixture of seawater and meteoric water at near–surface conditions.

On the other hand, the coarser D2 dolomite (30–400μm), associated with enhanced porosity are interpreted to have formed in mid–burial settings from hotter basinal fluid(s). This phase is divided into 2 subphases (D2a, D2b) at Daniel's Harbour, based on distinct petrographic features. It is associated with disconformity zones at Main Brook, similar to that at Isthmus Bay, whereas it is dispersed throughout the formation at Daniel's Harbour. The D3 dolomite (125 μm to 7mm) which has sweeping extinction is interpreted to have formed as a late stage dolomite of a deep burial setting, from hot fluids delivered through fractures developed by orogenic events.

The intensity of burial dolomitization in the formation is associated with the two major disconformities, substrate and to a limited extent, tectonic activity. Meteoric dissolution associated with the disconformities enhanced porosity development, through which dolomitizing fluids were able to circulate more efficiently during later and deeper burial stages.

Subsequently, dolomitization and formation of D2 dolomite around the Lower Boat Harbour Disconformity zone enhanced porosity by up to 8 % within 10 – 15 m below the disconformity at Main Brook section. On the other hand, similar porosity enhancement is associated with the Upper Boat Harbour Disconformity at Isthmus Bay, whereas at Daniel's Harbour, porosity ranging from 7–12% is indiscriminately found throughout the sequence.

REFERENCES

Al–Aasm, I. S., J. Lonnee, and J. Clarke, J, 2002, Multiple fluid flow events and the formation of saddle dolomite: Case studies from the Middle Devonian of the Western Canada sedimentary basin: Marine and Petroleum Geology, 19(3), 209-217. doi:10.1016/S0264-8172(02)00013-2.

Anderson, W., 2010, Algal thrombolites, dolomitization and porosity development in the Knox dolomite; Implications for carbon dioxide sequestration in Kentucky: Environmental Geosciences, 17(2; 2), 108-109.

Arvidson, R. S., M. W. Guidry, and F. T. Mackenzie, 2011, Dolomite controls on Phanerozoic seawater chemistry: Aquatic Geochemistry, 17(4-5; 4-5), 735-747. doi:10.1007/s10498-011-9130-7.

Arvidson, R. S., M. Guidry, and F. T. Mackenzie, 2008, Chemostatic modes of the Phanerozoic; calcite-dolomite versus aragonite seas and their control by weathering, carbonate precipitation, and basalt-seawater reactions: Abstracts with Programs - Geological Society of America, 40(6; 6), 268-268.

Azmy K., I. Knight, D. Lavoie, G. Chi, 2009, Origin of dolomites in The Boat Harbour Formation, St. George Group, in Western Newfoundland, Canada: Implications for porosity development: Canadian Petroleum Geology, 57(1), 81-104.

Azmy K., D. Lavoie, I. Knight, G. Chi, 2008, Dolomitization of the Lower Ordovician Aguathuna Formation Carbonates, Port au Port Peninsula, Western Newfoundland,

Canada: Implications for a hydrocarbon reservoir: Canadian Journal of Earth Sciences, 45, 795-813. doi:10.1139/E08- 020.

Azmy, K., & J. Conliffe, 2010, Dolomitization of the Lower St. George Group on the Northern Peninsula in Western Newfoundland; implications for lateral distribution of porosity: Bulletin of Canadian Petroleum Geology, 58(4; 4), 361-374. doi:10.2113/gscpgbull.58.4.361.

Banner, J. L. 1995, Application of the trace element and isotope geochemistry of strontium to studies of carbonate diagenesis: Sedimentology, 42, 5;5(805-824).

Bodnar, R. J. 1992, Revised equation and table for freezing-point depressions of H (sub 2) O salt fluid inclusions: Program and Abstracts; Biennial Pan-American Conference on Research on Fluid Inclusions, 4, 15-15.

Brand, U. and J. Veizer, 1980, Chemical diagenesis of a multicomponent carbonate system; 1, Trace elements: Journal of Sedimentary Petrology, 50, 1219-1236.

Brand, U., A. Logan, N. Hiller, and J. Richardson, 2003, Geochemistry of modern brachiopods: applications and implications for oceanography and paleoceanography: Chemical Geology, 198, 305-334.

Broadhead, R. F., W. D. Raatz, S. P. Dutton, and E. M. Kim, 2004, Play analysis and digital portfolio of major oil reservoirs in the Permian basin; New Mexico. Annual Meeting Expanded Abstracts - American Association of Petroleum Geologists, 13, 17-17.

Budd, D. A., 1997, Cenozoic dolomites of carbonate islands; their attributes and origin: Earth Science Review, 42, 1-2; 1-47. Netherlands: Elsevier: Amsterdam, Netherlands.

Clark, I. and P. Fritz, 1997, Environmental isotopes in hydrogeology. Lewis Publishers; Boca Raton, FL.USA.

Coleman, M. L., J.N., Walsh, and R.A., Benmore, 1989, Determination of both chemical and stable isotope composition in milligramme-size carbonate samples. Sedimentary Geology, 65(3-4; 3-4), 233-238.

Conliffe, J., K. Azmy, S. A Gleeson, and D. Lavoie, 2010, Fluids associated with hydrothermal dolomitization in St. George Group, Western Newfoundland, Canada: Geofluids, 10, 422-437. doi:doi: 10.1111/j.1468-8123.2010.00295.

Conliffe, J., K. Azmy, and M. Greene, 2012, Dolomitization of the Lower Ordovician Catoche Formation: Implications for hydrocarbon exploration in Western Newfoundland: Marine and Petroleum Geology, 30(1), 161-173. doi:10.1016/j.marpetgeo.2011.10.007.

Conliffe, J., K. Azmy, I. Knight, and D. Lavoie, 2009, Dolomitization of the Lower Ordovician Watts Bight Formation of the St. George Group, Western Newfoundland; evidence of hydrothermal fluid alteration. Canadian Journal of Earth Sciences = Revue Canadienne Des Sciences De La Terre, 46(4; 4), 247-261. doi: 10.1139/E09-019.

Cooper M., J. Weissenberger, I. Knight, D. Hostad, D. Gillespie, H. Williams, E. Burden, J. Porter- Chaudhry, D. Rae, and E. Clark, 2001, Basin evolution in Western Newfoundland: New insights from hydrocarbon exploration: AAPG Bulletin, 83(3), 393-418.

Dickson, J. A. D., 1966, Carbonate identification and genesis as revealed by staining. Journal of Sedimentary Petrology, 36(2; 2), 491-505.

Drever, J. I., 1988, The geochemistry of natural waters. United States: Prentice-Hall: Englewood Cliffs, NJ, United States, 437.

Flügel, E., 2010, Microfacies of carbonate rocks: Berlin Heidelberg: Springer, 984.

Friedman, I., J. R. O'Neil, and M. Fleischer, 1977, Compilation of stable isotope fractionation factors of geochemical interest: U.S. Geological Survey Professional Paper. United States: U. S. Geological Survey: Reston, VA, United States, 440-KK, 49.

Goldstein, Robert H., and J. Reynolds, 1994, Systematics of fluid inclusions in diagenetic minerals: SEPM (Society of Sedimentary Geology) Short course 31, 199.

Gregg J. M., 2004, Basin fluid, base-metal sulphide mineralization and the development of dolomite petroleum reservoirs. In Braithwaite, C.J.R, Rizzi, G and Darke, G (Ed.), In: The geometry and petrogenesis of dolomite hydrocarbon reservoirs. (pp. 157-175). London: Geological Society, London, Special Publications, 235, 141-155.

Gregg, J. M., and D. F. Sibley, 1984, Epigenetic dolomitization and the origin of xenotopic dolomite texture. Journal of Sediment Petrologists. 54, 3; 3, 908-931, United States: Society of Economic Paleontologists and Mineralogists: Tulsa, OK, United States.

James, N. P., R. K. Stevens, C. R. Barnes, and I. Knight, 1989, Evolution of a Lower Paleozoic continental-margin carbonate platform, Northern Canadian Appalachians:SEPM (Society for Sedimentary Geology), 44, 123-146.

Knight I., K. Azmy, W. D. Boyce, and D. Lavoie, 2008, Tremadocian carbonate rocks of the Lower St. George Group, Port au Port Peninsula, Western Newfoundland: Lithostratigraphic setting of diagenetic, isotopic and geochemistry studies: Newfoundland and Labrador Department of Natural Resources Geological Survey, Report, 08-1, 115-149.

Knight I., and N. P. James, 1987, The stratigraphy of the Lower Ordovician St. George Group, Western Newfoundland: The interaction between eustasy and tectonics: Canadian Journal of Earth Sciences, 24, 1927-1951.

Knight, I., K. Azmy, M. G. Greene, and D. Lavoie, 2007, Lithostratigraphic setting of diagenetic, isotopic and geochemistry studies of Ibexian and Whiterockian carbonate rocks of the St. George and Table Head Groups, Western Newfoundland: (Current Research (2007) No. 07-1, Pages 55- 84). Canada: Newfoundland and Labrador Department of Natural Resources, Geological Survey.

Kupecz, J. A., and L.S. Land, 1991, Late-stage dolomitization of the Lower Ordovician Ellenburger Group, West Texas: Journal of Sedimentary Petrology, 61(4; 4), 551-574. doi:10.1306/D426775D-2B26-11D7-8648000102C1865D.

Land, L. S., 1983, The application of stable isotopes to studies of the origin of dolomite and to problems of diagenesis of clastic sediments. in: Stable isotopes in sedimentary geology. M.A. Arthur, T.F. Anderson, I.R. Kaplan, J. Veizer and L.S. land (eds.). 10, p. 4-1– 4-22: SEPM Short Course Notes, 10(4-1), 4-22.

Land, L. S., 1980, The isotopic and trace element geochemistry of dolomite; the state of the art. Special Publication-Society of Economic Paleontologists and Mineralogists. 28(87-110): United States: SEPM (Society for Sedimentary Geology): Tulsa, OK, United States.

Lane, T. E., 1990, Dolomitization, brecciation and zinc mineralization and their paragenetic, stratigraphic and structural relationships in the Upper St. George Group (Ordovician) at the Daniel's Harbour, western Newfoundland: (Unpublished PhD). Memorial University of Newfoundland, Canada.

Lavoie, D., G. Chi, P. Brennan-Alpert, A. Desrochers, and R. Bertrand, 2005, Hydrothermal dolomitization in the lower Ordovician romaine formation of the Anticosti Basin; significance for hydrocarbon exploration: Bulletin of Canadian Petroleum Geology, 53(4; 4), 454-471. doi:10.2113/53.4.454.

Lavoie, D., and G. Chi, 2008, Paleozoic hydrothermal dolomites in eastern Canada; Multiple new targets for oil and gas exploration. Abstracts: Annual Meeting - American Association of Petroleum Geologists, 2008.

Lavoie, D., and G. Chi, 2010, Lower Paleozoic foreland basins in Eastern Canada; tectono-thermal events recorded by faults, fluids and hydrothermal dolomites: Bulletin of Canadian Petroleum Geology. 58, 1(17-35).

Lindholm, R. C., and R. B. Finkelman, 1972, Calcite staining; semiquantitative determination of ferrous iron: Journal of Sedimentary Petrology, 42(1; 1), 239-242.

Lippmann, F., 1973, Sedimentary carbonate minerals: Berlin, New York: Springer-Verlag, 6, 228.

Lonnee, J., and H. G. Machel, 2006, Pervasive dolomitization with subsequent hydrothermal alteration in the Clarke Lake gas field, Middle Devonian Slave Point Formation, British Columbia, Canada: AAPG Bulletin, 90(11; 11), 1739-1761. doi:10.1306/03060605069.

Lucia, F. J., and R. P. Major, 1994, Porosity evolution through hypersaline reflux dolomitization: Special Publication of the International Association of Sedimentologists. 21(325-341). International: Blackwell: Oxford.

Machel, H. G., 2004, Concepts and models of dolomitization: A critical reappraisal. In Braithwaite, C.J.R, Rizzi, G and Darke, G (Ed.), In: The geometry and petrogenesis

of dolomite hydrocarbon reservoirs (pp. 7-63). London: Geological Society of London, Special Publications.

Machel, H. G., 1997, Recrystallization versus neomorphism, and the concept of 'significant recrystallization' in dolomite research: Sediment Geology. 113, 3-4(161-168).

Machel, H. G., 2005, Investigations of burial diagenesis in carbonate hydrocarbon reservoir rocks: Geoscience Canada, 32(3; 3), 103-128.

Maliva, R. G., D.A. Budd, E.A. Clayton, T.M. Missimer, and J.A.D. Dickson, (2011). Insights into the dolomitization process and porosity modification in sucrosic dolostones, Avon Park Formation (Middle Eocene), East-Central Florida, U.S.A. Journal of Sedimentary Research, 81(3; 3), 218-232.

Merino, E. and A. Canals, 2011, Self-accelerating dolomite-for-calcite replacement; self-organized dynamics of burial dolomitization and associated mineralization: American Journal of Science, 311(7), 573-607.

Montanez I.P., 1994, Late diagenetic dolomitization of Lower Ordovician Upper Knox carbonates: A record of the hydrodynamic evolution of the southern Appalachian Basin: American Association of Petroleum Geologists, 78(8), 1210-1239.

Montanez, I. P., 1992, Fluid-rock interaction history during stabilization of early dolomites, Upper Knox Group (Lower Ordovician), U.S. Appalachians: Journal of

Sedimentary Petrologists, 62, 5(753-778). Society of Economic Paleontologists and Mineralogists.

Montanez, I. P., 1997, Secondary porosity and late diagenetic cements of the Upper Knox Group, Central Tennessee Region; a temporal and spatial history of fluid flow conduit development within the Knox regional aquifer: SEPM. 57(101-117).Society for Sedimentary Geology.

Pratt, B. R., and N.P. James, 1986, In James N. P. (Ed.), The St George Group (Lower Ordovician) of Western Newfoundland; tidal flat island model for carbonate sedimentation in shallow epeiric seas. International: Blackwell: Oxford-Boston, International.

Prokoph, A., G. A. Shields, and J. Veizer, 2008, Compilation and time series analysis of a marine carbonate delta 18) O, delta (super 13) C, (super 87) sr/ (super 86) Sr and delta (super 34) S database through earth history: Earth Sciences Review. 87, 3-4 (113-133).

Radke, B. M. and Mathis, R. L. 1980. On the formation and occurrence of saddle dolomite. Journal of Sedimentary Petrology, 50, 4 (1149-1168). United States: Society of Economic Paleontologists and Mineralogists : Tulsa, OK, United States.

Saller, A. H. 2004, Palaeozoic dolomite reservoirs in the Permian basin, SW USA; Stratigraphic distribution, porosity, permeability and production. Geological Society Special Publications, 235, 309-323.

Selleck, B. W. 2004, Exposing the roots of hydrothermal dolomite hydrocarbon reservoirs in the Adirondack lowlands; fluid alteration and fault systems. Abstracts with Programs - Geological Society of America, 36(2; 2), 119-119.

Shields, G. A., G. A. F. Carden, J. Veizer, T. Meidla, J. Rong, and R. Li, 2003, Sr, C, and O isotope geochemistry of Ordovician brachiopods: A major isotopic event around the Middle-Late Ordovician transition: Geochimica Et Cosmochimica Acta, 67(11), 2005-2025. DOI: 10.1016/S0016-7037(02)01116-X .

Sibley, D. F., T. R. Bartlett, and R. E Didoes, 1987, Kinetics of dolomitization: Geology [Boulder], 15, 12(1112-1114). United States: Geological Society of America (GSA): Boulder, CO, United States.

Sibley, D. F., 1990, Unstable to stable transformations during dolomitization: The Journal of Geology, 98(5), pp. 739-748. The University of Chicago Press.

Smosna, R., K. R Bruner, and R.A. Riley,2005, Paleokarst and reservoir porosity in the Ordovician Beekmantown dolomite of the Central Appalachian basin. Carbonates and Evaporites, 20(1; 1), 50-63.

Usdowski, E., 1994, Synthesis of dolomite and geochemical implications. In M. Purser, M. Tucker and Zenger (Eds.), Dolomites: A volume in honour of dolomieu (pp. 345-360): Great Britain: Blackwell Publishing Ltd. doi:10.1002/9781444304077.ch19.

Veizer J., D. Ala, K. Azmy, P. Brochschen, D. Buhl, and F. Bruhn, G.A.F. Carden, A. Diener, S. Ebneth, Y. Godderis, T. Jasper, C. Korte, F. Pawellek, O.G. Podlaha, H. Strauss, 1999, (Super 87) Sr/ (super 86) Sr, delta (super 13) C and delta (super 18) O evolution of Phanerozoic seawater: Chemical Geology, 161(1-3; 1-3), 59-88.

Veizer, J., 1983, Chemical diagenesis of carbonates; theory and application of trace element technique: SEPM Short Course, 10, 3.1-3.1. United States: Society of Sedimentary Geology: Tulsa, OK, United States.

Warren, J., 2000, Dolomite: Occurrence, evolution and economically important associations: Earth Science Reviews, 52(1–3), 1-81. doi:10.1016/S0012-8252(00)00022-2.

Wierzbicki, R., J. J. Dravis, I. Al-Aasm, and N. Harland, 2006, Burial dolomitization and dissolution of Upper Jurassic Abenaki platform carbonates, deep pancake reservoir, Nova Scotia, Canada: American Association of Petroleum Geologists Bulletin, 90, 1843-1861.

Williams S.H., E.T Burden, P.K. Mukhopadhyay,1998. Thermal maturity and burial history of Paleozoic Rocks in Western Newfoundland. Canada: Canadian Journal of Earth Sciences, 35, 1307-1322.

Zhang, S., and C. R. Barnes, 2004, Arenigian (Early Ordovician) sea-level history and the response of conodont communities, Western Newfoundland: Canadian Journal of Earth Sciences, 41(7; 7), 843-865.

APPENDIX: VOLUMETRIC ABUNDANCE OF CARBONATE PHASES IN SAMPLES FROM MAIN BROOK, DANIEL'S HARBOUR AND ISTHMUS BAY LOCALITIES.

MAIN BROOK

NO	Depth (m)	Sample ID	C1	D1	D2	D3	C3	Total
1	42	P42	0	100	0	0	0	100
2	44	P44	50	50	0	0	0	100
3	46	P46	60	40	0	0	0	100
4	48	P48	75	25	0	0	0	100
5	50	P50	90	10	0	0	0	100
6	52	P52	95	5	0	0	0	100
7	54	P54	100	0	0	0	0	100
8	56	P56	10	90	0	0	0	100
9	58	P58	80	20	0	0	0	100
10	60	P60	95	5	0	0	0	100
11	62	P62	30	70	0	0	0	100
12	64	P64	95	5	0	0	0	100
13	67	P66.8	65	0	35	0	0	100
14	68	P68	50	30	20	0	0	100
15	70	P70	90	10	0	0	0	100
16	72	P72	90	10	0	0	0	100
17	74	P74	35	65	0	0	0	100
18	75	P75D	35	65	0	0	0	100
19	76	P76	100	0	0	0	0	100
20	79	P78.5	80	20	0	0	0	100
21	80	P80	80	0	20	0	0	100
22	82	P81.5	5	95	0	0	0	100
23	84	P84	95	5	0	0	0	100

DANIEL'S HARBOUR

NO	Depth (m)	Sample ID	D1	D2a	D2b	D3	C3	Non-Carbonate	TOTAL
1	113	6-132	15	85	0	0	0	0	100
2	115	6-134	65	35	0	0	0	0	100
3	131	6-138	35	55	10	0	0	0	100
4	113	6-140	60	35	0	0	5	0	100
5	115	6-142	25	75	0	0	0	0	100
6	131	6-144	30	65	5	0	0	0	100
7	113	6-152	30	60	0	10	0	0	100
8	115	6-154	35	65	0	0	0	0	100
9	131	6-150	25	40	15	20	0	0	100
10	113	6-158	0	100	0	0	0	0	100
11	115	6-160	30	60	0	10	0	0	100
12	131	6-162	15	50	25	10	0	0	100
13	113	6-164	30	60	0	10	0	0	100
14	115	6-166	0	90	0	10	0	0	100
15	131	6-168	20	80	0	0	0	0	100
16	113	6-170	0	100	0	0	0	0	100
17	115	6-172	0	0	100	0	0	0	100
18	131	6-174	0	60	20	15	5	0	100
19	113	6-176	0	100	0	0	0	0	100
20	115	6-178	0	90	0	10	0	0	100
21	131	6-180	10	80	10	0	0	0	100
22	113	6-182	0	85	0	15	0	0	100
23	115	6-184	0	15	85	0	0	0	100

24	86	P86	95	5	0	0	0	100
25	88	P88	85	15	0	0	0	100
26	90	P90	90	10	0	0	0	100
27	92	P92	5	95	0	0	0	100
28	94	P94	95	5	0	0	0	100
29	96	P96.2	95	5	0	0	0	100
30	98	P98	10	90	0	0	0	100
31	100	P100	5	0	95	0	0	100
32	102	P102	95	5	0	0	0	100
33	104	P104	100	0	0	0	0	100
34	106	P106	90	10	0	0	0	100
35	108	P108	5	15	80	0	0	100
36	110	P110	90	10	0	0	0	100
37	112	P112	80	20	0	0	0	100
38	114	P114	95	5	0	0	0	100
39	116	P116	60	40	0	0	0	100
40	118	P118	90	10	0	0	0	100
41	120	P120	95	5	0	0	0	100
42	122	P121.5	95	5	0	0	0	100
43	124	P124	70	30	0	0	0	100
44	126	P126	80	20	0	0	0	100
45	128	P128	10	90	0	0	0	100
46	138	P138	95	5	0	0	0	100
47	140	P140	95	5	0	0	0	100
48	142	P142	50	50	0	0	0	100
49	144	P144	30	70	0	0	0	100
50	146	P146	20	40	40	0	0	100
51	148	P148	90	10	0	0	0	100
52	150	P150	70	30	0	0	0	100
53	152	P152	50	30	20	0	0	100
54	154	P154	0	5	95	0	0	100
55	155	P154.5	5	0	0	95	0	100
56	156	P156	50	50	0	0	0	100
57	158	P158	0	5	95	0	0	100
58	160	P160	0	5	95	0	0	100
59	162	P162	80	20	0	0	0	100
60	164	P164	85	10	5	0	0	100
61	166	P166	95	0	5	0	0	100
62	168	P168	0	0	0	9	1	100

24	131	6-186	0	100	0	0	0	0	100
25	113	6-188	0	65	35	0	0	0	100
26	115	6-170	0	100	0	0	0	0	100
27	131	6-190	0	100	0	0	0	0	100
28	113	6-192	5	85	10	0	0	0	100
29	115	6-194	30	60	0	10	0	0	100
30	131	6-196	0	0	10	25	25	40	100
31	113	6-198	0	90	0	10	0	0	100
32	115	6-199	10	0	0	90	0	0	100
33	131	6-200	80	20	0	0	0	0	100
34	113	6-202	60	40	0	0	0	0	100
35	115	6-204	0	85	15	0	0	0	100
36	131	6-206	30	50	20	0	0	0	100
37	113	6-208	55	35	0	10	0	0	100
38	115	6-210	60	30	0	10	0	0	100
39	131	6-212	50	0	20	15	0	15	100
40	113	6-214	0	40	45	0	0	15	100
41	115	6-216	0	0	80	20	0	0	100
42	131	6-218	25	0	60	10	5	0	100
43	113	6-220	40	35	15	10	0	0	100
44	115	6-222	35	55	5	5	0	0	100
45	131	6-224	0	65	35	0	0	0	100
46	113	6-226	0	0	65	25	0	10	100
47	115	6-228	0	0	45	35	0	20	100
48	131	6-230	0	0	55	35	0	10	100
		Average	**19**	**53**	**16**	**9**	**1**	**2**	**100**

63	170	P170	95	0	0	00	05	100
64	171	P171.3	0	0	0	80	20	100
65	172	P172	90	5	0	0	5	100
66	174	P174.3	95	5	0	0	0	100
67	183	P183.3	0	0	0	90	10	100
68	184	P184	0	0	5	95	0	100
69	184	P184.5	0	0	0	95	5	100
70	186	P186	95	0	0	0	5	100
		Average	**60**	**22**	**9**	**8**	**1**	**100**

Table 2.A1. Volumetric abundance (visual estimate) of carbonate phases in the cores from Main Brook and Daniel's Harbour localities.

ISTHMUS BAY

NO	Depth (m)	Sample ID	C1	D1	D2	D3	C2	C3	NON-CARBONATE	TOTAL	NO	Depth (m)	Sample ID	C1	D1	D2	D3	C2	C3	Non-Carbonate	TOTAL
1	0	BH73	70	0	10	0	20	0	0	100	71	112	BH12	50	50	0	0	0	0	0	100
2	1	BH72	90	0	0	0	10	0	0	100	72	113	BH29	0	60	25	5	10	0	0	100
3	2	BH71	75	10	0	0	10	5	0	100	73	116	BH10	70	0	0	0	30	0	0	100
4	3	BH70	70	15	0	0	15	0	0	100	74	117	BH9	65	0	0	0	35	0	0	100
5	4	BH69	90	10	0	0	0	0	0	100	75	119	BH8	0	65	35	0	0	0	0	100
6	5	BH68	85	0	0	0	15	0	0	100	76	122	BH7	55	30	0	0	15	0	0	100
7	6	BH67A	75	15	0	0	10	0	0	100	77	124	BH6	60	0	0	0	40	0	0	100
8	6	BH67A	80	10	0	0	10	0	0	100	78	125	BH5-FC	55	0	0	0	35	10	0	100
9	8	BH66	70	0	0	0	30	0	0	100	79	126	BH5B	75	0	0	0	25	0	0	100
10	10	BH65	75	5	0	0	20	0	0	100	80	126	BH5	75	10	0	0	15	0	0	100
11	12	BH64	60	0	0	0	40	0	0	100	81	128	BH4	5	95	0	0	0	0	0	100
12	13	BH63	100	0	0	0	0	0	0	100	82	134	BH3	100	0	0	0	0	0	0	100
13	15	BH62	100	0	0	0	0	0	0	100	83	132	BH2	95	0	0	0	0	5	0	100
14	17	BH61	95	5	0	0	0	0	0	100	84	138	BH1	85	0	0	0	5	10	0	100
15	19	BH60	30	70	0	0	0	0	0	100	85	136	BHA23	55	0	25	0	15	5	0	100
16	20	BH59	100	0	0	0	0	0	0	100	86	138	BHA22-2	0	45	55	0	0	0	0	100
17	22	BH58	10	90	0	0	0	0	0	100	87	138	BHA22-1	0	0	100	0	0	0	0	100
18	24	BH57	15	70	15	0	0	0	0	100	88	141	BHA21	0	0	90	0	0	0	10	100
19	26	BH56-1	80	20	0	0	0	0	0	100	89	170	BH6	60	0	0	0	40	0	0	100
20	26	BH56	0	60	40	0	0	0	0	100	90	143	BHA19-2	0	40	60	0	0	0	0	100
21	28	BH55	60	0	0	0	35	5	0	100	91	145	BHA19-1	20	0	0	0	0	0	80	100
22	28	BH55-1	0	75	25	0	0	0	0	100	92	145	BHA19	0	0	100	0	0	0	0	100
23	28	BH55B	70	15	0	0	15	0	0	100	93	147	BHA18-B	55	0	15	0	30	0	0	100
24	28	BH51-VC	0	50	30	5	15	0	0	100	94	147	BHA18	0	30	70	0	0	0	0	100
2	30	BH5	8	5	0	0	1	0	0	100	9	15	BH	0	7	3	0	0	0	0	100

52		4	5				0				59	0	A17		0	0					
26	32	BH53	5	65	30	0	0	0	0	100	96	152	BH A16	0	30	70	0	0	0	0	100
27	34	BH52	70	0	15	0	10	5	0	100	97	155	BH A15	0	35	65	0	0	0	0	100
28	36	BH51	65	10	0	0	25	0	0	100	98	156	BH A14	65	0	35	0	0	0	0	100
29	38	BH50	0	50	50	0	0	0	0	100	99	158	BH A 13	0	35	65	0	0	0	0	100
30	39	BH49	40	40	15	0	5	0	0	100	100	159	BH A12-A	55	30	5	0	0	10	0	100
31	40	BH48	5	35	60	0	0	0	0	100	101	161	BH A11	0	65	30	0	0	5	0	100
32	42	BH47	100	0	0	0	0	0	0	100	102	163	BH A10	0	85	0	0	5	10	0	100
33	44	BH46	0	40	55	0	5	0	0	100	103	165	BH A9	0	25	65	0	0	10	0	100
34	45	BH45	0	80	20	0	0	0	0	100	104	167	BH A8	0	20	75	0	0	5	0	100
35	47	BH44	0	35	60	0	5	0	0	100	105	169	BH A7	0	15	85	0	0	0	0	100
36	50	BH43	85	0	15	0	0	0	0	100	106	169	BH A7-1	0	15	85	0	0	0	0	100
37	52	BH42	40	0	60	0	0	0	0	100	107	168	BH A6	0	50	50	0	0	0	0	100
38	53	BH43A	90	10	0	0	0	0	0	100	108	170	BH A5-2	55	15	15	0	15	0	0	100
39	54	BH41	50	0	50	0	0	0	0	100	109	172	BH A5	0	85	15	0	0	0	0	100
40	55	BH40	50	0	50	0	0	0	0	100	110	175	BH A4-2	65	0	0	0	25	0	10	100
41	57	BH39	0	0	0	0	0	70	30	100	111	175	BH A4-1	55	0	0	0	35	10	0	100
42	58	BH38B	0	1000	0	0	0	0	0	100	112	177	BH A3	0	70	30	0	0	0	0	100
43	59	BH38A	0	40	60	0	0	0	0	100	113	179	BH A2	80	10	0	0	5	5	0	100
44	60	BH37	65	0	10	0	25	0	0	100	114	181	BH A1-1	85	0	15	0	0	0	0	100
45	62	BH36	80	15	0	0	0	0	5	100	115	183	BH A13	0	30	65	0	0	5	0	100
46	64	BH35	0	0	0	25	0	40	35	100			**Average**	**37**	**29**	**22**	**0.6**	**7.2**	**3**	**1.6**	**100**
47	64	BH35A	0	0	1000	0	0	0	0	100											
48	64	BH35	0	20	55	0	0	0	25	100											
49	66	BH34	0	35	65	0	0	0	0	100											

50	66	BH34B	0	100	100	30	0	50	0	100
51	68	BH33	0	30	60	0	0	10	0	100
52	70	BH32	0	1000	0	0	0	0	0	100
53	72	BH31	60	100	10	0	0	20	0	100
54	74	BH30	0	1000	0	0	0	0	0	100
55	76	BH28	65	35	0	0	0	0	0	100
56	78	BH27	55	15	0	0	30	0	0	100
57	82	BH26	15	80	0	0	5	0	0	100
58	84	BH25	50	50	0	0	0	0	0	100
59	86	BH24	0	1000	0	0	0	0	0	100
60	91	BH22	80	0	0	0	15	5	0	100
61	92	BH21	15	85	0	0	0	0	0	100
62	95	BH20	0	1000	0	0	0	0	0	100
63	96	BH19	0	80	20	0	0	0	0	100
64	98	BH18	0	85	15	0	0	0	0	100
65	100	BH17	70	0	0	0	10	20	0	100
66	102	BH16	65	30	0	0	0	5	0	100
67	104	BH15A	0	90	0	3	0	7	0	100
68	105	BH1HB	85	15	0	0	0	0	0	100
69	106	BH14	0	1000	0	0	0	0	0	100
70	108	BH13	65	25	0	0	0	10	0	100

Table 2.A2. Volumetric abundance (visual estimate) of carbonate phases in the outcrop samples from the Isthmus Bay locality.

3 CHAPTER 3.

SECONDARY ION MASS SPECTROMETER STUDY OF DOLOMITE: EVALUATION OF GROWTH PROCESSES AND MECHANISMS.

BABATUNDE JOHN OLANIPEKUN [a*]***; KAREM AZMY*** [a]***; UWE BRAND*** [b]

[a] Department of Earth Sciences, Memorial University of Newfoundland. St. John's, NL, Canada A1B 3X5.

[b] Department of Earth Sciences, Brock University. St. Catharines, ON, Canada L2S 3A1. *Corresponding Author: E-mail address: bjo852@mun.ca.

Re-submitted to Chemical Geology and assigned manuscript number CHEMGE9253

ABSTRACT

Dolostone remains an important hydrocarbon reservoir but its origin and mechanism of formation have some issues that are still enigmatic. Recrystallization to more stoichiometric dolomite is usually accompanied by characteristic textural and geochemical signatures. These signatures are primarily studied using multiple populations of crystals by comparison of modern and ancient dolomites or from results of high temperature dolomite formation experiments.

Representative burial dolomite samples of Lower Ordovician St. George Group carbonates from both Main Brook and Daniel's Harbour localities (about 150km apart) were chosen for study. The investigation used multi proxy high resolution approaches to carry out imaging and elemental analyses of individual dolomite crystals viz: Scanning Electron Microscopy (SEM), SEM based cathodoluminescence (SEM-CL) and Secondary Ion Mass Spectrometer (SIMS). This is to better understand geochemical variations across the crystal traverses and also to constrain their mechanism of crystal growth.

Data from SIMS analyses showed that there are coupled core-to-rim variations in the trace elements (Na, Sr, Y, REE, Mn and Fe) as well as, but subtly, in the major element (Mg) in the CL-zoned dolomite crystals while CL homogeneous dolomite crystals at the Daniel's Harbour locality did not yield systematic or significant core to rim compositional variations. These suggest that CL zoned crystal facies from Main Brook locality grew at relatively slower rate than the rate at which the pore fluid's chemistry changed. On the other hand, lack of distinct systematic geochemical zoning in CL homogeneous crystal facies of Daniel's Harbour locality suggests that the crystals grew at relatively faster rate

than the rate at which the pore fluid's chemistry changed. This is consistent with the relatively higher temperature of formation of the dolomite crystals at Daniel's Harbour than at Main Brook locality.

The current study reveals multiple mechanisms of dolomite crystal growth within constrained diagenetic settings and also shows that recrystallization and episodes of dolomitization shown by multi-crystal population are also apparent within dolomite crystals.

3.1. INTRODUCTION

Mechanisms of dolomite formation are still an issue of debate (Land, 1992; Machel, 2004), and experimental studies have shown that inorganic dolomite forms through a series of discrete recrystallization steps with calcium-rich dolomite being the first phase to form before recrystallization to more stoichiometric and ideal dolomite (Nordeng and Sibley, 1994; Kaczmarek and Sibley, 2011). At the micrometer scale of the local reaction site of carbonate diagenesis, the occurrence of fluid-rock interaction (e.g., dolomitization) and aqueous diffusion of ions and molecules through a thin-film layer connected to the evolving bulk fluid, implies that the discrete growth phases of dolomite crystals record the changes in intervening fluid composition (Pingitore, 1982; Veizer, 1983). Therefore, distinct crystal growth increments have varying geochemical compositions (e.g., Borg et al., 2014) and are sometimes revealed by trace element activated cathodoluminescence.

The thin-film layer is an interphase boundary where series of chemisorption and co-precipitation reactions take place (Morse and Mackenzie, 1990). It is common within the diagenetic setting of a sedimentary sequence and defined by an interphase boundary 'halo' (*sensu* Machel, 1990) that exist between a growing and a dissolving crystal during replacement reactions such as dolomitization (e.g., Pingitore, 1982).This layer is ultimately connected to the bulk pore fluid and has a composition gradient that evolves as the water-rock interaction and bulk fluid composition change. To understand the feedback of this dynamic thin-film 'halo' on resulting precipitated carbonate crystals, high resolution petrographic (SEM) and geochemical (microprobe) methods are required

to study the µm-scale variation of properties in the minerals grown within the local reaction sites.

In addition to the intervening fluid composition, the crystal structure of dolomite has been found to impose some control on the elemental incorporation during its crystal growth. For instance, Hendry and Marshall (1991) suggest that rhombohedral faces of dolomites incorporate more 'impurity' trace metals into their crystal structure than do their non-rhombohedral faces, therefore partitioning coefficients of the reactants are different for non-equivalent but time equivalent faces. Likewise, Reeder and Prosky (1986) found lattice site preference during dolomites' formation that resulted in compositional sector zoning.

Much of what is known about the mechanisms of recrystallization and replacement of dolomites have usually come from the study of different populations of their crystals and stratigraphic relationships in the field (e.g., Montanez, 1994; Azmy et al., 2009; Iannace et al., 2012; Azomani et al., 2013). Such studies have employed the dolomites texture and major and trace element compositions to constrain their depositional and diagenetic settings (Montanez, 1994; Machel et al., 1997; Allwood et al., 2010; Collen et al., 2011; Zhao and Zheng, 2013). However, these studies used bulk geochemical analytical techniques carried out on different populations of dolomite crystals, which are likely to be an aggregate of numerous dolomitization episodes that had multiple parent fluids. This approach could therefore yield ambiguous interpretations of the origin and nature of the dolomites. Especially, given that in a zoned dolomite crystal, its over-growth cement (rim) may be formed from a different fluid and separated in time from the replacement

section (i.e., core) of the crystal. This implies that a single crystal of dolomite may bear multiple episodes of dolomitization (e.g., Jones, 2005). Thus, in complement to the bulk analytical technique of studying the origin of dolomites, the study of variations in geochemical compositions across the traverse of dolomite crystals may reveal key information about the processes of dolomites' formation. In view of this, the current study examines the variation of geochemical compositions across traverses of dolomite crystals in order to better understand the process of dolomite formation.

Micrometer scale investigation of compositional variations of carbonate minerals have been previously documented. Riciputi et al. (1994) and Machel et al. (1997) utilized Secondary Ion Mass Spectrometer (SIMS) technique to analyze various generations of calcite and dolomites within Devonian carbonate samples in an attempt to examine their trace element compositional variations to constrain the nature of their parent diagenetic fluids. This technique was necessary due to the spatial proximity of their target mineral phases in their studied samples. However, the scope of their work excluded elemental variations across dolomite crystal traverses. Fraser et al. (1989) and Wogelius et al. (1992) used Proton Induced X-ray emission (PIXE) to examine variations of trace elements across the traverse of Cretaceous Gargano as well as Cenozoic Enewatok atoll and Bahama bank dolomites. Their results did not reflect a step-wise recrystallization of dolomite crystals as it did not show systematic variations of major (Mg) and trace elements (Mn, Fe, Sr and Zn) that have been suggested to be usually coupled during dolomite recrystallization or 'ripening' (e.g., Veizer, 1983; Budd, 1997).

Furthermore, among the authors that used trace element proxies to study the origin of dolomites, very few (e.g., Xiaolin et al., 2009) presented high resolution data on the Rare Earth Elements (REE) variations within dolomite crystals. Xiaolin et al. (2009), in their diagenetic study of Lower Paleozoic dolomites of the Tarim Basin, used Laser Ablation Inductively Coupled Mass Spectrometer (LA-ICPMS) to analyze dolomite crystals and their results show systematic variations in REEs composition at the micrometer scale. However, the width of zones within dolomite crystals may be smaller than the beam size (30μm) of their LA-ICPMS. They presented only REE compositions of the dolomites while other important trace elements such as Sr, Mn, Fe were not reported, at this scale, even though incorporating these elements would have been very useful proxies in constraining diagenetic processes in carbonate systems.

Luminescence has been effective in discerning the impact of diagenesis on carbonate minerals formation in diagenetic settings and has also been used to reveal crystal growth zones within carbonate minerals. Luminescence is the emission of visible light that occurs in solids when excited electrons return to lower energy levels or ground energy states in atoms or ions (Machel and Burton, 1991; Goetze and Kempe, 2009). Manganese (Mn^{2+}) is regarded as the most important activator of luminescence in carbonate minerals, even though REEs have also been documented as activator elements (Mason and Mariano, 1990; Habermann et al., 1996), while Fe^{2+} is the most important quencher of luminescence in carbonate minerals (e.g., Machel and Burton, 1991; Richter et al., 2003).

The current study presents results of a robust suite: Mg, Sr, Mn, Fe, Na, and REEs, that used Secondary Ion Mass Spectrometer, carried out on dolomite crystals. In combination

with the luminescence features of the studied dolomites, this suite of elements was used to carry out the following main objectives:

1. Study the controls on compositional zonation across dolomite crystal growth zones;
2. Evaluate dolomite crystal growth patterns within and between horizons;
3. Evaluate how dolomite crystal growth relates to diagenetic fluid chemistry evolution during the burial history of Boat Harbour Formation.

3.2. DOLOMITIZATION OF ST. GEORGE GROUP CARBONATES

The St. George Group located in western Newfoundland (Fig. 2.1) consists of Lower Ordovician carbonate mega-sequences deposited during the rifting phase of the Iapetus Ocean. From the base upwards (Fig. 3.1), it consists of the Watts Bight, Boat Harbour, Catoche and Aguathuna Formations (Knight et al., 2008) . The deposition of the mega-sequences is punctuated by 2 major disconformities namely, the Boat Harbour Disconformity (BHD) and the St George disconformity.

The St. George Group carbonates have been affected by varying degrees of dolomitization (Fig. 3.1; Azmy et al., 2008; 2009). Dolomitization commenced at the near surface and continued through burial. In the Boat Harbour Formation, the early dolomites are finely (<4-30 μm) crystalline, fabric retentive and commonly stratiform. The mid-burial phase is pervasive and characterized by coarser (50-300 μm), euhedral to subhedral crystals and commonly fabric destructive. The late-stage dolomites consist of coarse and anhedral crystals (up to 3 mm) with sweeping extinction and usually occur as cement filling vugs and fractures (Olanipekun et al., 2014).

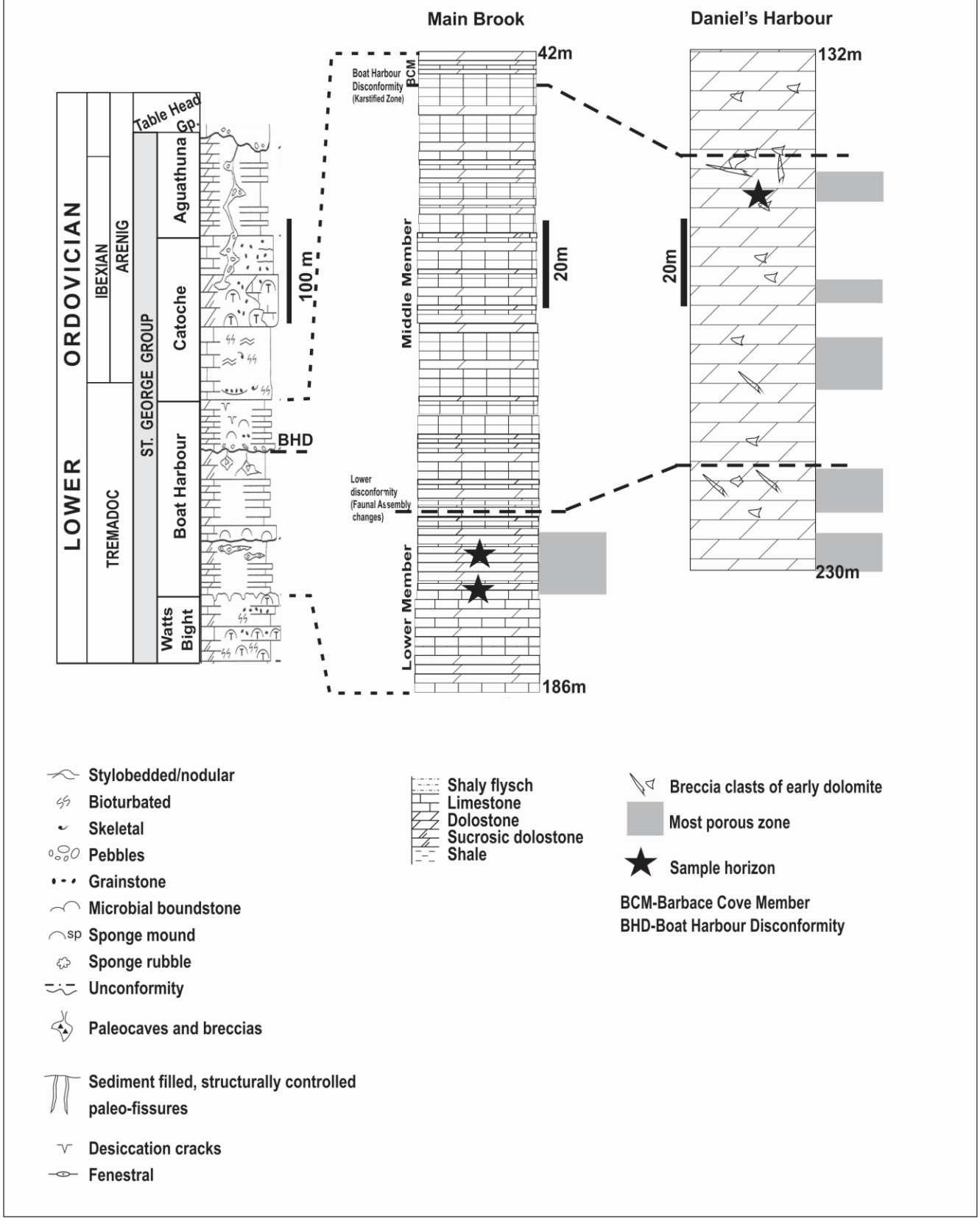
Main Brook
Daniel's Harbour
LOWER ORDOVICIAN
TREMADOC
IBEXIAN
ARENIG
ST. GEORGE GROUP
Table Head Gp.
Aguathuna
Catoche
Boat Harbour
Watts Bight
100 m
BHD
Boat Harbour Disconformity (Karstified Zone)
BCM
Middle Member
20m
Lower disconformity (Faunal Assembly changes)
Lower Member
42m
186m
132m
20m
230m
Stylobedded/nodular
Bioturbated
Skeletal
Pebbles
Grainstone
Microbial boundstone
Sponge mound
Sponge rubble
Unconformity
Paleocaves and breccias
Sediment filled, structurally controlled paleo-fissures
Desiccation cracks
Fenestral
Shaly flysch
Limestone
Dolostone
Sucrosic dolostone
Shale
Breccia clasts of early dolomite
Most porous zone
Sample horizon
BCM-Barbace Cove Member
BHD-Boat Harbour Disconformity

Figure 3.1: Simplified lithostratigraphy of the St. George Group in Isthmus Bay area (Modified from Knight et al., 2008) showing detailed distribution of dolostone in the Boat Harbour Formation section at Main Brook and Daniel's Harbour (Modified from Olanipekun et al., 2014).

3.3. METHODOLOGY

Burial dolomite samples P-154 (depth of 154 m) and P-158 (depth of 158 m) were taken from drill hole 12P/1-12 (N51º08′23′′, W56º10′54′′) at Main Brook and 6-172 (depth of 172 m) from drill hole 12i/6-121 (N51º17′46′′, W57º27′22′′) at Daniel's Harbour of the Boat Harbour Formation (Fig. 2.1; Olanipekun et al., 2014). Two polished sections were prepared, one each, from samples P-154 and P-158 of the Main Brook drill core and one polished section from sample 6-172 was selected from the Daniel's Harbour drill core (Fig. 3.1). Dolomite crystals in each of the polished section were thoroughly studied using SEM and CL. Representative burial dolomite crystals were subsequently chosen for SIMS analyses.

SEM-CL (scanning electron microscopy-cathodoluminescence) examination was used as a guide to select core-to-rim crystal traverses analyzed by SIMS (secondary ion mass spectrometer) (see Fig. 3.A1 to A3 in appendix section). Core and rim sections of the dolomite crystals in the sample from Daniel's Harbour could not be delineated in SEM-CL, therefore their cloudy core and clear rim as observed in plane polarized light were selected for analyses (Fig. 3.A3 in appendix section) to test for compositional variation between their core and rim sections. The zones at the rims of crystals sometimes contain disseminated silica grains. These grains were detected by CL and therefore avoided during sampling in order to minimize trace element contamination from these minerals.

High magnification CL images were obtained using a Gatan Chroma CL detector attached to a FEI Quanta 400 SEM which is equipped with energy dispersive X-ray microanalytical system (EDS). This CL system is equipped with 3 detectors that

correspond to red, green and blue colours thus showing image colours that are very close to those of real luminescence emitted from the studied samples. The best CL images were obtained when the SEM was set to operate at 20 KV acceleration voltage, 8.74 beam spot size and 13nA beam current. Persistent luminescence inherent in SEM-CL study of carbonate (Reed and Milliken, 2003; Bouch, 2006) did not have significant effect on the luminescence of these crystals. This was confirmed by comparing images obtained by SEM-CL and by cold cathodoluminescence.

A total of 199 sputtered spots were reported from thirty eight representative crystals in burial dolomite samples of the Boat Harbour Formation at Main Brook (samples P-154 and P-158) whereas a total of 56 sputtered spots were reported from fifteen crystals in its counterpart from Daniel's Harbour (sample 6-172). Note that spots that yielded erroneous analytical result due inconsistent operational settings or instabilities during analyses were discarded.

The average compositions of corresponding zones of the dolomite crystals within each studied sample is presented, as it is believed to be representative of their intervening fluid composition, and, potentially, condition of formation, on a broader scale. This is because each sample is a product of a specific pre-defined (Olanipekun et al., 2014) diagenetic settings, thereby strongly suggesting that the studied dolomite crystals, given their micrometer scale spatial relationships within a thin section, originated from the same bulk parent fluid. Thus crystal growth of the dolomites is regarded as both chronologically and genetically related. Broadly speaking, it therefore implies that the same core-to-rim

compositional trend is prevalent for the dolomite crystal of each respective studied sample.

All major, trace and rare earth element analyses (Tables 3.A4A-C in the appendix section) were performed using a Cameca IMS 4f Secondary Ion Mass Spectrometer (SIMS). Samples were bombarded with a primary ion beam of O^- with 7-20 nA current through a 10 kV potential and focused into a 5-15µm spot size. Each spot was pre-sputtered for 120 seconds with a 25 µm square raster applied to the beam, then sputtered again using a 10 µm raster for 100 seconds. Positively charged sputtered secondary ions were transmitted into the mass spectrometer through a potential of 4.5 keV. To minimize interference, the instrument was operated at an energy offset of 80 eV with a Medium Contrast Aperture (150 µm) and Entrance and Exit Slits paired to give flat topped peaks at a Mass Resolving Power (MRP) of 2975.

Count time for ^{23}Na, ^{24}Mg, ^{42}Ca, ^{55}Mn was 2 seconds each, but that of ^{54}Fe, ^{57}Fe, ^{88}Sr, ^{89}Y and Rare Earth Elements REEs (^{139}La, ^{140}Ce, ^{146}Nd, ^{147}Sm, ^{151}Eu, ^{153}Eu, ^{163}Dy, ^{167}Er, ^{174}Yb) was generally 4 seconds. After the first run, a separate run was set up for the REEs in which the primary beam current was increased from about 8 nA to 20 nA. In addition, the count time was increased to 6 seconds to acquire more counts to improve the detection limit of some of the heavy REEs which had low counts in previous sessions. However, these adjustments resulted in enlarged beam to about 25µm and thus crystal zones smaller than the beam spot were not analyzed for REE.

Calcium was used as a reference ion and peak signals were collected with an ETP 133H multiple-dynode electron multiplier. OKA-C (calcite from Oka carbonatite complex, Quebec) standard was analysed by SIMS and compiled results were compared to those by Gladney et al. (1987). The initial set of runs (Samples P-154 and 6-172) yielded low values for ^{57}Fe as a result of suspected spectra interference ($^{40}Ca^{16}OH^{+}$), therefore ^{54}Fe was analyzed in the subsequent runs for the samples and all results for ^{57}Fe were not reported.

Since calcite was used as standard, the difference in CaO between calcite and dolomite was normalized using (calcite-56.03 wt% and dolomite-30.41 wt. %). BaO correction was done on ^{151}Eu and ^{153}Eu using the formula: Eu (ppm) – [Ba (ppm) * REE pattern correction factor). Then ^{151}Eu and ^{153}Eu were averaged to obtain the Eu concentration of the samples. Some of the heavy rare earth elements were below detection limits therefore ∑REE is the sum of those REEs that were above their detection limits and common to all analyzed samples viz: La, Ce, Nd, Sm, Eu, Dy which represent the full spectrum of the lanthanides. The precision expressed as the relative standard deviation of the SIMS equipment is reasonably good: <6% for Mg, Mn Sr, La, Ce, Nd, Dy and Sm while it is <20% for Na, Fe, Yb and Y.

3.4. RESULTS

3.4.1. SEM - Cathodoluminescence

In the Main Brook locality, CL examination shows that dolomite crystals display mainly concentric zoning pattern and also reveals two dominant crystal facies. Crystal facies of the burial dolomite (Fig. 3.2A) with distinctly (planar boundaries) zoned core section (DZC), assigned consecutive core-to-rim zone identities Zone 1 to 5 (Figs. 3.2B and 3.3) and crystal facies of the burial dolomite (Fig. 3.4A) with indistinctly zoned core section (IZC), assigned core-to-rim zone identities Zones 1, 4 and 5 (Fig. 3.4B and 3.5). The bands of concentric zones, at times, contain very thin laminae (e.g., Fig. 3.2B) that do not warrant nomenclature on the basis of their relatively small size and the consequent assumption that most of their geochemical properties are closely similar to those of their host bands.

Core section (Zones 1, 2 and 3): The core section in DZC crystal facies is sub-divided into 3 main concentric zones (Zones 1, 2 and 3) made up of green luminescent bands. At times, these zones do not possess visible discontinuities thereby showing a homogeneous zone before Zone 4 (Fig. 3.2B). Zone 1 is the innermost band of the core section and Zone 2 is assigned to a band (where present) that occurs between Zone 1 and Zone 3 (Figs. 3.2B) while Zone 3 is assigned to the inward green band that precedes the thick red band, Zone 4 (Fig. 3.3). Unlike in the DZC, the core section of IZC crystal facies is not distinctly segmented forming a lobate structure that typically has rough outline of an incompletely developed rhomb (Fig. 3.4B).

Rim section (Zones 4 and 5): Zone 4 is the red luminescent band regarded as a distinguishing zone between the core and the rim sections (Fig. 3.3). It forms planar concentric boundaries with the cores of the DZC crystals (Fig. 3.2B; depth 154m). However, in IZC crystal facies (depth 158m), the red luminescent band is regarded as a transition zone from core to rim section. It typically forms irregular boundary with the innermost core section and planar boundary with the rim section (Fig. 3.4B). Zone 5 is a planar band which is the outermost cortex concentrically encasing other zones and forms the overall shape of the crystal (Figs. 3.3 and 3.5). It generally terminates in intercrystalline pore but absent in a mosaic of interlocking texture and is commonly silica-contaminated (Fig. 3.2B).

Unlike the dolomite crystals from Main Brook, those from Daniel's Harbour (Fig. 3.6A) lack distinctive CL core-rim zones (unzoned crystal facies) in whole dolomite crystals (Fig. 3.6B). Regardless, 2 zones that represent the rim (clear) and the core (cloudy) with gradational contact were observed under plane polarized light (Fig. 3.6A).

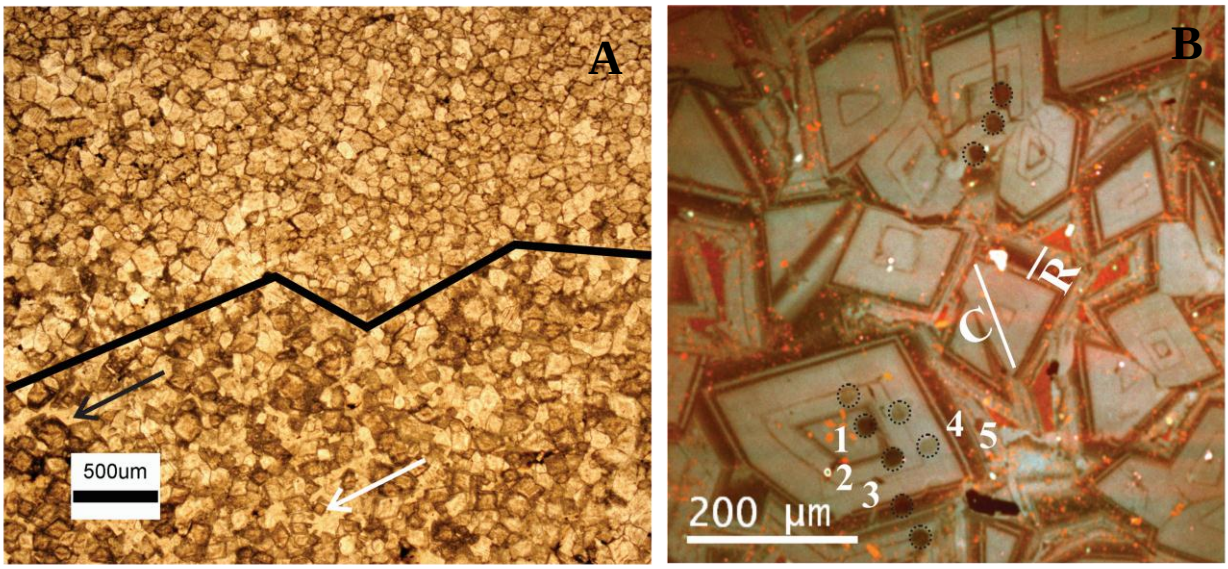

Figure 3.2: Sample id. P-154 at depth 154m from Main Brook.

A. Plane polarized light image of burial dolomite crystals. Black arrow points at cement in intercrystalline pores and white arrow points at floating dolomite rhomb in the pores. Note that the lower section is more porous than the upper section;
B. SEM-CL image showing typical zones (assigned Zones 1 to 5) in the burial dolomite crystals. It shows well developed planar boundary and concentric core and rim sections. Silicate grains are distributed in the rim section and most noticeable as randomly distributed bright spots in the rim section. (C) is core and (R) is rim sections. Broken line circles in dolomite crystals are SIMS beams spots. Labelled SIMS spots are presented in the appendix section.

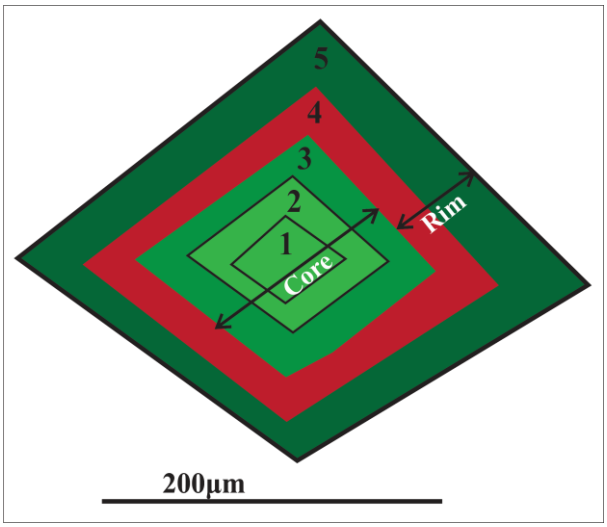

Figure 3.3. Schematic diagram of a simplified zoning pattern in dolomite sample at depth 154m (Sample id. P-154) from Main Brook.

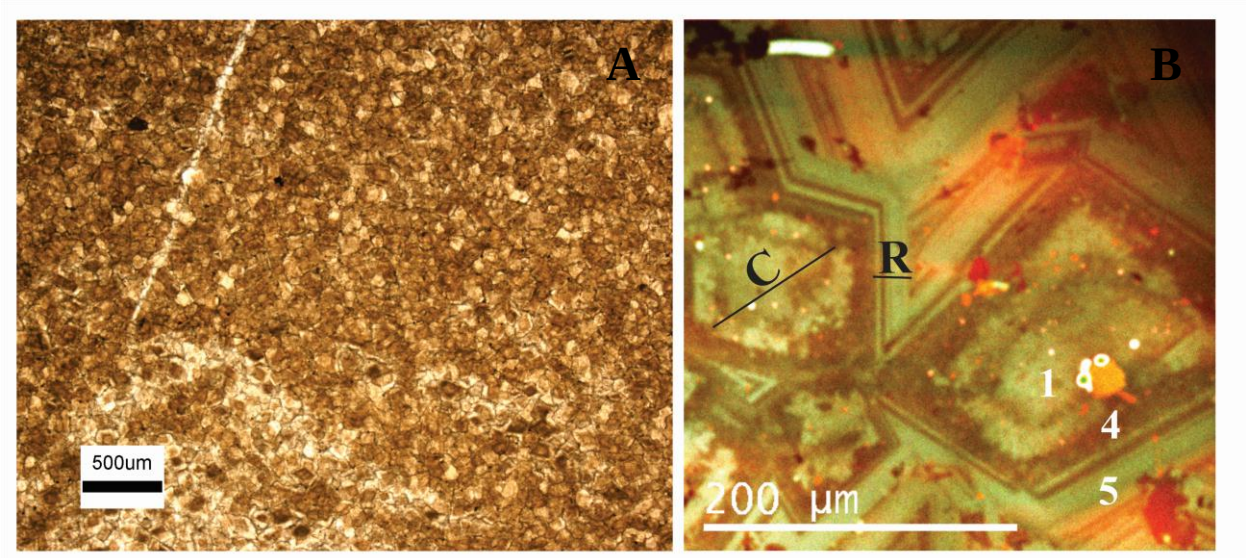

Figure 3.4: Sample id. P-158 at depth 158m from Main Brook.

A. Plane polarized light image of the burial dolomite. Note denser cloudy core and clear rim as well as lower porosity compared with its counterpart (depth 154m) in Figure 3.2A;

B. SEM-CL image showing typical zones (assigned Zones 1, 4 and 5) in the burial dolomite crystals. It shows concentric zoning pattern but ‘embryonic’ core section with poorly developed planar boundaries in the core section of the burial dolomite crystals. Compare with the well-developed core section and sharp planar boundaries in concentric zoning shown in 3.2B (from depth 154m). The core (C) and rim (R) sections are also shown. Labelled SIMS spots are presented in the appendix section.

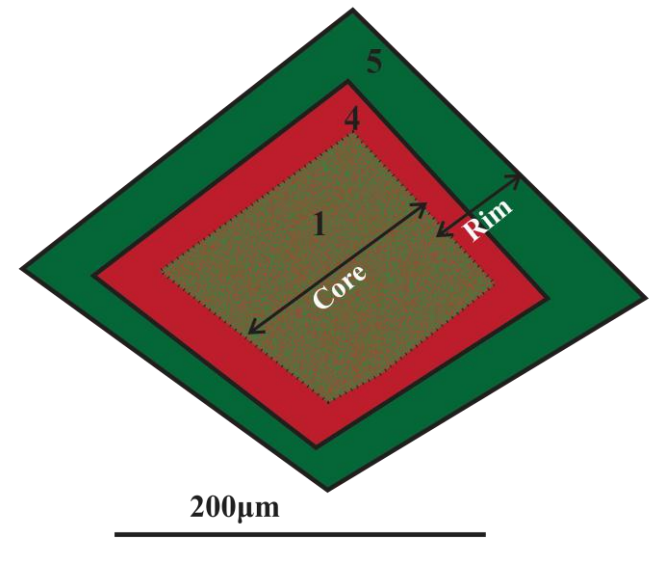

Figure 3.5. Schematic diagram of a simplified zoning pattern in sample at depth 158m (Sample id. P-158) from Main Brook.

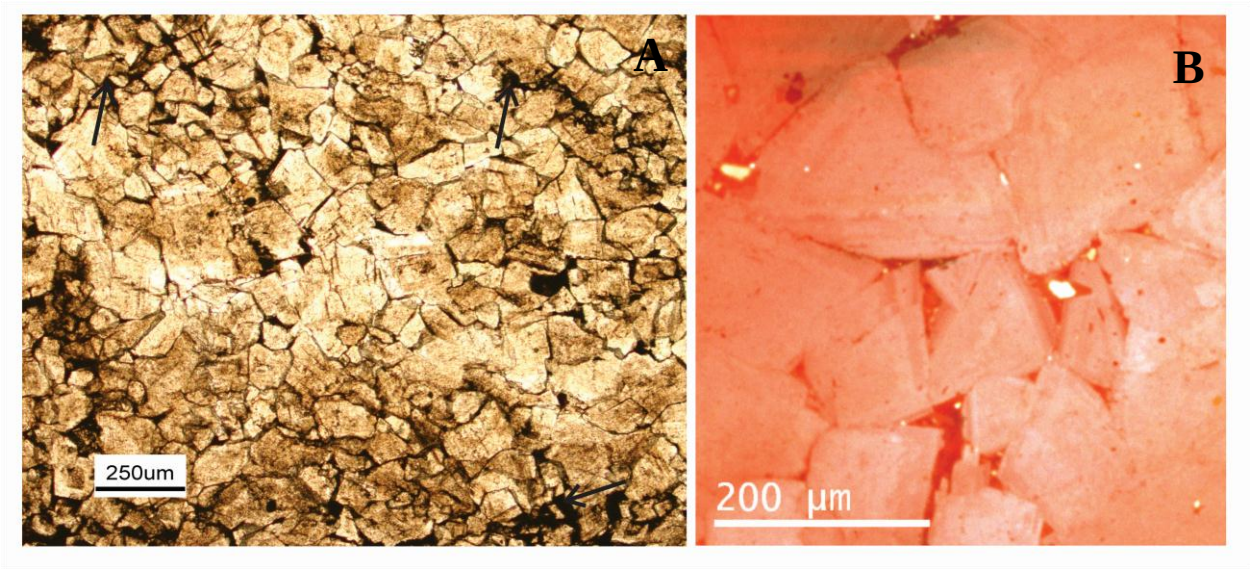

Figure 3.6: Sample id. 6-172 at depth 172m from Daniel's Harbour

A. Plane polarized light image of burial dolomite at Daniel's Harbour, showing cloudy core and clear rim in dolomite crystals. Black arrows point at bituminous materials in intercrystalline areas;
B. SEM-CL image of a region of interest in the burial dolomite showing poor (relatively homogeneous) zoning despite having cloudy core and clear rim in plane polarized light.

3.4.2. SIMS GEOCHEMISTRY

At Main Brook, Figures 3.7 to 3.10 show the plots of the major element (Mg) and respective trace element (Na, Sr, Fe, Mn, Y and REE) composition (in ppm) of each crystal and those of average compositions of each of these elements for each zone in the dolomite crystal facies. In general, the results (Table 3.1, Appendix 3.A4) show that DZC (Figs. 3.2B and 3.3; depth 154 m) and IZC (Figs. 3.4B and 3.5; depth 158 m) crystal facies have distinct but broadly similar compositional trends (Figs. 3.7 to 3.10). For the trace elements, this trend is a systematic variation from core to rim section depicted by increase in core to rim compositions of Mn and Fe but decrease in Na, Sr, Y and ∑REE. The major element (Mg) showed subtle (<25% difference in composition) increase from core to rim section of the dolomite crystal facies (Table 3.1).

In detail, as for DZC crystal facies, four (Crystals B, H, I, L) out of the ten (Crystals B, C, H, I, J, K, L, M, N, O; total of 15 crystals were documented) crystals that have available data from core (Zones 1, 2, 3) to rim sections (Zones 4 and 5) each shows distinct systematic compositional variations from their core to their rim sections. These variations are exhibited by increase in core to rim compositions of Mg, Mn and Fe (Figs. 3.7A, B and C, respectively) and decrease in core to rim compositions of Sr, Na, and Y (Figs. 3.7D, E and F respectively).

The systematic compositional variations were exhibited by other crystals but masked largely by the subtle core-to-rim trend in Mg contents of the DZC crystal facies. Regardless, when the trace elements were considered according to groups with similar trend, the following observations were apparent:

- With the exception of crystal K, each of these ten crystals also shows distinct increase in Mn (Fig. 3.7B) and Fe (Fig. 3.7C) contents from the core to the rim section. Despite the coupled variations, caution is advised for Fe content due to contamination from pyrite micro rhombs and/or fine clay mineral particles that could not be avoided during microprobe analyses;
- Each of the ten crystals (crystals B, C, H, I, J, K, L, M, N, O; total of 15 crystals were documented) that have available data from core and rim section shows distinct decrease in Sr (Fig. 3.7D) and Na (Fig. 3.7E) contents from the core to the rim section;
- Yttrium (Fig. 3.7F), measured alongside other trace elements in the ten crystals that have available data from core and rim section, shows distinct decrease from the core to the rim section in each of seven (crystals B, H, I, K, L, N, O) crystals. On the other hand, REEs was measured separately from other trace elements and has data from five crystals (crystals A, B, C, D and E). Each of these crystals, except crystal A, has ∑REE (Fig. 3.7G) data from core and rim section and similar to Y, the ∑REE exhibits decrease in composition from core to the rim section.

Consistent with the compositional variation in DZC, of the 18 crystals documented for IZC crystal facies, four (crystals D, H, M, P) of fifteen (crystals A, B, C, D, E, G, H, J, K, L, M, O, P, Q, R) crystals that have data from core and the rim sections show systematic variations, but with a fewer suite of elements, exhibited by increase in Mg and Mn (Figs. 3.9A and B respectively) and decrease in Sr and Na (Figs. 3.9D and E, respectively).

Independently, Mg shows subtle (<25%) increase from the core to the rim section whereas the trace elements, when grouped according to Mn and Fe, Sr and Na and Y and ∑REE, exhibit the following trends:

- The Mn (Fig. 3.9B) and Fe (Fig. 3.9C) compositions are mostly decoupled showing opposite core-to-rim trends. Fe composition in twelve (crystals A, B, C, D, E, H, K, L, O, P, Q, R) of the fifteen (crystals A, B, C, D, E, G, H, J, K, L, M, O, P, Q, R) crystals that have data from core and the rim sections appears to decrease from the core to the outermost band of the rim section. However, data from most crystals show that the Fe composition distinctly increases to Zone 4 of the rim section before depletion in the outermost band of the crystal. On the other hand, seven (crystals C, D, H, L, M, P, R) of the fifteen crystals that have data from core and the rim sections exhibit increasing (most common trend) Mn composition from the core to the rim section. Only two (crystals A and E) of the crystals show decreasing trend while the rest show similar and subtle (<25%) difference in composition from the core to the rim sections;
- Eight (crystals B, C, D, G, H, J, M, P) of the fifteen (crystals A, B, C, D, E, G, H, J, K, L, M, O, P, Q, R) crystals that have data from core and the rim sections exhibit coupled decrease in Sr (Fig. 3.9D) and Na (Fig. 3.9E) composition from the core to the rim section;
- The Y (Fig. 3.9F) and REEs (Fig. 3.9G) compositions are intricately coupled in core-to-rim trend, despite being measured as separate packages. Eight crystals (crystals A, B, C, D, E, G, O, R) have Y and ∑REE values from both core and rim

sections. Except crystal D, these crystals show distinct decrease in Y as well as REE from core to rim section. Individually, Y composition (Fig. 3.9F) decreases from core to rim in all the fifteen crystals (crystals A, B, C, D, E, G, H, J, K, L, M, O, P, Q, R) that have data from core and the rim sections, except in crystals D and H (Fig. 3.9F). More so, except crystals D, all the eight crystals (crystals A, B, C, D, E, G, O, R) that have REE values from both core and rim sections show decreasing ∑REE from core to rim (Fig. 3.9G).

Mean values of the respective major and trace element from each zone are summarized in Table 3.1. It shows that overall, the DZC (Figs. 3.2B and 3.3) and IZC (Figs. 3.4B and 3.5) crystal facies also exhibit distinct and broadly similar core-to-rim compositional trends (Figs. 3.8 and 3.10 respectively). In both DZC and IZC crystal facies, Mg subtly increases from the core (89,543±3275 ppm and 88,018±7112 ppm, respectively) to the rim (93,153±7091 ppm and 90,147±6014 ppm, respectively; Table 3.1, Figs.3.8A and 3.10A respectively). In DZC crystal facies, Mn composition (Table 3.1 and Fig. 3.8B) increases from the core (42 ±10ppm innermost core, Zone 1) to the rim (70 ±8 ppm in outermost cortex, Zone 5) section and Fe composition (Table 3.1, Fig. 3.8C) also increases from core (944±532 ppm) to the rim (4155±1295 ppm). In counterpart IZC crystal facies, Fe shows a distinct ‘cap’ distribution pattern across the crystal transect (Fig. 3.10C) while Mn subtly increases (compared to DZC; Fig. 3.10B) from core (47±5 ppm) to rim (59±23 ppm). As shown in Table 3.1, the Fe contents increase from Zone 1 in the core (1,519±676 ppm) to Zone 4, the connecting band between core and rim section

(2,265±837 ppm) and decreases to the outermost cortex in the rim section (Zone 5= 1,050±673 ppm).

Table 3.1: Summary of statistics of SIMS analytical results: Note that for Main Brook locality: Zones 1-3 represent the crystal core section while Zones 4-5 represent the crystal rim section. The number of values (*n*) includes means of duplicate points where more than one SIMS spots are located in the same zone. See Tables 3.A4A-C in appendix section for the individual intra-crystal SIMS measured data points. See appendix section for data repository.

Zone ID	Mg (ppm)	Na (ppm)	Sr (ppm)	Mn (ppm)	Fe (ppm)	Y (ppm)	∑REE (ppm)
Distinctly Zoned Core DZC crystal facies (P-154, Main Brook locality)							
1	89,543±3275 (*n*=12)	292±166 (*n*=12)	210±37 (*n*=12)	42±10 (*n*=12)	944±532 (*n*=13)	0.76±0.37 (*n*=12)	21±9 (*n*=6)
2	89,291±3144 (*n*=7)	382±213 (*n*=7)	207±20 (*n*=7)	38±10 (*n*=7)	972±476 (*n*=6)	1.01±0.44 (*n*=7)	19±12 (*n*=4)
3	90,003±3193 (*n*=12)	327±195 (*n*=12)	202±53 (*n*=12)	59±18 (*n*=12)	1,647±1687 (*n*=11)	0.48±0.30 (*n*=12)	9±1.2 (*n*=6)
4	91,201±3418 (*n*=9)	177±72 (*n*=9)	124±57 (*n*=9)	64±11 (*n*=9)	2,885±1633 (*n*=8)	0.43±0.13 (*n*=9)	11±0.75 (*n*=2)
5	93,153±7091 (*n*=8)	196±84 (*n*=7)	94±12 (*n*=8)	70±13 (*n*=8)	4,155±1295 (*n*=9)	0.48±0.15 (*n*=8)	13±1.1 (*n*=3)

Zone ID	Mg (ppm)	Na (ppm)	Sr (ppm)	Mn (ppm)	Fe (ppm)	Y (ppm)	∑REE (ppm)
Indistinctly Zoned Core IZC crystal facies (P158, Main Brook locality)							
1	88,018±7112 (*n*=20)	167±112 (*n*=20)	105±28 (*n*=20)	47±5 (*n*=20)	1,519±676 (*n*=20)	0.48±0.36 (*n*=20)	11.21±1.56 (*n*=10)
4	89,944±7438 (*n*=14)	152±91 (*n*=14)	78±11 (*n*=14)	53±10 (*n*=14)	2,265±837 (*n*=14)	0.33±0.20 (*n*=15)	8.61±0.74 (*n*=7)
5	90,147±6014 (*n*=17)	80±57 (*n*=17)	82±20 (*n*=17)	59±23 (*n*=17)	1,050±673 (*n*=17)	0.23±0.22 (*n*=17)	8.46±4.46 (*n*=9)

Zone ID	Mg (ppm)	Na (ppm)	Sr (ppm)	Mn (ppm)	Fe (ppm)	Y (ppm)	∑REE (ppm)
Unzoned dolomite crystal facies (6-172, Daniel's Harbour locality)							
Core (Zone 1)	98,293±2330 (*n*=14)	109±75 (*n*=14)	42±6 (*n*=14)	170±57 (*n*=14)	615±308 (*n*=15)	0.22±0.05 (*n*=14)	10.39±2.13 (*n*=12)

Rim (Zone 2)	97,057±5677 (*n*=12)	121±115 (*n*=12)	36±8 (*n*=12)	200±79 (*n*=12)	878±688 (*n*=13)	0.16±0.07 (*n*=12)	10.73±2.82 (*n*=12)

Table 3.2: Comparison of SIMS measured data with that of bulk analysis excluding Fe because of contribution of pyrite rhombs and fine clay particles to the ICP-MS bulk (wet) analyses.

Analytical Method	Carbonate Formation	Mg	Mn (ppm)	Sr (ppm)
SIMS(current study)[1]	Boat Harbour Formation, Main Brook	90,599 (ppm)	54	125
Bulk Analyses (ICP-MS)[2]	Boat Harbour Formation, Daniel's Harbour	101,295 (ppm)	185	39
	Boat Harbour Formation, Main Brook	39 (wt.%)	86	169
	Boat Harbour Formation, Daniel's Harbour	45 (wt.%)	156	45
SIMS Analyses	Devonian Nisku Formation Alberta[3]	n/a	65	40
Bulk Analyses	Modern 'Island' dolomites[4]	n/a	20-200	156-200

[1] Average composition of elements across the analyzed dolomite crystal transects.
[2] Mean values as contained in Olanipekun et al., 2014.
[3] Machel et al., 1997.
[4] Budd, 1994. This is a range of data from various depositional environments.

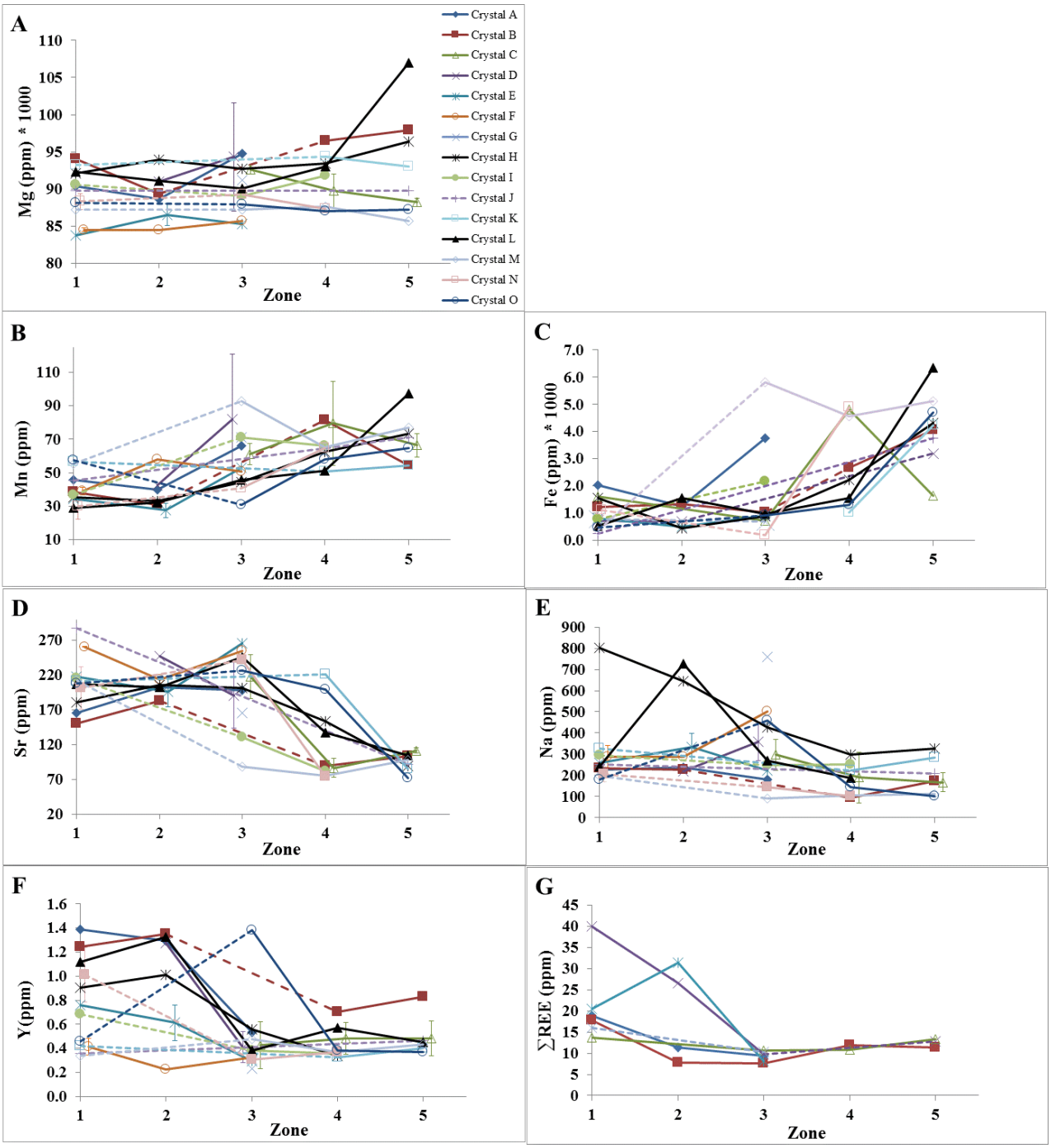

Figure 3.7: Plot of (A) Mg, (B) Mn, (C) Fe, (D) Sr, (E) Na, (F) Y, and (G) ∑REE concentrations of individual crystal measured from (DZC; Sample P-154 from Main Brook, depth 154m) each crystal zone, showing their trends from core (Zone 1) to rim

(Zone 5). The error bars are standard deviations (1σ) of mean values for zones that have more than one data point. See appendix section for data repository.

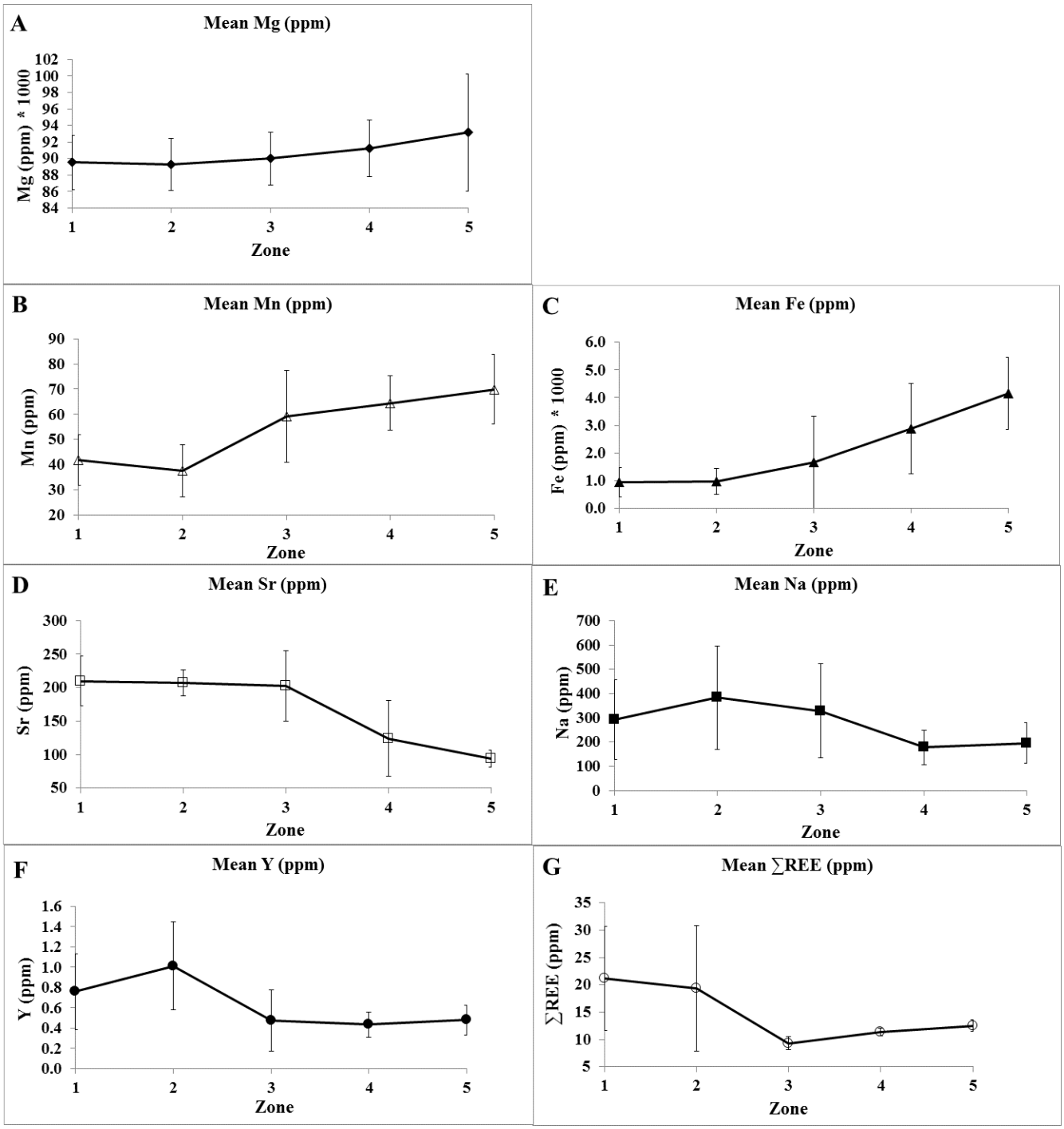

Figure 3.8: Plot of mean contents of (A) Mg, (B) Mn, (C) Fe, (D) Sr, (E) Na, (F) Y, and (G) ∑REE concentrations measured from (DZC; Sample P-154 from Main Brook, depth

154m) each of the crystal facies' zone showing their trends from core (Zone 1) to rim (Zone 5). Error bars (1σ) are also displayed. See appendix section for data repository.

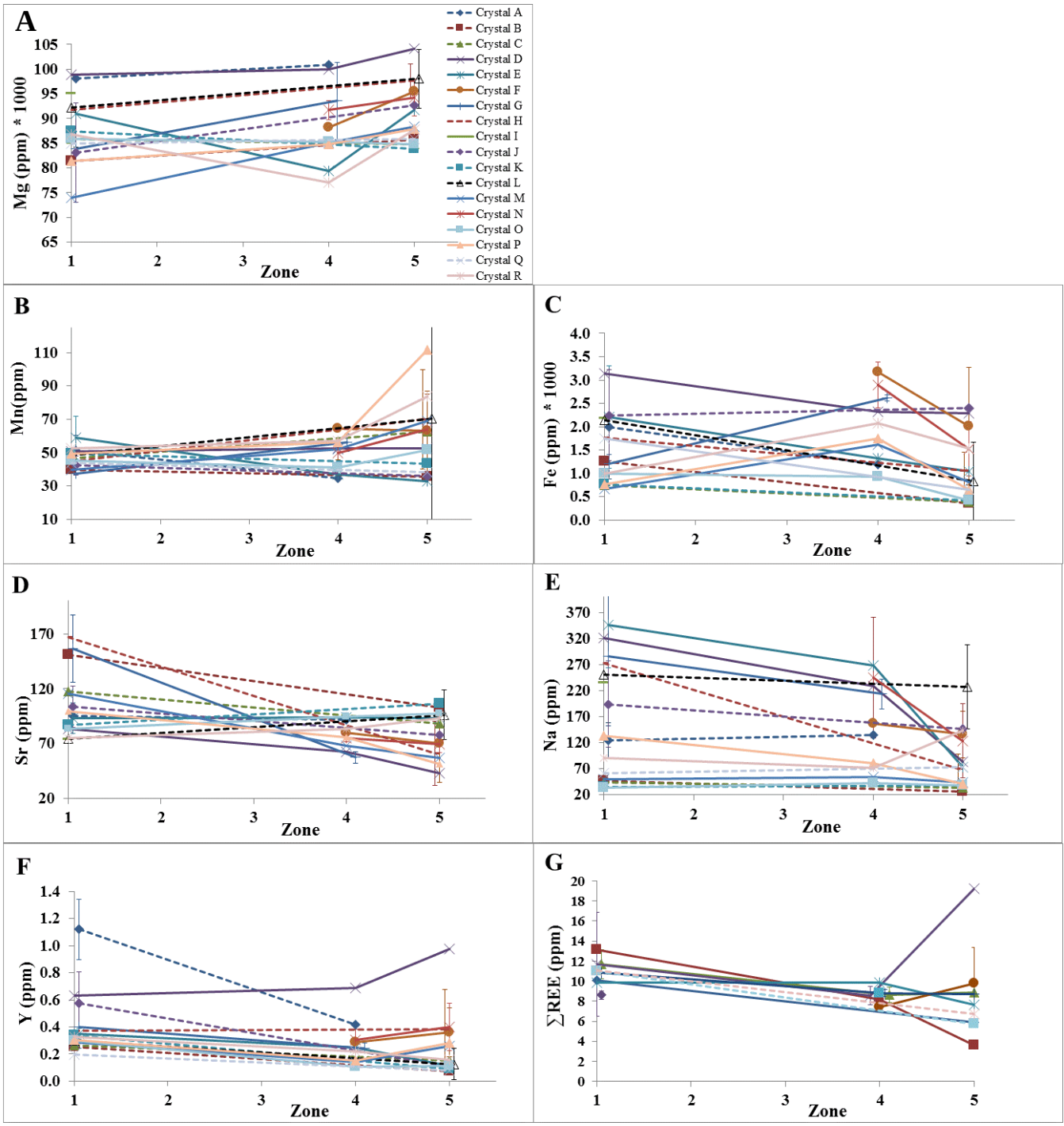

Figure 3.9: Plot of (A) Mg, (B) Mn, (C) Fe, (D) Sr, (E) Na, (F) Y, and (G) ∑REE concentrations of individual crystal measured from (IZC; Sample P-158 from Main

Brook, depth 158m) each crystal core (Zone 1), transitional (Zone 4) and outermost cortical zone (Zone 5) zones. They show their trends from core (Zone 1) to rim (Zone 5) section. The error bars (1σ) are standard deviations of the mean values for zones that have more than one data point. See appendix section for data repository.

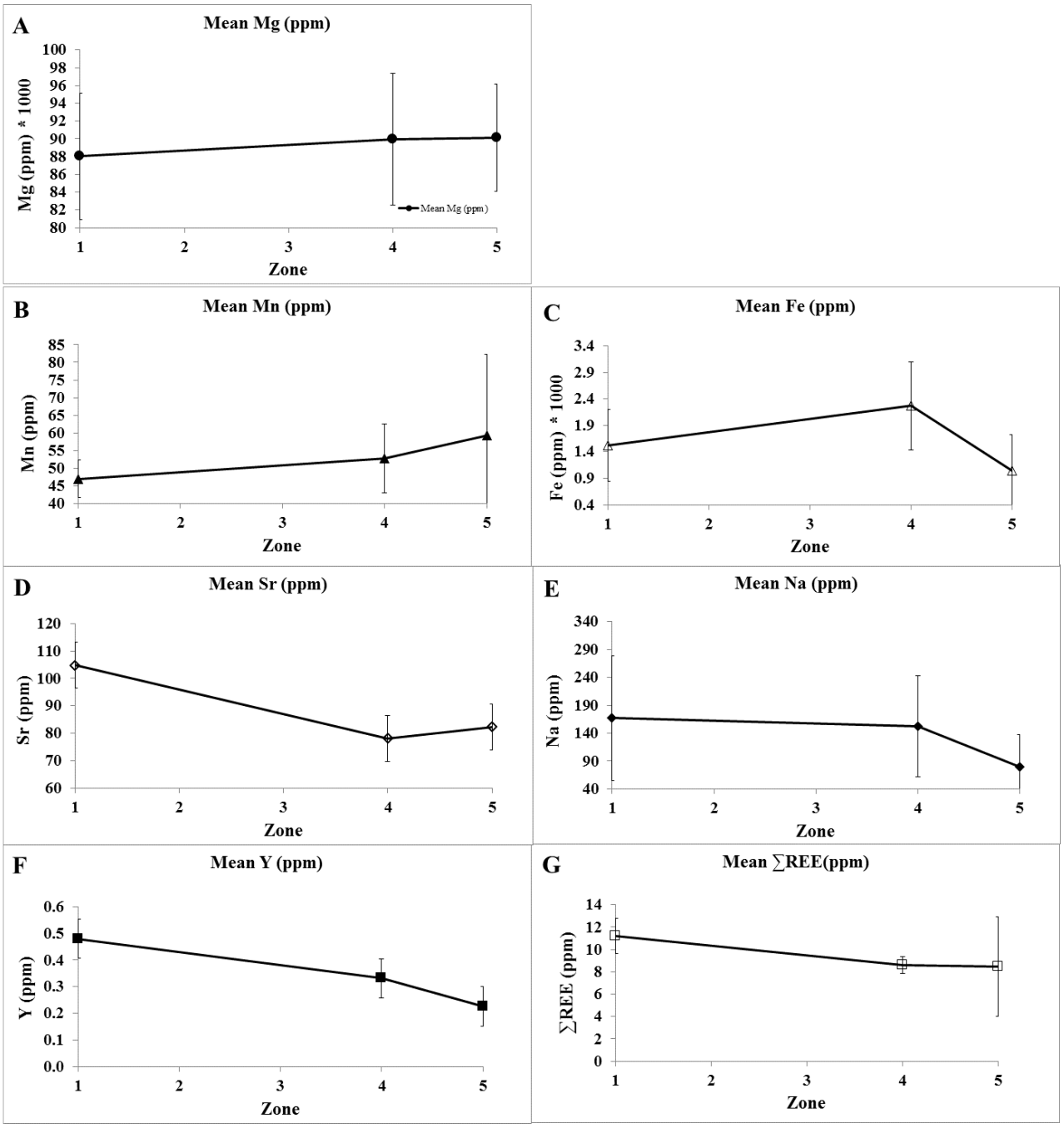

Figure 3.10: Plot of mean values of (A) Mg, (B) Mn, (C) Fe, (D) Sr, (E) Na, (F) Y, and (G) ∑REE concentrations measured from (IZC; Sample P-158 from Main Brook, depth 158m) each of the facies' crystal zone showing the trends from core (Zone 1) to rim

(Zone 5) section. Error bars (1σ) are also displayed. See appendix section for data repository.

Unlike the broadly ascending Mg, Mn and Fe core-to-rim trend in DZC and IZC, Table 3.1 shows that the Sr in DZC (Fig. 3.8D) and IZC (Fig. 3.10D) decreases from the core (210±37 ppm at the innermost core, Zone 1 in DZC; 105±28 ppm at Zone 1 in IZC) to the rim (94±12ppm at the outermost cortex, Zone 5 in DZC and 82±20 ppm at Zone 5 in IZC). Likewise, Na (Fig. 3.8E) in DZC also decreases from the core to the rim (292 ±166ppm at the innermost core, Zone 1; 196±84ppm at the outermost rim Zone 5; Table 3.1). Similarly, IZC crystal facies shows core-to-rim decreasing trend (167±112 ppm for Zone 1 and 80±57 ppm for Zone 5; Fig. 3.10E; Table 3.1).

In the same vein, in DZC, the Y (0.76±0.37 ppm at innermost core in Zone 1; 0.48±0.15 ppm in the rim at Zone 5, Table 3.1; Fig. 3.8F) and ∑REE (21±9 ppm at innermost core in Zone 1; 13±1.1 ppm at rim in Zone 5; Table 3.1; Fig. 3.8G) decrease from the core to the rim. This trend is also observed in Y and ∑REE of IZC (Fig. 3.10F and G respectively) where mean Y compositions in core and rim sections are 0.48±0.36 ppm and 0.23±0.22 ppm, respectively (Table 3.1) and ∑REE compositions in core and rim sections are 11.21±1.56 ppm and 8.46±4.46 ppm, respectively; Table 3.1).

Major and trace element compositions of CL unzoned dolomite crystals at Daniel's Harbour (Fig. 3.6A, Table 3.1, Table 3.A4C in appendix section), where the Boat Harbour Formation is completely dolomitized, did not exhibit any systematic and significant and at times show inconclusive variations (Fig. 3.11) unlike their zoned Main

Brook counterparts where the formation is partially dolomitized. Compared with their zoned Main Brook counterparts, the uniqueness of this crystal facies is its greater number of crystals that show similar to subtle (<25%) variations found in core-to-rim trace elements compositions.

Except in crystals G and J, the twelve crystals (crystals A, B, C, D, G, H, I, J, K, L, M, O) with data from cloudy core and clear rim sections have distinct similarity in the Mg composition of the crystal sections (Fig. 3.11A).

Subtle (<<25% in most cases) difference in core-to-rim Mn and Sr compositions is the most common trend observed in the twelve crystals that have data from core and rim sections (crystals A, B, C, D, G, H, I, J, K, L, M, N, O). Of the twelve crystals, the trend was exhibited by eight (crystals A, C, G, H, J, L, M, O) for Mn (Fig. 3.11B) and also for Sr (crystals C, D, H, I, K, L, M, O; Fig. 3.11D). Unlike in zoned Main Brook counterparts, Fe (Fig. 3.11C) is strongly decoupled from Mn in unzoned dolomite crystal facies at Daniel's Harbour. Only two (crystals D and I) of eleven crystals (crystals A, B, D, G, H, I, J, K, L, M, O) that have both Mn and Fe data show coupled (increasing in both) trend while the rest is strongly decoupled. Furthermore, considering Fe (Fig. 3.11C) independently, eight (crystals A, D, E, G, H, I, K, L) of the thirteen (crystals A, B, D, E, F, G, H, I, J, K, L, M, O) crystals that have Fe data show an increasing core to rim trend in its composition.

Sodium (Fig. 3.11E) is also decoupled from strontium (Fig. 3.11D) unlike in the zoned dolomite crystals from Main Brook. It shows decreasing core-to-rim trend in five crystals

(crystals B, J, K, M, O) out of twelve crystals (crystals A, B, C, D, G, H, I, J, K, L, M, O) and subtle core-to-rim trend in four (crystals A, G, H, L) of the twelve crystals. Taken together, among the ten crystals (crystals A, B, D, G, H, I, J, K, L, M) in which both Y (Fig. 3.11F) and ∑REE (Fig. 3.11G) values from core and rim sections are reported, three crystals (crystals I, L, M) show subtle variation while three crystals (crystals A, B, H) show decreasing core-to-rim trend. Trends are decoupled in others. Independently, Y decreases from core to rim in six (crystals A, B, C, G, H, O) of twelve crystals (crystals A, B, C, D, G, H, I, J, K, L, M, O) while it is subtle (<<25% difference) to similar in the remainder except in crystal D. Of the twelve crystals (crystals A, B, D, E, F, G, H, I, J, K, L, M), where ∑REE is reported, seven crystals (crystals D, E, F, G, I, L, M) were found to exhibit subtle intra-crystalline variation.

The lack of systematic and significant compositional core-to-rim variations is likewise depicted by the plot of mean values of the elemental compositions for each zone of the crystal facies (Fig. 3.12). The dolomite crystals have similar mean Mg concentrations with 98,293±2330 ppm and 97,057±5677 ppm at the cloudy core and clear rim, respectively (Table 3.1; Fig. 3.12A). The Sr concentrations (Table 3.1) is relatively low and shows subtle reduction from mean of 42±6 ppm at the cloudy core to 36±8 ppm at the clear rim (Fig. 3.12D), while Na composition (Fig. 3.12E) increases insignificantly from 109±75 ppm at the cloudy core to 121±115 ppm at the clear rim in contrast to its counterparts at Main Brook. The mean concentration of Y insignificantly decreases from 0.22±0.05 ppm at the cloudy core to 0.16±0.07 ppm at the clear rim (Table 3.1; Fig.

3.12F) of the crystal facies, while ∑REE is similar (10.39±2.13 ppm in core, 10.73±2.82 ppm in rim; Table 3.1; Fig. 3.12G) in both sections of the crystal facies.

However, Mn and Fe concentrations show more conclusive trend but still less significant compared with their counterparts in zoned dolomite crystals from Main Brook. Relative to the zoned dolomite facies, the mean Mn concentration subtly increases from 170±57 ppm at the cloudy core to 200±79 ppm at the clear rim (Table 3.1; Fig. 3.12B). On the other hand mean Fe concentration show more significant increases from cloudy core to clear rim section (615±308 ppm and 878±688 ppm, respectively; Table 3.1; Figs. 3.12C).

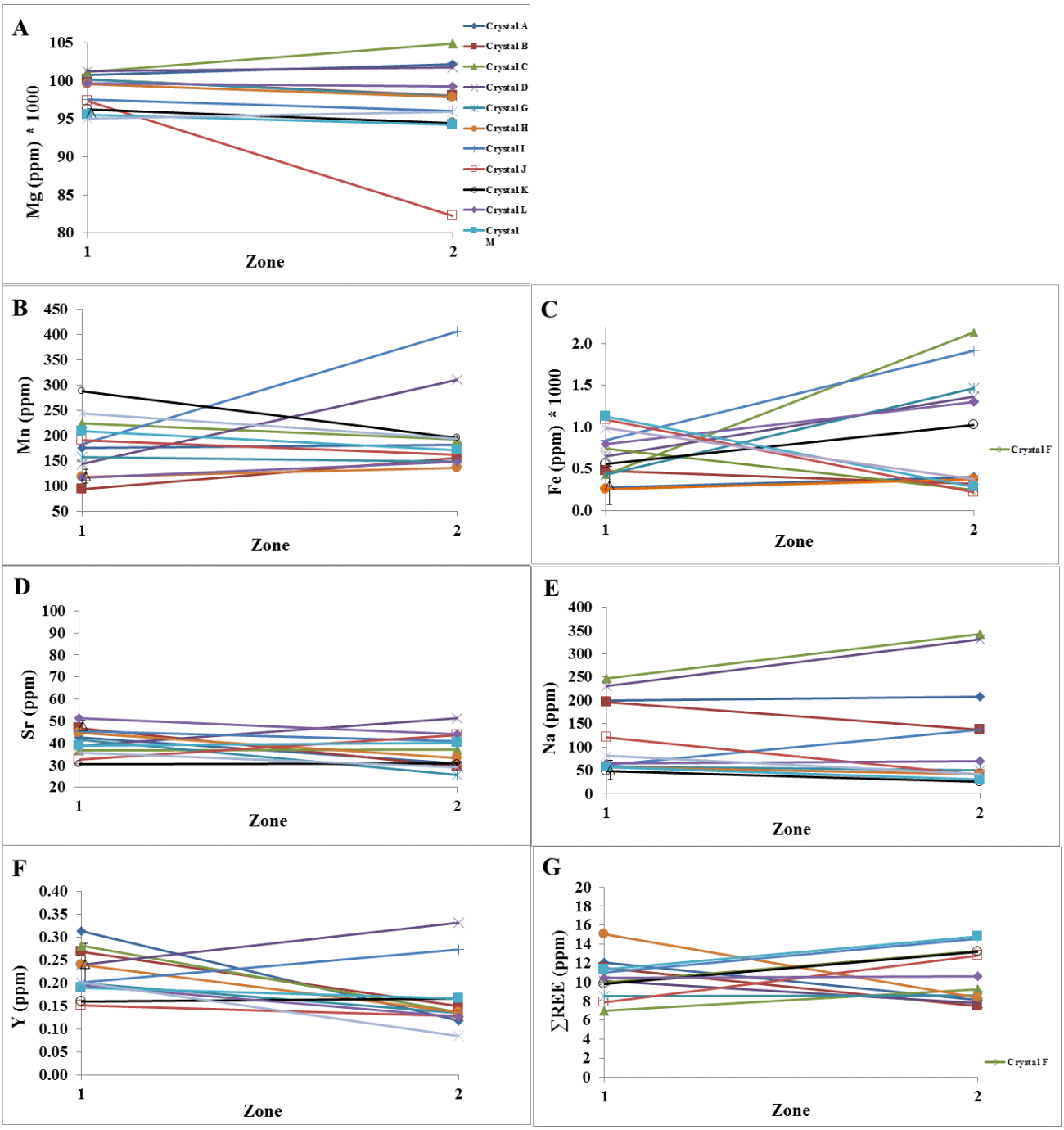

Figure 3.11: Plot of (A) Mg, (B) Mn, (C) Fe, (D) Sr, (E) Na, (F) Y, and (G) ∑REE concentrations of individual crystal measured from (Unzoned crystal facies; Sample 6-172 from Daniel's Harbour locality, depth 172 m) each of the crystals' cloudy core and

clear rim section showing the trends from core (Zone 1) to rim (Zone 2). The error bars are standard deviations (1σ) of mean values for zones that have more than one data point. See appendix section for data repository.

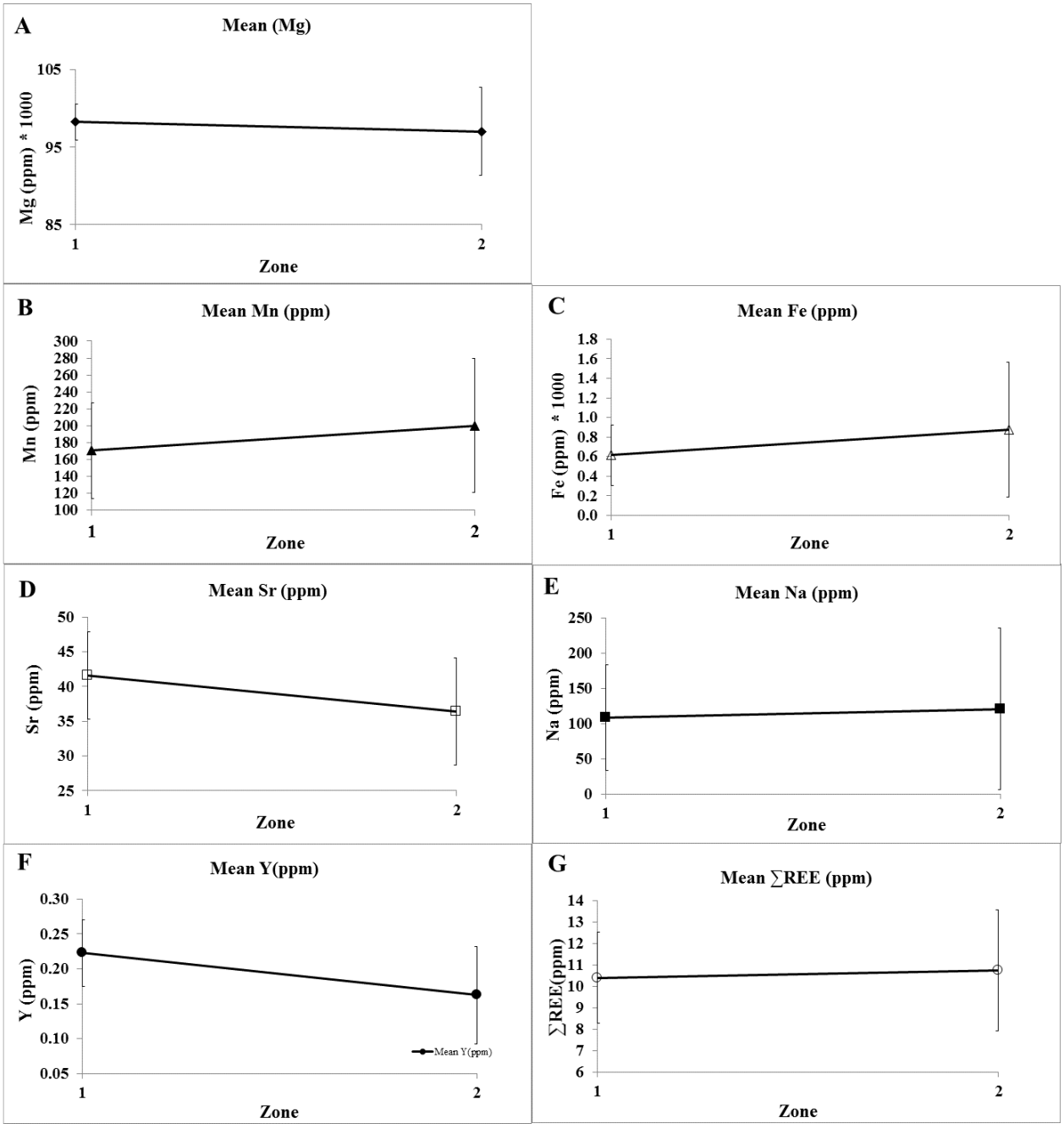

Figure 3.12: Mean plot of (A) Mg, (B) Mn, (C) Fe, (D) Sr, (E) Na, (F) Y, and (G) ∑REE concentrations measured from (Unzoned crystal facies; Sample 6-172 from Daniel's Harbour locality, depth 172 m) each of the crystals' cloudy core and rim section showing variations from core (Zone 1) to rim (Zone 2). Error bars (1σ) are also displayed. See appendix section for data repository.

The mean concentrations of all zones within both DZC and IZC crystal facies (Table 3.2) indicate that Mg (90,599 ppm) and Mn (54 ppm) are lower in Main Brook than in Daniel's Harbour (Mg = 101,295ppm; Mn= 185ppm). In contrast, the mean Sr concentration of all zones within the crystals (Table 3. 2) is higher in Main Brook (125 ppm) than in Daniel's Harbour (39 ppm). Compositions of Fe could not be compared objectively so as to avoid ambiguity because the bulk analyzed samples are vulnerable to contamination by pyrite.

3.5. DISCUSSION

SIMS data (Table 3.2) show that Mg and Mn compositions are higher and Sr concentration is much lower in dolomite crystals from Daniel's Harbour relative to their Main Brook counterparts. This trend is remarkably similar to that exhibited by bulk wet analytical (ICP-MS) results (Olanipekun et al., 2014) and also within the range of values reported by other sources (Table 3.2), thus supporting the reliability and consequently the interpretations of the current SIMS analyzed data. Furthermore, it is noteworthy that the zone identity tagging for each analyzed spot was done by examining SEM-CL (Main Brook locality samples) and plain light images (Daniel's Harbour locality samples) of sputtered areas of interest subsequent to the SIMS analyses to confirm the band that was sputtered for analytical measurements.

In general, dissolved trace elements in intervening pore fluid can be incorporated into precipitating minerals via: (1) impurities such as fluid or 'accidental' mineral inclusions, (2) sorption onto growing crystal surfaces, (3) occlusion in lattice defects, and (4) solid-solution substitution for a major element in the precipitated mineral (e.g., Land, 1980; Veizer, 1983; Banner, 1995; Budd, 1997) . The latter mechanism is considered the most important and better understood in carbonate diagenetic reactions (Morse and Mackenzie, 1990; Banner, 1995) and is controlled by partition coefficient (Pingitore, 1978; Morse and Mackenzie, 1990) of the respective element during crystal growth.

3.5.1. Distinctly zoned core (DZC) and indistinctly zoned core (IZC) dolomite crystal facies: Main Brook

Bulk analytical data (Olanipekun et al., 2014) have shown that the intermediate burial dolomite of Boat Harbour Formation at Main Brook is non-stoichiometric (~39 wt. % $MgCO_3$; Table 3.2) and poorly ordered (degree of order = ~0.56) compared to its counterpart at Daniel's Harbour which is nearly stoichiometric (~45 wt. % $MgCO_3$; Table 3.2) and better ordered (degree of order = ~0.74). This suggests that the Main Brook burial dolomite is thermodynamically unstable, thus has a higher drive for more episodes of recrystallization to more stoichiometric phase than its Daniel's Harbour counterpart (cf. Kaczmarek and Sibley, 2011).

Zoning, revealed under CL (Figs. 3.2B and 3.4B), is apparent evidence that the DZC and IZC dolomite crystal facies at Main Brook underwent series of recrystallization episodes in an attempt to improve their stoichiometry. Such zoning implies that the dolomite crystals likely equilibrated multiple times with the evolving pore fluid and that heterogeneous partition coefficient, HT-PC (Doerner and Hoskins, 1925; Curti, 1997) must have influenced elemental partitioning into the growing crystal. This accounts for the core-to-rim systematic compositional zoning (Figs.3.8 and 3.10, respectively) found in these crystal facies. To explain further, given the limited degree of openness and continuous water-rock interaction in a burial setting, evolution of local pore fluid should be expected. Consequently at slow crystal growth rate, common in a low temperature setting (<100^{o}C), in which the rate of diffusion of ions through the growing crystal is low (Curti, 1997), only the surface layer of the crystal is in equilibrium with intervening

solution at that growth instant. Notably there is paucity of two-phase fluid inclusions in samples from Main Brook (Olanipekun et al., 2014) suggesting less than 100^{o}C temperature of formation for the dolomite crystals.

DZC (Figs. 3.2B and 3.3) and IZC (Figs. 3.4B and 3.5) crystal facies co-exist within the same diagenetic setting and have the same concentric zoning pattern in CL. However, the key distinguishing factor that differentiates their growth process from each other is the extent of recrystallization, which in turn is a function of the extent of mineral-fluid interaction. It follows that the number of recrystallization episodes encountered by the dolomite is directly associated with the pore volume that hosts the pore dolomitizing fluid. If so, given DZC horizon's higher porosity (Fig. 3.2A; visual estimate), occluded by cement, it can be said that this facies has undergone several episodes of recrystallization such that it was formed in a localized high water-rock ratio setting (cf. Machel, 1990). In terms of the interphase boundary halo model (*sensu* Machel, 1990), this suggests that for DZC facies, the size of the dissolution boundary layer has been significantly reduced while that of the hydrodynamic boundary layer has been enlarged. This therefore implies that the composition of DZC crystal facies was controlled by that of the pore fluid.

On the other hand, the IZC crystal facies with lower porosity (Fig. 3.4A; visual estimate) has not undergone significant recrystallization hence was probably formed in low water-rock ratio setting. In support, the transitional red band, Zone 4 (Fig. 3.4B) has an irregular boundary that encases an otherwise 'embryonic' stage in the formation of euhedral dolomite rhomb of the core section (Zone 1). These suggest that although IZC crystal facies may have formed as replacive dolomite crystals, they have not been significantly

recrystallized relative to DZC crystal facies that has distinct and planar concentric zoning pattern for both core and rim sections. In terms of the interphase boundary halo theory (*sensu* Machel, 1990), such insignificant recrystallization indicates that the dissolution boundary layer is relatively larger than that of IZC and the hydrodynamic boundary layer (*sensu* Machel, 1990) is smaller than that of DZC. The major implication is that IZC composition, even though governed by HT-PC, is likely influenced by that of the host rock or at least a combination of host rock and fluid properties (*sensu* Machel, 1990). This also means that IZC equilibrated to lesser extent with the intervening fluid, which is interpreted to account for the less significant zoning in IZC relative to DZC crystal facies.

3.5.1.1. Magnesium (Mg)

Dolomite has been found to nucleate as a metastable calcian phase with subsequent "ripening" (Sibley, 1990; Nordeng and Sibley, 1994; Kaczmarek and Sibley, 2011) and discrete stepwise crystal growth from non-stoichiometric state ultimately to stable stoichiometric state (e.g., Warren, 2000; Kaczmarek and Sibley, 2011), with non-linear relationship to the Mg/Ca composition of the dolomitizing fluid (Kaczmarek and Sibley, 2011). This is denoted by an increase in concentration of Mg, at the expense of the concentration of Ca, as it occupies the Ca structural site of the dolomite crystal during the formation of dolomite.

The currently studied burial dolomite at Main Brook locality has been recrystallized beyond their primary sedimentary properties even though they are still non-stoichiometric (Olanipekun et al., 2014). Crystals of primary sedimentary dolomites commonly have enriched Ca and depleted Mg composition in their core sections (e.g., Jones, 2005). In

Main Brook locality, this signature must have been largely over-written during subsequent recrystallization episodes (e.g., Kupecz et al., 1993), leaving behind the subtle increase in Mg composition from core to rim section as seen in DZC and IZC dolomite crystal facies (Table 3.1). Furthermore, even though the observed trend appears subtle in character, it represents an important record of the recrystallization process. Notably, review of zoning characters in various minerals documented by Shore and Fowler (1996) likewise shows that the composition of major elements in zoned crystals exhibit much less variability than that of trace elements. In the same vein, Lumsden and Lloyd (1984) found that narrow range in major element compositions is accompanied by an otherwise significant variability in trace element compositions in a group of ancient dolomite samples they studied.

3.5.1.2. Manganese (Mn) and Iron (Fe)

Manganese and iron content of carbonate minerals is a measure of the redox state (redox potential) of the setting within which they are formed, as only reduced Mn and Fe ions can substitute for major divalent elements (Ca and Mg) in dolomite crystals (Veizer, 1983). Notably Fraser et al. (1989) found Mn and Fe zonations within dolomite crystals which they attributed to varying redox potential during the dolomite formation. The Mn and Fe compositions of dolomites, like other carbonates, are controlled by their respective partition coefficients, which are greater than unity (Veizer, 1983) and in turn depend on the activity of dissolved elements in the bulk solution (e.g., Veizer, 1983; Morse and Mackenzie, 1990). Progressive increase in reduction potential (Eh), consistent with changing pore fluid chemistry, at the local burial setting likely controlled the

concentrations of Mn and Fe available for partitioning in the pore fluid. In tandem with changing fluid chemistry, the increasing core-to-rim trend observed in DZC (Fig. 3.8B and C) and IZC (Fig.3.10B and C; though with a 'hat' shape Fe distribution pattern) dolomite crystal facies of Main Brook suggests that HT-PC influenced Mn and Fe incorporation into the growing dolomite crystals.

Alternatively, Mn, and by analogy Fe, partitioning into dolomite crystals favours Mg sites (Kretz, 1982; Lumsden and Lloyd, 1984; Morse and Mackenzie, 1990). Lumsden et al. (1989) showed that stoichiometric dolomites have higher Mn partition ratios than non-stoichiometric dolomites. Therefore, it can be said that increasing Mn (Figs. 3.8B and 3.10B) and Fe (Figs. 3.8C and 3.10C) from core to rim (Table 3.1) is as a result of increasing stoichiometry that typically accompanies successive recrystallization of dolomites (e.g., Kupecz et al., 1993). However, while this explains the lower Mn composition of whole dolomite crystals at Main Brook relative to those of Daniel's Harbour (Tables 3.1 and 3.2), the subtleness of intra-crystal core-to-rim variation in Mg composition of the DZC and IZC crystal facies does not account for the distinct increasing core-to-rim Mn and Fe compositions.

The compositional zoning of Mn and Fe within the dolomite crystals was likely controlled by the prevailing local redox condition, irrespective of their Mg compositions. This is because progressive burial of the formation during which the crystals grew, is known to favour increase in reduction potential of the burial fluids (e.g., Machel et al., 1997). The depletion in Fe content (Fig. 3.10C), even though decoupled in trend from Mn content (Fig. 3.10D), of the outermost cortex of the IZC crystal facies may be a result of a

shift in redox pattern possibly caused by a flux of oxidizing fluid through secondary porosity associated with disconformities within the Boat Harbour Formation (Knight et al., 2008). Lack of such trend in counterpart DZC (Fig. 3.8B for Mn and Fig. 3.8C for Fe) may be as a result of further recrystallization episodes in a locally more reducing setting.

3.5.1.3. Strontium (Sr) and Sodium (Na)

Strontium and sodium contents in different dolomite generations may be used to constrain the nature of their dolomitizing fluids, if contamination by solid inclusions that have high Sr (Banner, 1995) and Na concentrations (Land, 1980; Veizer, 1983; Budd, 1997) can be minimized. Given the SIMS technique used in the current study, the effect of the latter is considered insignificant, hence it can be said that the dolomitizing fluid's chemistry influenced the Sr and Na composition of the dolomite crystals sampled for SIMS analyses. In particular, Na in solid carbonate has been found to vary with Na^+ dissolved in solution, indicating degree of salinity of the dolomitizing fluid (Ishikawa and Ichikuni, 1984; Busenberg and Plummer, 1985; Oomori et al., 1985). Coupled variations of Sr and Na in dolomites, as also seen in zoned dolomite of the current study (Figs. 3.8D, E and Figs. 3.10D and E; respectively), further underscores the validity of Na for characterization of dolomites as usually done with Sr (e.g., Wogelius et al., 1992; Budd, 1997; Azmy, et al., 2008).

Crystals of the Main Brook dolomites (DZC and IZC crystal facies) show a general decrease in Sr and Na concentrations from the core to the rim (Figs. 3.8D, E for DZC and Figs. 3.10D, E for IZC).This suggests that the Sr and Na compositions in the dolomite crystals evolve with changes in their respective concentration or activity in the pore fluid

and thus, implies that the dolomitizing fluid was diluted with a fluid of lower salinity during crystal growth as would be expected from continuous dilution of seawater during burial. Possible source of reduced salinity is meteoric water ingress through secondary porosity associated with Boat Harbour disconformity (Knight et al., 2008).

Furthermore, the broad decrease in Sr from core to rim (Figs. 3.8D and 3.10D) could have been as a result of its partition coefficient (<1), which is affected by multiple factors such as concentration, reaction kinetics and temperature (Veizer, 1983; Banner, 1995; Malone and Baker, 1999). This could be associated with the concomitant increase in Mg composition that typically accompanies successively recrystallized dolomite crystals as Sr substitutes for Ca in carbonate minerals (Banner, 1995), if it is accepted that increasing Mg implies decreasing Ca composition. However, as explained for Mn and Fe trend in previous section, comparison of whole dolomite crystals at Main Brook relative and those of Daniel's Harbour (Tables 3.1 and 3.2) show this trend but the relatively subtle intra-crystal core-to-rim variation in Mg composition of the DZC and IZC crystal facies does not clearly account for the distinct Sr trend.

The mode of Na incorporation into dolomite is different from that of Sr. The disparity between the ionic charge of Na^{+}, Mg^{2+}, and Ca^{2+} suggests that substitution for a major divalent element will be difficult, instead Na is trapped in interstitial lattice positions during crystal growth (Ishikawa and Ichikuni, 1984; Busenberg and Plummer, 1985; Morse and Mackenzie, 1990). Thus, the composition of Na in the dolomite crystals should show decreasing trend during crystal growth as the salinity of the pore fluid decreases. The dolomite crystals' chemistry is therefore a reflection of the absolute

elemental concentration in their respective diagenetic fluids. Similarly, fluid type, rather than partition coefficient, is also fingered as the primary control on the Sr composition of dolomite (Wogelius et al., 1992).

3.5.1.4. Rare Earth Elements (REE) and Yttrium (Y)

There is a chemical similarity among the REE and Y because their partially filled inner 4f electrons are too shielded by outer electrons to allow significant chemical reactivity. More so, the implied reduced fractionation makes the REE concentrations reliable for the reconstruction of the geochemical composition of the parent dolomitizing fluids (Banner et al., 1988; Qing and Mountjoy, 1994; Nothdurft et al., 2004; Xuefeng et al., 2008; Kucera et al., 2009; Azmy et al., 2011). Earlier studies (e.g., Banner et al., 1988; Qing and Mountjoy, 1994; Nothdurft et al., 2004; Kucera et al., 2009; Azmy et al., 2011) applied bulk solution methods, which could cause erroneous interpretation of paragenesis. This is because they are vulnerable to contamination from REE and Y-rich clay minerals and other episodes of post depositional carbonate replacements particularly when as small as 1% shale contamination in dissolved samples could significantly alter the REE signature of a carbonate mineral (Nothdurft et al., 2004). SIMS analyses, utilized in the current study, minimized the possibility of REE and Y contamination. Nevertheless, REEs concentrations obtained from bulk analyses of the same samples in the current study are unexpectedly similar to those from their SIMS analyzed counterparts (Table 3.2), which suggests that the examined dolomites are ‘pure’ and contain very insignificant REE contribution from clastic inclusions.

REE and Y concentrations are generally more enriched in fluids derived from terrestrial environment (e.g., meteoric) relative to those from marine environment (e.g., Fleet, 1984; Azmy et al., 2011). This is because the bulk of REEs are incorporated into terrigenous secondary minerals such as clays (Fleet, 1984) and transported in river water with eventual deposition in seawater (Fleet, 1984; Alibo and Nozaki, 2000). More so, McLennan (1989) presented REEs concentrations (his Table 3) of natural waters which indicate that the total REE concentrations of river water is more than one order of magnitude higher than that of seawater. Given that diagenetic fluids in burial environments have contributions from meteoric environment, it would be expected that there would be REE and Y enrichment in the rim of crystals that were precipitated in a deeper burial environment, relative to their cores.

On the contrary, zoned dolomite crystal facies of Main Brook (DZC and IZC), interpreted to have formed in a fluid dominated setting, contain lower Y and REE composition in their rims than in their core sections (Figs. 3.8F and G respectively; cf. Xiaolin et al., 2009). This localized disparity suggests that the rim and the core are formed from fluids of different compositions and that the formation of the core and rim sections were separated in time. This is a key finding in light of previous studies that concluded that recrystallization of dolomites does not alter the REE signature of their precursor carbonate minerals (Banner et al., 1988; Qing and Mountjoy, 1994). However, while the results of Banner et al. (1988) did not yield significant difference between the REE signature of recrystallized and earlier formed dolomite, they found evidence of REE

enrichment of the intervening pore fluid in associated carbonate cements formed in vugs and solution cavities.

The diagenetic fluid that formed the rim was likely low in REE and Y concentrations. Compared to the fluid that formed the core, the diagenetic pore fluid might have been diluted with a fluid of lower salinity such that the cortices of the crystals have lower REE and Y compositions (Sholkovitz and Szymczak, 2000). This is consistent with lower Sr and Na concentrations in the rim, which is interpreted to be a result of reduced salinity in the evolving pore fluid. In support of the salinity factor, the results of Xiaolin et al. (2009), show core-to-rim increase in REE compositions of their diagenetic dolomite crystals (vice versa in the current study) which was attributed to relatively higher salinity in the diagenetic dolomitizing fluid that formed the rim of their dolomite crystals.

In addition to the factors governing the bulk solution concentration of REEs, it can be inferred from the mode of REE partitioning into calcite (Zhong and Mucci, 1995) and their role during alteration of albites (Klinkhammer et al., 1994) that REEs partitioning into dolomite may be influenced by the Ca^{2+} composition of the growing dolomite crystals, given the similarity in ionic sizes between Ca^{2+} and REE $^{3+}$. Of course during incorporation, the charge difference between REEs and Ca may be compensated for by Na^{+} incorporation (Zhong and Mucci, 1995). The burial dolomite of the current study has been recrystallized, with implied concomitant decrease in Ca believed to complement an increase in Mg. Even though this trend is marginally noticeable in the zoned dolomite crystals, Na still shows a distinct decrease from core to rim section (Fig. 3.8E) suggesting

that these factors may have contributed to the decrease in Y and REE from the core to the rim section (Figs. 3.8F and G respectively).

In IZC crystal facies, Y decreased with higher magnitude than the ∑REE (Figs. 3.10F and G) from the core to the rim section. The ∑REE trend is likely not reaction controlled because the interpreted low water-rock ratio setting of IZC formation and consequent state of disequilibrium condition imply that REE concentration in the fluid and the rock may not be properly mixed.

In all, clues from compositional zoning character of DZC and IZC have enabled better understanding of their crystal growth conditions. However it is acknowledged that standard errors may be relatively high in few data points (Figs. 3.7 and 3.9; Table 3.1). This is likely due to the varying influence of sector zoning with respect to specific partitioning ion within the individual crystals. Paquette and Reeder (1990), Paquette and Reeder (1995) and Reeder and Prosky (1986) have found, in calcite and dolomite crystals respectively, significant variations in partition coefficients of Sr^{2+}, Mn^{2+} and Mg^{2+} from crystal face to crystal face. However, sector zoning did not control the overall trend in elemental partitioning as analyzed crystals exhibit concentric luminescent zoning pattern. In summary, the variations across the crystal zones indicate that crystal growth occurred in discrete phases, with the trace elements compositions controlled by the partition coefficient of the respective element as well as their concentrations in the evolving pore fluid during discrete crystal growth phases.

3.5.2. Unzoned dolomite crystal facies: Daniel's Harbour

Unlike Main Brook dolomite crystals, most of the analyzed elements did not show significant or systematic core-to-rim compositional variation in the unzoned dolomite crystal facies of Daniels' Harbour (Table 3.1; Fig. 3.12). Distinct similarity observed in Mg composition of core and rim sections of the unzoned dolomite crystal facies is interpreted to be an indication that evidence of increasing stoichiometry within the crystals has been completely obliterated, most likely due to more iterative episodes of recrystallization during its crystal growth than its Main Brook counterpart. (Fig. 3.12A; Table 3.1). These multiple episodes of recrystallization of the crystal facies at this locality must have resulted in stoichiometry (Olanipekun et al., 2014) and relatively higher Mg content of the whole dolomite crystals (Tables 3.1 and 3.2).

The SIMS measurements (Table 3.1) suggest that Sr and Na lack zoning or are poorly zoned within the crystals. Likewise Mn compositions in the unzoned dolomite crystal facies have relatively insignificant core-to-rim variability but Fe shows consistent increasing core-to-rim trend for the crystal facies. Note that Na (Fig. 3.11E) and Fe (Fig. 3.11C) data are more widely scattered compared to those of their counterparts. This is not unusual given the fact that results of a similar earlier microprobe study on dolomites (Riciputi et al., 1994; their Table 2) showed wide variations in trace elements at very fine scale. Similar to the result obtained from the unzoned crystal facies of the current study, the wide variations are more noticeable in Na and Fe compositions of their dolomite samples while reported Sr (Fig. 3.11D) and Mn (Fig. 3.11B) are better tightly clustered. Na and Fe are prone to contamination from, for instance, halite inclusions and pyrite

rhombs respectively which may bear some influence on results of their measurements. The increasing core-to-rim trend observed in Fe and which is decoupled from Mn can be explained by two possible factors. If contamination from pyrite did not greatly influence the result, such trend could be an indication that Fe is less mobile than Mn (Lumsden and Lloyd, 1984) and thus preserved the trend associated with previous recrystallization episodes (i.e., its precursor). On the other hand, local changes in redox potential of the dolomitizing fluid in microenvironment could have differently affected compositions of Mn and Fe in the intervening fluid (see Fraser et al., 1989).

As for Y and ∑REE, considered independently, subtle to similar is the dominant trend in ∑REE composition for the crystals (Figs. 3.11G and 3.12G), while decreasing trend is marginally the most common trend followed by subtle to similar core-to-rim trend in Y (Figs. 3.11F and 3.12F) composition of the studied crystals. It is noteworthy that core-to-rim trends in Y and ∑REE compositions of the crystals are mostly decoupled (Fig. 3.11F and Fig. 3.11G respectively), which is unusual as there are no factors in the currently studied system known to be responsible for fractionation of these geochemically similar elements.

Importantly, the relatively homogeneous zoning revealed by CL has indicated, in a broad sense, a lack of significant variability in trace element distribution within the crystals of unzoned dolomite. In support, the SIMS data show that overall, subtle to similar core-to-rim trend is the prevailing compositional trend in the unzoned dolomite crystal facies from Daniel's Harbour. This lack of or poor intra-crystalline compositional zoning (Fig. 3.6B) is an indication that homogeneous partition coefficient, HM-PC (Henderson and

Kracek, 1927; Curti, 1997), dominantly controlled elemental partitioning during crystal growth. Therefore, it is suggested that the whole crystal, in its present form, was most likely in thermodynamic equilibrium with the pore fluid and thus grew as a single episode of dolomitization (or recrystallization). Such growth condition may be a result of relatively high crystal growth rate compared to that of the Main Brook dolomites. The interpretation is supported by possible high rate of diffusion of reactants as implied by a relatively high estimated minimum formation temperature for the dolomite crystals (>100^{o}C; Olanipekun et al., 2014).

Comparison of whole crystals of the unzoned crystal facies with that of zoned crystal facies lends good or even better support to the concepts advanced for intra-crystalline variations in the currently studied dolomites. The higher Mg composition of the unzoned crystal facies relative to that of zoned crystal facies of Main Brook accounts for the higher Mn composition of its whole dolomite crystals relative to that of the Main Brook dolomites. This is consistent with the conclusion of Lumsden et al. (1989), which averred that increasing stoichiometry of dolomites yields an increase in Mn. This is not shown in Fe composition (Tables 3.1 and 3.2) because its trend, by implication, should accompany that of Mn. As explained previously, pyrite contamination and complex variations in redox potential of the dolomitizing fluid could have influenced the reported Fe results. In addition, the relatively higher Mg composition in the unzoned crystal facies Daniel's Harbour dolomite crystals is also likely responsible for its associated lower Sr and Y and ∑REE (within the margin of error) compositions relative to those in the zoned crystal facies of Main Brook (Tables 3.1 and 3.2).

On the other hand, Na contents are similar to those in the core sections of the zoned dolomite crystal facies of Main Brook (Table 3.1). Even though this suggests similar level of salinity for the pore fluids, their sources of salinity are likely different. Lastly, as shown in Table 3.1, Na composition of the zoned dolomites decreases from core to the rim section. It is believed that the earliest formed core section is likely a product of a pore fluid that has a high seawater component, which was largely reduced as a result of progressive burial prior to the formation of the unzoned dolomite crystal facies later in the (higher temperature) burial setting.

3.5.3. Implications

SIMS has enabled fine scale and high resolution analyses of dolomite crystal traverses that could not be isolated in previous micro-sampling-based studies that employed ICP-MS analytical techniques. A key finding in the results obtained from SIMS is that episodes of dolomitization exist within individual crystals as much as it does among dolomite crystal populations. For the zoned crystals (DZC and IZC crystal facies), the data reveals decreasing trend from core to rim for Sr (Figs. 3.8D and 3.10D) while Mg (Figs. 3.8A and 3.10A) and Mn (Figs. 3.8B and 3.10B) show an opposite trend. The same trend was also noticeable on the regional and bed scales.

On the regional scale, burial dolomites of partially dolomitized Boat Harbour Formation at Main Brook contain higher Sr concentration, lower Mg and Mn than in their counterparts from the completely dolomitized section in Daniel's Harbour (Olanipekun et al., 2014; Table 3.2). Similarly, the core–to-rim trend found in dolomite crystal facies from Main Brook is also noticeable on the bed-scale dolomitization study in the same

locality. The bed-scale study shows that near-surface to shallow burial early dolomite had higher Sr and lower Mg compositions (228±30ppm and 35±2 wt. %, respectively) than the successive mid-burial dolomites (169±90ppm and 39±2 wt. %, respectively; Olanipekun et al., 2014). Likewise, the currently studied dolomite crystal facies were initially formed as primary dolomite with subsequent recrystallization to burial dolomite and the comparison of data from their earlier formed core section to their later formed rim section suggests that their earlier form had higher Sr and lower Mg. This could not be shown for Mn composition as it is reportedly lower in burial dolomites (86±28ppm) than in early dolomite (104±32ppm) of the formation due to availability of Mn in the diagenetic setting (see Olanipekun et al., 2014).

This study also shows better understanding of the mechanism of dolomite crystal growth during dolomitization in natural setting. Especially, the multiple conditions of crystal growth revealed in this study implies that the state of thermodynamic equilibrium needs to be established prior to selecting crystal zones for analyses in the study of cement stratigraphy. The study also supports the notion that correlation of crystal zones over a km-wide region as has been previously advanced (e.g., Vuillemin et al., 2011) may be too optimistic in the investigation of cement stratigraphy (e.g., Machel, 1990) of sedimentary sequences.

3.6. CONCLUSIONS

- Three crystal facies were identified in the Ordovician Boat Harbour Formation of western Newfoundland, Canada.
- Distinctly and indistinctly zoned core dolomite crystal facies are zoned crystal facies found in Main Brook while the unzoned dolomite crystal facies occur in Daniel's Harbour.
- Distinctly zoned core crystal facies has undergone multiple recrystallization episodes while indistinctly zoned core, in the same diagenetic setting, on the other hand has not.
- Geochemically zoned DZC and IZC crystal facies of Main Brook can be interpreted as crystals that grew at relatively slower rate than the rate at which the pore fluid's chemistry changed whereby HT-PC controlled elemental partitioning during crystal growth. This means that each growth sector within the crystals is only in thermodynamic equilibrium with the composition of its inter-phase boundary layer, which in turn is a function of the extent of mineral-fluid interaction (Veizer, 1983; Curti, 1997).
- Crystal growth occurred in an evolving redox setting and fluid composition (e.g., reducing salinity from the core to the rim section).
- Lack of distinct systematic and significant geochemical zoning in CL unzoned crystal facies of Daniel's Harbour suggests that crystals grew at relatively faster rate than the rate at which the pore fluid's chemistry changed whereby elements were partitioned by means of HM-PC.

- Elemental incorporation into IZC is also interpreted to be by means of HT-PC. However the water-rock ratio is very low hence there was relatively less significant geochemical core-to-rim trend for Sr, Na, Y and REE.
- High water-rock interaction is needed to change the Y and REE composition of rocks, which is not to be expected at the micron scale during a single dolomitization event. Relative depletion of Y and REE at the rim of the investigated crystals suggests formation from a parent fluid of different chemistry (e.g., salinity) compared with that of the core.
- Thus, the formation of core and the rim sections are likely separated in time. This is consistent with the zonation found in the core-to-rim compositions of the Fe, Mn, Sr and Na.
- Decoupling of Fe from Mn trend in IZC and unzoned dolomite crystal facies is interpreted to be a result of local fluctuations in redox potential (IZC and unzoned crystal facies) of the microenvironment as well as retention of precursor trend (unzoned crystal facies).

REFERENCES

Alibo, D.S., Nozaki, Y., 2000. Dissolved rare earth elements in the South China Sea: geochemical characterization of the water masses. Journal of Geophysical Research 105(C12), 28.

Allwood, A.C., Kamber, B.S., Walter, M.R., Burch, I.W., Kanik, I., 2010. Trace elements record depositional history of an early Archean stromatolitic carbonate platform. Chemical Geology 270(1-4), 148-163.

Azmy, K., Brand, U., Sylvester, P.J., Gleeson, S.A., Logan, A., Bitner, M.A., 2011. Biogenic and abiogenic low-Mg calcite (bLMC and aLMC): evaluation of sea water-REE composition, water masses and carbonate diagenesis. Chemical Geology 280(1-2), 180-190.

Azmy, K., Knight, I., Lavoie, D., Chi, G., 2009. Origin of dolomites in the Boat Harbour Formation, St. George Group, in western Newfoundland, Canada: implications for porosity development. Bulletin of Canadian Petroleum Geology 57(1), 81-104.

Azmy, K., Lavoie, D., Knight, I., Chi, G., 2008. Dolomitization of the Lower Ordovician Aguathuna Formation carbonates, Port au Port Peninsula, western Newfoundland, Canada: implications for a hydrocarbon reservoir. Canadian Journal of Earth Sciences = Revue Canadienne des Sciences de la Terre 45(7), 795-813.

Azomani, E., Azmy, K., Blamey, N., Brand, U., Al-Aasm, I., 2013. Origin of Lower Ordovician dolomites in eastern Laurentia: controls on porosity and implications from geochemistry. Marine and Petroleum Geology 40, 99-114.

Banner, J.L., 1995. Application of the trace element and isotope geochemistry of strontium to studies of carbonate diagenesis. Blackwell, Oxford-Boston, International, pp. 805-824.

Banner, J.L., Hanson, G.N., Meyers, W.J., 1988. Rare earth element and Nd isotopic variations in regionally extensive dolomites from the Burlington-Keokuk Formation (Mississippian): implications for REE mobility during carbonate diagenesis. Journal of Sedimentary Petrology 58(3), 415-432.

Borg, S., Liu, W., Pearce, M., Cleverley, J., MacRae, C., 2014. Complex mineral zoning patterns caused by ultra-local equilibrium at reaction interfaces. Geology [Boulder], Pre-Issue Publication 42(5). doi:10.1130/G35287.1.

Bouch, J.E., 2006. Development of capability in the SEM-CL of carbonates. British Geological Survey, Nottingham, UK, 25pp.

Budd, D.A., 1997. Cenozoic dolomites of carbonate islands: their attributes and origin. Elsevier, Amsterdam, Netherlands, pp. 1-47.

Busenberg, E., Plummer, N.L., 1985. Kinetic and thermodynamic factors controlling the distribution of SO_3^{2-} and Na^+ in calcites and selected aragonites. Geochimica et Cosmochimica Acta 49(3), 713-725.

Collen, J.D., Atkinson, J.E., Patterson, J.E., 2011. Trace metal partitioning in a nearshore tropical environment: geochemistry of carbonate reef flats adjacent to Suva Harbor, Fiji Islands. Pacific Science 65(1), 95-107.

Cooper, M.,Weissenberger, J., Knight, I., Hostad, D., Gillespie, D.,Williams, H.,Burden,E., Porter-Chaudhry, J., Rae, D., Clark, E., 2001. Basin evolution in

western Newfoundland: new insights from hydrocarbon exploration. AAPG (American Association of Petroleum Geologists) Bulletin 85(3), 393-418.

Curti, E., 1997. Coprecipitation of radionuclides: basic concepts, literature review and first applications. NAGRA (National Cooperative for the Disposal of Radioactive Waste) in Wettingen, Wettigen, Schweiz, 99pp. http://trove.nla.gov.au/work/157941214 (Assessed on April 13, 2014).

Doerner, H.A., Hoskins, W.M., 1925. Co-precipitation of radium and barium sulfates. Journal of the American Chemical Society 47(3), 662-675.

Fleet, A.J., 1984. Aqueous and sedimentary geochemistry of the rare earth elements Developments in geochemistry. In: Henderson, P. (Ed.), Rare Earth Element Geochemistry. Elsevier, Amsterdam, Netherlands, pp. 343-373.

Fraser, D.G., Feltham, D., Whiteman, M., 1989. High-resolution scanning proton microprobe studies of micron-scale trace element zoning in a secondary dolomite: implications for studies of redox behaviour in dolomites. Sedimentary Geology 65(3-4), 223-232.

Gladney, E.S., O'Malley, B.T., Roelandts, I., Gills, T.E., 1987. Standard reference materials: compilation of elemental concentration data for NBS clinical, biological, geological, and environmental standard reference materials. National Bureau of Standards Special Publication, 260-11.

Goetze, J., Kempe, U., 2009. Physical principles of cathodoluminescence (CL) and its applications in geosciences. In: Gucsik, A., (Ed.), Cathodoluminescence and its Application in the Planetary Sciences. Springer, Berlin-Heidelberg, pp. 1-22.

Habermann, D., Neuser, R.D., Richter, D.K., 1996. REE-activated cathodoluminescence

of calcite and dolomite: high-resolution spectrometric analysis of CL emission (HRS-CL). Sedimentary Geology 101(1-2), 1-7.

Henderson, L.M., Kracek, F.C., 1927. The Fractional Precipitation of Barium and Radium Chromates. Journal of American Chemical Society 49(33), 738-749.

Hendry, J.P., Marshall, J.D., 1991. Disequilibrium trace element partitioning in Jurassic sparry calcite cements; implications for crystal growth mechanisms during diagenesis. Journal of the Geological Society of London 148, Part 5, 835-848.

Iannace, A., Gasparrini, M., Gabellone, T., Mazzoli, S., 2012. Late Dolomitization in Basinal Limestones of the Southern Apennines Fold and Thrust Belt (Italy). Oil and Gas Science and Technology – Revue d' IFP Energies nouvelles 67(1), 59-75. http://dx.doi.org/10.2516/ogst/2011166.

Ishikawa, M., Ichikuni, M., 1984. Uptake of sodium and potassium by calcite. Chemical Geology 42(1–4), 137-146.

Jones, B., 2005. Dolomite crystal architecture: genetic implications for the origin of the Tertiary dolostones of the Cayman Islands. Journal of Sedimentary Research 75(2), 177-189.

Kaczmarek, S.E., Sibley, D.F., 2011. On the evolution of dolomite stoichiometry and cation order during high temperature synthesis experiments: an alternative model for the geochemical evolution of natural dolomites. Sedimentary Geology 240(1-2), 30-40.

Klinkhammer, G.P., Elderfield, H., Edmond, J.M., Mitra, A., 1994. Geochemical implications of rare earth element patterns in hydrothermal fluids from mid-ocean ridges. Geochimica et Cosmochimica Acta 58(23), 5105-5113.

Knight, I., Azmy, K., Boyce, W.D., Lavoie, D., 2008. Tremadocian carbonate rocks of the lower St. George group, Port au Port peninsula, western Newfoundland: lithostratigraphic setting of diagenetic, isotopic and geochemistry studies. Newfoundland and Labrador Department of Natural Resources Geological Survey, Report, 08-1, 115-149.

Kretz, R., 1982. A model for the distribution of trace elements between calcite and dolomite. Geochimica et Cosmochimica Acta 46(10), 1979-1981.

Kucera, J., Cempirek, J., Dolnicek, Z., Muchez, P., Prochaska, W., 2009. Rare earth elements and yttrium geochemistry of dolomite from post-Variscan vein-type mineralization of the Nizky Jesenik and Upper Silesian Basins, Czech Republic. Journal of Geochemical Exploration 103(2-3), 69-79.

Kupecz, J., Montanez, I., Gao, G., 1993. Recrystallization of dolomite with time. In: Rezak, R., Lavoie, D. (Eds.), Carbonate Microfabrics. Springer, New York, pp. 187-193.

Land, L.S., 1980. The isotopic and trace element geochemistry of dolomite: the state of the art. SEPM (Society for Sedimentary Geology), Tulsa, OK, United States, pp. 87-110.

Land, L.S., 1992. The dolomite problem: stable and radiogenic isotope clues, In: Clauer, N. and Chaudhuri, S. (Eds.). Isotopic Signature of Sedimentary Records. Lecture Notes in Earth Science 43, 49-68.

Lumsden, D.N., Lloyd, R.V., 1984. Mn(II) partitioning between calcium and magnesium sites in studies of dolomite origin. Geochimica et Cosmochimica Acta 48(9), 1861-1865.

Lumsden, D.N., Shipe, L.G., Lloyd, R.V., 1989. Mineralogy and Mn geochemistry of laboratory-synthesized dolomite. Geochimica et Cosmochimica Acta 53(9), 2325-2329.

Machel, H.G., 1990. Bulk solution disequilibrium in aqueous fluids as exemplified by diagenetic carbonates. AAPG (American Association of Petroleum Geologists) Memoir, 49, 71-83.

Machel, H.G., 2004. Concepts and models of dolomitization: a critical reappraisal. In: Braithwaite, C.J.R., Rizzi, G., Darke, G. (Eds.), The Geometry and Petrogenesis of Dolomite Hydrocarbon Reservoirs. Geological Society of London, special publications, London, UK, pp. 7-63.

Machel, H.G., Burton, E.A., 1991. Factors governing cathodoluminescence in calcite and dolomite and their implications for studies of carbonate diagenesis. In: Barker, C.E., Kopp, O.C., (Eds), Luminescence Microscopy and Spectroscopy: Qualitative and Quantitative Applications. SEPM (Society for Sedimentary Geology) Short Course Note 25, pp. 37-57.

Machel, H.G., Riciputi, L.R., Cole, D.R., 1997. Ion microprobe investigation of diagenetic carbonates and sulfides in the Devonian Nisku Formation, Alberta, Canada. Special Publication - SEPM (Society for Sedimentary Geology) 57, 157-165.

Malone, M.J., Baker, P.A., 1999. Temperature dependence of the strontium distribution coefficient in calcite: an experimental study from 408 degrees to 2008 degrees C and application to natural diagenetic calcites. Journal of Sedimentary Research 69(1), 216-223.

Mason, R.A., Mariano, A.N., 1990. Cathodoluminescence activation in manganese-bearing and rare earth-bearing synthetic calcites. Chemical Geology 88(1-2), 191-206.

McLennan, S.M., 1989. Rare earth elements in sedimentary rocks: influence of provenance and sedimentary processes. Reviews in Mineralogy and Geochemistry 21, 169-200.

Montanez, I.P., 1994. Late Diagenetic dolomitization of Lower Ordovician,Upper Knox carbonates: a record of the hydrodynamic evolution of the Southern Appalachian Basin. AAPG (American Association of Petroleum Geologists) Bulletin 78(8), 1210-1239.

Morse, J.W., Mackenzie, F.T., 1990. Geochemistry of sedimentary carbonates. Developments in sedimentology. Elsevier, Amsterdam, New York, xvi, 707 pp.

Nordeng, S.H., Sibley, D.F., 1994. Dolomite stoichiometry and Ostwald's step rule. Geochimica et Cosmochimica Acta 58(1), 191-196.

Nothdurft, L.D., Webb, G.E., Kamber, B.S., 2004. Rare earth element geochemistry of Late Devonian reefal carbonates, Canning Basin, Western Australia: confirmation of a seawater REE proxy in ancient limestones. Geochimica et Cosmochimica Acta 68(2), 263-283.

Olanipekun, B.-J., Azmy, K., Brand, U., 2014. Dolomites of the Boat Harbour Formation in the Northern Peninsula, western Newfoundland, Canada: implications for dolomitization history and porosity control. AAPG (American Association of Petroleum Geologists) Bulletin 98(4), 765-791.

Oomori, T., Nakasone, M., Kaneshima, K., Kitano, Y., 1985. Incorporation of Sodium into Calcium Carbonate and Protodolomite. Bulletin of the College of Sceince. University of the Ryukyus 39, 51-56.

Paquette, J., Reeder, R.J., 1990. New type of compositional zoning in calcite: insights into crystal-growth mechanisms. Geology [Boulder] 18(12), 1244-1247.

Paquette, J., Reeder, R.J., 1995. Relationship between surface structure, growth mechanism, and trace element incorporation in calcite. Geochimica et Cosmochimica Acta 59(4), 735-749.

Pingitore, N.E., Jr., 1978. The behavior of Zn (super 2) + and Mn (super 2) + during carbonate diagenesis: theory and applications. Journal of Sedimentary Petrology 48(3), 799-814.

Pingitore, N.E., Jr., 1982. The role of diffusion during carbonate diagenesis. Journal of Sedimentary Petrology 52(1), 27-39.

Qing, H., Mountjoy, E.W., 1994. Rare earth element geochemistry of dolomites in the Middle Devonian Presqu'ile barrier, western Canada sedimentary basin: implications for fluid-rock ratios during dolomitization. Sedimentology 41(4), 787-804.

Reed, R.M., Milliken, K.L., 2003. How to overcome imaging problems associated with carbonate minerals on SEM-based cathodoluminescence systems. Journal of Sedimentary Research 73(2), 328-332.

Reeder, R.J., Prosky, J.L., 1986. Compositional sector zoning in dolomite. Journal of Sedimentary Petrology 56(2), 237-247.

Richter, D.K., Goette, T., Goetze, J., Neuser, R.D., 2003. Progress in application of

cathodoluminescence (CL) in sedimentary petrology. Mineralogy and Petrology 79(3-4), 127-166.

Riciputi, L.R., Machel, H.G., Cole, D.R., 1994. An ion microprobe study of diagenetic carbonates in the Devonian Nisku Formation of Alberta, Canada. Journal of Sedimentary Research, Section A, Sedimentary Petrology and Processes 64(1), 115-127.

Sholkovitz, E., Szymczak, R., 2000. The estuarine chemistry of rare earth elements: comparison of the Amazon, Fly, Sepik and the Gulf of Papua systems. Earth and Planetary Science Letters 179(2), 299-309.

Shore, M., Fowler, A.D., 1996. Oscillatory zoning in minerals: a common phenomenon. Canadian Mineralogist 34, Part 6, 1111-1126.

Sibley, D.F., 1990. Unstable to Stable Transformations during Dolomitization. The Journal of Geology 98(5), 739-748.

Veizer, J., 1983. Chemical diagenesis of carbonates: theory and application of trace element technique. SEPM (Society of Sedimentary Geology) Short Course 10(3.1), 3-100.

Vuillemin, A., Ndiaye, M., Martini, R., Davaud, E., 2011. Cement stratigraphy: image probes of cathodoluminescent facies. Swiss Journal of Geosciences 104, 55-66. Warren, J., 2000. Dolomite: occurrence, evolution and economically important associations. Earth-Science Reviews 52(1–3), 1-81.

Wogelius, R.A., Fraser, D.G., Feltham, D.J., Whiteman, M.I., 1992. Trace element zoning in dolomite: proton microprobe data and thermodynamic constraints on fluid compositions. Geochimica et Cosmochimica Acta 56(1), 319-334.

Xiaolin, W., Zhijun, J., Wenxuan, H., Juntao, Z., Yixiong, Q., Jingquan, Z, Qing, L., 2009. Using *in situ* REE analysis to study the origin and diagenesis of dolomite of Lower Paleozoic, Tarim Basin. Science in China Series D: Earth Sciences 52(5), 681-693.

Xuefeng, Z., Wenxuan, H., Juntao, Z., Xiaolin, W., Xiaomin, X., Zhijun, J., Dongya, Z., Yixiong, Q., Jingquan, Z., 2008. REE compositions of lower Ordovician dolomites in Central and North Tarim Basin, NW China: a potential REE proxy for ancient seawater. Acta Geologica Sinica [English Edition] 82(3), 610-621.

Zhao, Y.-Y., Zheng, Y.-F., 2013. Geochemical constraints on the origin of post-depositional fluids in sedimentary carbonates of the Ediacaran system in South China. Precambrian Research 224(0), 341-363.

Zhong, S., Mucci, A., 1995. Partitioning of rare earth elements (REEs) between calcite and seawater solutions at 25 degrees C and 1 atm, and high dissolved REE concentrations. Geochimica et Cosmochimica Acta 59(3), 443-453.

3 APPENDICES

Appendix 3.A1. SIMS Spot locations in burial dolomite crystals from depth 154m Main Brook (Sample P-154).

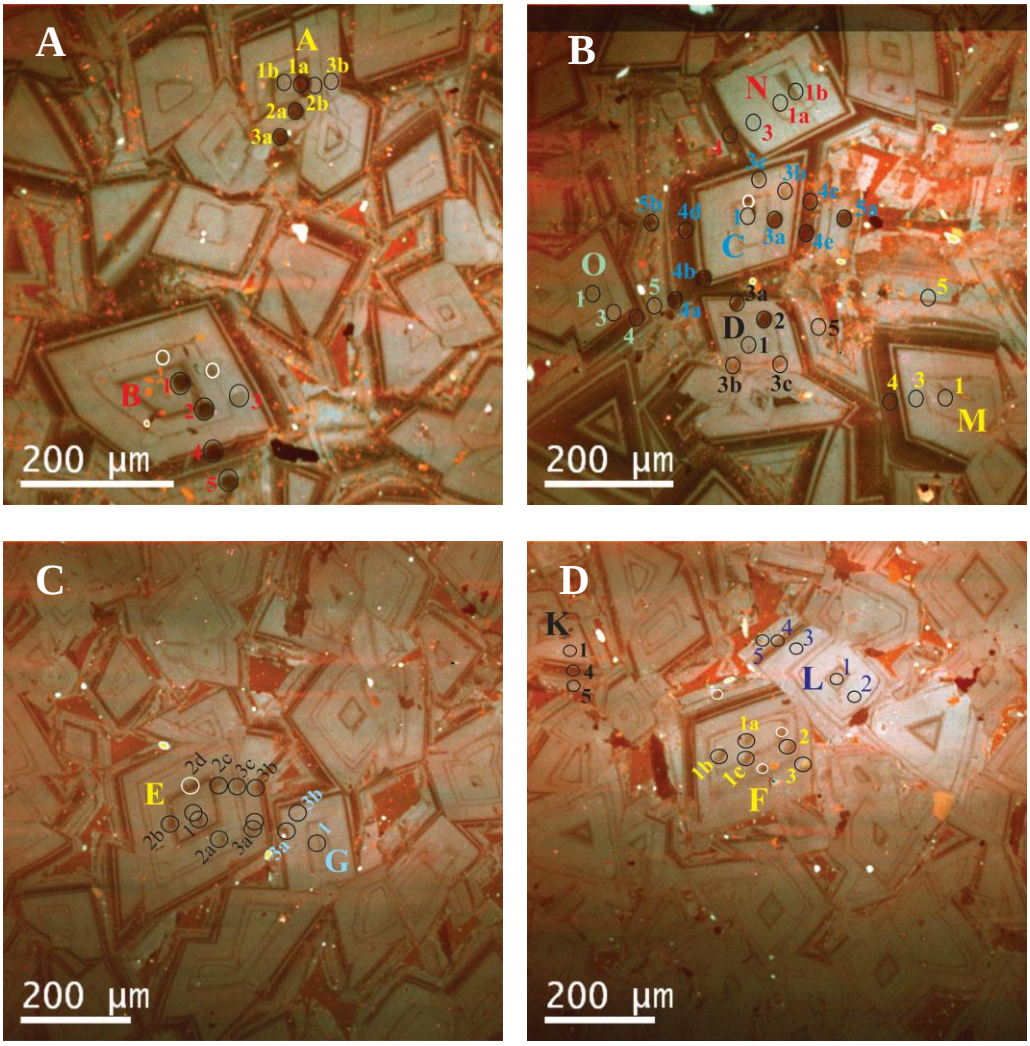

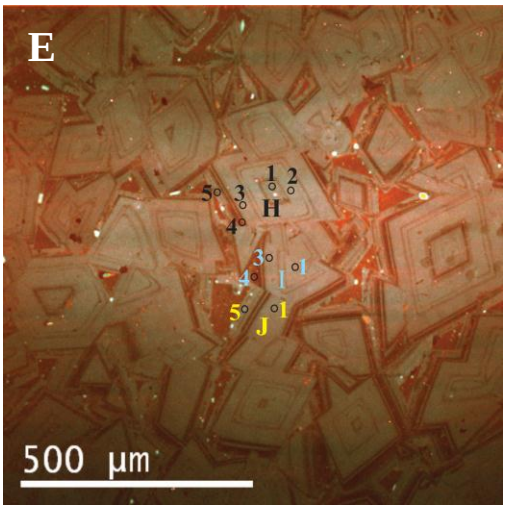

Figure 3.A1:

A. SEM-CL showing the locations of SIMS beam spots (labelled black circles) within the zones of crystals A (yellow fonts) and B (red fonts). Note that white circles within crystal B are spots where data were rejected due to machine error. Black elongated object (bottom centre) is pyrite grain;
B. SEM-CL showing the locations of SIMS beam spots (labelled black circles) within crystals C (blue fonts), D (black fonts), M (yellow fonts), N (red fonts) and O (green fonts). Note that white circle within crystal C is spot where data were rejected due to machine error;
C. SEM-CL showing the locations of SIMS beam spots (labelled black circles) within crystals E (yellow font) and G (blue fonts). Note that white circle within crystal E is spot where data were rejected due to machine error;
D. SEM-CL showing the locations of SIMS beam spots (labelled black circles) within crystals F (yellow font), K (black font) and L (blue font). Note that white circle within crystal F are spots where data were rejected due to machine error; and

E. SEM-CL showing the locations of SIMS beam spots (labelled black circles) within crystals H (black font), I (blue font) and J (yellow font).

Appendix 3.A2. SIMS Spot locations in burial dolomite crystals from depth 158m Main Brook (Sample P-158).

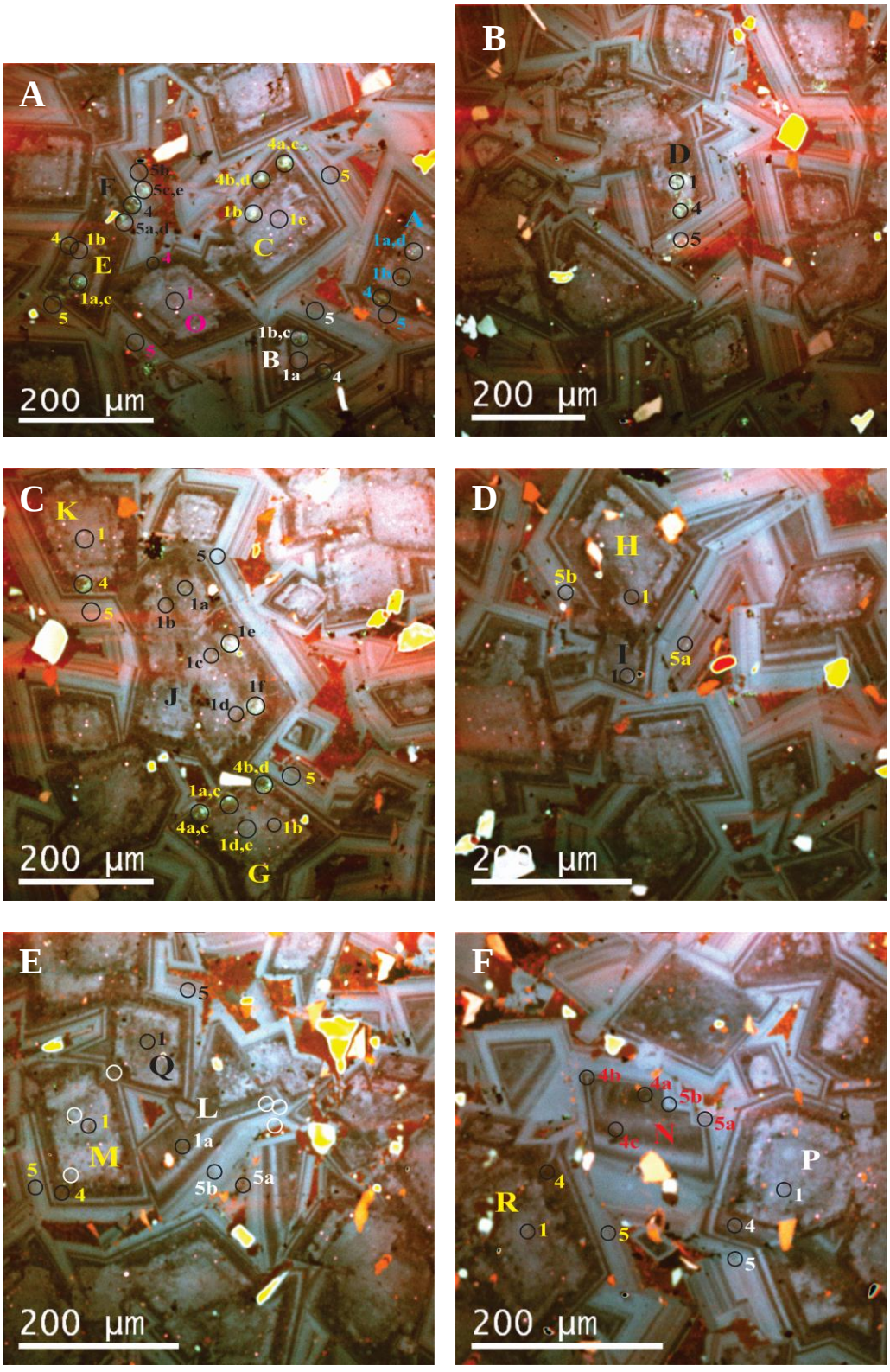

Figure 3.A2

A. SEM-CL showing the locations of SIMS beam spots (labelled black circles) within zones 1 (green band core), 2 (dark red transition band) and 5 (outermost thick green band rim) in crystals A (blue font), B (white font), C (yellow font), E (yellow font) and F (black font);

B. SEM-CL showing the locations of SIMS beam spots (labelled black circles) within zones 1 (green band core), 2 (dark red transition band) and 5 (outermost thick green band rim) in crystal D (black font);

C. SEM-CL showing the locations of SIMS beam spots (labelled black circles) within zones 1 (green band core), 2 (dark red transition band) and 5 (outermost thick green band rim) in crystals G (yellow font), J (black font) and K (yellow font);

D. SEM-CL showing the locations of SIMS beam spots (labelled black circles) within zones 1 (green band core), 2 (dark red transition band) and 5 (outermost thick green band rim) in crystals H (yellow font) and I (black font);

E. SEM-CL showing the locations of SIMS beam spots (labelled black circles) within zones 1 (green band core), 2 (dark red transition band) and 5 (outermost thick green band rim) in crystals L (white font), M (yellow font) and Q (black font). Note that white circles within crystals L and M are spots where data were rejected due to machine error; and

F. SEM-CL showing the locations of SIMS beam spots (labelled black circles) within zones 1 (green band core), 2 (dark red transition band) and 5 (outermost thick green band rim) in crystals N (red font), P (white font) and R (yellow font).

Appendix 3.A3. SIMS Spot locations in burial dolomite crystals from Daniel's Harbour (Sample 6-172 at 172 m).

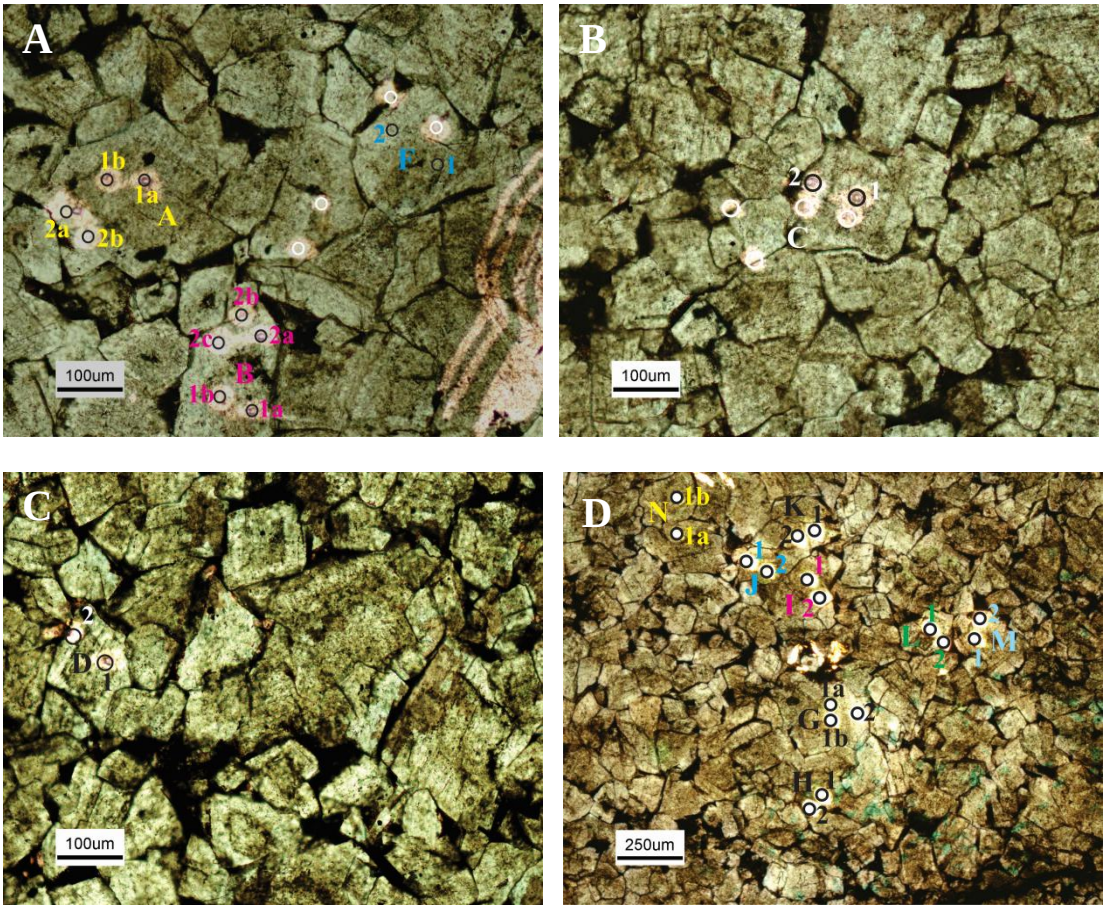

Figure 3.A3

A. Plane polarized light image showing locations of SIMS beam spots (labelled black circles) within the cloudy core and clear rims of crystals A (yellow font), B (pink font), and F (blue font). Note that white circles are spots where data were rejected due to machine error. Lighter colored line bands on right side are artifact scratches imposed to aid in locating areas of interest under SIMS;
B. Plane polarized light image showing locations of SIMS beam spots (labelled black circles) within the cloudy core and clear rims of crystal C (white fonts). Note that white circles are spots where data were rejected due to machine error;
C. Plane polarized light image showing locations of SIMS beam spots (labelled black circles) within the cloudy core and clear rims of crystal D (black and white fonts).;
D. Plane polarized light image showing locations of SIMS beam spots (labelled black circles) within the cloudy core and clear rims of crystals G (black font), H (black font), J (blue font), L (green font), M (blue font) and (yellow font).

Appendix 3.A4. Tables of geochemical measurements

Table 3.A4A: The Na, Mg, Mn, Fe, Sr, Y and ∑REE concentrations (in ppm) obtained from the SIMS spots. Mean values of duplicate SIMS spots in a zone are shown in orange font. ∑REE (in red font) is the sum of La, Ce, Nd, Sm, Eu and Dy as they are REEs above detection limits that are common to all the spots analyzed for REEs. Zones that contain decimal points are adjusted values to ensure data points are visible on the chart. Sample P-154 at depth of 154m from Main Brook locality.

SIMS SPOT -SEM-CL	Zone id	Na	Na-St. Dev	Mg	Mg-St. Dev	Fe	Fe-St. Dev	Mn	Mn-St. Dev	Sr	Sr-St. Dev	Y	Y-St. Dev	∑REE	N
A-1 (1a,1b)	1	226		90385		2027		46		165		1.39		**19**	
A-2	2	236		88668		1256		40		203		1.30		**11**	
A-3(3a,3b)	3	179		94789		3747		66		199		0.53		**9**	
B-1(1a,1b)	1	234		94082		1221		38		150		1.25		**18**	
B-2	2	228		89376		1348		31		182		1.35		**8**	
B-3	3					1038								**8**	
B-4(4a,4b)	4	94		96455		2671		81		89		0.70		12	
B-5(5a,5b)	5	173		97898		4064		54		103		0.83		11	
C-1	1					1619								14	
C-3a	3					717								11	
C-3 (3a, 3b, 3c)	3.1	296	72	92598	620			61	6	218	32	0.43	0.19		3
C-4e (4a,4b,4e)	4					4805								11	2
C-4 (4a, 4b, 4c, 4d)	4.1	190	119	89722	2317			80	25	86	14	0.48	0.13		4
C-5(5a1, 5a2)	5					1645								13	
C-5 (5a1, 5b)	5.1	168	45	88206	542			66	7	112	4	0.49	0.15		2
D-1	1					718								40	
D-2(2a, 2b)	2	221		91031		705		43		247		1.28		27	2
D-3a	3													10	

D-3 (3a, 3b, 3c)	2.9	359	91	94325	7266		82	39	191	47	0.41	0.13		3
D-5	5					3205							13	
E-1	1	260		83789		802	35		218		0.76		21	
E-2 (2a, 2b)	2.1	334	65	86538	1474		28	4	196	22	0.61	0.15		2
E-2c	2					512							31	
E-3a1	3	223		85244		931	53		266		0.30		8	
E-3 (3a2, 3c)	3													2
F-1 (1a, 1b)	1.1	287	53	84493	237		39	2	261	0.49	0.41	0.07		2
F-2	2	286		84426			58		213		0.23			
F-3	3	503		85689			51		255		0.33			
G-1	1					788							16	
G-3	3	760		91222		689	71		166		0.23		10	
H-1	1	801		92136		1560	35		181		0.91			
H-2	2	644		93927		444	33		205		1.01			
H-3	3	428		92709		886	44		201		0.56			
H-4	4	298		93422		2235	63		153		0.34			
H-5	5	325		96385		4318	73		90		0.40			
I-1	1	296		90628		776	37		216		0.68			
I-3	3	249		89002		2178	71		131		0.38			
I-4	4	252		91825			66		81		0.36			
J-1	1	253		89733		267	45		288		0.36			
J-5	5	209		89754		3768	71		91		0.46			
K-1	1	326		93227			57		211		0.42			
K-4	4	224		94330		1024	51		221		0.33			
K-5	5	285		93061		4226	55		85		0.40			
L-1	1	241		92341		546	29		207		1.12			
L-2	2	728		91070		1563	32		203		1.33			
L-3	3	270		90086		985	46		246		0.38			
L-4	4	188		93062		1573	51		137		0.57			
L-5	5			107010		6343	98		104		0.45			

M-1	1	198		87257		371		55		212		0.34		
M-3	3	89		87210		5826		93		88		0.48		
M-4	4	105		87607		4558		65		75		0.37		
M-5	5	112		85673		5119		77		97		0.44		
N-1(1a,1b)	1.05	205	37	88311	1085	1105	196	30	8	201	30	1.01	0.22	2
N-3	3	145		89267		198		41		242		0.31		
N-4	4	100		87351		4900		65		74		0.37		
O-1	1	181		88141		477		57		209		0.46		
O-3	3	457		87901		920		31		227		1.39		
O-4	4	143		87034		1315		58		199		0.38		
O-5	5	100		87239		4709		65		72		0.37		

Table 3.A4B. The Na, Mg, Mn, Fe, Sr, Y and ∑REE concentration (in ppm) obtained from the SIMS spots. Mean values of duplicate SIMS spots in a zone are shown in orange font. ∑REE (in red font) is the sum of La, Ce, Nd, Sm, Eu and Dy as they are REEs above detection limits that are common to all the spots analyzed for REEs. Zones that contain decimal points are adjusted values to ensure data points are visible on the chart. Sample P-158 at depth of 158m from Main Brook locality.

SIMS SPOT-SEM-CL	Zone	Na	Na-St. Dev	Mg	Mg-St. Dev	Mn	Mn-St. Dev	Fe	Fe-St. Dev	Sr	Sr-St. Dev	Y	Y-St. Dev	∑REE	∑REE-St. Dev	N
								20								
A-1 (A-1a, A-1b)	1.05	125	34	9810 101	600	51	9	00	1127	95	0.58	1.12	0.22			2
A-1d	1													10		
								11								
				1008				11								
		135		1042		3		84		9		0.42				
A-4a	4					5				2						
A-5b	5													6		
								12								
				8135				58		15						
B-1a	1	48		8		0				1		0.25				
B-1(1b, 1c)	1													13	0.42	2
B-4b	4													8		
				8568				35		10						
B-5	5	26		7		6		55		3		0.07				
B-5b	5													4		
				8582				75		11						
C-1	1	44		8		7		51		8		0.27				
C-1(1b, 1c)	1													12	1.4	2
C-4 (C-	4.1													9	0.7	2

4c, C-4d)																3	
C-5a	5	33		84876		63		3		89		0.15					
C-5b	5													9			
D-1a	1	321		98816		51		31		84		0.63					
D-1 (D-1b, D-1c, D-1d)	1													12	5.18	3	
D-4a	4	229		99907		53		23		63		0.69					
D-4 (D-4b, D-4c)	3.9													9	0.91	2	
D-5a	5	84		10242906		97		20		43		0.98					
D-5b	5													19			
E-1 (E-1a, E-1b)	1.05	346	82	90915	3930	59	13	203	1098	93	14	0.35	0.04			2	
E-1c	1													10			
E-4a	4	268		79401		37		13		94		0.25					
E-4b	4													10			
E-5a	5	74		91693		33		10		43		0.11					
E-5b	5													8			
F-4a	4	158		88163		64		31		80		0.29					
F-4b	4													7			
F-5 (F-5a, F-5b,F-	5	136	45	95449	1089 3	63	24	201	1266	70	35	0.36	0.18			3	

5e)								1								
F-5(F-5c, F-5d)	5													10	3.56	2
G-1 (G-1a, G-1b)	1.05	286	133	8309	289	38	0	1205	199	156	31	0.40	0.16			2
G-1(1c, 1e)	1.05													11	0.4	2
G-4 (G-4a, G-4b)	4.1	214	29	9355	7775	56	5	2617	65	157	5	0.24	0.04			2
G-4 (G-4c, G-4d)	4.05													9	0.33	2
G-5b	5													9		
H-1	1	273		9177 8		45		1761		167		0.37				
H-5 (H-5a, H-5b)	4.95	70	28	9760 4	3500	70	30	1064	389	161	29	0.39	0.29			2
I-1	1	237		9509 5		52		2182		174		0.30				
J-1 (J-1a, J-1b, J-1c, J-1d)	1.05	194	83	8313 0	1010 2	42	6	2243	975	103	19	0.58	0.23			4
J-1 (J-1e, J-1f)	1.05													9	0.45	2
J-5	5	147		9276 7		36		2407 0		178		0.11				
K-1a	1	35		8751 0		50		7707		187		0.34				
K-1b	1													14		
K-5	5	37		8389 2		43		4182		106		0.09				
K-4c	4													9		
L-1	1	25		92		4		2		7		0.30				

		2		21		9		1		5					
				1				4							
								4							
L-5 (L-				98				8					0.		
5a, L-	5.0	22		08		7		3		9			1		
5b)	5	8	81	8	5952	1	70	2	836	6	23	0.12	2		2
				74				6		1					
				03		4		6		1					
M-1	1	50		7		0		6		5		0.29			
								1							
				85				6							
				09		5		1		6					
M-4	4	54		2		2		9		8		0.14			
				88				8							
				42		6		2		5					
M-5	5	43		6		9		2		7		0.26			
N-4 (N-								2							
4a, N-				91				8					0.		
4b, N-		24		71		5		9		7			0		
4c)	4	5	116	4	1890	0	4	5	498	5	4	0.31	8		3
								1							
N-5 (N-				94				5					0.		
5a, N-		12		20		6		2		6			1		
5b)	5	4	71	8	3668	4	21	5	577	9	8	0.40	7		2
								1							
				85				0							
				96		4		0		8					
O-1	1	34		1		5		2		3		0.30			
O-1b	1													11	
				85				9							
				27		4		2		9					
O-4	4	43		9		1		3		4		0.10			
				84				4							
				81		5		2		9					
O-5	5	38		7		2		9		8		0.11			
O-5b	5													6	
				81				7		1					
		13		36		4		6		0					
P-1	1	4		8		9		0		0		0.30			
								1							
				84				7							
				72		5		4		7					
P-4	4	81		9		6		6		6		0.15			
				87		1		6							
				94		1		4		5					
P-5	5	42		5		1		4		1		0.28			
								1							
				85				7							
				00		4		4		8					
Q-1	1	62		2		4		6		3		0.20			

			85		6			
			93	3	4	9		
Q-5	5	73	2	8	4	8	0.08	
			86		9			
			88	5	8	7		
R-1	1	91	8	2	8	5	0.33	
R-1b	1							11
					2			
			77		0			
			13	5	8	8		
R-4	4	71	4	7	1	3	0.22	
					1			
			87		5			
		14	70	8	3	9		
R-5	5	3	4	4	8	3	0.16	
R-5b	5							7

Table 3.A4C: The Na, Mg, Mn, Fe, Sr, Y and ∑REE concentrations (in ppm) obtained from the SIMS spots. Mean values of duplicate SIMS spots in a zone are shown in orange font. ∑REE (in red font) is the sum of La, Ce, Nd, Sm, Eu and Dy as they are REEs above detection limits that are common to all the spots analyzed for REEs - Zones that contain decimal points are adjusted values to ensure data points are visible on the chart. Sample 6-172 at depth of 172m from Daniel's Harbour locality.

SIMS SPOT-SEM-CL	Zone id (adjust for error bar fit)	Na	Na-St. Dev	Mg	Mg-St. Dev	Fe	Fe-St.Dev	Mn	Mn-St.Dev	Sr	Sr-St.Dev	Y	Y-St.Dev	∑REE	N
A-1a	1	199		100784				175		43		0.31			
A-1b	1					271								12	
A-2a	2	208		102169				182		31		0.12			
A-2b	2					401								8	
B-1a	1	197		100165				94		47		0.27			
B-1c	1					474								12	
B-2a	2	137		98059				156		30		0.15			
B-2b	2					317								7	
C-1a	1	247		101178				225		37		0.28			
C-1b	1					426								7	
C-2a	2	342		104870				192		37		0.14			
C-2b	2					2137								9	
D-1a	1	230		101316		648		144		39		0.24		10	
D-2a	2	331		101823				310		51		0.33			
D-2b	2					1364								8	
F-1	1					737								10	
F-2	2					249								13	
G-1a	1	59		100203		425		157		42		0.20			
G-1b	1													8	
G-2a	2	50		97904		1463		148		26		0.13			
G-2b	2													9	
H-1a	1	56		99522		250		119		45		0.24			
H-1b	1													15	
H-2a	2	41		97861		371		136		33		0.14			

H-2b	2													8		
I-1a	1	62		97531		837		184		45		0.20				
I-1b	1													11		
I-2a	2	136		96007		1914		407		41		0.27				
I-2b	2													15		
J-1a	1	121		97351		1092		191		33		0.15				
J-1b	1													8		
J-2a	2	40		82221		220		163		44		0.13				
J-2b	2													13		
K-1a	1	48		96252		560		288		31		0.16				
K-1b	1													10		
K-2a	2	25		94391		1026		195		31		0.17				
K-2b	2													13		
L-1a	1	64		99659		799		116		51		0.19				
L-1b	1													10		
L-2a	2	70		99210		1302		148		44		0.13				
L-2b	2													11		
M-1a	1	57		95576		1125		209		39		0.19				
M-1b	1													11		
M-2a	2	29		94204		278		171		40		0.17				
M-2b	2													15		
N-1a	1.01	51	20	95773	95	299	226	120	13	48	2	0.24	0.04		2	
O-1a	1	81		95023		990		244		36		0.20				
O-2a	2	41		95971		376		194		29		0.08				

Table 3.A4D: The Na, Mg, Mn, Fe, Sr and Y concentrations (in ppm) as obtained from the reference standard material (OKA-C, a carbonatite) SIMS spots. Other reference standard (Fran in orange font) is occasionally included in the measurements to also check for consistency.

File name	Na	Mg	Mn	Fe	Sr	Y
Oka c 1 Oct 18 2012	263	1002	2307	194	13592	24
Oka C 1 May 9 2013	259	1027	2338	420	13775	33
Oka C 2 May 9 2013	263	994	2327	361	13792	23
Oka C 3 May 9 2013	265	990	2301	305	14016	20
Oka C 4 May 9 2013	270	982	2295	287	14186	19
Oka C 1 May 21 2013	149	1031	2334	428	14140	30
Oka C 2 May 21 2013	154	981	2266	332	14126	21
Oka C 3 May 21 2013	257	968	2280	181	13810	24
Oka C 1 May 22 2013	280	993	2265	374	14086	27

Oka C 2 May 22 2013	274	972	2266	283	14271	20
Oka C 3 May 22 2013	272	991	2259	372	13974	26
Oka C 2 May 23 2013	278	1019	2379	309	13879	25
Oka C3 May 23 2013	254	1035	2386	444	13733	27
Oka C4 May 23 2013	242	1000	2363	352	13671	21
Oka C5 May 23 2013	255	990	2351	317	13731	19
Oka C 1 July 18 2014	265	970	2305	346	13923	25
Oka C 2 July 18 2014	265	989	2260	377	13761	24
Oka C 3 July 18 2014	252	1006	2327	331	13853	24
Oka C 4 July 18 2014	274	1026	2369	301	14234	24
Oka C 1 July 23 2014	237	1001	2309	327	13797	35
Oka C 2 July 23 2014	274	1005	2320	354	13844	25
Oka C 3 July 23 2014	280	988	2317	336	14188	23
Oka C 1 July 25 2014	308	1008	2326	337	15127	34
Oka C 2 July 25 2014	154	1006	2328	313	13006	25
Oka C 3 July 25 2014	307	993	2327	360	15042	27
Oka C 4 July 25 2014	176	985	2279	346	12598	20
Oka C 1 Mar 10 2015	246	1012	2356	326	14080	31
Oka C 2 Mar 10 2015	269	1000	2310	376	14126	23
Oka C 3 Mar 10 2015	264	995	2306	312	13890	22
Oka C 4 Mar 10 2015	275	985	2288	342	13676	19
Oka C 3 May 28 2015	198	1007	2298	358	14138	26
Oka 7 May 29 2015	280	999	2367	378	14013	18
Oka 10 May 29 2015	241	1016	2316	303	13999	29
Oka c 1 June 3 2013				336		
Oka c 2 June 3 2013				342		
Oka c 1 June 4 2013				339		
Oka c 2 June 4 2013				339		
oka c 2 REE June 1 2015				333		
oka c 3 REE June 1 2015				376		
Oka_c_June_2_2015@1				324		
Oka_c_June_2_2015@2				325		
Oka_c_June_2_2015@3				349		
oka_c_June_3_2015_REE@3				311		
oka_c_June_3_2015_REE@4				355		
Oka c 2 June 3 2013				331		
Oka c 1 June 3 2013				347		
Oka c 1 June 4 2013				346		
Oka c 2 June 4 2013				332		
oka REE 1 July 18 2014				339		
Oka c 1 July 24 2014				344		
Oka c 2 July 24 2014				334		

Table 3.A4E: The REEs concentrations (in ppm) as obtained from the standard material (OKA-C, a carbonatite) SIMS spots.

File name	La	Ce	Nd	Sm	Eu	Dy	Er	Yb
oka REE 1 July 18 2014	443	525	142	19	8	5	1.65	2.43
Oka c 1 July 24 2014	435	513	147	20	9	5	2.16	2.32
Oka c 2 July 24 2014	451	537	151	21	9	5	2.14	2.22
Oka c 2 Mar 5 2015	448	536	153	23	9	5	2.59	2.74
Oka c 1 Mar 5 2015	440	526	145	21	9	5	2.35	2.34
oka c 2 Mar 6 2015	446	521	149	20	8	5	2.23	2.59
oka c 1 Mar 6 2015	450	527	146	20	8	5	2.41	2.53
Oka c 2 Mar 9 2015	437	521	145	21	9	5	2.13	2.76
Oka c 1 Mar 9 2015	436	519	148	22	9	5	2.04	2.69
oka c 2 REE June 1 2015	446	527	148	21	9	6	2.10	2.49
oka c 3 REE June 1 2015	450	536	152	21	9	5	2.04	2.23
Oka_c_June_2_2015@1	443	529	143	22	9	5	1.97	2.24
Oka_c_June_2_2015@2	449	535	149	22	9	5	2.17	2.49
Oka_c_June_2_2015@3	425	503	145	21	9	5	2.44	2.50
oka_c_June_3_2015_REE@3	447	529	146	23	9	5	2.27	2.58
oka_c_June_3_2015_REE@4	440	517	145	22	9	5	2.17	2.26

4 CHAPTER 4: IMPLICATIONS FOR THE CONTROL ON DOLOMITE LUMINESCENCE: APPLICATIONS OF SECONDARY ION MASS SPECTROMETER

ABSTRACT

At low concentrations (<200 ppm), the correlation of activators (Mn and REE-Y) and quenchers (Fe) with occurrence and intensity of luminescence remains speculative.

The current study correlates the Secondary Ion Mass Spectrometer (SIMS) measured Mn, Fe and REE-Y content of zoned and unzoned dolomite crystal facies with their luminescence characters. Luminescence was obtained using SEM-CL (Cathodoluminescence) and epifluorescence microscope (photoluminescence, PhL).

Concentric zoning pattern exhibited by the distinctively zoned burial dolomite crystal facies from Main Brook in CL is also seen in PhL images implying that the same activators and quenchers controlled luminescence emissions in both CL and PhL. Mn composition of the crystal zones shows complex correlation with their luminescence. Regardless, the only zone in rim section of the zoned dolomite crystal facies that emit Mn-activated red luminescence in both CL and PhL also has relatively higher absolute Mn concentration than the core section. The core section did not show distinct visible Mn-activated red luminescence but emits shorter wavelength luminescence thus suggesting that intrinsic factors such as lattice defects also controlled its exhibited luminescence character.

The unzoned dolomite crystal facies from Daniel's Harbour contains generally higher Mn than the zoned dolomite crystal facies and is believed to account for its brighter reddish-luminescence in CL which was not noticeable in PhL. Inorganic composition controlled the luminescence observed under CL as well as PhL in the distinctively zoned dolomite

crystal facies from Main Brook. On the other hand, while inorganic composition also controlled the luminescence observed under CL of the unzoned dolomite crystal facies from Daniel's Harbour, mature organic (bituminous) materials seems to have played dominant role in the exhibited luminescence features of its PhL and thus masked the expected Mn-activated red luminescence.

Broadly speaking, the results suggest that the REE-Y content was too low to control luminescence and Fe could not be conclusively demonstrated, using the employed methods, to have caused quenching.

4.1. INTRODUCTION

Luminescence is the emission of visible lights that occurs in solids as excited electrons radiatively cascade to lower energy levels or ground energy states in atoms, ions or molecules (e.g., Machel and Burton, 1991; Goetze and Kempe, 2009). Luminescence in carbonates has been effective in discerning the impact of diagenesis on carbonate minerals formation in diagenetic settings and in revealing crystal growth zones of carbonate minerals. Mn is the most important activator of luminescence in carbonate minerals and has been satisfactorily demonstrated (e.g., Hemming et al., 1989; Walker et al., 1989; Bruhn et al., 1995; Habermann et al., 1999; Gillhaus et al., 2001; Goette and Richter, 2004), even though REEs have also been documented as activator elements (Mason and Mariano, 1990; Habermann et al., 1996; Habermann et al., 1999), while Fe^{2+} is the most important quencher in carbonate minerals (e.g., Hemming et al., 1989; Machel and Burton, 1991; Budd et al., 2000).

Intensity and occurrence of visible luminescence in carbonates is attributed mainly to the molar ratio of Mn^{2+} / Fe^{2+} (Rush and Chafetz, 1990; Machel and Burton, 1991; Budd et al., 2000; Goetze and Kempe, 2009) and individual concentration of Mn or Fe (Kaufmann et al., 1999; Budd et al., 2000), although co-existing organic matter is also considered a luminescence activator in photo-luminescence (PhL) examination of dolomites (Dravis and Yurewicz, 1985; Pedone et al., 1990; Haeri-Ardakani and Sanei, 2015). However, several carbonate minerals have defied these expectations to various extent (e.g., Savard, et al., 1995, their Figs. 3 A and B; Budd et al., 2000, their Table 2 and Fig. 5). In most

cases such anomalous emissions have been shown to be ‘intrinsic’ luminescence rather than emissions by impurity elements.

Emission of intrinsic luminescence has been associated with variations in crystal defect density of the respective minerals and commonly leads to shift in luminescence spectra towards shorter wavelengths. The phenomenon has been clearly demonstrated in carbonates as well as silicates (e.g., Demars et al., 1996; Cazenove et al., 2003; Bouch, 2006; Gotze and Kempe, 2008). In calcite, it is known to cause emission in UV, violet (e.g., Bouch, 2006) and blue (e.g., Machel et al., 1991; Cazenove et al., 2003; Edwards et al., 2007) wavelength bands rather than in or in addition to Mn-activated orange band (e.g., Machel and Burton, 1991; El Ali et al., 1993; Boggs and Krinsley, 2006) in calcite. In like manner, when Mn-activated red luminescence spectrum was excised from the SEM-CL luminescence spectra of dolomite, the resulting bright luminescence (in panchromatic mode) was attributed to intrinsic luminescence (Reed and Milliken, 2003; Bouch, 2006). Intrinsic luminescence is considered visible only with high excitation energy, and if the composition of activator elements are not significant enough in the lattice to mask it (Machel et al., 1991). Thus, it is often revealed in SEM-CL and rarely in optical CL due to the fact that the former is a much more sensitive equipment.

The most widespread method of studying visible luminescence in sedimentary rocks are cathodoluminescence (CL) and photo-luminescence (PhL, Ultra-Violet luminescence, <200-400 nm; Blue light 425-490nm luminescence; Marshall, 1988) with CL being the most popular. Cathodoluminescence is generated as a result of high energy electron bombardment of samples. There are two main approaches to CL imaging of geological

materials namely: optical CL and SEM-CL. Optical CL refers to CL generated by an electron excitation source (hot or cold cathode source) attached to a regular petrographic microscope whereby the resulting luminescence is viewed through the objective of the microscope.

As for SEM-CL, it is the latest development in the CL imaging. A specimen placed on a SEM stage is bombarded by a beam, as small as 1µm, of electron, resulting in various kinds of emissions such as secondary electrons, backscattered electrons, X-rays and photons. The emissions are captured using appropriate detectors. The CL detector attached to the SEM collects photon emissions delivering them to a viewing screen via a photomultiplier tube (Boggs and Krinsley, 2006). However, most CL images acquired by standard SEM are usually monochromatic (i.e., gray scale) images which vary in intensity in proportion to the density of luminescence centres (e.g., Boggs and Krinsley, 2006; Götze and Kempe, 2008; Götze, 2012) but some are equipped with red, green and blue signals that capture and display nearly representative CL colors of the samples examined (Boggs and Krinsley, 2006). Even with promising results from SEM-CL, persistent luminescence may suppress luminescent zones in carbonate minerals. This has inhibited the use of SEM-CL by carbonate researchers (Boggs and Krinsley, 2006; Bouch, 2006; Götze and Kempe, 2008). The problem arises as a result of phosphorescence which is caused by the relative delay in decay of excited electrons (Boggs and Krinsley, 2006; Bouch, 2006; Götze and Kempe, 2008). The current study examined dolomite crystals under SEM-CL and persistent luminescence did not compromise the results (Bouch,

2006), as most of the zones identified under optical CL microscopy are also recognized under SEM-CL.

UV and BL luminescence (photo-luminescence) are fluorescent properties studied using epifluorescence microscope. Photo-luminescence occurs as a result of bombardment with photon energy (visible or ultra violet light), which results in emission in the visible light spectrum (Machel and Burton, 1991). In general, the petrographic information revealed by CL and PhL are similar (e.g., Machel et al., 1991), but PhL, at times, reveals more diagenetic features (Dravis and Yurewicz, 1985). For example, while CL and photo-luminescence may yield the same crystal growth features, PhL may show organic material diagenesis and precursor depositional grains in pervasively dolomitized formations (Dravis and Yurewicz, 1985). In spite of its advantage, it is less often used in carbonate petrography, perhaps because it has been suggested that carbonates do not yield meaningful photo-luminescence (Walker et al., 1989; Machel et al., 1991) except under short wave Ultra Violet light (100-280nm; Machel et al., 1991). This is due to the notion that photon bombardment at about mean 3.4eV is believed to be less energetic than electron bombardment involved in cathodoluminescence (Machel et al., 1991).

The main objectives of this study are to correlate SIMS measured Mn, Fe and REE-Y concentrations with respective luminescence characters (under CL and PhL) of dolomite crystals and to examine the contribution of other factors, aside from elemental compositions, to luminescence. These will serve to deepen our understanding of the factors that control the luminescence (CL and PhL) features of carbonate minerals, especially in those that contain low Mn (<200 ppm. Notably Budd et al. (2000) indicated

that factors that control luminescence in carbonate minerals with low Mn (<200 ppm) have remained speculative.

4.2. METHODOLOGY

The samples and SIMS-measured composition data used for discussion are the same as those of Chapter 3. The discussion is focused mainly on the factors that control the luminescence characters observed in the burial dolomite samples of Boat Harbour Formation at Main Brook (P-154 and P-158, depths 154m and 158m respectively) and Daniel's Harbour (6-172, depth 172m) (Figs., 2.1 and 3.1).

As stated in Chapter 3 the Gatan Chroma SEM-CL was used to obtain SEM-CL images and is equipped with 3 detectors that correspond to red, green and blue wavelengths thus showing image colors that are very close to the real luminescence colors emitted from the studied samples. CL images were taken under the same analytical conditions of 20 KV acceleration voltage, beam spot size of 8.74HV and beam current of 13nA. It is key to understand that persistent luminescence inherent in previously reported SEM-CL (Reed and Milliken, 2003; Bouch, 2006) images did not compromise the luminescence features needed to undertake the current research objectives. This was confirmed by comparing the images of SEM-CL and cold cathodoluminescence (optical) of the currently studied dolomites.

On the other hand, photo-luminescence was obtained using the Axio Imager-D1m epifluorescence microscope. The dolomite samples were bombarded with wavelengths 365nm (Long wavelength Ultra Violet light, UV) and 450-490nm (blue light, BL) generated by respective exciter filters, using halogen light source (Marshall, 1988). Images were captured using CRAIC software attached to the epifluorescence microscope. Photo-luminescence excitation and examination of the emitted luminescence were carried

out using the method described in Dravis and Yurewicz (1985). More so, in line with the recommendation of Cercone and Pedone (1987), to ensure that extraneous luminescence did not influence the intrinsic visually observed luminescence of the reported samples, counterpart chips from doubly polished wafers of the dolomite samples were observed on non-luminescent (very dark to black in UV and BL) glass slides without a mounting medium (such as glue). All samples mounted on thin sections and their counterpart chips (without mounting medium) exhibited similar visually observed luminescence colors and intensities when excited by UV and BL.

4.3. LUMINESCENCE (CATHODO- AND PHOTO-LUMINESCENCE)

Results discussed in this study have been adequately described in Chapter 3 and therefore, only the very important closely related points are presented in the current chapter, where necessary. This chapter focuses on discussion and comparison of luminescence characters of distinctively zoned dolomite crystal facies from Main Brook and those of unzoned dolomite crystal facies from Daniel's Harbour localities.

Trace elements are considered the major activators (Mn^{2+} and REEs) and quenchers (Fe^{2+}) of extrinsic luminescence in carbonate minerals (e.g., Mason and Mariano, 1990; Pedone et al., 1990; Machel and Burton, 1991;Gillhaus et al., 2001; Boggs and Krinsley, 2006). In addition, intrinsic luminescence which is enhanced by defects in crystal structures is a known contributory factor to luminescence (Boggs and Krinsley, 2006). Most notably, spectral measurements indicate that emission of Mn-activated luminescence peaks at 575 nm (yellow) if Mn^{2+} occupies the Ca lattice site and 656 nm (red) if Mn^{2+} occupies the Mg^{2+} in dolomite (El Ali et al., 1993; Habermann et al., 1999; Richter et al., 2003). However, the red peak should occur more often than the yellow peak in dolomite, especially in stoichiometric phases, because of a greater affinity of Mn for Mg sites than for Ca lattice sites in the dolomite crystal structure (Walker et al., 1989). Generally speaking, Mn composition is the most important factor known to control the visible luminescence color and intensity of carbonate minerals (e.g., Machel and Burton, 1991) while varying degrees of intensity quenching appear effective at high Fe compositions (>3000 ppm; Pierson, 1981; Habermann et al., 1998).

The concentric zoning pattern observed in the distinctly zoned dolomite crystals from Main Brook in CL (Figs. 4.1A and B) is also apparent in UV and BL (Figs. 4.1D and E). This key finding supports the notion that the same activators and quenchers, or at least many of them, control inorganic-activated luminescence emissions in both cathodoluminescence and photo-luminescence (PhL) (e.g., Mason and Mariano, 1990; Pedone et al., 1990; Machel and Burton, 1991; Gillhaus et al., 2001).

Zone ID	Mn (ppm)	Fe (ppm)	Y (ppm)	∑REE (ppm)	Mn/Fe
Distinctly Zoned Core DZC crystal facies (P-154, Main Brook locality)					
1	42±10 (*n*=12)	944±532 (*n*=13)	0.76±0.37 (*n*=12)	21±9 (*n*=6)	0.073±0.06 (*n*=9)
2	38±10 (*n*=7)	972±476 (*n*=6)	1.01±0.44 (*n*=7)	19±12 (*n*=4)	0.041±0.02 (*n*=6)
3	59±18 (*n*=12)	1,647±1687 (*n*=11)	0.48±0.30 (*n*=12)	9±1.2 (*n*=6)	0.061±0.06 (*n*=9)
4	64±11 (*n*=9)	2,885±1633 (*n*=8)	0.43±0.13 (*n*=9)	11±0.75 (*n*=2)	0.030±0.01 (*n*=7)
5	70±13 (*n*=8)	4,155±1295 (*n*=9)	0.48±0.15 (*n*=8)	13±1.1 (*n*=3)	0.015±0.002 (*n*=7)

Zone ID	Mn (ppm)	Fe (ppm)	Y (ppm)	∑REE (ppm)	Mn/Fe
Indistinctly Zoned Core IZC crystal facies (P158, Main Brook locality)					
1	47±5 (*n*=20)	1,519±676 (*n*=20)	0.48±0.36 (*n*=20)	11.21±1.56 (*n*=10)	0.037±0.02 (*n*=20)
4	53±10 (*n*=14)	2,265±837 (*n*=14)	0.33±0.20 (*n*=15)	8.61±0.74 (*n*=7)	0.025±0.01 (*n*=14)
5	59±23 (*n*=17)	1,050±673 (*n*=17)	0.23±0.22 (*n*=17)	8.46±4.46 (*n*=9)	0.075±0.04 (*n*=17)

Zone ID	Mn (ppm)	Fe (ppm)	Y (ppm)	∑REE (ppm)	Mn/Fe
Unzoned dolomite crystal facies (6-172, Daniel's Harbour locality)					
Core (Zone 1)	170±57	615±308	0.22±0.0	10.39±2.1	0.338±0.2

	(*n*=14)	(*n*=15)	5 (*n*=14)	3 (*n*=12)	(*n*=13)
Rim (Zone 2)	200±79 (*n*=12)	878±688 (*n*=13)	0.16±0.07 (*n*=12)	10.73±2.82 (*n*=12)	0.352±0.22 (*n*=10)

Table 4.1. Summary of statistics of SIMS analytical results for Mn, Fe and Y. Note that for the zoned dolomite crystal facies of Main Brook locality, Zones 1 to 3 represent the crystals' core section while Zones 4 and 5 represent the crystals' rim section. Mn/Fe is molar ratio.

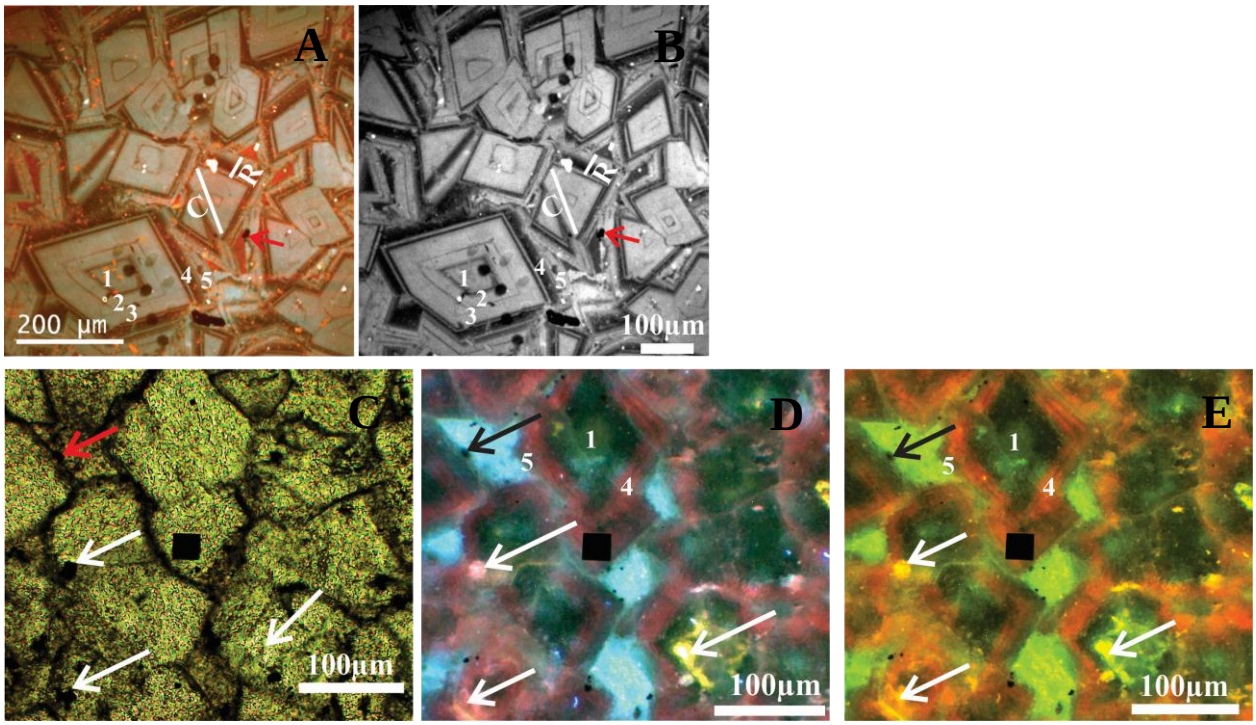

Figure 4.1. Distinctively zoned dolomite crystals from Main Brook (Sample P-154, depth 154 m)

A. SEM-CL showing typical zones (assigned Zones 1 to 5) in the burial dolomite. It shows well developed planar boundary and concentric core and rim sections Silicate grains are distributed in the rim section and most noticeable as randomly distributed bright spots in Zone 4 of the rim section. Red arrow points at non-luminescent (black) pyrite grains. (C) is core and (R) is rim sections;

B. Green component image filtered from composite color image A. Note that longer wavelength red component has been subtracted from the bulk luminescence without any loss of detail. It shows that intrinsic luminescence in addition to Mn-activated red luminescence contributed to the bulk luminescence. Red arrow points at non-luminescent (black) pyrite grains;

C. Plane polarized light image of the burial dolomite where photoluminescence images were taken (White arrows point at bituminous organic matter; red arrow indicate example of pyrite). Black box in the center is an image artifact where data were not captured by the camera;

D. UV light image of C. White arrows point at fluorescent bituminous material seen in C and black arrow points at pyrite indistinguishable from bituminous matter in C. Corresponding zones to those of SEM-CL (A and B) are labelled 1, 4, and 5. Note that Zones 2 and 3 are inconspicuous hence not labelled, however the common concentric zoning pattern in both SEM-CL and UV light is apparent. Black box in the center is an image artifact where data were not captured by the camera;

E. BL image of C. White arrows point at fluorescent bituminous material seen in C and black arrow points at pyrite indistinguishable from bituminous matter in C. Corresponding zones to those of SEM-CL (A and B) are labelled 1, 4, and 5. Note that Zones 2 and 3 are inconspicuous hence not labelled, however the common concentric zoning pattern in both SEM-CL and UV light is apparent. Black box in the center is an image artifact where data were not captured by the camera.

The inner band of the rim sections (Zone 4) of these zoned dolomite crystal facies, which emit distinct red luminescence in both CL (dull in CL; Fig. 4.1A) and PhL (Figs. 4.1D and E), has higher Mn concentration (64±11 ppm; Table 4.1) than that of the innermost band of the core sections (Zone 1; 42±10 ppm; Table 4.1) which emits predominantly greenish luminescence in CL, UV and BL (Figs. 4.1A, D and E). Plausible explanation for this phenomenon is that higher absolute Mn concentrations were the dominant control on emission of the red luminescence (e.g., Bruhn et al., 1995) of Zone 4 as expected for Mn-activated luminescence regardless of excitation method (CL, UV or BL; Pedone et al., 1990; Machel et al., 1991). Meanwhile, it seems that molar Mn/Fe ratios, lower in Zone 4 (0.03±0.01; Table 4.1) than in Zone 1 (0.073±0.06; Table 4.1), did not influence activation of the Mn-activated red luminescence except that it may probably have reduced its luminescence intensity in CL and PhL. However there is no means of verifying the extent or existence of quenching as only Zone 4 distinctly shows the red luminescence associated with Mn-activated luminescence in dolomite.

The correlation of Mn content with luminescence color in the studied dolomites is more complex than as explained above as it does not clearly account for the suppression of Mn-activated red luminescence in zones adjacent to Zone 4 (i.e. Zones 3 and 5; Table 4.1). This is seen in Zone 5 which has marginally higher Mn contents than those in the red luminescent Zone 4 (70±13 ppm in Zone 5 and 64±11 ppm in Zone 4) of the distinctly zoned dolomite crystals. However, it is interpreted that the relatively higher Fe content of Zone 5 (4,155±1,295 ppm in Zone 5 vs. 2,885±1,633 ppm in Zone 4) may have quenched its luminescence, probably supported by lower Mn/Fe ratio (Zone 5 ~ 0.015±0.002 and

Zone 4 ~ 0.03±0.01). On the other hand, it is acknowledged that suppression of red-luminescence in Zone 3 with very similar Mn contents and significantly lower Fe than those of Zone 4 is inexplicable (Fig. 4.1A). Regardless, the fact that the innermost bands of the core section (Zones 1 and 2), which are most distal to the red luminescent Zone 4 of the rim section, do not exhibit dominant visible Mn-activated red luminescence strongly implies that Mn content plays a major role in activation of the red luminescence exhibited by Zone 4 (Fig. 4.1A).

Complexity in variation of activator and quenching elements with luminescence character of carbonates has been documented in earlier studies. A comparison of SIMS analytical results with the optical CL of natural calcite reported by Savard et al. (1995) reveals 'erratic' behaviour such that any type of luminescence (viz: dull, luminescent or non-luminescent) can occur between 20-225ppm Mn composition of a carbonate under CL. These authors further suggested that parameters other than Fe and Mn concentrations also dominantly control luminescence. Furthermore, Fraser et al. (1989) reported decoupling of Mn from Fe contents with respect to the luminescence character of their zoned dolomite crystals. Although they found significant agreement between Mn contents and luminescence intensity across transects of their zoned dolomite crystals, they also realized that Fe composition, which did not show covariation with that of Mn, did not yield significant reduction in luminescence intensity (their Figs. 4 and 5).

Thus, it is possible that low Mn compositions of the currently investigated crystals (<200ppm; Table 4.1; cf. Bruhn et al., 1995), combined with other intrinsic factors such as lattice defects (Bruhn et al., 1995; Boggs and Krinsley, 2006), which are also

luminescence centers, may have resulted in a luminescence character (especially the luminescence color) that shows limited correlation with trace element (activators and quenchers) compositional zoning in crystal transects.

Intrinsic luminescence is known to occur at shorter wavelengths in carbonates. It has been shown to shift emission spectrum from orange to blue in calcite (e.g., Machel et al., 1991; Cazenove et al., 2003; Edwards et al., 2007). In support, an extraction of the green component (shorter wavelength) of the CL image of distinctively zoned dolomite crystal facies (Fig. 4.1B)-which mimics their respective composite color versions shows that Zones 1, 2, 3 and 5 of distinctively zoned dolomite crystal facies (Fig. 4.1B)-have moderate grey scale intensity (i.e., moderately bright luminescence). On the other hand the previously red luminescent Zone 4 (Fig. 4.1A) now appears non-luminescent (Fig. 4.1B). Given that Mn-activated red luminescence (longer wavelength) has been eliminated from the composite color images, it is therefore likely that the SEM-CL detector was able to image variations in intrinsic luminescence which exhibits shorter wavelength (green in this case) emissions. Variations in crystal defects is likely to be specific for each growth zone and likely varies (closely overlaps) with Mn content, thus resulting in the observed concentric zoning pattern.

Similar in concept to the luminescence features displayed by zoned dolomite crystal facies from Main Brook (Figs 4.1A and B), the lack of or poor zoning exhibited in CL by the dolomite crystals from Daniel's Harbour is also apparent in UV and BL (Figs. 4.2A to D). This lack of CL zones (unzoned crystal facies; Figs. 4.2B and C) suggests homogeneous distribution of activators and/or quenching elements. Indeed Mn content of

cloudy core and clear rim sections of most crystals are similar or show very subtle variation (Table 4.1). More so, the reported SIMS measured Mn composition in each of the core and rim section of this crystal facies is at least twice that of red luminescent Zone 4 (Fig. 4.1A) of distinctively zoned crystal facies (Table 4.1). Therefore, this may explain the brighter red luminescence displayed in CL of the unzoned dolomite crystals (Fig. 4.1A, Fig. 4.2A). In fact the red luminescence was observed to cause more significant persistent luminescence, seen in non-luminescent pyrite grain smeared by the red luminescence (Fig. 4.2A), than it did in the zoned dolomite crystal facies (Fig. 4.1A). Note that extraction of the green component (shorter wavelength) of SEM-CL image of the unzoned dolomite crystal facies (Fig. 4.2B) has moderate grey scale intensity (i.e., moderately bright luminescence) likewise suggesting that intrinsic luminescence contributed to the observed bulk luminescence.

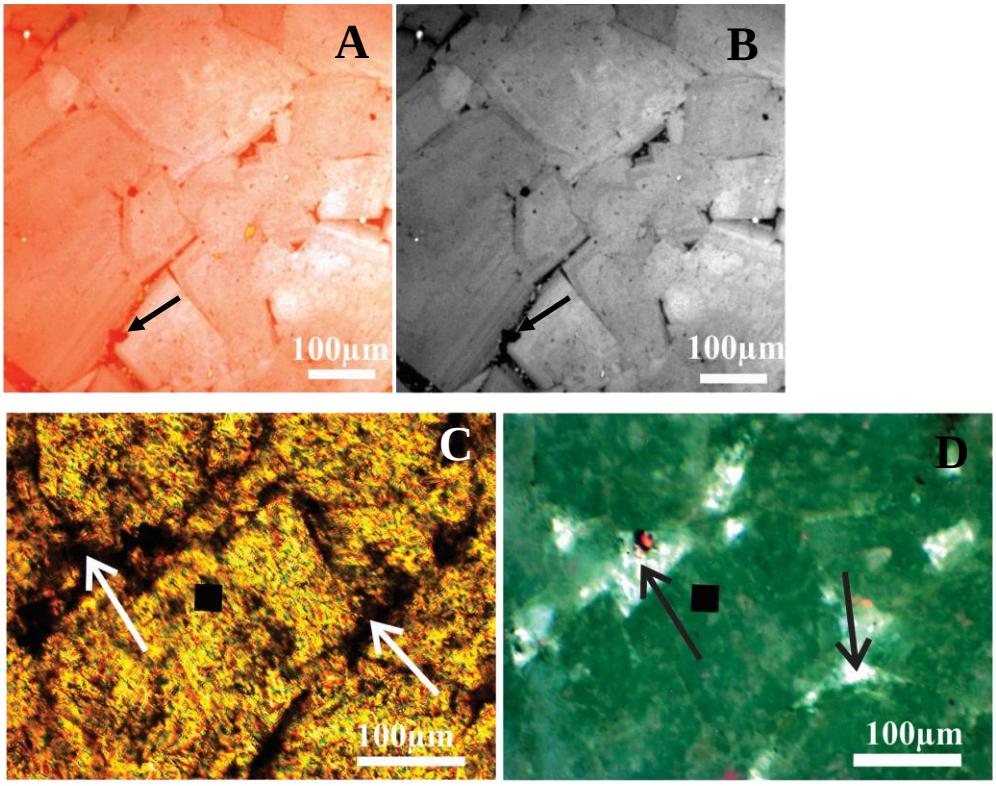

Figure 4.2. Unzoned/poorly zoned dolomite crystals from Daniel's Harbour (Sample 6-172, depth 172 m)

A. SEM-CL image showing reddish luminescence with poor (homogenous) zoning despite having cloudy core and clear rim in plane polarized light. Note that left-right 'shadow' is an artifact that imposed differential luminescence intensity on the sample. Black arrow is explained in B;

B. Green component image filtered from composite color image A. Note that longer wavelength red component has been subtracted from the bulk luminescence without any loss of detail. It shows that intrinsic luminescence in addition to Mn-

activated red luminescence contributed to the bulk luminescence. Note that non-luminescent pyrite grain (black arrow) was smeared by the red luminescence in A;

C. Plane polarized light image of the same burial dolomite where photo-luminescence image was obtained. White arrows point at bituminous matter. Black box in the center is an image artifact where data were not captured by the camera;

D. UV image of C showing poor (homogenous) zoning. Organic matter in intercrystalline areas exhibits bright fluorescence (black arrows). Black box in the center is an image artifact where data were not captured by the camera.

However, beyond the interpretation put forward, the effect that ought to accompany the magnitude of the difference in Mn composition was surprisingly elusive when the visually observed red luminescence intensity by both zoned and unzoned dolomite crystal facies in PhL was compared. This is because unlike the unzoned crystal facies, the Zone 4 in distinctively zoned dolomite crystal facies shows distinct red luminescence and even brighter (Figs. 4.1D and E) than seen in the unzoned crystal facies (Figs. 4.2D). If it is accepted that Mn content controlled the red luminescence exhibited by these dolomite crystals. Notably, this observation is in contrast to the documented notion that Mn concentration between 10-1000 ppm has a linear relationship with Mn-activated luminescence intensity in carbonates (Gillhaus et al., 2001).

Although, despite the consideration that the same activator accounts for luminescence in both CL and PhL, various photo-luminescence colors viz: red, green (bright and dark), greenish yellow, yellow, have been reportedly emitted by dolomite crystals (e.g., Durocher and Al-Aasm, 1997; Wendte et al., 1998; Haeri-Ardakani and Sanei, 2015). Haeri-Ardakani and Sanei (2015) concluded that ambient temperature of dolomite formation was responsible for the photo-luminescence colors of dolomites. The role of temperature in the photo-luminescence feature exhibited by the currently studied dolomites cannot be ascertained. This is because the same green photo-luminescence is seen in both zoned (its core section) and unzoned dolomite crystals (Figs. 4.1D, 4.1E and 4.2D, respectively), yet they were formed under different temperature regimes. Note that it was previously documented that zoned dolomite from Main Brook was likely formed in temperature of <60 ^{o}C due to lack of primary two-phase fluid inclusions while unzoned dolomite from Daniel's Harbour was formed in temperature in excess of 100^{o}C (Olanipekun et al., 2014).

It is no surprise that the REE-Y compositions of the distinctively zoned crystal facies and the unzoned dolomite crystal facies do not show a conclusive variation with luminescence characters of their dolomite crystals. This is because REEs are extrinsic luminescence centers (Boggs and Krinsley, 2006) that compete with Mn activated luminescence. However, Mn activated luminescence blots out the luminescence activated by REEs (Habermann et al., 1996) and the minimum REE concentration necessary for activation of visible luminescence in carbonates has been experimentally found to be greater than 10-20 ppm (Mason and Mariano, 1991; Habermann et al., 1999) (Table 4.1).

The combination of Mn and Fe composition with CL and PhL examination of the burial dolomite crystals therefore offers the following deductions:

- Inorganic composition controlled the luminescence observed under CL (Figs. 4.1A) as well as PhL (Figs. 4.1D and E) in the zoned dolomite crystals of sample P-154 (depth of 154 m) from Main Brook. Although fluorescing organic materials are ubiquitous in the sample but they clearly post-date the formation of the crystal (compare Figs. 4.1C, D, and E) and do not control its observed visible photo-luminescence;
- Within the same locality, while inorganic composition controlled the luminescence observed under CL, immature residual organic materials from precursor limestone controlled the luminescence observed in PhL for dolomite crystals of sample P-158 (depth of 158 m). PhL was able to reveal morphologies of precursor fossil clasts as well as other diagenetic features but it did not show the prominent concentric zoning pattern showed by its CL image (Figs. 4.3A to C). Compared with its zoned counterpart (P-154) from depth 154 m (Figs. 4.1A), this dolomite crystal facies contain relatively subtle SIMS measured Mn variations across its crystal traverse (Table 4.1) as well as incompletely developed ('embryonic') zone boundaries and mottled appearance in CL (Fig. 4.3A). Notably, earlier interpretation (Chapter 3) indicated that this sample has not been significantly/pervasively recrystallized;
- Inorganic composition controlled the luminescence observed under CL of unzoned dolomite crystal facies from Daniel's Harbour (sample 6-172; depth of

172 m). However, mature organic (bituminous) materials that coat the rhombs of the dolomite crystals likely played dominant role in the exhibited photo-luminescence features and thus dims the expected Mn-activated red luminescence. Interestingly, this sample contains dead oil in both matrix and intercrystalline pores areas in plain polarized light and it luminesces brightly in PhL (Fig. 4.2C).

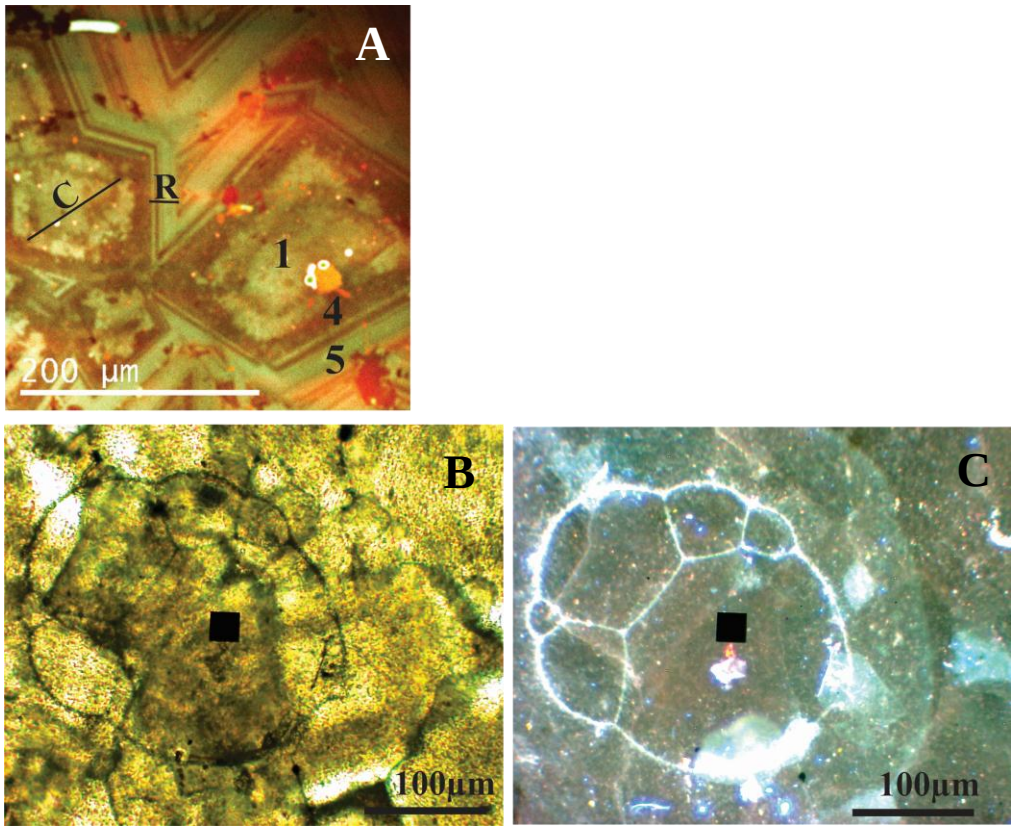

Figure 4.3. Indistinctively zoned dolomite crystals from Main Brook (Sample P-158, **depth 158 m)**

A. Typical SEM-CL image, showing concentric zoning pattern that has 'embryonic' (mottled appearance) core section with poorly developed planar boundaries in the core section of the burial dolomite crystals. Compare with the well-developed core section and sharp planar boundaries in concentric zoning shown in Fig. 4.1A. It shows the core (C) and rim (R) sections. Typical zones (assigned Zones 1, 4 and 5) are shown;

B. Plain light image of the sample showing dolomitized bioclast with invasive dolomite crystal rhombs. Such ghost of precursor calcite indicate that the dolomite

sample has not been pervasively recrystallized. Black box in the center is an image artifact where data were not captured by the camera;

C. UV light image of B showing brightly fluorescing frame of the bio-clast in B. Note that both the brown rhomb outline and the edges of the dolomite crystal in the bottom right corner in B which invades the bioclast are now much less conspicuous. Black box in the center is an image artifact where data were not captured by the camera.

It can therefore be concluded that luminescence features of the studied burial dolomite samples in PhL cannot be objectively compared with one another or with their CL features. This is because different preferential factors are exclusively responsible for the respective visible luminescence features exhibited by each of the studied sample. In perspective, this is demonstrated in the case of P-154 and P-158 from the same locality where CL features show similar concentric zoning while only residual organic materials show luminescence in PhL of P-158 without any significant noticeable inorganic trace element luminescence zoning.

4.4. CONCLUSION

- Concentric zoning pattern is exhibited by the zoned dolomite crystals from Main Brook in CL and PhL images implying that the same activators and quenchers, or at least many of them control luminescence emissions in both CL and PhL. The same phenomenon applies to unzoned dolomite crystal facies.
- The only zone in rim section of the distinctively zoned dolomite crystal facies, that emit Mn-activated red luminescence in both CL and PhL, also has relatively higher absolute Mn concentration than the core section.
- The core section lacks Mn-activated red luminescence but emits shorter wavelength luminescence. This suggests that intrinsic factors such as lattice defects also controlled its luminescence character. Removal of wavelength in red spectrum from SEM-CL image reveals moderately bright luminescence (in panchromatic mode), supporting the notion that such factor perhaps contributed to luminescence.
- The unzoned dolomite crystal facies contain higher Mn than the zoned dolomite crystals facies and is believed to account for its brighter reddish-luminescence in CL which was not noticeable in PhL.
- The absolute concentration of Mn and Fe show complex variation with the luminescence characters of the studied samples under CL and PhL. REE-Y concentrations show no variation with luminescence, perhaps due to their low absolute concentrations.

- Inorganic composition controlled the luminescence observed under CL as well as PhL in the distinctively zoned dolomite crystal facies from Main Brook.
- Inorganic composition also controlled the luminescence observed under CL of the unzoned dolomite crystal facies from Daniel's Harbour. However, mature organic (bituminous) materials play dominant role in the exhibited luminescence features of PhL and thus mask the expected Mn-activated red luminescence.

REFERENCES

Boggs, S. and Krinsley, D. H. (2006). *Application of cathodoluminescence imaging to the study of sedimentary rocks*. Cambridge, UK; New York: Cambridge University Press.

Bouch, J. E. (2006). *Development of capability in the SEM-CL of carbonates* (Scanning electron microscopy, Carbonates ed.). Nottingham, UK: British Geological Survey.

Bruhn, F., Bruckschen, P., Richter, D. K., Meijer, J., Stephan, A. and Veizer, J. (1995). Diagenetic history of sedimentary carbonates: Constraints from combined cathodoluminescence and trace element analyses by micro-PIXE. *Nuclear Instruments and Methods in Physics Research Section B: Beam Interactions with Materials and Atoms, 104*(1–4), 409-414. doi:http://dx.doi.org/10.1016/0168-583X(95)00418-1.

Budd, D. A., Hammes, U. and Ward, W. B. (2000). Cathodoluminescence in calcite cements; new insights on Pb and Zn sensitizing, Mn activation, and Fe quenching at low trace-element concentrations. *Journal of Sedimentary Research, 70*(1; 1), 217-226. doi:10.1306/D4268BD0-2B26-11D7-8648000102C1865D.

Cazenave, S., Chapoulie, R. and Villeneuve, G. (2003). Cathodoluminescence of synthetic and natural calcite: The effects of manganese and iron on orange emission. *Mineralogy and Petrology, 78*(3-4), 243-253. doi:10.1007/s00710-002-0227-y.

Cercone, K. R. and Pedone, V. A. (1987). Fluorescence (photoluminescence) of carbonate rocks; instrumental and analytical sources of observational error. *Journal of Sedimentary Petrology*, *57*(4; 4), 780-782.

Demars, C., Pagel, M., Deloule, E. and Blanc, P. (1996). Cathodoluminescence of quartz from sandstones; interpretation of the UV range by determination of trace element distributions and fluid-inclusion P-T-X properties in authigenic quartz. *American Mineralogist, 81*(7-8; 7-8), 891-901.

Dravis, J. J. and Yurewicz, D. A. (1985). Enhanced carbonate petrography using fluorescence microscopy. *Journal of Sedimentary Petrology*, *55*(6; 6), 795-804. doi:10.1306/212F8800-2B24-11D7-8648000102C1865D.

Durocher, S. and Al-Aasm, I. (1997). Dolomitization and neomorphism of mississippian (visean) upper debolt formation, blueberry field, northeastern British Columbia; geologic, petrologic, and chemical evidence. *AAPG Bulletin*, *81*(6; 6), 954-977. doi:10.1306/522B49AB-1727-11D7-8645000102C1865D

Edwards, P. R., Martin, R. W. and Lee, M. R. (2007). Combined cathodoluminescence hyperspectral imaging and wavelength dispersive X-ray analysis of minerals. *American Mineralogist, 92*(2-3; 2-3), 235-242. doi:10.2138/am.2007.2152

El Ali, A., Barbin, V., Calas, G., Cervelle, B., Ramseyer, K. and Bouroulec, J. (1993). Mn (super 2+) -activated luminescence in dolomite, calcite and magnesite; quantitative

determination of manganese and site distribution by EPR and CL spectroscopy. *Chemical Geology, 104*(1-4; 1-4), 189-202.

Fraser, D. G., Feltham, D. and Whiteman, M. (1989). High-resolution scanning proton microprobe studies of micron-scale trace element zoning in a secondary dolomite; implications for studies of redox behaviour in dolomites. *Sedimentary Geology, 65*(3-4; 3-4), 223-232.

Gillhaus, A., Richter, D. K., Meijer, J., Neuser, R. D. and Stephan, A. (2001). Quantitative high resolution cathodoluminescence spectroscopy of diagenetic and hydrothermal dolomites. *Sedimentary Geology, 140*(3-4; 3-4), 191-199.

Goette, T. and Richter, D. K. (2004). Quantitative high-resolution cathodoluminescence spectroscopy of smithsonite. *Mineralogical Magazine, 68*(1; 1), 199-207. doi:10.1180/0026461046810181.

Goetze, J. and Kempe, U. (2008). A comparison of optical microscope- and scanning electron microscope-based cathodoluminescence (CL) imaging and spectroscopy applied to geosciences. *Mineralogical Magazine, 72*(4; 4), 909-924. doi:10.1180/minmag.2008.072.4.909.

Goetze, J. and Kempe, U. (2009). Physical principles of cathodoluminescence (CL) and its applications in geosciences. (pp. 1-22) Springer.

Götze, J. (2012). Application of cathodoluminescence microscopy and spectroscopy in geosciences. *Microscopy and Microanalysis*, *18*, 1270-1284. doi:10.1017/S1431927612001122.

Habermann, D., Meijer, J., Neuser, R. D., Richter, D. K., Rolfs, C. and Stephan, A. (1999). Micro-PIXE and quantitative cathodoluminescence spectroscopy: Combined high resolution trace element analyses in minerals. *Nuclear Instruments and Methods in Physics Research Section B: Beam Interactions with Materials and Atoms*, *150*(1), 470-477. doi:http://dx.doi.org/10.1016/S0168-583X(98)00926-4.

Habermann, D., Neuser, R. D. and Richter, D. K. (1996). REE-activated cathodoluminescence of calcite and dolomite; high-resolution spectrometric analysis of CL emission (HRS-CL). *Sedimentary Geology*, *101*(1-2; 1-2), 1-7.

Habermann, D., Neuser, R. D. and Richter, D. K. (1998). Low limit of mn (super 2+) - activated cathodoluminescence of calcite; state of the art. *Sedimentary Geology*, *116*(1-2; 1-2), 13-24.

Haeri-Ardakani, O. and Sanei, H. (2015). Dolomite fluorescence Red/Green quotient; a potential new thermal maturity indicator. *International Journal of Coal Geology*, *137*, 165-171. doi:10.1016/j.coal.2014.12.005.

Hemming, N. G., Meyers, W. J. and Grams, J. C. (1989). Cathodoluminescence in diagenetic calcites; the roles of fe and mn as deduced from electron probe and

spectrophotometric measurements. *Journal of Sedimentary Petrology, 59*(3; 3), 404-411. doi:10.1306/212F8FA8-2B24-11D7-8648000102C1865D.

Kaufmann, B., Schauer, M. and Reinhold, C. (1999). Concentric-zoned calcite cements of middle devonian carbonate mounds of the mader basin (eastern anti-atlas, morocco); a combined cathodoluminescence and microprobe study. *Neues Jahrbuch Fuer Geologie Und Palaeontologie. Abhandlungen, 214*(1-2; 1-2), 95-110.

Machel, H. G. and Burton, E. A. (1991). Factors governing cathodoluminescence in calcite and dolomite and their implications for studies of carbonate diagenesis. *SEPM Short Course Notes, 25*, 37-57.

Machel, H. G., Mason, R. A., Mariano, A. N. and Mucci, A. (1991). Causes and measurements of luminescence in calcite and dolomite. *SEPM Short Course Notes, 25*, 9.

Marshall, D. J. (1988). *Cathodoluminescence of geological materials*. United Kingdom: Unwin Hyman: London, United Kingdom.

Mason, R. A. and Mariano, A. N. (1990). Cathodoluminescence activation in manganese-bearing and rare earth-bearing synthetic calcites. *Chemical Geology, 88*(1-2; 1-2), 191-206.

Olanipekun, B., Azmy, K. and Brand, U. (2014). Dolomites of the Boat Harbour formation in the Northern Peninsula, western Newfoundland, Canada: Implications for dolomitization history and porosity control. *AAPG Bulletin, 98*(4), 765-791.

Pedone, V. A., Cercone, K. R. and Burruss, R. C. (1990). Activators of photoluminescence in calcite; evidence from high-resolution, laser-excited luminescence spectroscopy. *Chemical Geology, 88*(1-2; 1-2), 183-190.

Pierson, B. J. (1981). The control of cathodoluminescence in dolomite by iron and manganese. *Sedimentology, 28*(5; 5), 601-610.

Reed, R. M. and Milliken, K. L. (2003). How to overcome imaging problems associated with carbonate minerals on SEM-based cathodoluminescence systems. *Journal of Sedimentary Research, 73*(2; 2), 328-332.

Richter, D. K., Goette, T., Goetze, J. and Neuser, R. D. (2003). Progress in application of cathodoluminescence (CL) in sedimentary petrology. *Mineralogy and Petrology, 79*(3-4; 3-4), 127-166. doi:10.1007/s00710-003-0237-4.

Rush, P. F. and Chafetz, H. S. (1990). Fabric-retentive, non-luminescent brachiopods as indicators of original delta (super 13) C and delta (super 18) O composition; a test. *Journal of Sedimentary Petrology, 60*(6; 6), 968-981. doi:10.1306/D4267659-2B26-11D7-8648000102C1865D.

Savard, M. M., Veizer, J. and Hinton, R. (1995). Cathodoluminescene at low Fe and Mn concentrations; a SIMS study of zones in natural calcites. *Journal of Sedimentary Research, Section A: Sedimentary Petrology and Processes, 65*(1; 1), 208-213.

Walker, G., Abumere, O. E. and Kamaluddin, B. (1989). Luminescence spectroscopy of Mn (super 2+) centres in rock-forming carbonates. *Mineralogical Magazine, 53*, 201-211.

Wendte, J., Qing, H., Dravis, J. J., Moore, S. L. O., Stasiuk, L. D. and Ward, G. (1998). High-temperature saline (thermoflux) dolomitization of Devonian Swan Hills platform and bank carbonates, Wild River area, west-central Alberta. *Bulletin of Canadian Petroleum Geology, 46*(2; 2), 210-265.

5 CHAPTER 5.

GENESIS AND MORPHOLOGY OF INTRACRYSTALLINE NANOPORES AND MINERAL MICRO INCLUSIONS HOSTED IN BURIAL DOLOMITE CRYSTALS: APPLICATION OF BROAD ION BEAM-SCANNING ELECTRON MICROSCOPE (BIB-SEM).

BABATUNDE JOHN OLANIPEKUN [a*]***; KAREM AZMY*** [a]

[a] **Department of Earth Sciences, Memorial University of Newfoundland. St. John's, NL, Canada A1B 3X5.**

***Corresponding Author: E-mail address: bjo852@mun.ca.**

In revision: Marine and Petroleum Geology and assigned manuscript number JMPG-D-15-00365.

ABSTRACT

Dolomites are important hydrocarbon reservoirs but the origin of porosity associated with dolomitization however remains, to some extent, a matter of debate. The study of porosity in dolomites is commonly focused on macro- and micro-meter (greater than tens of micrometer) scale intercrystalline pores that are visible in thin sections and at times in hand specimens. Meanwhile, comprehensive formation evaluation of such reservoirs should also incorporate properties of pores at the nanometer scale.

Burial dolomites of the Lower Ordovician (Tremadocian) Boat Harbour Formation of the St. George Group carbonates in western Newfoundland, Canada was subjected to Broad Ion Beam (BIB) argon milling. Thereafter, Scanning Electron Microscope (SEM) was used to examine, at high resolution, micrometer to nanometer scale pores hosted in the dolomite crystals. The ion milling is a novel approach, which provides flat surfaces that lack topography caused by differential hardness and it also reduces the probability of creating artifact induced pores that may be caused by plucking during manual sample polishing.

The study shows micro- to nanopores (<<500nm- ~3µm) that occur in the dolomite crystals. The pores are indiscriminately distributed within the core sections of dolomite crystals, which are rimmed by non-porous cortices. Rather than dissolution pits, the morphology of these intracrystalline pores indicates that they most likely originate from coalescence of anhedral-subhedral crystallites nucleated in close proximity to one another during the formation of a major dolomite crystal face. Some of the nano- to micro-pores

may have remained open while others trapped fluid or ‘accidental’ mineral (mainly calcite) inclusions as the crystals grew to form euhedral rhombs.

Calcite (the most abundant) and silicate inclusions were formed as ‘accidental’ minerals rather than as daughter minerals and are petrogenetically associated with the iterative mechanism of dolomitization.

5.1. INTRODUCTION

Research on the petrophysical properties, most especially pores at the micro- to nanometer scales, of tight formations has received tremendous attention since technological advances boosted hydrocarbon production in unconventional reservoirs. More so, the geophysical significance of nanopores has been shown to have effects on sonic velocity, fluid flow properties and electrical conductivity of a reservoir (e.g., Walker et al., 1995; Vanden Berg et al., 2014) with ultimate influence on hydrocarbon recovery. Indeed micropores could have limited connectivity such that they do not form part of the effective porosity of the reservoir. However, for carbonate hydrocarbon reservoirs, if acidized or fractured during stimulation operations, these nanopores can effectively become porous and permeable (Carbonate stimulation: Schlumberger, 2007; Fullmer et al., 2014).

A major challenge to undertaking the study of nanopores is the preservation of the pores' original morphologies during sample processing. Mechanical polishing would most certainly alter the morphology of the pores. More so, fluids used for mechanical polishing would also dissolve hydrophilic mineral inclusions (e.g., halite inclusions) thereby prohibiting accurate *in-situ* study of such inclusions that have paragenetic importance. A method that has worked well, but in silicate rocks, is examining the pores and inclusions on a freshly broken surface along cleavage planes (e.g., Anthony et al., 1984; Walker et al., 1995; Ruiz-Conde et al., 2012). However, this method is not feasible for processing carbonate minerals as they have very few large cleavable crystals and are much softer than quartz. The best known method that has proven most effective in the last decade is

dry argon milling (e.g., Loucks et. al., 2009; Heath et al., 2011; Klaver et al., 2015). It ensures that nanopores and the constituent mineral inclusions in the dolomite crystals can be studied in their natural setting. Although, X-ray micro-tomography (micro-CT) scan is a promising non-destructive application for 3D examination (e.g., Sok et al., 2010; Al-Ratrout et al., 2014) of the pores but the resolution capacity of most micro-CT equipment makes it unsuitable for micropores smaller than 1-5 microns.

Unlike siliciclastic mudstones, study of nanoporosity in carbonates is rare and most previous research on nanopores in carbonates has been done on Recent carbonates (e.g., Norbisrath et al., 2013) that retain high primary depositional porosities. More so, despite the fact that the study of porosity in dolomite is quite common in the literature (e.g., Amthor and Friedman, 1991; Gregg, 2004; Saller, 2004; Maliva et al., 2011), most of these earlier investigations focused mainly on the macro-intercrystalline pores of dolomitized carbonate sequences.

The current investigation sheds more light on the generation of nanopores in Ordovician dolomite crystals in attempt to better understand its association (as well as that of mineral inclusions) with the replacement mechanism involved in dolomitization of limestone. This is regardless of the fact that the development of porosity through dolomitization has been questioned by various authors (e.g., Lucia, 2004; Merino and Canals, 2011). Even though, it has been shown that development of micropores can be associated with dolomitization (Bubb and Perry, 1968). The main objectives of the current study are:

1. To investigate the morphology and origin of micro- and nanopores in burial dolomite crystals of Boat Harbour Formation;
2. To better understand the origin of mineral inclusions in the dolomite crystals;

5.2. DOLOMITIZATION OF ST. GEORGE GROUP CARBONATES

The St. George Group is located in western Newfoundland (Fig. 2.1) and consists of Lower Ordovician carbonate mega-sequences that were deposited during the rifting phase of the Iapetus Ocean. From the base upwards (Fig. 5.1), it consists of the Watts Bight, Boat Harbour, Catoche and Aguathuna Formations (Knight et al., 2008). The deposition of the mega-sequences is punctuated by two major disconformities namely: the Boat Harbour Disconformity (BHD) and the St. George disconformity (Fig. 5.1).

The St. George Group carbonates have been affected by varying degrees of dolomitization (Fig. 5.1; Azmy et al., 2008; 2009). Dolomitization commenced at the near surface and continued through burial. In the Boat Harbour Formation, the early dolomites are finely (<4-30 μm) crystalline, fabric retentive and commonly stratiform. The mid-burial phase is pervasive and characterized by coarser (50-300 μm), euhedral to subhedral crystals and commonly fabric destructive. The late-stage dolomites consist of coarse anhedral crystals (up to 3 mm) with sweeping extinction and usually occur as cement filling vugs and fractures (Olanipekun et al., 2014). The formation at Daniel's Harbour is completely dolomitized and the dolomites are stoichiometric in composition (Olanipekun et al., 2014). At Main Brook, dolomites account for about 40 % of the formation and the dolomites are non-stoichiometric (i.e calcium rich) (Olanipekun et al., 2014).

Development of secondary porosity in the St. George carbonates has been mainly attributed to dolomitization but minor dissolution porosity has also been reported (e.g., Azmy 2008; Knight et al., 2008). Unconformities (St. George Unconformity and Boat Harbour Disconformity; Fig. 5.1) within the Group have been fingered to play significant

role in the extent of intermediate burial dolomitization of the carbonates (Azmy et al., 2008; Knight et al., 2008; Olanipekun et al., 2014). This dolomite phase is more pervasive within the units underlying the unconformity surfaces and contains abundant intercrystalline porosity (e.g., Azmy et al., 2008; Conliffe et al., 2012; Olanipekun et al, 2014). Petrographic and geochemical results showed that the porous burial dolomite phase occurred as a result of limestone replacement rather than of earlier formed dolomite (e.g., Conliffe et al., 2012; Olanipekun et al., 2014).

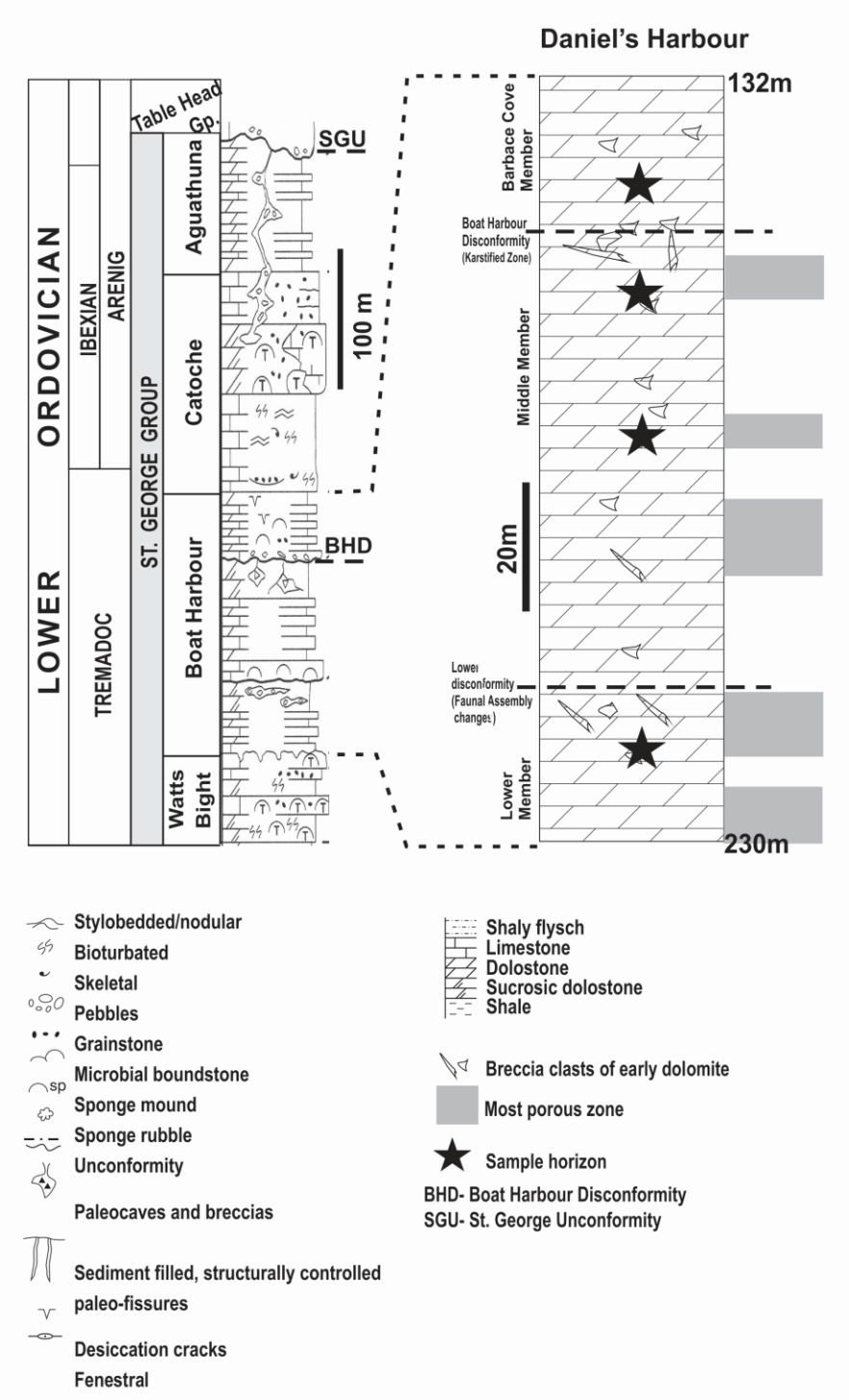

Figure 5.1. Simplified lithostratigraphy of the St. George Group in Isthmus Bay area (Modified from Knight et al., 2008) showing detailed distribution of dolostone in the Boat

Harbour Formation section at Daniel's Harbour locality (Modified from Olanipekun et al., 2014).

5.3. METHODS

Four intermediate burial dolomite samples [6-166 (depth 166 m), 6-172 (depth of 172 m), 6-184 (depth of 184 m), and 6-216 (depth of 216 m)] were taken from drill hole 12i/6-121 (N51°17′46′′, W57°27′22′′) of the Boat Harbour Formation at Daniel's Harbour (Figs. 1 and 2; Olanipekun et al., 2014). Thin sections of the dolomite samples were prepared using standard methods of grinding and polishing. Preliminary SEM examination of the samples revealed numerous pores. However, as also previously noted by Loucks et al. (2009), there is a valid concern that a significant volume of these pores might be plucked artifacts and also that the morphology of the pores might have been altered.

Ion milling was found to be the best choice for eliminating the limitations above mentioned and for achieving high quality flatness of the regions of interest in the samples. Unlike the Focused Ion Beam (FIB) milling that can only process nm^2 area of a sample, the Broad Ion Beam (BIB) argon milling has the capability to cross section a much wider (mm^2) surface area of a material. Thus all samples were prepared using the BIB argon cross section polishers.

Sample 6-172 was BIB argon polished in a Leica ion milling system EM TIC 3X cryo cross section polisher. The equipment was set to operate at 7kV acceleration voltage, 2.6mA gun current, -70°C cooling temperatures and 4.5 hours milling time. Samples 6-166, 6-184, 6-216 were BIB argon polished in a Hitachi ion milling system IM 4000. It was set to operate at 6kV acceleration voltage, 1.5kV discharge voltage and a rotation of ±30° at 30 reciprocation/minute.

Subsequent to BIB argon cross section milling, the samples were examined uncoated by high resolution (< 10nm at 30kV) FEI MLA 650F Scanning Electron Microscope (SEM) which is equipped with energy dispersive X-ray (EDX) microanalytical system. The samples were not coated in order to avoid a deposition of the coating material in pores thereby masking the morphology of the pore walls and basal parts.

5.4. RESULTS

For descriptive purposes, the studied crystals are at times delineated into core and rim sections. The core is regarded as the inner section of the crystal that has abundant nanopores and calcite inclusions which are rare or lacking in the rim sections (Fig. 5.2A). Such division is less distinct for crystals in which nanopores are indiscriminately distributed across the whole crystal surface. Furthermore, description of pores is based on morphology as revealed by SEM examination, subsequent to ion milling of the samples.

5.4.1. Micropores

Shape, size and abundance

Visual estimate revealed by SEM examination suggests that nano- and micro-pores abundance ranges from 7 to 27% in each examined dolomite crystal (Figs. 5.2 to 5.4). These dolomite crystals contain abundant pores particularly within the exposed rhombohedral {10bar14} crystal face. The intracrystalline pores are commonly confined to the core sections of crystals while their rim sections, which abut against intercrystalline pores, contain much fewer pores and mineral inclusions (e.g., Fig. 5.2A).

Using the pore-size classification of Loucks et al. (2012; their Figure 3), the intracrystalline pores of the Boat Harbour dolomites, as shown in 2-D SEM images (Figs. 5.2 and 5.3) fall within the designated size ranges of nanopores (<1nm to <1 μm) and micropores (<1 μm and <62.5 μm). However, based on visual estimates, more than 40%

of the total number of intracrystalline pores in the dolomite crystals are much less than <0.25 μm. Thus they could not be measured with high level of accuracy, because of limitations in the optimal resolution at which the images were obtained. Therefore, the pores are collectively referred to as nanopores henceforth. It is noteworthy that as much as 70% of the nanopores in sample 6-166 (Fig. 5.4A) from depth 166m, shallowest of the studied samples, are < 0.15 μm (approximately).

The nanopores are mostly polyhedral (Figs. 5.2 and 5.3). In cross section, longest dimensions of the measured pores range from <0.25μm to ~9μm (1.57±0.97μm; Fig. 5.5) while their length/width ratio (L/W) range from 0.78 to 5.24 (1.71±0.72 and median of 1.53; Fig. 5.5; in perspective, the L/W ratio of a square is 1). Furthermore, Figure 5.2 reveals that the morphology of the intracrystalline pores (Figs. 5.2B and F) as well as their distribution patterns (Fig. 5.2B, 5.2E and F) congruently depict regular crystallographic orientation, which mimics a dolomite crystal's perfect rhomboidal shape of the {10bar14} face.

Individual pore morphology is commonly made up of planar and straight outlines that depict their polygonal shapes and in some cases combined with curved outlines resulting in ellipsoidal shapes (Figs. 5.2 and 5.3). Pores that have combination of planar and curved edges are less common and many of the pores are elongated (i.e. have relatively high L/W ratio; Fig. 5.5). The nanopore geometries are commonly shaped and oriented to form protruding apices of micro-rhombs that have apical angle range of 60^{o} to 90^{o} (e.g., Fig. 5.2C). Relatively larger (>4 μm) nanopores often have bulbous outgrowths on their walls and basal parts (Fig. 5.2C).

The intracrystalline nanopores may be partially or completely filled with mineral inclusions (Fig. 5.2C) that are often euhedral (Fig. 5.2D). These pores, occasionally, assume the shapes of the euhedral mineral inclusions within the dolomite rhombic crystal face (Fig. 5.2B). Notably, nanopores are much less abundant in the dolomite crystals that exist in intercrystalline pores and in rim sections of some crystals (Fig. 5.2A). More so, where nanopores are found in rim sections, they are generally smaller (visual estimate) than those found in their respective core sections (e.g., Figs. 5.2A and 5.4B).

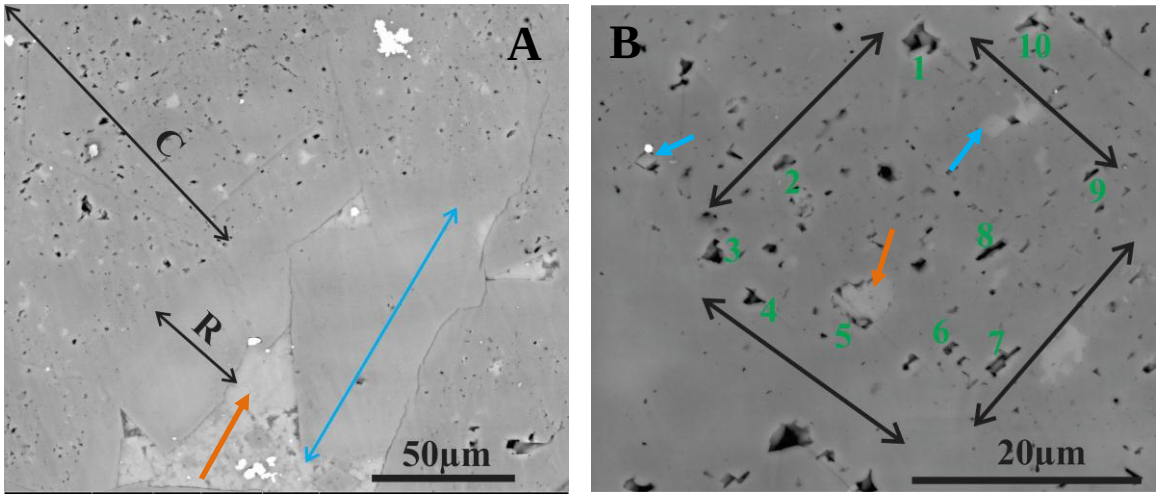

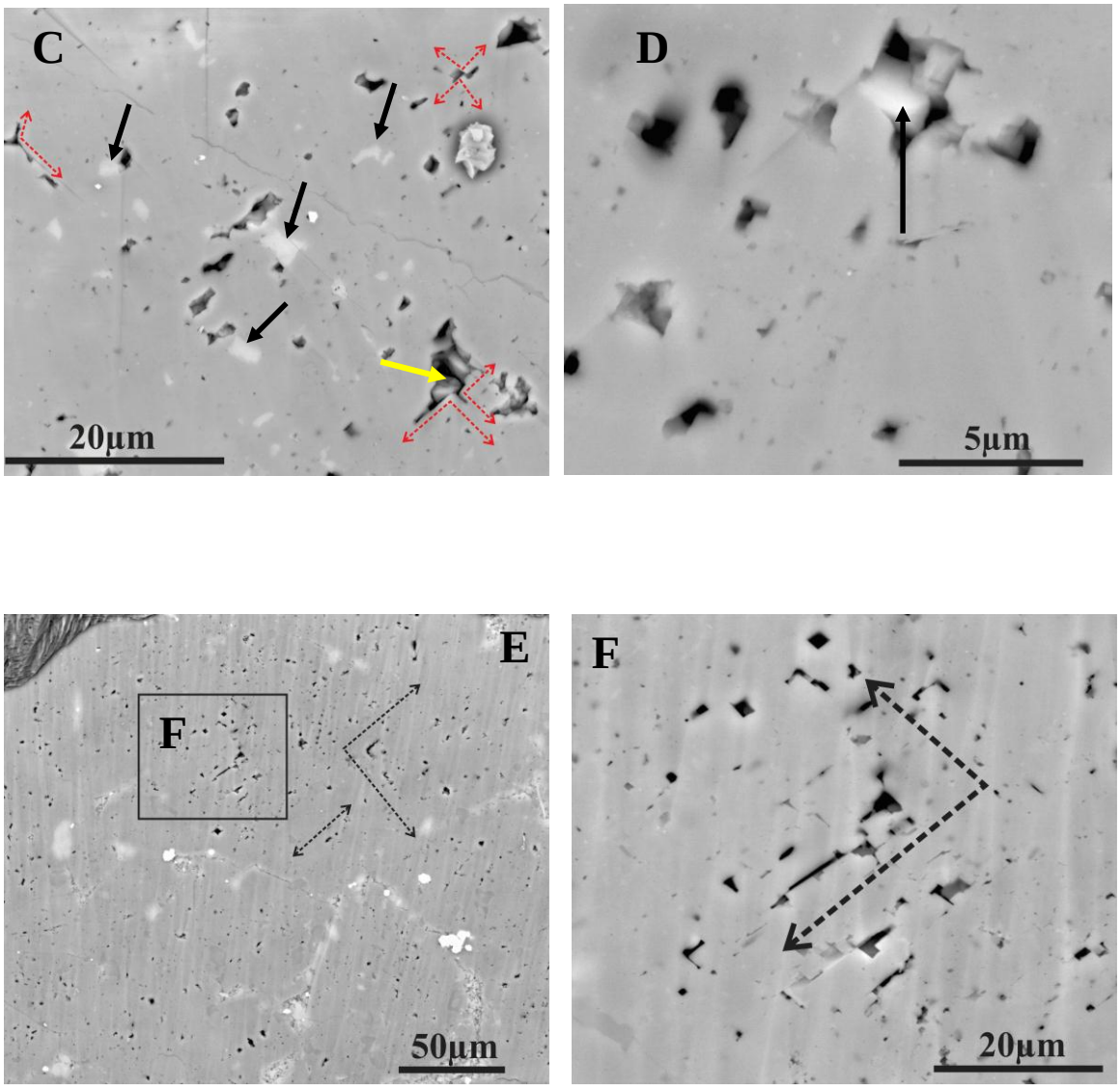

Figure 5.2 (A-F).

A: SEM image showing dolomite crystals. “C” is core and “R” is rim of a crystal. Blue arrow points at a dolomite crystal in intercrystalline pore. Note the paucity of nanopores in rim compared with their dense distribution within the core section of the crystals. Orange arrow points at typical authigenic K-feldspar in intercrystalline areas. Sample 6-172 (depth 172m);

B: SEM image showing spectrum of nanopores with some having calcite inclusions (blue arrows) and a K-feldspar inclusion (orange arrow) within a dolomite crystal. Note that the morphologies of pores (e.g., pores labelled 1 to 10) enclosed by double headed arrows show their edges are oriented such that they mimic the shape of rhombs if extended to join one another in the directions indicated by the arrow heads. Sample 6-172 (depth 172m).

C: SEM image showing spectrum of nanopores and calcite inclusions (black arrows) within a dolomite crystal. Note bulbous outgrowth in pore (yellow arrow). Red double headed arrows trace the apices of micro-rhombs that form pore edges. Sample 6-172 (depth 172m).

D: SEM image showing spectrum of nanopores within a dolomite crystal at higher magnification. The euhedral mineral inclusion enclosed in pore (black arrow) is a calcite crystal. Sample 6-172 (depth of 172m).

E: SEM image showing suite of nanopores and the crystallographic orientation depicted by their edges and their distributions (double headed arrows). Feature on the top left corner is an edge of the BIB cross section. Sample 6-216 (depth 216m).

F: SEM image of spot F in Fig. 5.2E at higher magnification. It shows a suite of nanopores and the crystallographic orientation depicted by their edges and their distribution patterns (double headed arrow). Sample 6-216 (depth 216m).

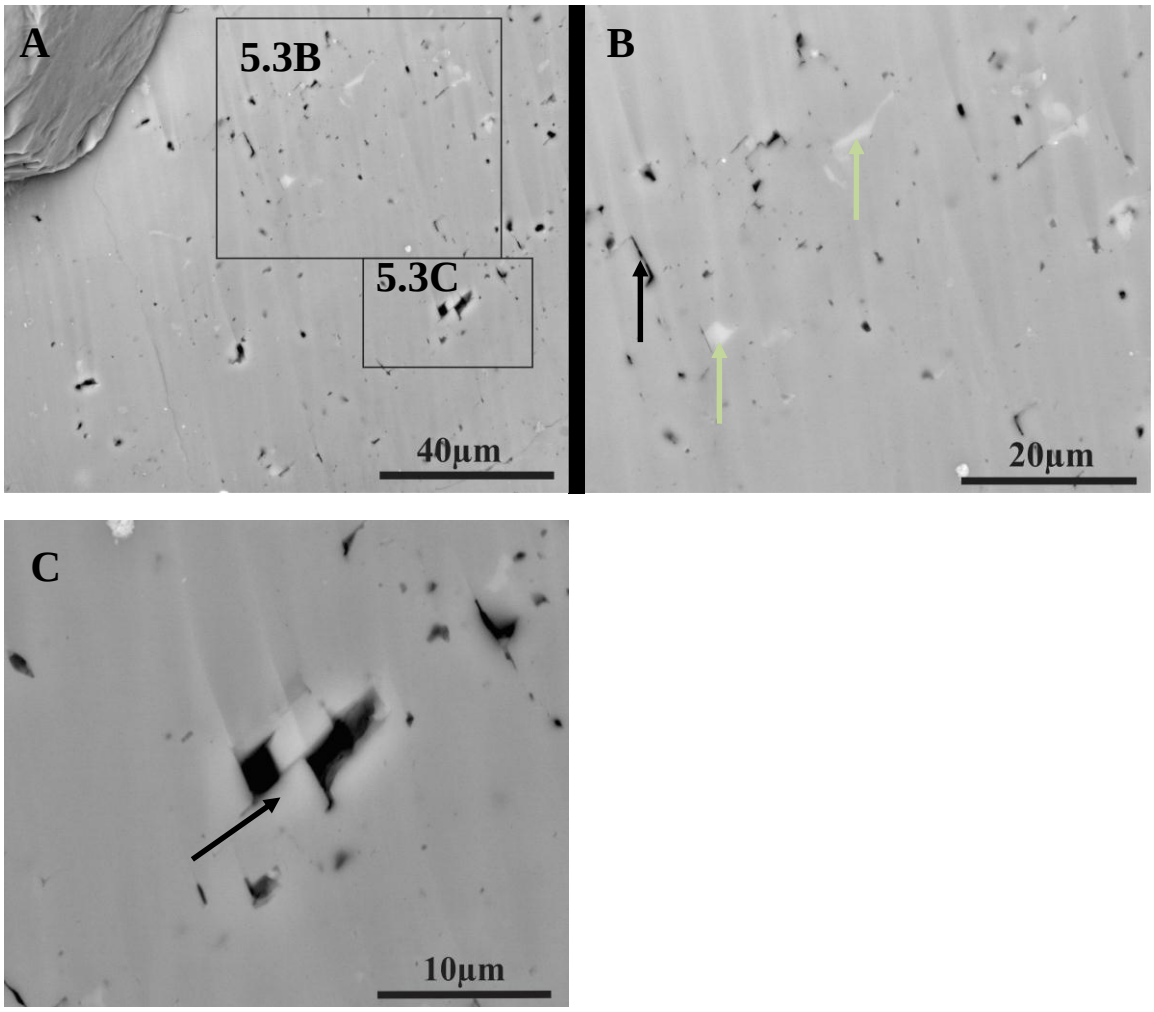

Figure 5.3 (A-C).

A. SEM image of nanopores and calcite distribution within a crystal in sample 6-184. (Depth 184 m). The top left corner is an edge of the BIB cross section.

B: SEM image spot 5.3B (inset) in 5.3A at higher resolution. Black arrow points at an area showing the edge and apices of a micro-rhomb and void space beside it. Typical calcite inclusions are shown by green arrows.

C: SEM image of spot 5.3C (inset) in 5.3A at higher resolution. Black arrow point at an area showing the apices of a micro-rhomb protruding into pore located at the centre.

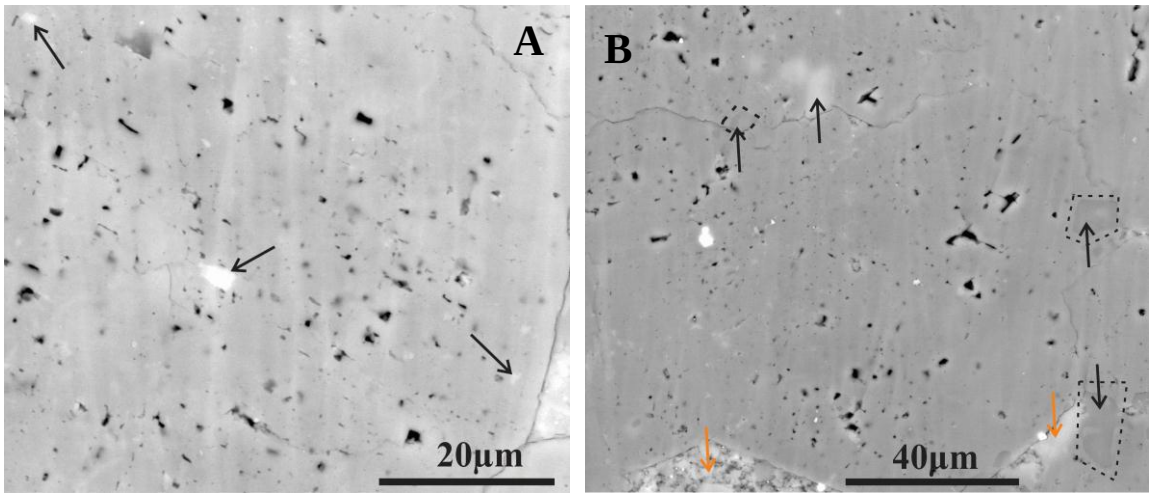

Figure 5.4 (A-B).

A: SEM image showing abundant calcite inclusions (black arrows) and nanopores within a dolomite crystal of sample 6-166 (Depth 166m - shallowest examined sample);

B: SEM image showing nanopores distribution in sample 6-216 but paucity of calcite inclusion. Black arrows point at authigenic silicates intruding into crystal edges; purple arrows refer to silicates in intercrystalline pores. Note that lighter grey silicate grains are K-feldspar while the darker grey counterparts are authigenic silica (as revealed in BSE mode). Depth 216m (deepest sampled depth).

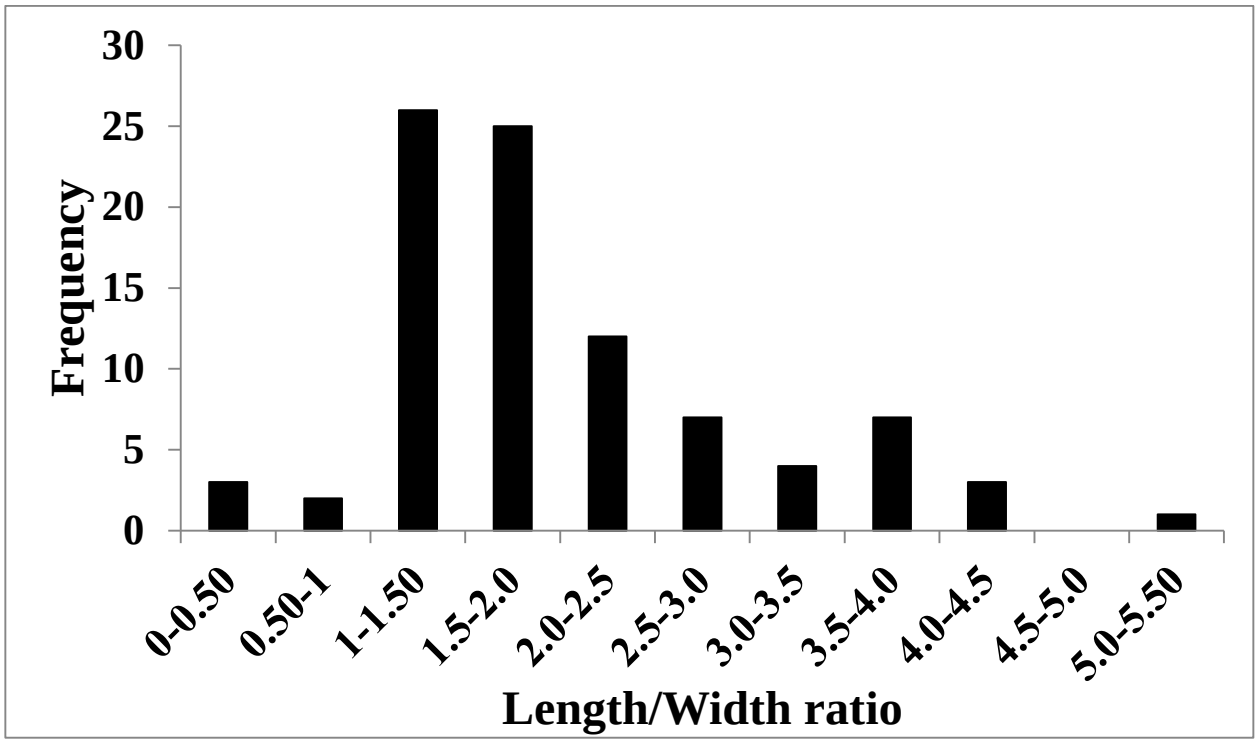

Figure 5.5. Frequency distribution chart showing the length/width) ratios of the studied nanopores. It exhibits the dominance of elongate pores. Detail in text.

5.4.2.Mineral inclusions

Calcite is the most abundant mineral inclusion found in the dolomite crystals from depths 166 m, 172m, and 184m and. While calcite inclusions are most abundant in the sample from 166 m (sample 6-166; Fig 5.4A), shallowest sampled depth, they were not observed in the sample from 216 m (Sample 6-216 at 216 m; Fig 5.4B), deepest sampled depth.

Calcite inclusions are mostly confined to the cores sections of the dolomite crystals. Their shapes are either irregular or euhedral (Figs. 5.2A, 5.2B, 5.2C, 5.3B) and at times silica rich. Similar to nanopores, they were not observed in the rims of the dolomite crystals that have core and rim sections. They were also not observed in crystals nucleated as cement (Figs. 5.2A) in intercrystalline areas. On the other hand, silicate mineral inclusions are less abundant within the crystal (Fig. 5.2B) but commonly occur as intrusive grains at the edges, at times sandwiched between adjoining dolomite crystal boundaries (e.g., Fig. 5.4B). Silicate minerals typically occur as cements, especially, co-existing silica and K-feldspar occur alongside pyrite crystals in intercrystalline areas of the studied dolomites (Figs. 5.2A and 5.4B).

5.5. DISCUSSION

5.5.1. Origin of intracrystalline nanopores

The described morphology of the nanopores is best explained by the physical process of crystal growth. The formation of a dolomite crystal (like most crystals) is initiated by the formation of various nuclei. Once formed, by addition of more major elements, these nuclei grow to become crystallites (i.e. sub-crystals that are mostly nanometer sized rhombs) that coalesce to form a major crystal face. This major crystal face is thus a sub-crystal aggregate (Dhanaraj et al., 2010). At this stage, the nuclei are typically bounded by specific lattice planes that depict the dolomite's crystal structure. Notably, similar process has been documented by Casey et al. (1988) who reported individual rutile grains that grow from aggregates of smaller crystals. The alignment of the crystallites' faces during the agglomeration of the crystallites is commonly imperfect such that it may occur in a random fashion. The resulting misalignments thus create void spaces between the crystallites. This is in agreement with Goldstein and Reynolds (1994, Pp 13) which averred that voids are created between 'sub-crystals of composite crystals' and that they commonly trap fluids.

Consistent with the crystal growth process explained above, the morphology of most of the examined intracrystalline nanopores is defined by planar edges and protuberance of micro-rhombic apices (Figs. 5.2C, 5.2F and 5.3C). More so, it is likely that this process also accounts for the crystallographic orientation exhibited by the systematic intracrystalline pore distributions (Figs. 5.2C, 5.2F and 5.3C) in the studied dolomite crystals.

Constraining the origin of nanopores requires a sound understanding of the paragenetic sequence associated with the formation of the host crystal. Therefore, it is imperative to determine if these nanopores are primary or secondary in origin, with respect to the genesis of their host dolomite crystals. Primary pores are those that are syngenetic with their host while secondary pores are those that post-date the formation of their host (e.g., as a result of dissolution) crystals. As explained, the nanopores in the currently studied dolomite crystals occur as voids between crystallites, especially where three or more crystallites abut against each other (Figs. 5.2B, 5.2C, 5.2D, 5.2F, 5.3B and 5.3C). Given that the agglomeration of these crystallites' respective faces formed the dolomite crystals' major faces, the formation of the nanopores has to be associated with the dolomite crystal growth condition hence they are primary in origin. Once formed, some of these nanopores likely remained open while some trapped fluid or solid 'accidental' inclusions during dolomite crystal growth.

Furthermore, it is possible that the development of these nanopores is strongly associated with the dissolution-precipitation process involved in dolomitization (replacement) of the precursor carbonate. This interpretation is based on the notion that mineral replacement processes often yield microporosity due to molar volume changes and solubility differences between the dissolving and the precipitating mineral (e.g., Putnis and Putnis, 2007). Most specific to the current study, Zempolich and Baker (1993) carried out dolomitization experiment on aragonite ooids and found that the dolomite formation started with nucleation of small clusters of sub-hedral (1-2μm) crystallites which grew to

form euhedral crystals. Their results show that dolomitization process yields microporosity in the replacive dolomite.

Dolomite replacement of calcite has been reported to account for, in theory, 13% volume decrease (Dolomite unit cell volume ~ 320Å; Calcite unit cell volume ~368Å) in the resulting dolomite. Thus it yields a porosity increase (Warren, 2000; Lucia, 2004) due to the molar volume difference between dolomite and calcite. However some authors may disagree with this hypothesis. This is because such magnitude of volume decrease, associated with dolomitization is not always ubiquitous in natural dolomites (e.g., Lucia, 2004; Merino and Canals, 2011); although it seems that the role played by conditions of dolomitization (open vs. closed system) are often not comprehensively considered. Regardless, porosity generation as a result of volume reduction in low temperature replacement mineral reactions has been documented in recrystallization of feldspar and KBr-KCl replacement reactions (Putnis and Mezger, 2004). This is a viable clue that such mechanism could take place during dolomitization. In a similar fashion, the replacive sections (core) of the currently studied dolomite crystals (Fig. 5.2A) contain abundant nanopores. On the other hand, those dolomite crystals interpreted to have formed as cement (rim sections and crystals nucleated in intercrystalline pores) rarely have pores, even though they most likely grew under the same condition as the former. In fact, replacement reactions, regardless of volume difference can yield nanoporosity because those that involve volume increase have also been shown to generate microporosity (e.g., Ruiz-Agudo et al., 2014). This has been documented for the replacement reaction of aragonite by calcite (cf. Al-Aasm and Azmy, 1996) whereby the calcite overgrowth

(cement) formed nearly perfect rhombohedral calcite crystals devoid of porosity while the pseudomorphic replacement calcite crystals contain abundant pores (Perdikouri et al., 2011). However, Merino and Canals (2011) which promoted coupled dissolution-precipitation mechanism for dolomitization, averred that it is a volume-for-volume process that essentially does not yield porosity except through dissolution by intervening fluids. In contrast, the intracrystalline nanopores in the current study have mostly planar edges and have distributions that attain a crystallographic bias. Molar volume reduction and the process of coalescence of crystallites with misaligned faces offers the best explanation for the origin of nanopores found within these dolomite crystals.

Alternatively, these nanopores could be dissolution pits formed as a result of dissolution of calcite inclusions. This possibly occurred due to higher solubility of calcite (Ksp ~ -8.45; Morse and Mackenzie, 1990; their Table 2.3) than that of dolomite (ordered dolomite: Ksp ~ -8.6; Langmuir, 1997; their Table 6.1) during the replacement reaction and subsequently filled or partially filled with mineral inclusions. Dissolution would have resulted in high abundance of round edged pores. As seen in the images and confirmed by the mean and median L/W ratio (Fig. 5.5), most of the pores are elongated and not circular. More so, paucity of rounded edges around the nanopores suggests that dissolution was not likely. Regardless, etch pits in dolomite minerals usually develop preferential dissolution feature that mimics micro rhomb (e.g., Kaczmarek and Sibley, 2007, their Figures. 9, 11 and 12; Jones, 2013, his Figure 5).

The nanopores of the core section (e.g., Fig. 5.2A) should have been occluded by cement or simply closed during the subsequent formation of the rim and intercrystalline cement.

Possibly, the interconnectivity of the pores probably became limited and micro-permeability was also likely reduced due to pore coarsening during textural equilibration of the dolomite crystals. This could have led to a suspected isolation of the intracrystalline nanopores (Figs. 5.2 to 5.4), many of which likely trapped fluids during the process (cf. Ruiz-Agudo et al., 2014).

5.5.2. Mineral inclusions and their petrogenetic significance

Calcite inclusions are the most abundant inclusion in the dolomite crystals and are typically distributed within the core sections of the crystals. Chiefly, the Ca for these calcite inclusions is most likely sourced from the precursor calcite during dolomitization. If so, given that the calcite inclusions are hosted in and restricted to the core section (Fig. 5.2C); it can thus be said that the core section is a replacive section of the crystal. The core sections of replacive dolomites are commonly known to contain evidence of replacement (see e.g., Sibley, 1982; Warren, 2000 for reviews). Thus, as nanopores and calcite inclusions are largely considered exclusive replacive features of the studied dolomite crystals, their relatively low distribution density in the rim section suggests that the overgrowth rim formed as cement. This is further supported by the paucity of nanopores and calcite inclusions in dolomite cement crystals precipitated in intercrystalline areas (e.g., Fig. 5.2A).

Calcite inclusions are relatively scarce in the deepest sample (Sample 6-216 at 216 m; Fig. 5.4A) relative to its shallowest counterpart (Sample 6-166 at 166 m; Fig. 5.4B). If it is accepted that precursor calcite chiefly supplied the Ca for dolomitization, this suggests

that the deeper section has probably undergone more iterative episodes of dolomitization than the shallower section. Thus likely resulting in the removal of calcite inclusions due to replacement or dissolution.

In detail, the dolomitization process that resulted in formation of the calcite inclusion is better understood from the dolomitization mechanism advanced by Merino and Canals (2011). This mechanism is most applicable to dolomite formation in burial environment where relatively high temperature overcomes kinetic inhibition. The mechanism takes place at the nano- to micro-meter scale of the local reaction site and it involves a brine that is not originally super-saturated with respect to dolomite. Rather, the Mg-rich and CO_3^{2-} basinal brine is said to be a slightly acidic fluid (Merino and Canals, 2011) that can also be super-saturated with respect to several minerals including silicate minerals. In the case of dolomitization of calcite, the fluid dissolves the precursor calcite and becomes saturated with dolomite as the dissolving phase contributes more Ca, and CO_3^{2-}. The process is a high rate of episodic dissolution-precipitation event (Merino and Canals, 2011) where Mg is sequestered and shortly replenished at the end of each episode by a pulse of fluxing Mg-rich brine that also causes more matrix calcite dissolution. During the replacement process, calcite sub-grains may grow as foreign minerals instead of dolomite sub-grains, if the system temporarily reached relatively higher Ca/Mg in the brine prior to the flux of more Mg-rich brine or if the solvent is not well mixed/homogeneous. Such calcite grains may be trapped in the dolomite during its crystal growth (Figs. 5.2A, 5.2B and 5.3B).

This is even more so if the effect of crystal growth rate is considered. High growth rate has been found to favour development of mineral inclusions and pores (Watanabe, 1987) while low growth rate gives room for 'self purification' (Zerfoss and Slawson, 1956) in the growing crystals such that the impurities are concentrated in the residual fluid and eventually precipitate out as cement in intercrystalline pores (e.g., Figs. 5.2A and 5.4B).

This may explain the relatively homogeneous surface (paucity of nanopores and calcite inclusions) exhibited by the rim section of some matrix dolomite crystals and dolomite crystals nucleated as cement in intercrystalline areas (Fig 5.2A). Most likely, at this stage of the dolomite crystal formation, reduction in the fluid concentration of Ca, Mg and CO_3^{2-} at the culmination of episodic dolomite formation led to a drastic decrease in rate of dolomite crystal growth. This likely gave room for 'self purification' (Zerfoss and Slawson, 1956) that resulted in relative homogeneity of the crystal faces. Indeed fluid and mineral inclusions have been demonstrably found in carbonate cement crystals (see examples in Benito et al., 2006). However, the fact that these defect-induced features were rarely observed in the currently studied dolomite cement crystals (e.g., Fig. 5.2A) suggests that the cement phase grew with less defect density than the replacive phase (i.e., the crystal's core section). Notably, slow growth rate has been shown to contribute to better growth of crystal forms (Dhanaraj et al., 2010; Pp 97, 133) with minimal defects. In tandem, change in solution stoichiometry has been documented to influence the growth rate of carbonate minerals and the extent of their replacement reactions (Perdikouri et al., 2011, Pp 11).

Silicate minerals are volumetrically less abundant in intracrystalline pores of the dolomite crystals, except when they bridge adjoining crystals (Fig. 5.2), relative to calcite inclusions (Fig. 5.4). Rather, the silicate cement fills most of the intercrystalline areas, which post-date the formation of the dolomite crystals (Fig. 5.4). This implies that the silicates that fill both the intercrystalline and occasionally intracrystalline pores are cogenetic. If so, such intracrystalline pores must have remained open after the completion of the dolomite crystal growth as suggested in previous section.

The silicate cements, most abundant in the intercrystalline areas, including vein, consist mainly of authigenic feldspar and silica. They show extraordinary chemical purity (i.e., mono-mineralic; K, Al, Si and O) and microcline is the dominant feldspar member observed in the intercrystalline pores of the current study. Authigenic feldspars have been reported in Cambro-Ordovician carbonate sequences (Kastner, 1971; Buyce and Friedman, 1976; Parnell, 1994). It forms in the presence of K- rich fluid (Kastner, 1971), which when coupled with the occurrence of silica clearly indicates that the dolomitizing brine contain components that were derived from terrestrial sources (cf. Kastner, 1971). Interestingly, precipitation of silicate minerals is favoured at temperature >70-80^{o}C (Bjorlykke and Egeberg, 1993), which is the range documented as estimated formation temperature of the burial dolomites of Boat Harbour Formation (Olanipekun et al., 2014). Kastner (1971) noted that authigenic feldspar could precipitate from as small as a fluid volume hosted in intergranular pores; hence it is not necessary to invoke high pore volumes of fluid for the formation of authigenic feldspar.

It could be argued that the intracrystalline inclusions (Figs 5.2 to 5.4) were late phase cements that post-date the whole crystal formation and precipitated in pre-existing intracrystalline pore spaces. While this may hold true for the silicates, it doesn't explain the origin of the calcite inclusions. In light of the posited dolomitization process explained above, such calcite precipitation would occur if, after whole dolomite crystal growth, the pore fluid became supersaturated with respect to calcite. However, if the fluid precipitated calcite it would have done so into pre-existing intracrystalline void spaces, as well as into intercrystalline pore areas. Spectral analyses (EDX) did not reveal any occurrence of calcite in intercrystalline areas; clearly indicating that this notion is improbable for the origin of calcite inclusions in the studied dolomite crystals.

Furthermore, classification of the inclusions as daughter minerals or accidentally trapped minerals provides an important clue for understanding the paragenetic history of the dolomite crystals. Daughter minerals are precipitated from trapped fluid inclusions (Goldstein and Reynolds, 1994; Pp 26/213) hence post-date the formation of the whole dolomite crystals (Metzger et al., 1977). Broadly speaking, this is because, trapped fluids in inclusion cavities do not nucleate daughter minerals unless their condition (principally temperature and pressure) of entrapment is significantly changed (Goldstein and Reynolds, 1994). In most cases such changes occur if they are transferred to atmospheric conditions. The associated cooling effect causes most mineral phases, that have normal solubility, to crystallize out of the included solution, if they attain super saturation in the fluid, and they homogenize upon heating to their (estimated) entrapment temperature (cf.

Roedder, 1972). However, within the sedimentary environment, calcite is known for its retrograde solubility that causes it to remain in solution with decreasing temperature.

In view of the above, the observed calcite inclusions hosted in the currently studied dolomite crystals are likely not daughter minerals but accidentals. This implies that they are syngenetic with the discrete dolomite crystal growth section in which they are found. In support, daughter mineral inclusions are precipitated in a pre-defined cavity and are commonly surrounded by significant spatial volume within the cavity (e.g., Roedder, 1972; Metzger et al., 1977; Anthony et al., 1984; Frezzotti and Ferrando, 2007, their Fig. 5) as they precipitate out of the minute volume of trapped fluid in the respective cavities. More so, daughter minerals have been shown to be somewhat detachable from and not embedded in the cavity in which they are formed (cf. Metzger et al., 1977; Anthony et al., 1984; Frezzotti and Ferrando, 2007, their Figure 5). On the other hand, accidentals would be embedded in the cavity in which they are found as they become engulfed by their surrounding host growth sector during crystal growth. Thus they may occupy up 70% of, or completely fill the nanopore spaces. In agreement, most of the observed calcite inclusions completely fill their cavities as they are engulfed by the dolomite crystal matrices (e.g., Figs. 5.2A, C and Fig. 5.3B).

5.6. CONCLUSIONS

- Intracrystalline nanopores developed as a result of imperfection associated with the alignment process of crystallites' agglomeration. This scenario likely resulted in the morphology of the nanopores which is typically made up of protuberances of rhombic apices and has planar edges.
- The origin of mineral inclusions in intracrystalline nanopores is related to the mechanism of dolomitization that involves dissolution of precursor carbonate mineral (calcite or early dolomite) and precipitation of dolomite.
- The Ca for the calcite inclusions in nanopores is likely sourced from the precursor calcite. SEM examination shows that these inclusions are hosted in and restricted to the crystal cores. Thus it can be said that the core is a replacive section of the crystal. In contrast, the crystal rim likely formed as cement, as SEM examination suggests paucity of nanopores and calcite inclusions in them. Consistent with this notion, nanopores and calcite inclusions are relatively rare in dolomite cement crystals precipitated in intercrystalline areas.
- The calcite inclusions are interpreted to be accidental minerals, syngenetic with host growth zones and not daughter minerals that post-date the growth of whole dolomite crystals.

REFERENCES

Al-Aasm, I., Azmy, K., 1996. Diagenesis and evolution of microporosity of Middle-Upper Devonian Kee Scarp reefs, Norman Wells, Northwest Territories, Canada: petrographic and chemical evidence. AAPG Bulletin. 80, 82-100. doi:10.1306/64ED8750-1724-11D7-8645000102C1865D.

Al-Ratrout, A., Kalam, M.Z., Gomes, J.S., Jouini, M.S., Roth, S., Lemmens, H., Mtawaa, B., 2014. Narrowing the loop for microporosity quantification in carbonate reservoirs using digital rock physics and other conventional techniques. International Petroleum Technology Conference, Qatar (IPTC-17702-MS). doi:10.2523/IPTC-17702-MS.

Amthor, J.E., Friedman, G.M., 1991. Dolomite-rock textures and secondary porosity development in Ellenburger Group carbonates (Lower Ordovician), West Texas and southeastern New Mexico. Sedimentology 38, 343-362.

Anthony, E.Y., Reynolds, T.J., Beane, R.E., 1984. Identification of daughter minerals in fluid inclusions using scanning electron microscopy and energy dispersive analysis. Mineralogical Society of America 69, 1053-1058.

Azmy K., Knight I., Lavoie D., Chi G., 2009. Origin of dolomites in the Boat Harbour Formation, St. George Group, in western Newfoundland, Canada: implications for porosity development. Canadian Petroleum Geology 57, 81-104.

Azmy K., Lavoie D., Knight I., Chi G., 2008. Dolomitization of the lower Ordovician Aguathuna formation carbonates, Port au Port peninsula, western Newfoundland, Canada: implications for a hydrocarbon reservoir. Canadian Journal of Earth Sciences 45, 795-813.

Benito, M.I., Lohmann, K.C., Mas, R., 2006. Micro-sized dolomite inclusions in ferroan calcite cements developed during burial diagenesis of Kimmeridgian reefs, northern Iberian Basin, Spain. Journal of Sedimentary Research 76, 472-482. doi:10.2110/jsr.2006.042.

Bjorlykke, K., Egeberg, P.K., 1993. Quartz cementation in sedimentary basins. AAPG Bull. 77, 1538-1548.

Bubb, J.N., Perry, D., 1968. Porosity in some synthetic dolomites. Journal of Sedimentary Petrology 38, 247-249.

Buyce, M.R., Friedman, G.M., 1976. Significance of authigenic K-feldspar in Cambrian-Ordovician carbonate rocks of the proto-Atlantic shelf in North America: reply to discussion and new data. Journal of Sedimentary Petrology 46, 1039-1040.

Casey, W.H., Carr, M.J., Graham, R.A., 1988. Crystal defects and the dissolution kinetics of rutile. Geochim. Cosmochim. Acta 52, 1545-1556.

Conliffe, J., Azmy, K., Greene, M., 2012. Dolomitization of the lower Ordovician Catoche formation: Implications for hydrocarbon exploration in western Newfoundland. Mar. Pet. Geol. 30, 161-173.

Dhanaraj, G., Byrappa, K., Prasad, V., Dudley, M., 2010. Springer Handbook of Crystal Growth, Illustrated ed. Springer Science and Business Media, 2010, Heidelberg.

Frezzotti, M.L., Ferrando, S., 2007. Multiphase solid inclusions in ultrahigh-pressure metamorphic rocks: a petrographic approach. Periodico di Mineralogia 76, 113-125. doi:10.2451/2007PM0020.

Fullmer, S., Guidry, S., Gournay, J., Bowlin, E., Ottinger, G., Al Neyadi, A.M., … Edwards, H.E., 2014. Microporosity: characterization, distribution, and influence on oil recovery. Abu Dhabi International Petroleum Exhibition and Conference, 10-13 November, Abu Dhabi, UAE, Abu Dhabi, UAE.

Goldstein, R.H., Reynolds, J., 1994. Systematic of fluid inclusions in diagenetic minerals. SEPM (Society of Sedimentary Geology) Short course 31, 188 pp. DOI: 10.2110/scn.94.31.

Gregg, J.M., 2004. Basin fluid, base-metal sulphide mineralization and the development of dolomite petroleum reservoirs. In: Braithwaite, C.J.R, Rizzi, G., Darke, G. (Eds.), The Geometry and Petrogenesis of Dolomite Hydrocarbon Reservoirs. Geological Society, London, Special Publications, 235, pp. 157-175.

Heath, J.E., Dewers, T.A., McPherson, B.J.O.L., Petrusak, R., Chidsey, T.C., Jr., Rinehart, A.J., Mozley, P.S., 2011. Pore networks in continental and marine mudstones: characteristics and controls on sealing behavior. Geosphere 7, 429-454. doi:10.1130/GES00619.1.

Jones, B., 2013. Microarchitecture of dolomite crystals as revealed by subtle variations in solubility: Implications for dolomitization. Sediment. Geol. 288, 66-80. doi:http://dx.doi.org/10.1016/j.sedgeo.2013.01.004.

Kaczmarek, S.E., Sibley, D.F., 2007. A comparison of nanometer-scale growth and dissolution features on natural and synthetic dolomite crystals: implications for the origin of dolomite. Journal of Sedimentary Research 77, 424-432. doi:10.2110/jsr.2007.035.

Kastner, M., 1971. Authigenic feldspars in carbonate rocks. Mineralogical Society of America 56, 1403-1442.

Klaver, J., Desbois, G., Littke, R., Urai, J.L., 2015. BIB-SEM characterization of pore space morphology and distribution in postmature to overmature samples from the Haynesville and Bossier Shales. Mar. Pet. Geol. 59, 451-466. doi:http://dx.doi.org/10.1016/j.marpetgeo.2014.09.020.

Knight I., Azmy K., Boyce W D., Lavoie D, 2008. Tremadocian carbonate rocks of the lower St. George group, Port au Port peninsula, western Newfoundland: lithostratigraphic setting of diagenetic, isotopic and geochemistry studies.

Newfoundland and Labrador Department of Natural Resources Geological Survey, Report 08-1, 115-149.

Langmuir, D., 1997. Aqueous Environmental Geochemistry. Prentice Hall, Upper Saddle River, N.J, London.

Loucks, R.G., Reed, R.M., Ruppel, S.C., Hammes, U., 2012. Spectrum of pore types and networks in mudrocks and a descriptive classification for matrix-related mudrock pores. AAPG Bull. 96, 1071-1098.

Loucks, R.G., Reed, R.M., Ruppel, S.C., Jarvie, D.M., 2009. Morphology, genesis, and distribution of nanometer-scale pores in siliceous mudstones of the Mississippian Barnett Shale. Journal of Sedimentary Research 79, 848-861. doi:10.2110/jsr.2009.092.

Lucia, F.J., 2004. Origin and petrophysics of dolostone pore space. In: Braithwaite, C.J.R, Rizzi, G., Darke, G. (Eds.), The Geometry and Petrogenesis of Dolomite Hydrocarbon Reservoirs. Geological Society, London, Special Publications, 235, pp. 141-155.

Maliva, R.G., Budd, D.A., Clayton, E.A., Missimer, T.M., Dickson, J.A.D., 2011. Insights into the dolomitization process and porosity modification in sucrosic dolostones, Avon Park Formation (middle Eocene), east-central Florida, U.S.A. Journal of Sedimentary Research 81, 218-232.

Merino, E., Canals, A., 2011. Self-accelerating dolomite-for-calcite replacement: self-organized dynamics of burial dolomitization and associated mineralization. American Journal of Science 311, 573-607.

Metzger, F.W., Kelly, W.C., Nesbitt, B.E., Essene, E.J., 1977. Scanning electron microscopy of daughter minerals in fluid inclusions. Econ. Geol. Bull. Soc. Econ. Geol. 72, 141-152.

Moraila-Martinez, T., Dunkel, K.G., Putnis, A., Putnis, C.V., 2014. Experimental study of the mechanism of the calcite-dolomite replacement. EGU General Assembly 2014, Held 27 April - 2 May, 2014.Geophysical Research Abstracts 16, EGU2014-3990-1.

Morse, J.W., Mackenzie, F.T., 1990. Geochemistry of sedimentary carbonates. Elsevier; Distributors for the U.S. and Canada, Elsevier Science Pub. Co. Amsterdam, NY, U.S.A.

Norbisrath, J.H., Eberli, G., Weger, R.J., Verwer, K., Urai, J., Desbois, G., Laurich, B., 2013. Sub-micron digital image analysis (BIBSEM-DIA), pore geometries and electrical resistivity in carbonate rocks. Abstracts: Annual Meeting - American Association of Petroleum Geologists 2013. Search and Discovery Article #41200 (2013).

Olanipekun, B., Azmy, K., Brand, U., 2014. Dolomites of the Boat Harbour Formation in the Northern Peninsula, western Newfoundland, Canada: Implications for dolomitization history and porosity control. AAPG Bulletin 98, 765-791.

Parnell, J., Carey, P.F., Bottrell, S.H., 1994. The occurrence of authigenic minerals in solid bitumens. Journal of Sedimentary Research, Section A: Sedimentary Petrology and Processes 64, 95-100. doi:10.1306/D4267D20-2B26-11D7-8648000102C1865D.

Perdikouri, C., Kasioptas, A., Geisler, T., Schmidt, B.C., Putnis, A., 2011. Experimental study of the aragonite to calcite transition in aqueous solution. Geochim. Cosmochim. Acta 75, 6211-6224. doi:10.1016/j.gca.2011.07.045.

Putnis, A., Putnis, C.V., 2007. The mechanism of reequilibration of solids in the presence of a fluid phase. Journal of Solid State Chemistry 180, 1783-1786. doi:http://dx.doi.org/10.1016/j.jssc.2007.03.023.

Putnis, C.V., Mezger, K., 2004. A mechanism of mineral replacement: isotope tracing in the model system KCl-KBr-H (sub 2) O. Geochim. Cosmochim. Acta 68, 2839-2848. doi:10.1016/j.gca.2003.12.009.

Roedder, E., 1972. Composition of fluid inclusions. In: Fleischer, M. (Ed.), Data of Geochemistry, 6th edition, U.S. Geological Survey Professional Paper 440JJ.

Ruiz-Agudo, E., Putnis, C.V., Putnis, A., 2014. Coupled dissolution and precipitation at mineral–fluid interfaces. Chem. Geol. 383, 132-146. doi:http://dx.doi.org/10.1016/j.chemgeo.2014.06.007.

Ruiz-Conde, A., Garzón, E., Sánchez-Soto, P.J., 2012. Scanning Electron Microscopy (SEM) and Energy Dispersive X-Ray analysis (EDX) of daughter minerals in fluid

inclusions in layered silicate materials. In: Méndez-Vilas, A. (Ed.), Current Microscopy Contributions to Advances in Science and Technology. Formatex Research Center, Spain, Microscopy book series-Number 5. pp. 1137-1144.

Saller, A.H., 2004. Palaeozoic dolomite reservoirs in the Permian Basin, SW USA; stratigraphic distribution, porosity, permeability and production. In: Braithwaite, C.J.R, Rizzi, G., Darke, G. (Eds.), The Geometry and Petrogenesis of Dolomite Hydrocarbon Reservoirs. Geological Society, London, Special Publications, 235, pp. 309-323.

Sibley, D.F., 1982. The origin of common dolomite fabrics: clues from the Pliocene. J. Sediment. Petrol. 52, 1087-1110.

Skalinski, M., Kenter, J., Jenkins, S., 2009. Carbonate rock type definition and pore type classification in Tengiz Field. Petrophysics Houston, Tex. 50, 172-188.

Sok, R.M., Knackstedt, M.A., Varslot, T., Ghous, A., Latham, S., Sheppard, A.P., 2010. Pore scale characterization of carbonates at multiple scales: Integration of Micro-CT, BSEM, and FIBSEM. Society of Petrophysicists and Well-Log Analysts 51, 379-387.

Vanden Berg, B., Grammer, G.M., 2014. Combining sonic velocity and characterization of pore architecture to develop a proxy for reservoir permeability in unconventional carbonates: an example from the Mid-Continent Mississippian limestone.

SPE/AAPG/SEG Unconventional Resources Technology Conference, 25-27 August, Denver, Colorado, USA. URTec 1927131.

Walker, F.D., Lee, M.R., Parsons, I., 1995. Micropores and micropermeable texture in alkali feldspars: geochemical and geophysical implications. Mineralogical Magazine 59, 505-534.

Warren, J., 2000. Dolomite: occurrence, evolution and economically important associations. Earth-Sci. Rev. 52, 1-81. doi:10.1016/S0012-8252(00)00022-2.

Watanabe, K., 1987. Inclusions in flux-grown crystals of corundum. Cryst. Res. Technol. 22, 345-355. doi:10.1002/crat.2170220310.

Zempolich, W.G., Baker, P.A., 1993. Experimental and natural mimetic dolomitization of aragonite ooids. J. Sediment. Petrol. 63, 596-606. doi:10.1306/D4267B86-2B26-11D7-8648000102C1865D.

Zerfoss, S., Slawson, S.I., 1956. Origin of authigenic inclusions in synthetic crystals. Am. Mineral. 41, 598-607.

Web references

Enhanced oil recovery, *Commonwealth Scientific and Industrial Research Organisation, CSIRO.* http://www.csiro.au/Outcomes/Energy/Energy-from-oil-and-gas/EOR.aspx. Accessed on March 2, 2015.

Carbonate stimulation, Schlumberger. https://www.slb.com/~/media/Files/resources/mearr/num8/51_63.pdf. Accesses on March 3, 2015.

APPENDIX 5.A1

SEM images and EDX spectral analyses of regions of interest in the studied burial dolomites.

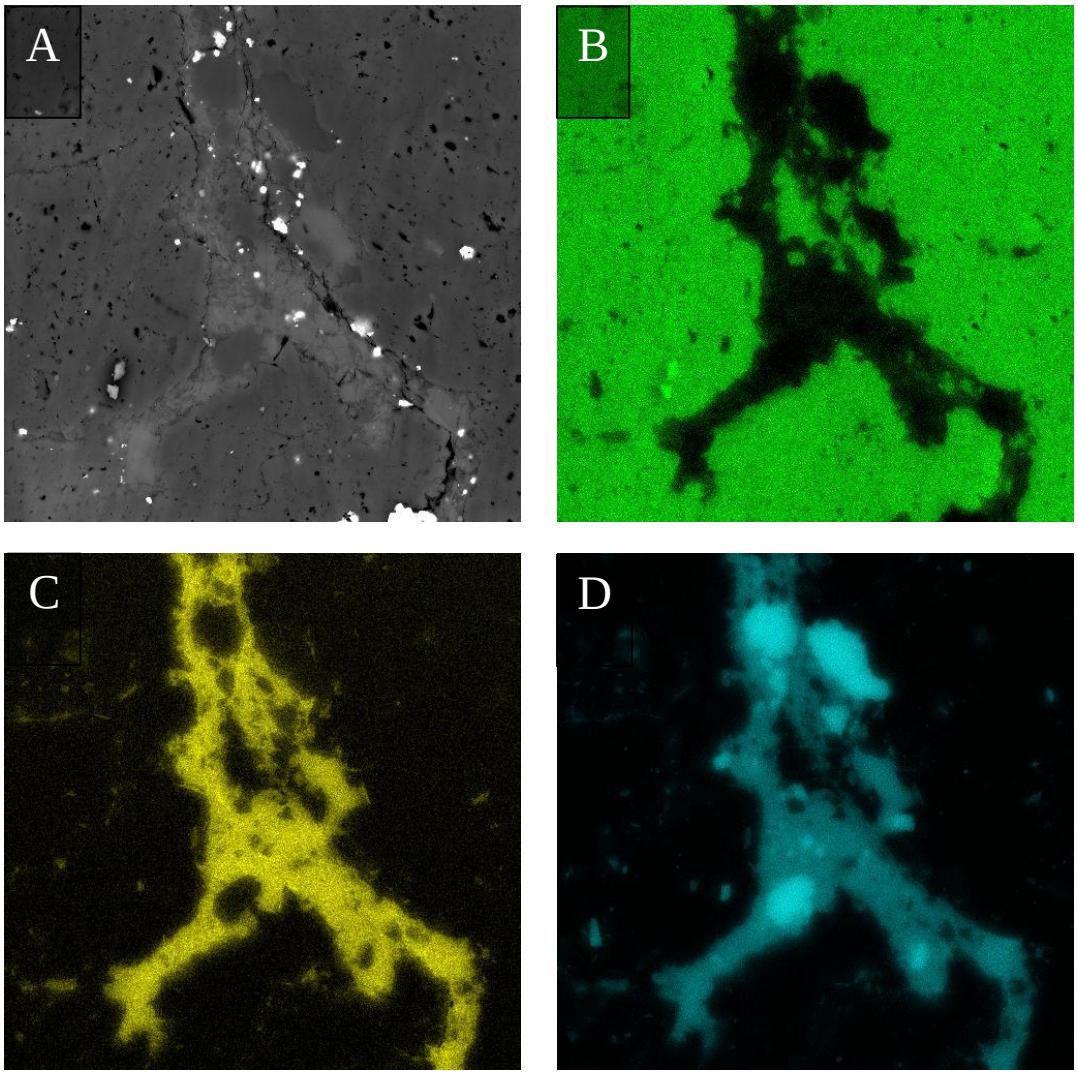

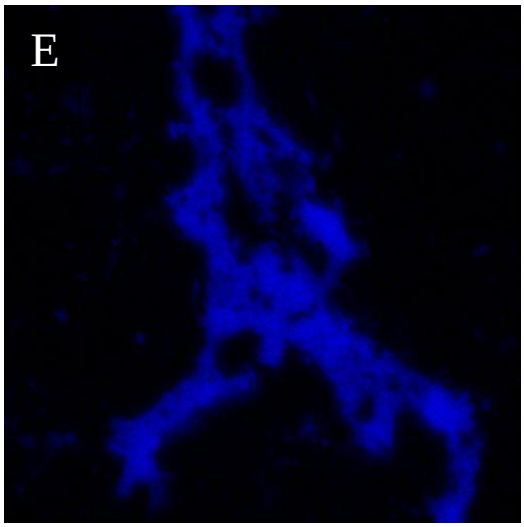

Fig. 5.A1. EDX spectra map of a region of interest in the burial dolomite sample. A is back scattered electron image, B is Mg, C is Al, D is Si and E is K. Sample 6-172.

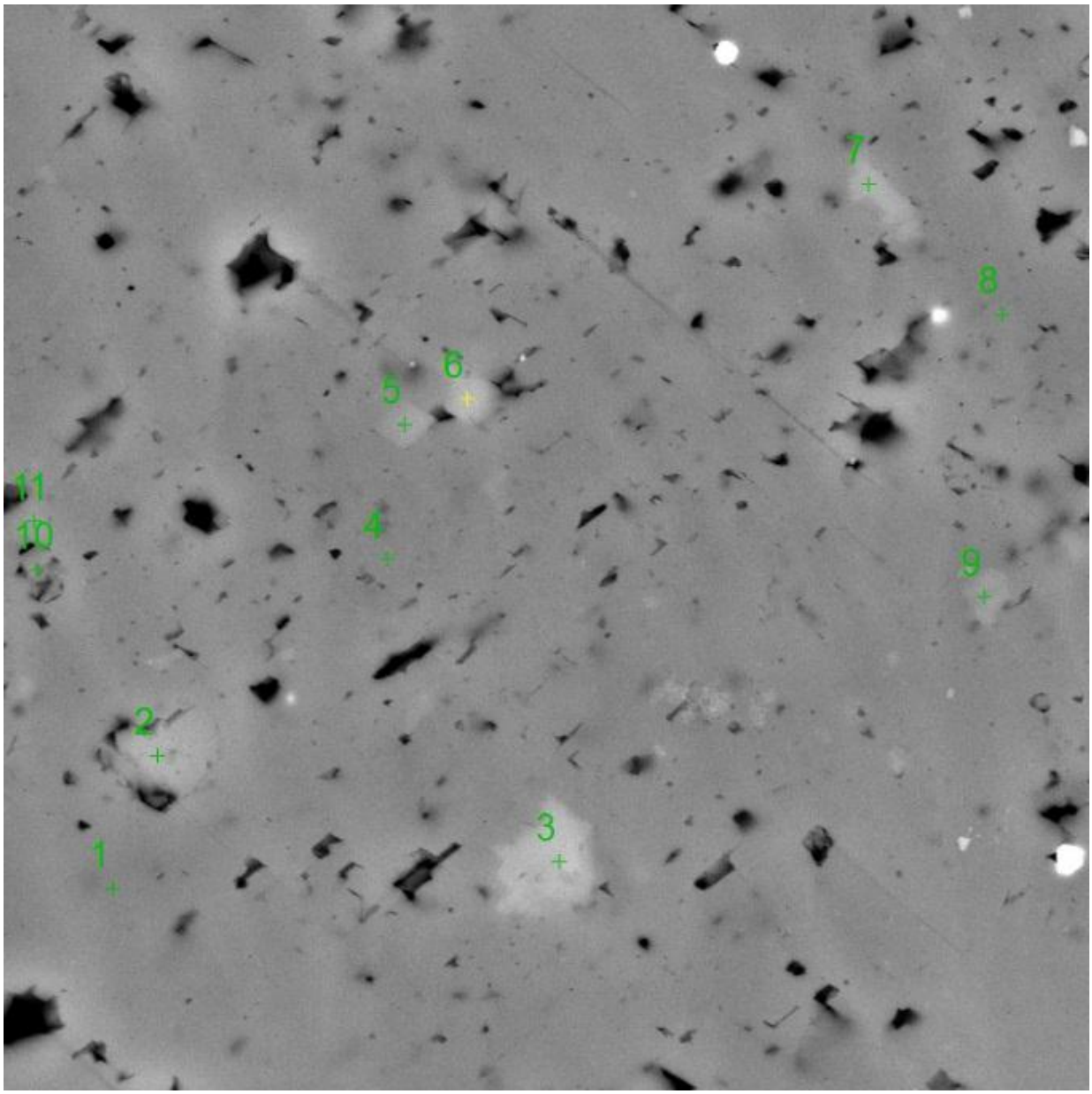

Fig. 5.A2A-F. SEM image showing spot locations (matrix and mineral micro-inclusions) probed by Energy Dispersive X-ray (EDX) analyses within a dolomite crystal. Burial dolomite sample 6-172 from Daniel's Harbour locality.

See below for the spectra data.

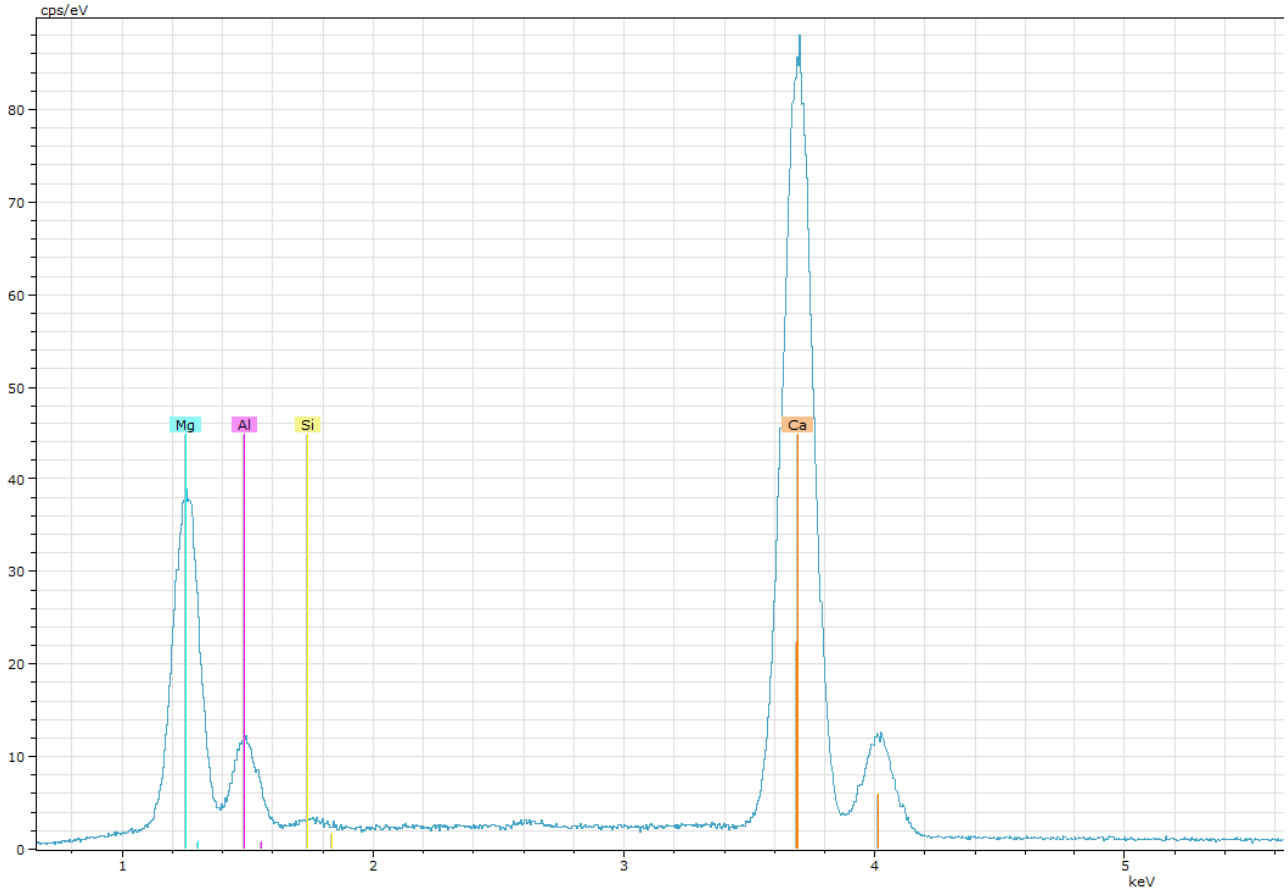

Fig. 5.A2A. Spot 1-Energy Dispersive X-ray (EDX) analyses showing typical spectrum for matrix of the dolomite crystal. Al peak is from the sample holder and not related to the sample, as the samples are not coated.

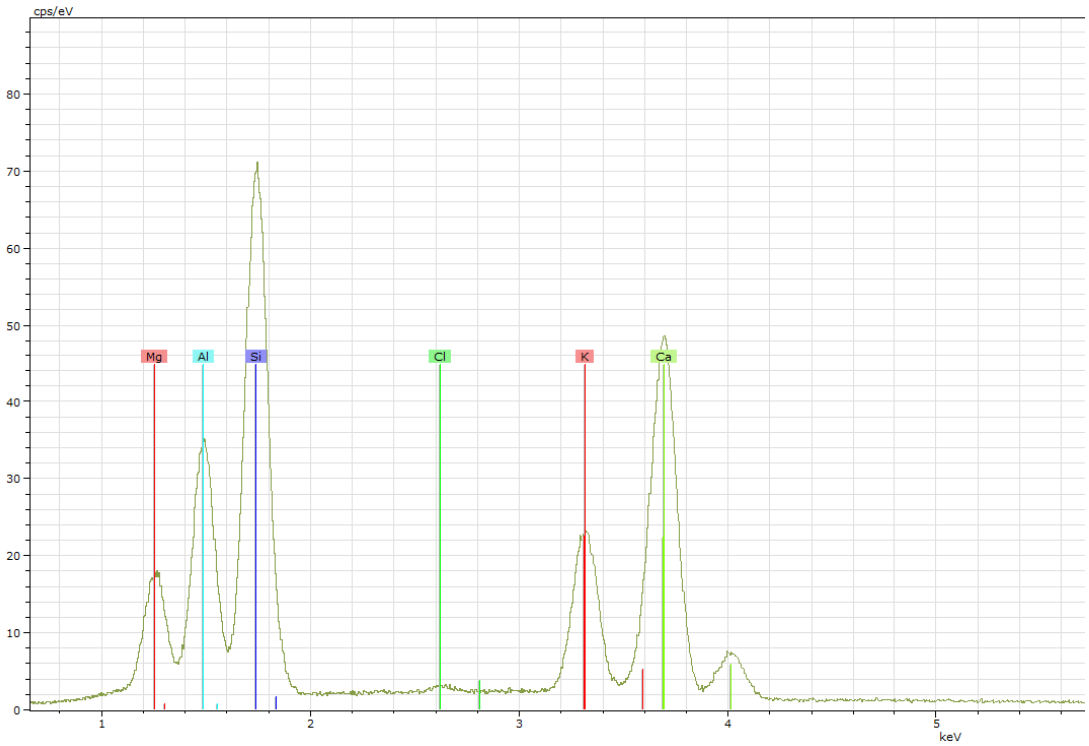

Fig. 5.A2B. Spot 2-EDX analyses showing typical spectrum that indicate K-Feldspar micro-inclusion within dolomite crystal. Note that such occurrence is rare in the studied sample. Al peak is contaminated by Al content of the sample holder, as the samples are not coated. Also note that Mg peak is mostly contamination by the matrix.

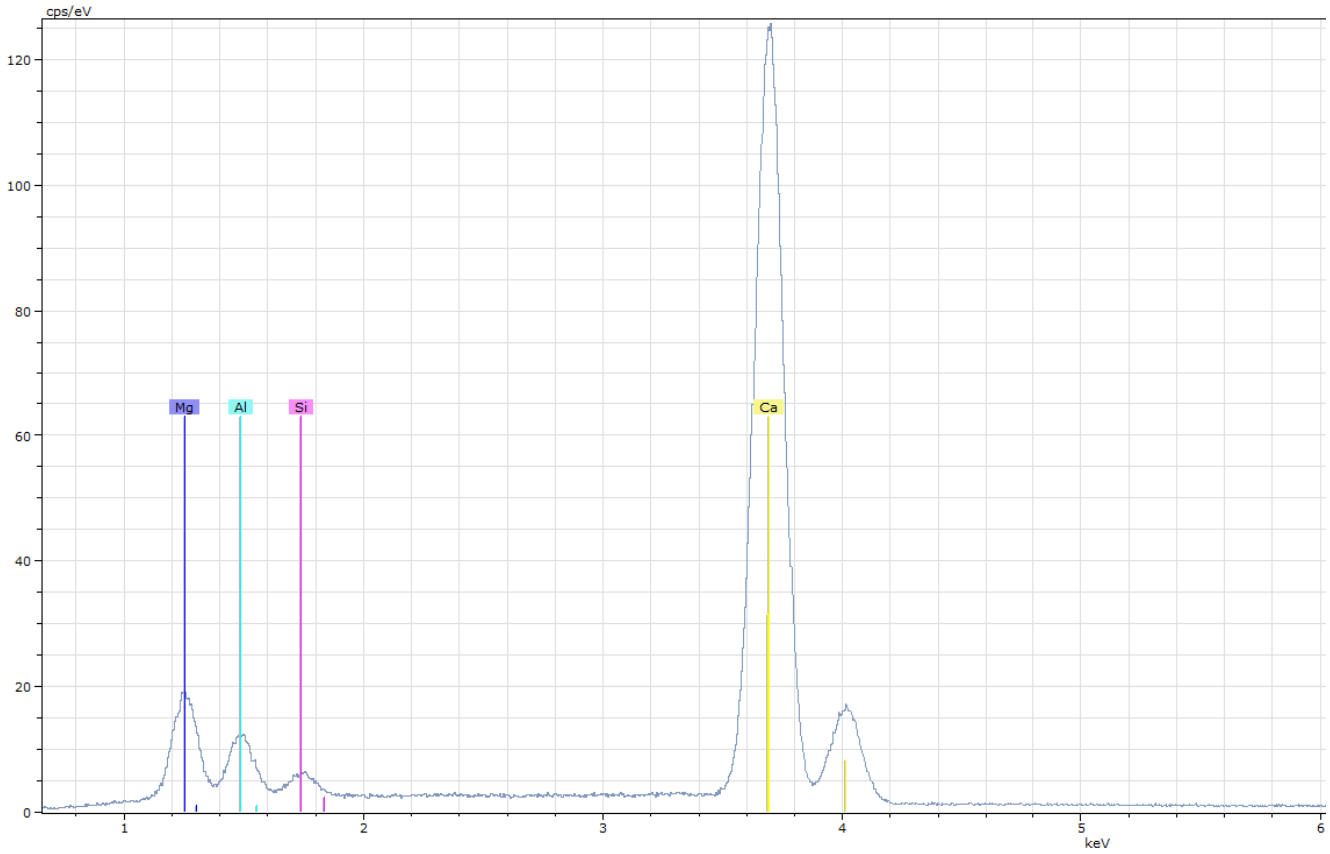

Fig. 5.A2C. Spot 3-EDX analyses showing typical spectrum that indicate calcite micro-inclusion within dolomite crystal. Al peak is from the sample holder and not related to the sample, as the samples are not coated. Also note that Mg peak is mostly contamination by the matrix.

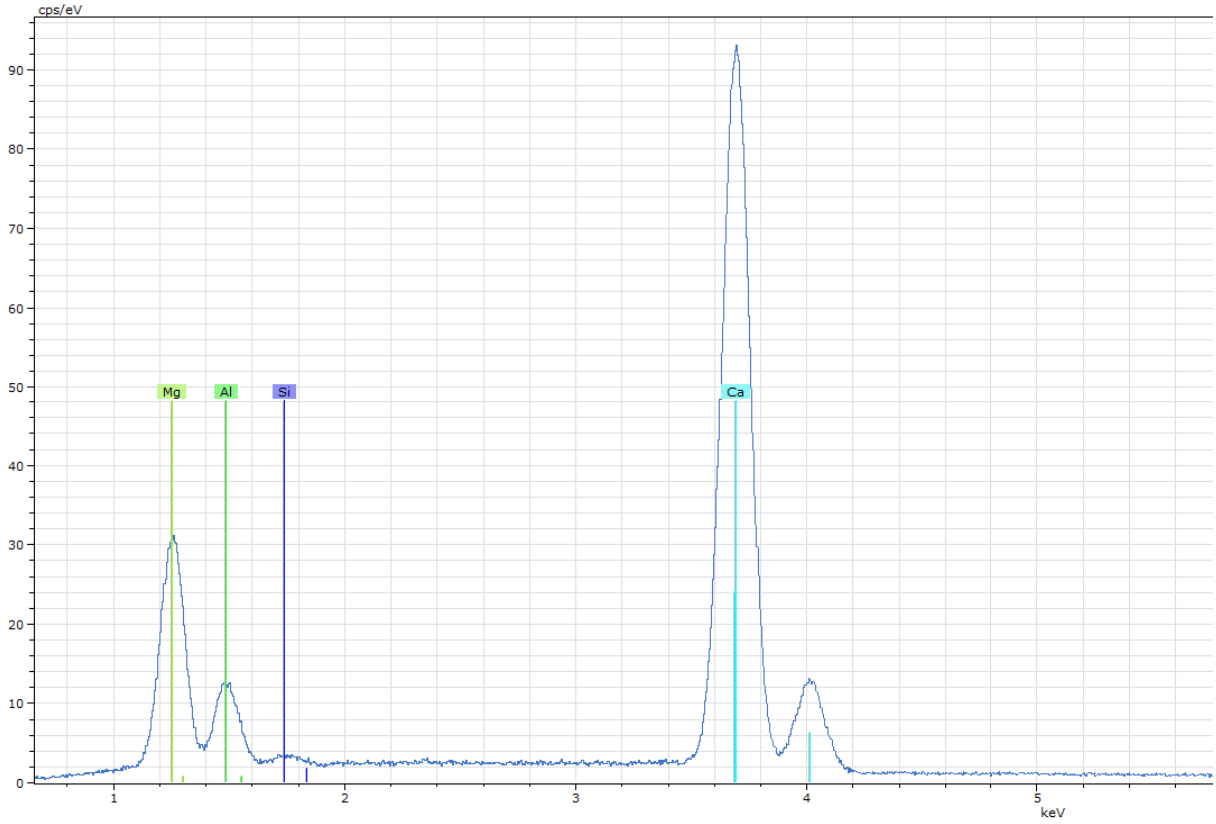

Fig. 5.A2D. Spot 5-EDX analyses showing typical spectrum that indicate Mg-rich calcite micro-inclusion within dolomite crystal. Al peak is from the sample holder and not related to the sample, as the samples are not coated. Note that the matrix contributed to the Mg peak.

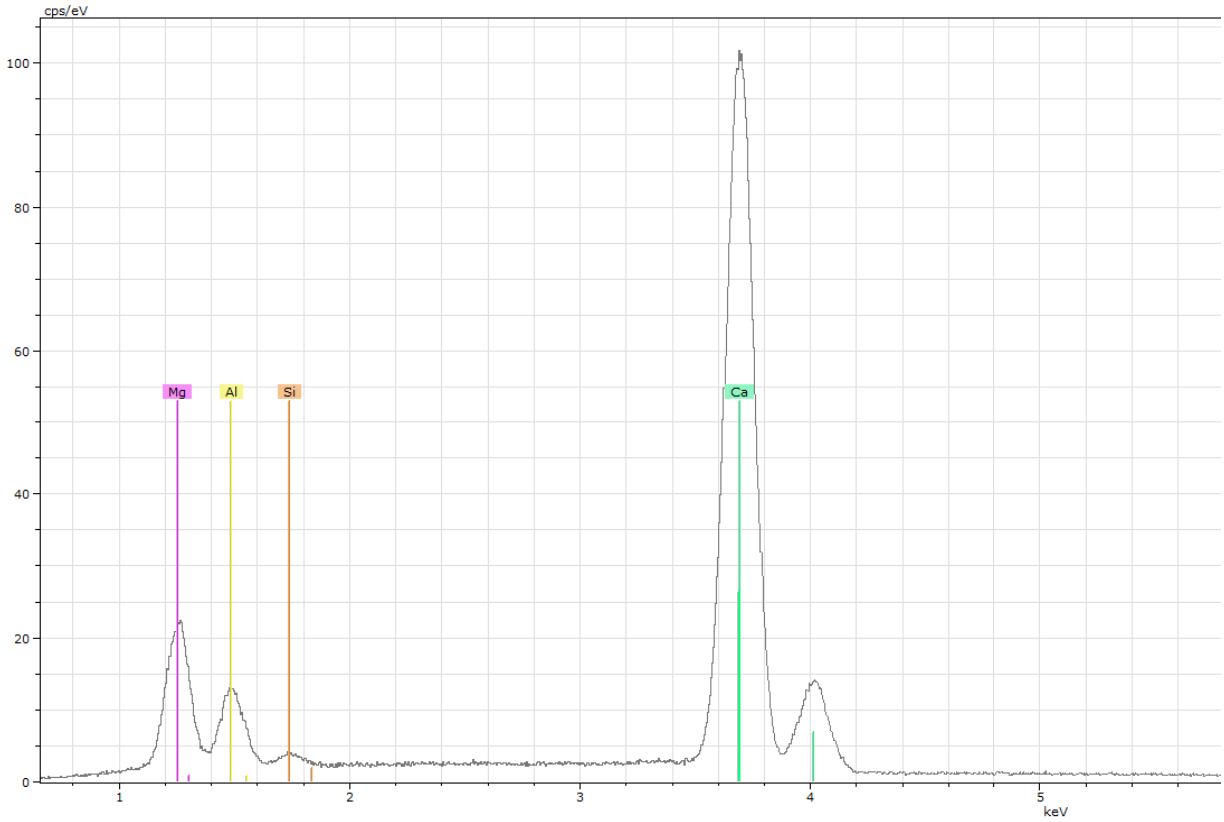

Fig. 5.A2E. Spot 6-EDX analyses showing typical spectrum that indicate calcite micro-inclusion within dolomite crystal. Al peak is from the sample holder and not related to the sample, as the samples are not coated. Also note that Mg peak is contamination by the matrix.

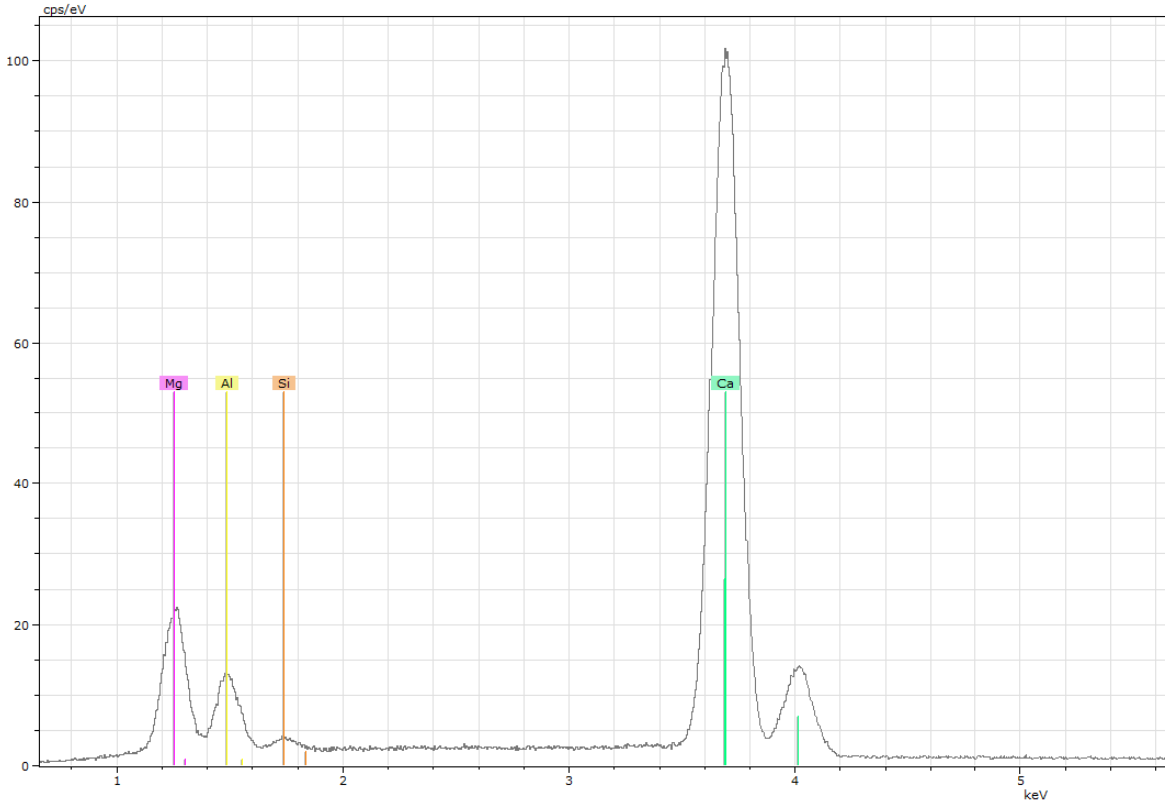

Fig. 5.A2F. Spot 7-EDX analyses showing typical spectrum that indicate calcite micro-inclusion within dolomite crystal. Al peak is from the sample holder and not related to the sample, as the samples are not coated. Also note that Mg peak is contamination by the matrix.

6 CHAPTER 6

OVERALL CONCLUSIONS

Study of the dolomite of Boat Harbour Formation and its associated porosity commenced with multiple crystal populations in Chapter Two to the study of zonations within individual dolomite crystals presented in Chapters Three to Five.

Chapter Two: petrographic examination reveals that the Boat Harbour Formation at the Main Brook location is sparsely dolomitized (~40% in volume), compared with its counterpart at Daniel's Harbour which is completely dolomitized. Near–pristine features indicative of the early dolomitization process are better preserved at Main Brook while more extensive dolomitization altered the geochemical signature of these early phases at Daniel's Harbour.

Data indicate that Boat Harbour Formation carbonates on the Northern Peninsula at Main Brook and Daniel's Harbour and similar to their Isthmus Bay counterparts, were subjected to three major phases of dolomitization. The earliest was D1 dolomicrite, followed by dolomite D2 from an intermediate burial setting, and then late–stage deep burial dolomite D3. The D1 dolomicrites (4–55μm) were likely formed from a mixture of seawater and meteoric water at near–surface conditions.

On the other hand, the coarser dolomite D2 (30–400 μm), associated with enhanced porosity is interpreted to have formed in mid–burial settings from hotter basinal fluid(s). This phase is divided into 2 subphases (D2a, D2b) at Daniel's Harbour, based on distinct petrographic features. It is associated with disconformity zones at Main Brook, similar to that at Isthmus Bay, whereas it is dispersed throughout the formation at Daniel's Harbour. The D3 dolomite (125 μm to 7 mm) which has sweeping extinction is interpreted to have

formed as a late stage dolomite of a deep burial setting, from hot fluids delivered through fractures developed by orogenic events.

The intensity of burial dolomitization in the formation is associated with the two major disconformities, substrate and to a limited extent, tectonic activity. Meteoric dissolution associated with the disconformities enhanced porosity development, through which dolomitizing fluids were able to circulate more efficiently during later and deeper burial stages.

Subsequently, dolomitization and formation of D2 dolomite around the Lower Boat Harbour Disconformity zone enhanced porosity by up to 8 % within 10 – 15 m below the disconformity at Main Brook section. On the other hand, similar porosity enhancement is associated with the Upper Boat Harbour Disconformity at Isthmus Bay, whereas at Daniel's Harbour, porosity ranging from 7–12% is indiscriminately found throughout the sequence.

Chapter 3: With regards to the formation of these dolomites at crystal scale, three crystal facies were identified. Distinctly Zoned Core (DZC) and Indistinctly Zoned Core (IZC) dolomite crystal facies are zoned crystal facies found in Main Brook while the unzoned dolomite crystal facies occur in Daniel's Harbour.

It was found that distinctly zoned core crystal facies has apparently undergone multiple recrystallization episodes while indistinctly zoned core crystal facies, in the same diagenetic setting, has not. Furthermore, geochemically zoned DZC and IZC crystal facies at Main Brook can be interpreted as crystals that grew at a relatively slower rate

than the rate at which the pore fluid's chemistry changed. Here a heterogeneous partition coefficient (HT-PC) controlled elemental partitioning during crystal growth. This means that each growth sector within the crystals is only in thermodynamic equilibrium with the composition of its inter-phase boundary layer, which in turn is a function of the extent of mineral-fluid interaction (Veizer, 1983; Curti, 1997). More so, it can be said that dolomite crystal growth occurred in an evolving redox setting and fluid composition (e.g., reducing salinity from the core to the rim section).

For the CL unzoned crystal facies at Daniel's Harbour, a lack of distinct systematic compositional zoning suggests that the crystals grew at a relatively faster rate than the rate at which the pore fluid's chemical composition changed; whereby elements were partitioned by means of a homogeneous partition coefficient (HM-PC).

Notably, even though elemental incorporation into IZC is also interpreted to be by means of HT-PC, the water-rock ratio is very low. Thus there was relatively less significant geochemical core-to-rim trend for Sr, Na, REE and Y.

Significant water-rock interaction is needed to change the REE and Y composition of rocks. Thus such changes is not expected at the micron scale during a single dolomitization event. Relative depletion of REE and Y at the rim of the dolomite crystals at Main Brook suggests formation from a parent fluid of different composition (e.g., salinity) compared with that of the core. This implies that the formation of core and the rim sections are separated in time. This interpretation is consistent with depletion of Fe

and Mn at the outermost cortex as also supported by a depletion of Na and Sr at the rim section.

Chapter 4: Data collected to understand the luminescence character of the dolomite samples show that, a concentric zoning pattern is exhibited by the zoned dolomite crystals from Main Brook in CL and PhL images. This implies that the same activators and quenchers, or at least many of them control luminescence emissions in both CL and PhL. These same phenomena apply to the unzoned dolomite crystal facies.

It was further found that the only zone in rim section of the distinctively zoned dolomite crystal facies, that emit Mn-activated red luminescence in both CL and PhL, also has relatively higher absolute Mn concentration than the core section. On the other hand the core section lacks Mn-activated red luminescence but emits shorter wavelength luminescence. This was interpreted to mean that intrinsic factors such as lattice defects also control the luminescence character of the core section. In support, removal of wavelength in red spectrum from SEM-CL image reveals moderately bright luminescence (in panchromatic mode) for the core, indicating that such factor perhaps contributed to luminescence.

The unzoned dolomite crystal facies at Daniel's Harbour contain higher Mn than the zoned dolomite crystals facies. This is believed to account for its brighter reddish-luminescence in CL, a color which was not noticeable in PhL.

In all, the data shows that the absolute concentration of Mn and Fe have complex variation with the luminescence characters of the studied samples under CL and PhL.

REE-Y concentrations show no variation with luminescence, perhaps due to their low absolute concentrations. Notably, inorganic components apparently controlled the luminescence observed under CL as well as under PhL in the distinctively zoned dolomite crystal facies from Main Brook. Likewise, inorganic components apparently controlled the luminescence viewed under CL of the unzoned dolomite crystal facies from Daniel's Harbour. However, in the latter, mature organic (bituminous) materials play dominant role in the exhibited luminescence features of PhL and thus mask the expected Mn-activated red luminescence.

Chapter 5: The major finding is that intracrystalline pores and micro-inclusions are shown to be associated with the dolomitization process. Intracrystalline nanopores are abundant in the burial dolomite crystals. They apparently developed as a result of imperfections associated with the alignment process of crystallites' agglomeration. This process also likely resulted in the morphology of the nanopores which is typically made up of protuberances of rhombic apices and has planar edges.

Furthermore, the origin of mineral inclusions in intracrystalline nanopores is likely related to the mechanism of dolomitization that involves dissolution of a precursor carbonate (calcite or early dolomite) and precipitation of dolomite. The Ca for the calcite inclusions in nanopores is likely sourced from a precursor calcite and thus the fact that it is hosted in and restricted to the dolomite crystal cores suggest that the core is a replacive section of the crystal. In contrast, the dolomite crystal rim likely formed as cement due to the fact that nanopores and calcite inclusions are relatively rare, which is similar to the scenario of dolomite cement crystals precipitated in intercrystalline areas. Another important

inference is that the calcite inclusions exhibit features that suggest they are ‘‘accidental’’ minerals, syngenetic with host growth zone and are not daughter mineral that post-date the growth of whole dolomite crystal.